



UNIVERSITÀ DEGLI STUDI
DI TRENTO

DEPARTMENT OF INFORMATION ENGINEERING AND COMPUTER SCIENCE
ICT International Doctoral School

ADVANCED METHODS FOR SIMULATION
AND PERFORMANCE ANALYSIS OF
PLANETARY RADAR SOUNDER DATA

Sanchari Thakur

Advisor

Prof. Lorenzo Bruzzone

Università degli Studi di Trento

January 2020

Dedicated to my father Satindranath Thakur and Godfather Prof. Alok Porwal

Abstract

Radarsounders (RS) are low frequency remote sensing instruments that profile the shallow subsurface of planetary bodies providing valuable scientific information. The prediction of the RS performance and the interpretation of the target properties from the RS data are challenging due to the complex electromagnetic interaction between many acquisition variables. RS simulations address this issue by forward modeling this complex interaction and simulating the radar response. However, existing simulators require detailed and subjective modeling of the target in order to produce realistic radargrams. For less-explored planetary bodies, such information is difficult to obtain with high accuracy. Moreover, the high computational requirements of conventional electromagnetic simulators prohibit the simulation of a large number of radargrams. Thus, it is not possible to generate and analyze a database of simulated radargrams representative of the acquisition scenario that would be very useful for both the RS design and the data analysis phase. To overcome these difficulties and to produce realistic simulated radargrams, this thesis proposes two novel approaches to the simulation and analysis of the radar response. The first contribution is a simulation approach that leverages the data available over geological analogs of the investigated target and reprocesses them to obtain the simulated radargrams. The second contribution is a systematic approach to the generation and analysis of a database of simulated radargrams representing the possible scenarios during the RS acquisition. The database is analyzed to predict the RS performance, to design the instrument parameters, and to support the development of automatic target detection algorithms. To demonstrate the proposed techniques the thesis addresses their use in two future RS instruments, which are at different phases of development: (1) the Radar for Icy Moons Exploration (RIME) and (2) a RS for Earth observation of the polar ice caps. The first contribution focuses on the analysis of the detectability of complex tectonic targets on the icy moons of Jupiter by RIME by simulating the radar response of 3D target models. The second contribution presents a feasibility study for an Earth orbiting RS based on the proposed simulation approaches.

Keywords [Radar sounder, Simulation, Geological Analogs, Planetary Exploration, Performance Assessment, Design]

Acknowledgements

This thesis is a result of the efforts, support and contributions of many to whom I am more grateful than just a mention in this one page of this document. Most importantly I am thankful to Prof. Lorenzo Bruzzone for giving me this opportunity to do a PhD with him, for patiently and compassionately forgiving my mistakes each time, and for the constant encouragement and motivation. I thank the very friendly staff of University of Trento for providing the shelter in which the thesis work was produced. I am specially grateful to Prof. Avik Bhattacharya for bringing me this life-changing PhD opportunity.

The research presented in the thesis chapters are collaborative efforts with my RSlab dear friends who made research a joyful activity: Elisa (for unveiling the 'secrets' of FDTD), Elena (for looking down to our Earth), Christopher (the creator of the MRS simulator), and all the course project and Master thesis students who worked with me (Andrea Vettor, Giulio Della Corte, Giulio Weikmann, Alex). I am particularly grateful to my friend and brother Abin who spend precious time from his busy schedule to proof-read the thesis.

The presence of enlightening seniors has been a guiding force in this journey. A special thanks to Leonardo for patiently demystifying the complex concepts of radar from time to time and answering my weird questions, to Francesca for coordinating the collaborative activities (and the delicious tiramisu), to Massimo for coming up with innovative solutions to practically all problems, to the RIME elders who left behind very systematic solutions to many common radar sounding problems (Ana-Maria, Davide, Adamo), to Aravind for generously sharing his special coding tricks, and to Begum for teaching me signal processing. Sincere thanks to Prof. Heggy and Dr. Scabbia for the useful discussions on FDTD simulations. My grateful regards to all RIME science team members for their valuable feedback on the parts of the thesis work presenting during the meetings.

My earnest gratitude to all my RSlab friends, specially Iwonka, Pat, Shaunak, Tatiana, Akshara, Sudipan, Milad, Davide Pirrone, Daniele, Claudia, Mahdi who provided the moments of joy and hope in the midst of frustrating failures. My PhD in this beautiful scenic city of Trento also gave me wonderful memories and friends Sumi, Arun, Shine, Jinu, Tinku, my little friend Arwen, Namita, Dr Bruno, Tadeus, Baharah, Ami, Prerana, Priya and Sunil. In closing the Trento chapter, I must convey my deepest gratitude to Balanand for facing my dark side with great maturity and compassion, and encouraging me to refocus on research.

Looking back at my homeland, I gratefully acknowledge Prof. Porwal and my friends from the PlanEx lab at CSRE, IIT Bombay for teaching me geology informally, specially Bijal, Malcolm and Ranjan (from whom I got the idea of analogs). My sincere gratitude

to Dr. Rajitha and Prakash sir who have a special contribution in laying the foundations of remote sensing in me during my Bachelors. A special thanks to my CSRE friends for remote sensing their good wishes across the oceans. The final words of gratitude are for my mother and father who faced my long absence from home with a cheerful and encouraging smile.

Sanchari

The works compiled in this thesis was partially supported by the Italian Space Agency (1) under Contract ASI/INAF n. 2013-056-R.O “Partecipazione italiana alla fase A/B1 della missione JUICE”; (2) under Grant No ASI 2018-25-HH.0 in the framework of “Attività scientifiche per JUICE fase C/D”; and (3) under the contract ASI n. 2016-14-U.O “SaTellite Radar sounder for eArTh sUb-surface Sensing (STRATUS).”

Contents

1	Introduction	1
1.1	Background	1
1.2	Problem definition and motivation	3
1.3	Novel contributions of the thesis	5
1.3.1	Proposed methods for simulation and analysis of radargrams	6
1.3.2	Performance assessment of future radar sounder missions	7
1.4	Structure of the Thesis	9
	Part I: Background	13
2	Radar sounders	13
2.1	Introduction	13
2.2	Principles of radar sounding	14
2.2.1	Signal transmission	14
2.2.2	Acquisition process	16
2.2.3	Interaction with the target	17
2.3	Radar echo processing	18
2.3.1	On-board processing	18
2.3.2	Low-level processing	19
2.3.3	High-level processing	22
2.4	RS instruments: past, present and future	25
2.4.1	MARSIS	27
2.4.2	SHARAD	28
2.4.3	Radar sounding of the Moon	28
2.4.4	CONSERT	29
2.4.5	Radar sounding of the Jovian icy moons	30
2.4.6	Subsurface sounding of Venus	31
2.4.7	Earth observation radar sounders	32

2.5	Conclusions	33
3	Radar response simulation and performance assessment techniques	35
3.1	Introduction	35
3.2	Modeling the acquisition scenario	37
3.2.1	Target modeling	37
3.2.2	Environment modeling	41
3.3	Performance assessment of radar sounders	43
3.3.1	Preliminary performance assessment	44
3.3.2	Radar sounder simulation techniques	49
3.4	Conclusions	53
	Part II: Proposed methods for simulation and analysis of radargrams	57
4	An approach to the simulation of RS radargrams based on geological analogs	57
4.1	Introduction	57
4.2	Geological analogs in planetary exploration	59
4.3	Methodology	60
4.3.1	Notation and terminology	60
4.3.2	Assumptions	61
4.3.3	Target models	63
4.3.4	Analog-based approach to the simulation of investigated radargrams	65
4.4	Case studies: Application of the proposed approach	69
4.4.1	Taxonomy of combinations of analog and investigated scenarios	69
4.4.2	Case I: Same observation target with different instruments	71
4.4.3	Case II: Different observation targets with similar instruments	75
4.4.4	Case III: Future missions on unexplored observation targets	80
4.5	Conclusions	86
5	An approach to the generation and analysis of databases of simulated RS data for performance prediction and target interpretation	89
5.1	Introduction	90
5.2	Comparison between different simulation techniques	92
5.3	Proposed Approach: Construction of the database	93
5.3.1	Definition of the acquisition scenarios	94
5.3.2	Database of geo-electrical models	94
5.3.3	Database of simulated radargrams	95

5.4	Proposed approach: Analysis of the databases	96
5.4.1	Performance analysis	96
5.4.2	Feature analysis	97
5.4.3	Similarity analysis	98
5.5	Experimental results	103
5.5.1	Construction of the databases	103
5.5.2	Analysis of the databases	107
5.5.3	Discussion	115
5.6	Conclusion	116
Part III: Performance assessment of future radar sounder missions		121
6	Performance assessment of RIME: subsurface sounding of the Jovian icy moons	121
6.1	Introduction	121
6.2	Methodology for performance assessment	123
6.2.1	Target geo-electrical modeling	124
6.2.2	FDTD simulation approach	129
6.3	Experimental results	132
6.3.1	Bright and dark terrain geo-electrical profiles	132
6.3.2	Grooved bright terrain: radar response of individual faults	133
6.3.3	Grooved bright terrain: detectability of the brittle-ductile interface	136
6.4	Discussions and Conclusions	137
7	Performance assessment of a radar sounder for Earth observation: subsurface sounding of the polar ice caps	139
7.1	Introduction	139
7.2	Methodology for performance assessment	141
7.2.1	Modified analog-based simulation approach	142
7.2.2	Analysis of the performances of the EORS	144
7.3	Experimental results	147
7.3.1	Description of the inputs	147
7.3.2	Simulated EORS radargrams	149
7.3.3	Layer detection performance	150
7.3.4	Basal interface detection performance	152
7.4	Discussions and Conclusions	152

8 Conclusions	155
8.1 Overall importance of the thesis	155
8.2 Novel contributions	156
8.3 Discussion and critical analysis	158
8.4 Future work	160
Bibliography	163

List of Tables

4.1	Main effects of radar and target parameters on the radargram	62
4.2	Taxonomy of cases for application of the proposed analogs approach	70
4.4	Instrument parameters of the existing and scheduled RSs used for demonstrating the proposed approach	71
4.5	Case I: Value of the mutual information for the case of SHARAD to MARSIS	75
4.6	Case II: Value of the mutual information for the case of LRS to MARSIS . . .	79
5.1	Comparison of available simulation techniques	92
5.2	Example of acquisition variables and the corresponding hypotheses for the Ganymede pedestal crater target	104
5.3	Sensitivity analysis of the contrast variable using the database of simulated radargrams (S')	109
5.4	Feature analysis of the database of simulated pedestal crater radargrams: p-values of the ANOVA test	110
5.5	Estimation of variable significance using similarity analysis	114
6.1	Proposed analysis for the RIME test cases of the geological features on Ganymede	125
7.1	Proposed EORS [16] and ARS [141] parameters	147
7.2	Basal interface detection performance (in percentage) for different targets .	152

List of Figures

1.1	Schematic representation of the simulation process	4
2.1	Schematic illustration of the process of subsurface mapping using radar sounding	15
2.2	Example of RS transmitted signal	16
2.3	Examples of algorithms for automatic target detection in RS data	24
2.4	Past and future satellite missions carrying on-board RS instruments	26
3.1	Schematic representation of the general scenario with respect to the design of the RS, the modeling of the target and the environment, and the required precision in the performance assessment with the progress of the mission . . .	36
3.2	Requirements in different phases of mission design	36
3.3	Example of 3D geo-electrical model representing the complex permittivities $\epsilon(x, y, z)$ for every quantitative cell (voxel).	40
3.4	Frequency-dependent galactic noise temperature	42
3.5	Schematic representation of radar performance evaluation	44
4.1	Flowchart describing the RS acquisition process and its relation with simulation and geological interpretation.	58
4.2	Nomenclature of the variables describing the analog and the investigated acquisition scenarios.	61
4.3	Methodology flowchart along with the notation used to represent the radar-gram and its row and column indices at each step.	63
4.4	Geo-electrical modeling for the analog-based simulation approach	64
4.5	Case I: Ground tracks for the analog SHARAD and the investigated MARSIS radargrams	72
4.6	Example of signal magnitude correction (Case I).	73
4.7	Case I: Reference analog radargram, average radar trace plots, simulated radargram and the real investigated radargram	74

4.8	Case I: Histograms showing the probability density plots of the analog and investigated radargrams	75
4.9	Case II: Ground tracks for the investigated MARSIS and analog LRS data. .	76
4.10	Case II: Reference analog radargram, average radar trace plots, simulated radargram and the real investigated radargram	77
4.11	Case II: Normalized average magnitude of the simulated, real investigated and reference analog radar traces	78
4.12	Case II: Histograms showing the probability density plots of the analog and investigated radargrams	78
4.13	Case III: Ground track for the analog SHARAD radargrams and the image of the investigated feature on Ganymede	81
4.14	Case III: Dark terrain geo-electrical model used as input for the proposed approach.	82
4.15	Case III: Boxplot of the analog radargram and simulated RIME radargrams for different parameter combinations.	83
4.16	Case III: Histograms showing the probability density plots of the analog and investigated radargrams	83
4.17	Case III: Reference analog SHARAD radargram and simulated RIME radargrams for different instrument parameters	84
4.18	Case III: Average radar trace magnitude normalized with respect to the surface	85
4.19	Case III: Average radar trace magnitude plot normalized with respect to the surface of the hypothetical geo-electrical models	86
4.20	Comparison between conventional and proposed simulation approaches . . .	87
5.1	Conceptual illustration of the proposed approach to the generation and analysis of the database of radar responses	91
5.2	Flowchart of the procedure for database generation and analysis. The figure also shows the notation used in the chapter.	93
5.3	Example of a sorted similarity matrix considering 3 acquisition variables $\bar{V}_1, \bar{V}_2, \bar{V}_3$ and the corresponding hypotheses.	99
5.4	Selected Mars analog features of the Ganymede pedestal craters.	103
5.5	Example of geo-electrical models of the Mars analog and Ganymede pedestal craters	105
5.6	Example of simulated radargrams of the pedestal craters	106
5.7	Plot of the performance measures of each simulated radargram for the pedestal craters P1 and P2.	107
5.8	RIME sensitivity to the contrast variable	108
5.9	Example of similarity matrices generated from the pedestal crater database	111

6.1	Flowchart of the FDTD simulation workflow for the performance assessment of RIME.	123
6.2	Galileo image of Ganymede showing the dark terrain cross-cut by swaths of the smooth and the grooved bright terrain. (Image credit: NASA/JPL) . . .	124
6.3	Geological model of the grooved bright terrain faults	126
6.4	Geophysical profiles of Ganymede	127
6.5	Geo-electrical models of Ganymede	127
6.6	Model of full grooved bright terrain with BDI	128
6.7	Input RIME waveform for FDTD simulations	130
6.8	Simulated normalized radar trace power for the dark and bright terrains . .	132
6.9	Grooved bright terrain - average normalized radar traces of individual fault under different hypotheses	133
6.10	Grooved bright terrain - simulated radargrams of individual faults under different hypotheses	135
6.11	Grooved bright terrain - FDTD results of the full model	136
7.1	Flowchart of the proposed methodology	142
7.2	Selected ARS radargram tracks labelled by the type of target: (a) in Greenland, (b) in Antarctica.	148
7.3	Examples of simulated radargrams and the average radar trace plots corresponding to the ARS data 20131127_01_041 in East Antarctica.	149
7.4	Results of the layer detection performance for different types of targets and values of P_tG	150
7.5	Feasible instrument parameter value for detectability of all cryosphere targets for different conditions on the layer detection metric and the cumulative fraction of radar traces	151

List of Abbreviations

ALSE Apollo 17 Lunar Sounder Experiment.

ANOVA analysis of variance.

ARS airborne radar sounder.

ASI Agenzia Spaziale Italiana.

BDI brittle-ductile interface.

BT bright terrain.

cb constant base temperature profile.

CLUSIM clutter simulator.

CMB cosmic microwave background.

CONSERT Comet Nucleus Sounding Experiment by Radiowave Transmission.

cont continuous structure.

COR pixel-to-pixel correlation.

CRESIS Centre for Remote Sensing of the Ice-Sheets.

cs constant slope temperature profile.

DIF average pixel-to-pixel difference.

discont discontinuous structure.

DT dark terrain.

ESA European Space Agency.

FDTD Finite Difference Time Domain.

GPR ground penetrating radar.

HRO High resolution orbit.

IAU International Astronomical Union.

Impf impurity profile.

JAXA Japan Aerospace Exploration Agency.

JUICE JUperiter ICy moons Explorer.

LRO Low resolution orbit.

LRS Lunar Radar Sounder.

MARSIS Mars Advanced Radar for Subsurface and Ionosphere Sounding.

MCoRDS Multi-channel Coherent Radar Depth Sounder.

MFF Medusae Fossae formation.

MI mutual information.

MOLA Mars Orbiter Laser Altimeter.

MRO Mars Reconnaissance Orbiter.

MRS Multi-layer coherent radar sounder simulator.

NASA National Aeronautics and Space Administration.

NPLD North Polar Layered Deposits.

OASIS Orbiting Arid Subsurface and Ice Sheet Sounder.

Pd probability of subsurface detection.

PML Perfectly Matched Layers.

PRF pulse repetition frequency.

PRI pulse repetition interval.

RDR radar dynamic range.

REASON Radar for Europa Assessment and Sounding: Ocean to Near-surface.

RIME Radar for Icy Moons Exploration.

RS radar sounder.

SAR Synthetic Aperture Radar.

SCR signal-to-clutter ratio.

SELENE Selenological and Engineering Explorer.

SHARAD Shallow Radar.

SHARSIM SHARAD Radargram SIMulator.

SNR signal-to-noise ratio.

SPLD South Polar Layered Deposits.

SRS Subsurface Radar Sounder.

SSIM structural similarity index measure.

SSNR subsurface signal to noise ratio.

SSR subsurface to surface power ratio.

SST time to subsurface.

Str structure.

STRATUS SaTellite Radar sounder for eArTh sUbsurface Sensing.

SurfSNR surface signal to noise ratio.

TEC total electron count.

Vfn void fraction.

List of Symbols

$k_{Boltzmann}$	Boltzmann constant
c	Speed of light in vacuum
ϵ_0	Dielectric permittivity of free-space
$\text{Re}\{\}$	Real part of the complex term in the braces
$\text{Im}\{\}$	Imaginary part of the complex term in the braces
I_1, I_2	General representation of a pair of images (radargrams or geo-electrical models)

SYMBOLS RELATED TO DISTANCE

x	Distance in the along-track direction
y	Distance in the cross-track direction
z	Distance in the nadir direction representing the depth below the surface
$z(r_A, c_A)$	Depth of the echo sample at index position (r_A, c_A) from $r_A = 1$
X_A	Along-track distance support axis of the analog radargram
ΔX_A	Along-track resolution of the analog radargram
X_I	Along-track distance support axis of the investigated radargram
ΔX_I	Along-track resolution of the investigated radargram

SYMBOLS RELATED TO FREQUENCY

ω_m	Frequency axis of the magnitude corrected radargram
ω_b	Frequency axis of the radargram after bandwidth correction

SYMBOLS RELATED TO TIME

Δt_A	Time resolution of the echo samples of the analog radargram
Δt_I	Time resolution of the echo samples of the investigated radargram
$t_A(r_A, c_A)$	Time delay between the echo sample at index position (r_A, c_A) and $r_A = 1$

$\tau_{sm}(r_A, c_A)$ Time delay between the echo sample at position (r_A, c_A) calculated using z and $\epsilon'_I(r_A, c_A)$

SYMBOLS RELATED TO DIELECTRIC PROPERTIES

ϵ General notation for complex dielectric permittivity of the subsurface medium

$\tan\delta$ General notation for the loss tangent of the subsurface medium

ϵ_{pure} Complex dielectric permittivity of a pure material

ϵ_{eff} Effective dielectric permittivity of a mixture of the pure material and impurities

$\epsilon_{3D}(x, y, z)$ Complex three-dimensional geo-electrical model defined at every point x, y, z in space

ϵ_{static} Debye parameter of low frequency (static) permittivity

ϵ_{∞} Debye parameter of high frequency permittivity

τ_{debye} Debye parameter of relaxation time

σ_{e-} Inelastic scattering of free charge carriers by the material

Γ_{SS} General representation of the subsurface wave propagation factor that includes the Fresnel reflection and transmission coefficients, and the attenuation loss in the subsurface medium

$\epsilon_A(r_A, c_A)$ Complex dielectric permittivity corresponding to the geo-electrical model of the analog scenario

$\epsilon_I(r_A, c_A)$ Complex dielectric permittivity corresponding to the geo-electrical model of the investigated scenario

$\Gamma_A(r_A, c_A)$ Wave propagation factor quantifying the echo power from the cell r_A , for the analog scenario

$\Gamma_I(r_A, c_A)$ Wave propagation factor quantifying the echo power from the cell r_A , for the investigated scenario

$R_A(r_A, c_A)$ Interface reflection coefficient between r_A and $r_A + 1$ for the analog scenario

$R_I(r_A, c_A)$ Interface reflection coefficient between r_A and $r_A + 1$ for the investigated scenario

$L_A(k, c_A)$ Attenuation loss corresponding to signal transmission between k and $k + 1$ positions, for the analog scenario

$L_I(k, c_A)$ Attenuation loss corresponding to signal transmission between k and $k + 1$ positions, for the investigated scenario

ϵ_b Average complex permittivity of the basal subsurface layer (substrata)
Cntr Dielectric contrast in the real permittivity between the surface and the subsurface layers

$\alpha(z)$ Target attenuation profile that depends on the dielectric properties

SYMBOLS RELATED TO GEOPHYSICAL TEMPERATURE

T(z) Geothermal temperature profile of Ganymede

Ts Surface temperature of Ganymede

Th Scale height of Ganymede temperature profile

SYMBOLS RELATED TO THE IONOSPHERE

f_{plasma} Plasma frequency of the ionosphere in Hz

ρ_e Electron density of the ionosphere in cubic meters

ϵ_{ta} Refractive index of the ionosphere

f Frequency components of the radar signal

ν Electron-neutral collision frequency of the ionosphere

α_{iono} Signal power attenuation caused by the ionosphere in dB/km

$\Delta\phi$ Phase shift in the signal caused by propagating through the ionosphere

SYMBOLS RELATED TO THE TOPOGRAPHY

Δx Horizontal scale at which surface topography parameters are evaluated (typically equal to the wavelength of the RS)

Δx_0 Horizontal scale at which the surface topography parameters are available (typically the resolution of the digital elevation data)

ζ Allan deviation of the surface heights at the horizontal scale Δx

ψ Allan deviation of the surface slope at the horizontal scale Δx

ζ_0 Allan deviation of the surface heights at the horizontal scale Δx_0

ψ_0 Allan deviation of the surface slopes at the horizontal scale Δx_0

H Hurst coefficient

λ_L Long wavelength of the grooved bright terrain topography

λ_S Short wavelength of the grooved bright terrain topography

A_L Amplitude of the long wavelength component of the grooved bright terrain topography

A_S	Amplitude of the short wavelength component of the grooved bright terrain topography
$A(x)$	Profile of the grooved bright terrain surface
$square()$	Function to generate square wave of a given periodicity

SYMBOLS REPRESENTING INDICES AND NUMBERS

r_A	Row index of reference analog radargram
N_{r_A}	Number of rows (samples) in the reference analog radargram
r_t	Row index of radargram after time resampling correction
N_{r_t}	Number of rows (samples) in the radargram after time resampling correction
r_I	Row index of the real investigated radargram
N_{r_I}	Number of rows (samples) of the real investigated radargram
c_A	Column index of the reference analog radargram
N_{c_A}	Number of columns (radar traces) in the reference analog radargram
c_h	Column index of the radargram after along-track resolution correction
N_{c_h}	Number of columns (radar traces) in the radargram after along-track resolution correction
c_I	Column index of the real investigated radargram
N_{c_I}	Number of columns (radar traces) of the real investigated radargram
i	Index of the acquisition variables
N_a	Number of acquisition variables
j	Index of the hypothesis values of the acquisition variables
n_i	Number of hypotheses of the variable \bar{V}_i
s	Index of the unique combination of the acquisition variable hypotheses
N_s	Number of unique combinations of the acquisition variable hypotheses
k	Index of the geo-electrical variables
N_g	Number of geo-electrical variables
l	Index of the hypothesis values of the geo-electrical variables
m_k	Number of hypotheses of the variable \bar{G}_k
e	Index of the unique combination of the geo-electrical variable hypotheses

N_e	Number of unique combinations of the geo-electrical variable hypotheses
T	Target label associated to each radar trace of the ARS and simulated EORS radargrams

SYMBOLS RELATED TO NOISE

\mathbf{T}_{cmb}	Galactic cosmic microwave background noise temperature in Kelvin
$\mathbf{T}_{eq,I}$	Equivalent noise temperature of the investigated scenario
P_{cmb}	Galactic noise power
P_n	Noise power of the radargram
$P_{n,A}$	Noise-power level of the analog radargram
$P_{n,I}$	Noise-power level of the investigated radargram
N_T	Noise threshold estimated from the noise samples in the free-space propagation region of the radargram
Z	Rayleigh distributed $N_{r_A} \times N_{c_A}$ noise samples

SYMBOLS RELATED TO RS PERFORMANCE

$SurfSNR$	Surface signal-to-noise ratio
σ_s	Radar cross section of the surface
θ	Radiation incidence angle
$\bar{\theta}$	Off-nadir radiation incidence angle contribution to the clutter
ρ_{alt}	Along-track footprint size
ρ_{act}	Across-track footprint size
ρ_{planet}	Radius of the investigated planetary body
D_F	Diameter of the Fresnel zone
D_{pl}	Diameter of the pulse-limited footprint
Δr	Range (vertical) resolution
ρ_{alt}^f	Maximum theoretical along-track resolution for a fully focused processed radargram
c_h^T	Radar traces of the simulated EORS radargram associated to the target label T
$\vartheta_L(c_h)$	Layer detection performance metric evaluated for the radar trace c_h

$N_{c_h}^{(T)}(\vartheta_L)$	Fraction of the total number of radar traces belonging to the target T for which the layer detection metric greater than ϑ_L
$\vartheta_B(c_h)$	Basal interface detection metric for the radar trace c_h

SYMBOLS RELATED TO THE ANALOG-BASED METHOD

V_A	Reference analog radargram complex echo
V_{sig}	Radargram complex echo after signal magnitude correction
V_m	Radargram complex echo after signal and noise magnitude correction
V_b	Radargram complex echo after bandwidth correction
V_t	Radargram complex echo after time resampling correction
V_{sm}	Simulated investigated radargram complex echo
V_I	Real investigated radargram complex echo
$P_{r,A}(r_A, c_A)$	Power received by the analog instrument
$P_{r,I}(r_A, c_A)$	Estimated power that would be received by the investigated instrument
$S_m(\omega_m)$	Fourier representation of the magnitude corrected radargram
$S_{bw}(\omega_b)$	Fourier representation of the radargram after bandwidth increase or decrease, prior to power compensation
$S_b(\omega_b)$	Fourier magnitude of bandwidth corrected and power compensated radargram
$\mathbf{v}(r_A, c_A)$	Binary signal-noise image produced as an intermediate output in the signal magnitude correction step
$\kappa(r_A, c_A)$	Soft noise-thresholded mask obtained by Gaussian-filtering the signal-noise image
σ_{kernel}	Standard deviation of the Gaussian kernel used for smoothing the binary signal-noise image
Ω	Size of the Gaussian-filter used in signal magnitude correction

SYMBOLS RELATED TO THE RS DESIGN PARAMETERS. SUBSCRIPTS ANALOG (A) AND INVESTIGATED (I)

$P_{t,A}, P_{t,I}$	Transmitted power
G_A, G_I	Antenna gain
λ_A, λ_I	Wavelength

$f_{c,A}, f_{c,I}$	Central frequency
f	Frequency components of the RS signal for the given bandwidth and central frequency
$H_A(c_A), H_I(c_A)$	Spacecraft altitude measured from the planetary surface
B_A, B_I	Receiver bandwidth
G_{range}	Range processing gain
G_{alt}	Along-track processing gain
t_{pulse}	Pulse-width of the radar signal
f_{PRF}	Pulse-repetition frequency of the RS
v_s	Speed of the platform (aircraft or satellite) carrying the RS
L_a	Length of the antenna oriented along the track

SYMBOLS RELATED TO THE DATABASE OF RADAR RESPONSE

V	Set of acquisition variables
\bar{V}_i	i^{th} acquisition variable
$\{h_{i,j}\}$	Set of hypotheses values taken by \bar{V}_i
$\mathbf{h}(s)$	Hypothesis vector of the s^{th} combination of the acquisition variable hypotheses
$\mathcal{Z}()$	Simulation function, producing the simulated radargrams from the hypothesis vector
$ V_{sm} _s$	Simulated radargram magnitude for the s^{th} combination
S	Database of simulated radargrams
G	Set of geo-electrical variables
\bar{G}_k	k^{th} geo-electrical variable
$\{g_{k,l}\}$	Set of hypothesis values taken by \bar{G}_k
$\mathbf{g}(e)$	Hypothesis vector of the e^{th} combination of the geo-electrical variable hypotheses
$\mathcal{W}()$	Geo-electrical transformation function, producing the complex geo-electrical models from the geo-electrical hypothesis vector
ϵ_e	Complex geo-electrical model derived for the hypothesis vector $\mathbf{g}(e)$

\mathbb{E}	Database of geo-electrical models
$Perf()$	Performance measure function applied on simulated radargram
$P_{perf}(s)$	Performance measure calculated on the simulated radargram R_s using the performance measure $perf$
$P_{SSNR}(s)$	Subsurface signal to noise ratio performance
$P_{SSR}(s)$	Subsurface to surface power ratio performance
$P_{SurfSNR}(s)$	Surface signal to noise ratio performance
$P_{Pd}(s)$	Probability of subsurface detection
$\chi_{perf}(V_i)$	Sensitivity of the RS to the variable V_i for the performance measure $perf$
$Feat()$	Feature extraction functions applied to the simulated radargrams
$F_{feat}(s)$	Feature value extracted from the simulated radargram R_s using the feature $feat$
$F_{SSNR}(s)$	Subsurface signal to noise ratio feature
$F_{SSR}(s)$	Subsurface to surface power ratio feature
$F_{SurfSNR}(s)$	Surface signal to noise ratio feature
$F_{SST}(s)$	Time to subsurface feature
\mathbf{C}_i	Set of clusters of features corresponding to unique hypotheses values of the variable V_i
$C_{i,j}$	Cluster of features representing the case in which the variable $\bar{V}_i = h_{i,j}$ and other variables assume all their respective hypotheses values
$Sim()$	Function for estimating pixel-to-pixel similarity between a pair of images
$M_{sim}^R(s_1, s_2)$	Similarity value between pair of simulated radargrams R_{s_1} and R_{s_2}
$M_{sim}^{Re(\epsilon)}(e_1, e_2)$	Similarity value between the real parts of the pair of geo-electrical models ϵ_{e_1} and ϵ_{e_2}
$M_{sim}^{Im(\epsilon)}(e_1, e_2)$	Similarity value between the imaginary parts of the pair of geo-electrical models ϵ_{e_1} and ϵ_{e_2}
$M_{MI}(I_1, I_2)$	Mutual information similarity measure between the image pair I_1 and I_2
$M_{COR}(I_1, I_2)$	Correlation similarity measure
$M_{SSIM}(I_1, I_2)$	Structural similarity index measure
$M_{DIF}(I_1, I_2)$	Average pixel-to-pixel difference

$mi(I_1, I_2)$	Function that computes the mutual information between a pair of images I_1 and I_2
q_1, q_2	Constants that depend on the dynamic range of the images for computing the SSIM metric
$\rho_{sim}(V_t)$	Variable significance of the variable V_t
U_t	Set of pairs of combination indices s used for variable significance estimation
N_p	Number of elements in U_t
W_t	Set of pairs of combination indices e used for variable significance estimation
N_q	Number of elements in W_t

Chapter 1

Introduction

This chapter introduces the work presented in the thesis. We briefly describe the background on radar sounders, the definition of the problem addressed by the thesis and the novel contributions. Finally, the structure of the thesis is outlined.

1.1 Background

Exploration of the Earth and other bodies in the Solar System has been of great scientific interest in the last century. Geological and geophysical investigations of these planetary bodies have largely relied on remote sensing systems, due to their capability of acquiring data of homogeneous quality, with a uniform spatial sampling, and in places that are inaccessible to humans. The data from the remote sensing systems have enabled us to image terrestrial and planetary surfaces at different spectral, spatial and temporal scales. Moreover, radar remote sensing has also enabled us to accurately model the surface elevation, thereby immensely improving the scientific knowledge of planetary bodies.

However, without direct measurements of the subsurface, knowledge obtained only from the surface images can be ambiguous. Subsurface measurements for several applications (civil, military and geophysical surveys) have been commonly obtained from ground-based platforms using the ground penetrating radar (GPR) profiling. The GPR instruments are also designed to operate from airborne and satellite-mounted platforms, and operate on the principles of radio echo sounding, a.k.a. radar sounding. Radar sounders (RS) are nadir looking instruments designed to operate at low frequency for profiling the subsurface of the Earth or of other planetary bodies. As the RS signal propagates through the subsurface medium, it is reflected from compositional, thermal or structural interfaces of significant dielectric contrast. As the RS moves along its trajectory, the received radar response of the subsurface targets is recorded and further processed on-board and in the ground segment to produce the RS data a.k.a radargrams. The radargrams are analyzed to extract scientific information about the target that can help to understand

and characterize planetary shallow subsurfaces.

The research on radio wave propagation dates back to early 1900s, when the focus was mainly on the radio communications and radar tracking technologies [2]. Around the mid of the century, there are reports of the first successful attempts to directly measure signals reflected from the subsurface, beginning with the imaging of the depth of the water table [45]. Further observations of radio propagation through subsurface were reported in connection with repeated altimeter errors that occurred during flight landing on the ice-sheets of Greenland [149]. These errors were occurring because the radio wave penetrated through the ice, instead of reflecting from the surface, thus giving a wrong estimate of the flight altitude from the surface. From then on, radio echo sounding in the polar ice caps and glaciers began gaining a significant impetus, leading to the establishment of several polar geophysical research centers. In early 1970s, the Apollo 17 was in development and one of the goals of the mission was to examine the characteristics of the lunar subsurface, which was hypothesised to be similar to ice. Consequently, the Apollo 17 mission carried on-board the Apollo 17 Lunar Sounder Experiment (ALSE), which was a pulsed RS in orbit around the Moon [125]. This era also saw the importance of the studies on the electrical properties of natural materials for interpreting and supporting RS acquisitions [102, 103].

On the Earth, several applications of the subsurface radar technology started growing towards the latter half of the 1970s. Apart from the geophysical surveys of the polar ice caps, GPR was applied to various commercial and engineering applications (such as the laying of oil and gas pipelines, in coal, salt and potash mines, and in road investigations) [4, 34, 2], to archaeological surveys [41], to the investigation of rock quality using bore-hole GPR for identifying suitable sites for nuclear waste disposal [37, 104], and to military applications [109]. The usefulness of the penetrating radar in high-resolution subsurface mapping began to be realised close to 1990s, when the technology was extended to environmental applications such as the investigation and clean-up of contaminated land [8], soil classification for agricultural applications [44], and seismic modeling [3]. Moreover, the technology evolved over the years leading to the development of more portable GPR instruments operating at lower frequencies [153, 37] and equipped with a full digital data storage and processing capabilities. The last decade of the twentieth century saw a significant growth in the subsurface radar technology, both commercially as well as scientifically, as demonstrated by the wide range of applications in several fields.

Presently there are RSs orbiting around Mars (i.e. Shallow Radar (SHARAD) [139] and Mars Advanced Radar for Subsurface and Ionosphere Sounding (MARSIS) [122]), and the Moon (i.e. Lunar Radar Sounder (LRS) [106]). These sounders have resolved many ambiguities in the geological interpretation of the Moon and Mars by providing direct

measurements of the subsurface and producing ground-breaking scientific results. For example, the MARSIS data were interpreted to reveal the first evidence of extra-terrestrial liquid water in the form of a subglacial lake on Mars [107]. SHARAD provided detailed subsurface profiles of the Martian polar layered deposits confirming the layers of ice and dust previously detected by MARSIS [121]. LRS detected evidences of stratification in the lunar maria, indicating episodes of volcanic resurfacing [105]. Among the terrestrial planets, Venus presents an interesting case for understanding the geological processes in the solar system. For subsurface exploration of Venus, the Subsurface Radar Sounder (SRS) has been recently selected on-board the EnVision mission and is currently in the Phase A study. SRS can acquire fundamental information on subsurface geology of Venus by mapping the vertical structures (mechanical and dielectric interfaces) and properties of the geological features such as tesserae, buried craters plains and lava flows.

In the outer planets of the solar system, the icy moons of Jupiter present opportunities for detecting important subsurface targets. The low temperature ice covering the Jovian moons would allow deep penetration of the RS signal at MHz frequencies. Previous missions provide indications of a vast body of liquid water ocean beneath the ice-shell and the surface expressions of complex geodynamic processes resulting from the geological evolution of the moons. To characterize the moons' ice-shells, two Jovian missions that will carry RSs are under development. These are the Radar for Icy Moons Exploration (RIME) [18], which is aimed at studying the icy moons Ganymede, Callisto and Europa, and Radar for Europa Assessment and Sounding: Ocean to Near-surface (REASON) [12], which is specifically targeted at Europa.

For imaging the subsurface of the Earth, there have been many airborne radar sounder (ARS) acquisition campaigns [141, 36] over Antarctica and Greenland. The ARS profiles down to the bedrock (in case of the ice-sheets) or the ice-ocean interface (in case of the ice-shelves) have allowed the mapping of the continent-wide ice thickness and basal topography of Antarctica [89], the detection of subglacial lakes at the base of the ice-sheets [110], and the characterization of the englacial layering [87]. Currently, studies are in progress for developing a satellite-mounted radar sounder for Earth observation of the cryosphere in the polar caps and the arid deserts [16, 67].

1.2 Problem definition and motivation

The radar response is a complex function, which depends on the RS instrument parameters, the acquisition geometry and the target properties (Figure 1.1). Typically in the case of planetary exploration missions, the available knowledge of the target is used to define the mission requirements, i.e. the properties of the target that the RS should detect. The design of the RS is based on selecting the instrument parameters and the

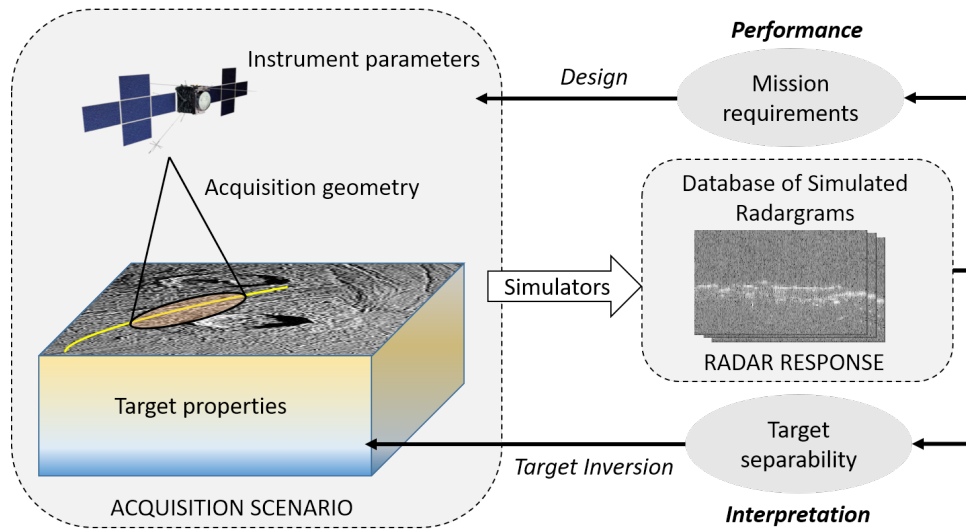


Figure 1.1: Schematic representation of the simulation process: the relationship between the acquisition scenario and the radar response.

acquisition geometry that fulfill the mission requirements. However, the radar response cannot be modeled with simple theoretical formulations as there is a huge uncertainty in both the knowledge of complex target properties and the nature of the electromagnetic interaction between the target and the signal. Nonetheless, the full understanding of the radar response is of fundamental importance, not only for designing the RS but also for retrieving the target properties from the radargrams acquired by a RS.

RS simulators are critical tools that predict the radar response resulting from different contributions of acquisition parameters (instrument, acquisition geometry and target properties), by emulating the acquisition scenario. The simulated radargrams can be considered as proxies of the actual acquired data, with the advantage that unlike the real radargrams, the underlying target properties of the simulated radargrams are known. Thus, simulation is a forward modeling of the data acquisition process and is used to understand the complex relationship between the radar response and the target properties. This understanding can then be applied to the acquired radargrams to interpret and invert the target characteristics. This interpretation can be visual or automatic. The simulated radargrams can also be used as a proxy data for developing automatic target interpretation algorithms. In summary, RS simulators can be exploited for:

1. Predicting the performance of the RS instrument;
2. Supporting the design of the RS based on the performance;
3. Guiding the interpretation and inversion of target characteristics from the acquired data;

4. Enabling the development of data analysis algorithms for automatic target detection in the acquired data.

Given the paramount importance of RS simulators for the design and planning of planetary exploration missions, there is the need to develop accurate simulation techniques that can represent in an effective way the complex interaction between the target and the instrument, producing data with characteristics similar to those of the acquired data. Radar sounder simulation techniques rely on the modeling of the target geo-electrical properties, i.e. defining the spatial variation of the complex dielectric permittivity values associated to the target's structure, composition and geophysical characteristics. Target modeling in current simulators relies on the expertise of the scientist in translating the available knowledge of the target into the geo-electrical models. Due to large number of model parameters (i.e. the complex dielectric permittivity value at every 3D spatial coordinate of the target), and the ambiguities in the available knowledge, the target representation is affected by subjective bias. Thus, the same target may be modeled differently by different scientists. The state-of-the-art target modeling techniques are described in detail in Chapter 3. However, subjective and simplified target modeling produces unrealistic simulated radargrams that typically overestimate the performance of the RS and, in many cases, are far from the real data.

From a different perspective, to better analyze a given scenario, it is necessary to generate a large amount of simulated radargrams corresponding to various combinations of the possible acquisition variables (Figure 1.1). Since conventional electromagnetic simulators require huge computational load, it is not possible to generate too many radargrams corresponding to realistic dimensions of the target. In this context, there is a lack of studies on the systematic generation and analysis of a large database of simulated radar responses for supporting large-scale planetary exploration missions.

In practice, for a given mission, the choice of the simulation technique and the approach to the analysis of the simulated data depends on several factors specific to the mission. These include the uncertainty in the geological knowledge of the investigated targets, the challenges in the acquisition process, and the requirements of the mission in the considered phase of development. Thus, the available approaches need to be adapted to the specific case of each mission, for properly optimising the specific requirement of the simulation task.

1.3 Novel contributions of the thesis

The novel contributions of the thesis are related to two main directions. On the one hand, we propose novel approaches to address two major open issues in the field of RS simulations: (1) the unavailability of a simulation technique that can produce realistic

radargrams by reducing the subjective bias in target modeling, and (2) the unavailability of methods for systematically generating and analyzing a large database of simulated radargrams. On the other hand, we demonstrate the use of the simulation approaches for performance assessment of RSs considered in two future missions, which are at different phases of development and aim to study different planetary bodies: (1) RIME on-board the JUICE mission, and (2) an Earth orbiting RS (EORS).

These contributions are briefly described as follows.

1.3.1 Proposed methods for simulation and analysis of radargrams

An approach to the simulation of radargrams based on geological analogs

The analogs are geological features that have similar surface morphology (and therefore are expected to have similar subsurface structure) to the planetary target to be investigated by the RS instrument under study. In this contribution, we propose a simulation approach that exploits the data available from existing RSs over the geological analogs to produce realistic simulations of the investigated target. The proposed simulation strategy is based on minimizing the differences between the analog and the investigated acquisition scenarios. This is done by applying a series of processing steps to the analog radargrams, which depend on the relation between the radargram characteristics and the physical variables describing both the target acquisition scenario and the acquisition process. By assuming that the subsurface structure of the investigated targets is approximately represented in the analog radargrams, the difference in composition is accounted for by imposing different dielectric and subsurface attenuation models. Next, the signal magnitude, range resolution and sampling intervals of the simulated radargram are estimated from the differences in the instrument parameters and the dielectric models of the analog and the investigated scenarios.

Experimental results present three case studies for different taxonomies of analog and investigated scenarios. First, we demonstrate the effectiveness of the proposed approach by simulating the radargrams of existing RS acquisitions and validating the simulations by comparing with the real data. The validation compares the simulated data with the acquired data (1) statistically (by comparing the histograms), (2) in terms of the surface and subsurface received power values (by comparing the radar traces), and (3) geometrically (by visual comparison and also by estimation of the value of mutual information between the real and simulated radargrams). Then, we illustrate a real application of this approach to the simulation of RIME radargrams for different combinations of the RIME parameters and possible icy moon dielectric models, using a SHARAD radargram acquired over a geological analog of a selected RIME target. The validation confirms the effectiveness and accuracy, while the application to the case of RIME analysis demonstrates the usefulness of the proposed approach.

An approach to the generation and analysis of databases of simulated RS data for performance prediction and target interpretation

The large number of variables involved in the RS acquisition process requires the development of a systematic approach to the organization of the RS simulation task that can support performance prediction and target detectability analysis. This contribution presents a novel approach to generate databases of geo-electrical models and simulated radargrams corresponding to combinations of: (i) target geo-electrical hypotheses; (ii) RS parameters; and (iii) the acquisition geometry configurations. The proposed approach also exploits the generated database for: (a) predicting the detection performance and sensitivity of a RS for a given target under different possible acquisition scenarios, and (b) understanding the interpretability of the underlying hypotheses using radargram features. In this framework, the similarity between pairs of geo-electrical models and between simulated radargrams is used to identify the hypothesis combinations that can be unambiguously inverted from the radargrams. We have presented different measures to analyse the similarity (e.g. mutual information, structural similarity index, correlation and difference), performance (e.g. subsurface to surface power ratio, signal to noise ratio, sensitivity of the radar response to differential changes in the acquisition variables), and features (e.g. time between surface). The choice of the analytical methods applied to the database depends on the specific objectives of the study.

For each of the analysis techniques, the approach is demonstrated using a case-study of a RIME simulation target on Ganymede. The main outcomes of the proposed technique are: i) the estimation of the target detection performance of RSs, ii) the characterization of the sensitivity to the small variations in target properties, iii) the analysis of the separability of radargram features, and iv) the identification of hypothesis combinations producing significantly different radar response. The number of parameters that can affect the instrument performance are typically very large, and the promising results suggest that it is possible to effectively reduce the uncertainty of the simulation space through the use of the proposed approach.

1.3.2 Performance assessment of future radar sounder missions**Performance assessment of RIME: subsurface sounding of the Jovian icy moons**

The goal of RIME, on-board the JUICE mission, is to study the ice-shells of the Jovian icy moons through multiple fly-bys and finally an orbital coverage of Ganymede. The scheduled launch for JUICE is 2022, and therefore RIME is currently in its final design phase. Thus, the requirements of RIME simulations are focused on understanding the detectability of complex icy targets on the Jovian icy moons. In this contribution, we analyze the detectability of selected targets on Ganymede using an electromagnetic simulator based on FDTD technique [158], which has the capability of handling targets

with complex 3D variations in geo-electrical properties. In particular, we model the following targets: (1) the dark terrain regolith, (2) the bright terrain dielectric profile, and (3) the grooved bright terrain. The analysis is performed in two levels. The first two targets are modeled as flat, parallel, horizontal layers representing the dielectric variations with depth. For the third target, the structure of the dielectric interfaces is also important in determining the simulated radar response, and we adopt a multi-level analysis of the detectability. For these targets, i.e. the grooved bright terrain, the main geological components are the normal faults. In the first level, the radar response of individual faults is simulated, varying their following characteristics: (1) dip angle (30° or 60°), (2) thickness (3 m or 6 m), (3) composition (20% voids mixed with pure ice and 100% pure void) (4) shape (listric or planar). The simulation experiments of the individual faults were conducted for a smaller simulation space consisting of only a single fault. In the next level, a more realistic geological arrangement of a combination of the normal faults is considered. The simulated radargrams are analyzed to assess the detectability of the subsurface interfaces and to guide the interpretation of the RIME data. The analysis consists of comparing the simulated radargram corresponding to a set of target hypotheses with (a) the cluttergram (radar response of the surface only), and (2) the baseline test case (radar response of a reference set of hypotheses).

Performance assessment of a radar sounder for Earth observation: subsurface sounding of the polar ice caps

The study of the subsurface of the polar ice caps on Earth is important for supporting global climatic models and predicting sea-level rise. These studies can significantly benefit from multi-temporal and continent-wide subsurface observations, that can be provided by an EORS. To support the design of such an instrument, we present a feasibility study that exploits the proposed simulation approach based on the reprocessing of analog radargrams. In this case, we use the available archives of airborne RS campaigns as the analog RS data and reprocess them to simulate the EORS data. The simulated EORS radargrams are then analyzed by extracting performance metrics that represent the detectability of two important ice targets: (1) the englacial layering, and (2) the basal interface. The analysis of the simulated radargrams is used to identify suitable instrument parameters of the EORS that will maximize the detection of the ice targets. The performance assessment and instrument parameter selection is demonstrated on a set of selected airborne radargrams covering different ice-sheet targets (grounded ice, floating ice, subglacial lakes) in Antarctica and Greenland. For each airborne data, the EORS simulated data are generated for different values of the antenna gain and transmitted power. The analysis demonstrates the feasibility of the radar sounding of the polar cryosphere from an orbital platform.

1.4 Structure of the Thesis

In this chapter, we have described the context of the thesis, the motivation, and we have briefly introduced the novel contributions. The rest of the dissertation is organized in three main parts as follows.

In part I, we briefly describe the theoretical background on RSs and their performance assessment. Chapter 2 reviews the principles of RSs, and presents the current and future RS instruments. Chapter 3 discusses the state-of-the-art approaches to the simulation and performance analysis of RSs designed for planetary exploration.

In part II, the proposed novel approaches to the simulation and analysis of radargrams are presented in detail and supported by illustrative case-studies. Chapter 4 presents the proposed simulation approach based on geological analogs. Chapter 5 describes the proposed technique for the systematic generation and analysis of a database of simulated radar responses.

In part III, the applications of the proposed performance assessment approaches for two future RS instruments are demonstrated. Chapter 6 presents the analysis of the RIME instrument. Chapter 7 describes the analysis of an EORS.

Finally, Chapter 8 discusses the overall conclusions of the thesis and addresses possible future developments.

Part I: Background

Chapter 2

Radar sounders

This chapter presents the background on radar sounders. First, we explain the principles of data acquisition by radar sounders and the multi-level processing of the received echoes. Then we introduce the heritage of past, existing and scheduled radar sounder instruments on-board satellite missions.

2.1 Introduction

RAdio Detection And Ranging (**radar**) is a technique for estimating the distance to a physical object of interest (i.e. target) by detecting the echo reflected by the target. Pulse-radars transmit a high-energy short-duration signal in the direction of the expected target and measure the power scattered by the target towards the receiver. The time delay between the transmitted and the received signal is used to estimate the distance to the target by knowing the velocity of the signal in the medium of propagation. Imaging radars are typically monostatic pulse-radars, i.e. the same antenna is used for transmitting and receiving, and thus the two-way travel time, from the radar to the target and back to the radar, is used to estimate the distance.

Radar sounders (RS) are a special class of monostatic pulse-radars operating at signals that are capable of penetrating planetary surfaces, thus estimating the range (depth) to subsurface reflectors. The subsurface imaging capability of RSs has been well-exploited in the past and current planetary and terrestrial geophysical exploration missions. Following in the heritage of the past and existing RSs, many future planetary missions are being designed to carry on-board RS instruments.

In this chapter, we briefly introduce the background and principles of radar sounding, citing examples of past, present and future RS instruments. In Section 2.2, we introduce the principles of radar sounding, focusing on the characteristics of the transmitted signal, the acquisition process and the interaction of the electromagnetic waves with the target. Section 2.3 briefly explains the important steps in the processing of the received radar

echoes. The state-of-the-art sounders that have been operating or are in development for future satellite missions for planetary exploration or Earth observation are described in Section 2.4.

2.2 Principles of radar sounding

Figure 2.1 illustrates the process by which a RS acquires information about the target. The RSs are mounted on a moving platform, i.e. a spacecraft or an aircraft, flying over the target. The direction of movement of the platform, represented by x is referred to as the along-track direction. The direction orthogonal to the along-track and pointing down towards the target is the nadir, represented by z . It represents the radar range i.e. the depth of the target reflectors. The third direction orthogonal to both the along-track and the nadir, represented by y , is the across-track direction. The signal received between successive pulse transmissions is referred to as an A-scan. Concatenated A-scans over multiple pulses are processed to obtain the final radar image, i.e. the radargram. In this section, we briefly describe each step in the radar acquisition process.

2.2.1 Signal transmission

RSs generally operate in the HF - VHF range of frequencies, i.e. 1 MHz - 300 MHz. The ability of the electromagnetic wave to penetrate through a material is inversely proportional to the frequency and depends on the complex dielectric permittivity. Due to the long wavelength of the RS signal in this frequency range, it has the capability to penetrate through low loss dielectric materials such as dry regolith and ice up to a depth of a few kilometers. Thus, the carrier frequency of the RS is designed with respect to the expected depth and the dielectric properties of the target subsurface.

The RS transmits electromagnetic pulses in the nadir direction as it moves along its track. The time interval between the transmission of two pulses is defined by the pulse repetition interval (PRI), which is equal to $1/\text{PRF}$ (pulse repetition frequency). The fraction of time for which the radar is transmitting (i.e. ratio of the pulse-width to the PRI) is the duty cycle, and is a measure of the rate of power consumption of the radar. The ability of the radar to distinguish between subsurface reflectors positioned closely in range is given by the radar range resolution.

RSs typically use a linear frequency modulated chirp with a small pulse width (of the order of a few hundred microseconds) and a bandwidth of a few MHz. The frequency modulation improves the range resolution by using the frequency-dependent phase information in addition to the time delay between transmission and reception according to a matched filter reception scheme. The advantage of this type of waveform is that it allows to define pulses, which are both relatively long in time and have a high spectral width.

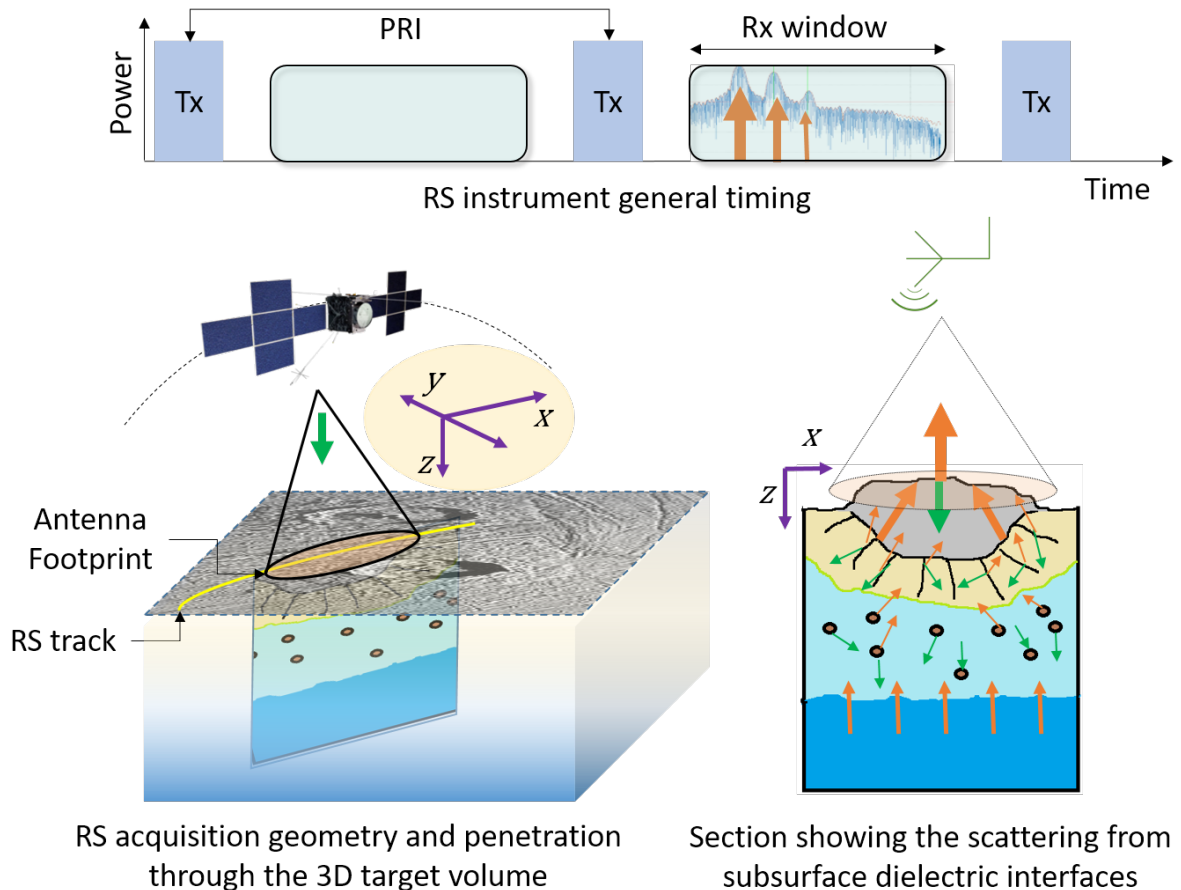


Figure 2.1: Schematic representation of the process of subsurface mapping using radar sounding. As the RS moves along its track, it transmits signal pulses at a time interval given by the PRI and illuminates the target region within the antenna footprint of the RS. The signal propagates through the target subsurface, where it undergoes scattering, absorption and transmission in its interaction with different types of dielectric interfaces. The time-varying signal received back at the antenna can then be interpreted to infer the characteristics of the target. The important direction vectors in the acquisition geometry are denoted by x (along-track), y (across track) and z (range or depth).

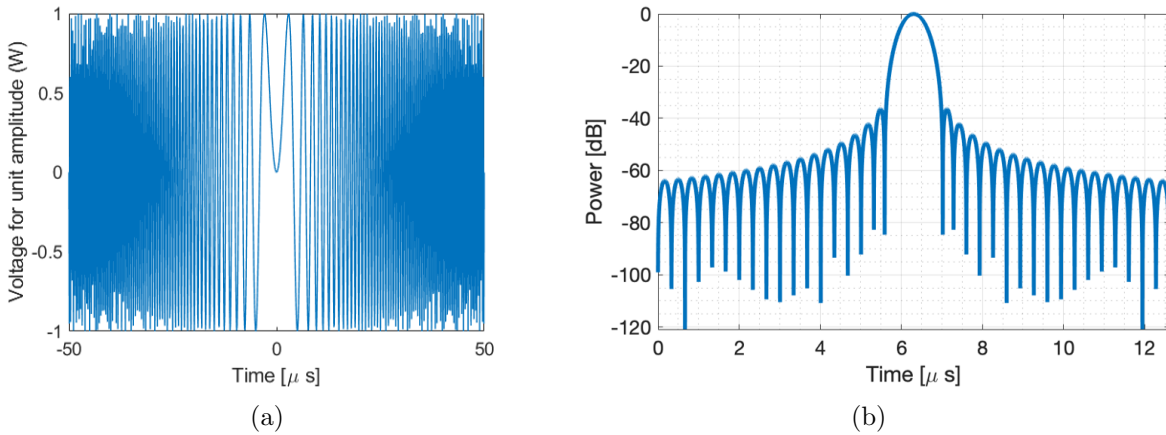


Figure 2.2: Example of RS transmitted signal: (a) The raw (unprocessed) transmitted linear frequency modulated chirp signal corresponding to a bandwidth of 3 MHz and pulse-width of 100 μs . (b) The range-compressed received echo, which takes the form of a sinc function, in which the width of the main lobe corresponds to the range resolution of the radar.

Long pulses grant to have sufficient energy to detect small targets at long distance. On the other hand, high spectral width allows to increase the range resolution.

Figure 2.2(a) shows an example of the transmitted chirp signal corresponding to a bandwidth of 3 MHz varying over a pulse-width of 100 μs . The signal is shown in base-band, although the real RS signal is modulated at the carrier frequency. Using appropriate processing of the received chirp (discussed in the next section), the target location can be resolved up to the width of the main lobe of the sinc function, as shown in Figure 2.2(b). Generally, RSs are designed to operate at a large fractional bandwidth ($\sim 20\text{-}60\%$ of the central frequency) to have an optimum trade-off between the achievable penetration (which increases by decreasing the carrier frequency) and the range resolution (which increases by increasing the bandwidth).

2.2.2 Acquisition process

RSs have a nadir looking geometry and should ideally collect signal from the nadir profile of the target (shown by the 2D target slice beneath the yellow line in Figure 2.1). However, the RS antenna of satellite systems is typically a dipole for mechanical constraints. A dipole is known to have low directivity, and thus results in a large antenna footprint illuminating the target (of the order of 2 - 10 km depending on the orbital altitude). Thus the radar also receives unwanted signals (i.e. clutter) from off-nadir surface reflectors that can arrive with the same time delay as the interesting subsurface echoes. The distance between the nadir positions of successive footprints is given by the product of the spacecraft velocity and the PRF.

The time-varying electromagnetic field scattered back from the target subsurface is recorded within the receiving window (Rx window in Figure 2.1). The duration and the position (start and stop time) of the receiving window is optimized to have the minimum data-rate, while ensuring that the signal from the full penetration depth of the target is collected. The position of the receiving window can be determined by closed-loop or open-loop tracking techniques. In open-loop tracking, the expected time of arrival of the surface and subsurface echoes is pre-determined from the knowledge of the spatial coordinates of the platform and the surface topography. However, uncertainties in these parameters can result in errors in the window position, and pose the risk of missing important portions of the echoes, specially for planetary bodies with unreliable data on surface topography. This problem can be addressed by using a closed-loop tracking in which an adaptive receive window position is determined in real time by tracking the position of the leading edge of the received surface echo and checking the coherency of the pulse arrival times [25].

Another aspect of the radar acquisition is the ability to collect the information on the Doppler spectrum, by exploiting the relative movement between the target and the radar. Although the large antenna footprint introduces noise in the recorded signal in the form of clutter, it also presents the advantage of overlapping acquisitions over the same target but with different Doppler shifts in the phase. In case of coherent radars, the accurate estimation of the signal phase allows the exploitation of this Doppler information to significantly improve the along-track resolution. The signal processing technique that allows the exploitation of the Doppler shift is described in the next section.

2.2.3 Interaction with the target

The interaction of the electromagnetic wave with the target electrical and magnetic properties can be generalized with three common phenomena: (1) the forward and backward scattering of the waves, determined by the orientation and contrast of the dielectric interfaces, (2) the transmission of the waves deeper into the subsurface, and (3) the loss in the power of the waves during transmission. This interaction is schematically represented by the arrows marked on the section of the subsurface in Figure 2.1. The thickness of the arrows are weighted by the strength of the signal. The orange arrows show the waves going back to the receiver, while the green arrows are waves going deeper into the medium. The nature of the interaction depends on the type of the dielectric interfaces encountered by the wave. From the perspective of radar sounding, the subsurface scatterers can be broadly represented by one or more combinations of the following types [18]:

1. *Smooth and horizontal interfaces of significant dielectric contrast.* They are characterized by a strong, horizontal, and specular reflection (e.g. the interface between ice

and an underlying subglacial lake).

2. *Compositional interfaces representing a change in the material dielectric properties.* They are characterized by a change in the signal strength (e.g. the interface between porous regolith overlying a solid bedrock).
3. *Structural interface represented by changes in the crystal properties.* They are also characterized by a change in the signal strength (e.g. the interface between brittle and ductile ice).
4. *Geological offset.* It is characterized by a vertical offset in the received echo, i.e. a vertical discontinuity in otherwise horizontally continuous distinct layers (e.g. a normal fault).
5. *Distributed subsurface scatterers.* They are small-sized reflectors of significant dielectric contrast, which are randomly distributed within an otherwise homogeneous background (e.g. pockets of water within ice). They are characterized by a loss of coherence in the signal and appear as diffused reflections of relatively low strength spread over many range and along-track samples in the radargram.
6. *Absorbing interfaces caused by highly conductive dielectric medium.* These interfaces result in the total loss of signal strength and no echoes are obtained from depths below them (e.g. air - seawater interface).

2.3 Radar echo processing

The signal received from the target undergoes three levels of processing:

1. *Level 0:* on-board processing prior to down-linking the data to the ground-segment
2. *Level 1:* low-level processing of the raw data in the ground-segment
3. *Level 2:* high-level processing, i.e. extraction of scientific information from the data

In this section, we briefly describe the main components of the three levels of processing.

2.3.1 On-board processing

The on-board processing applied to the received echoes differs for different RSs. One of the main purposes of the on-board processing is to reduce the data-rate. In this regard, a commonly applied processing involves the coherent summing of successive echoes (i.e. presumming) [35]. Presumming the echoes reduces the data rate while also reducing the along-track sampling frequency. For relatively smooth surfaces, a higher presumming factor is used since successive echoes are more strongly correlated to each other compared to

rough surfaces. Another commonly used on-board processing involves adaptively applying a compression to reduce the number of quantization levels to the expected dynamic range of the echo power, without loss of information. In some cases, on-board processing also includes a base-band conversion prior to the analog-to-digital sampling.

There are some instruments for which more extensive on-board processing is performed, such as the range and Doppler compression. This requires robust on-board electronics with high processing power and results in a significant reduction of data rate. However, this also poses the problem that the processing is irreversible, and thus the raw data cannot be retrieved and reprocessed with improved techniques if needed.

2.3.2 Low-level processing

Raw echo processing

The raw echoes down-linked from the spacecraft are processed in the ground-segment using a systematic and sequential processing chain (such as the one described in [1]). Each PRI is associated with the corresponding spacecraft telemetry information (e.g. position coordinates, the velocity vector, the system temperature, and the operation sequence). The signal is then demodulated to remove the carrier frequency, and thus converted to base-band. In case on-board compression is applied, the bit-stream is decompressed and converted to the appropriate real received voltage.

The next step is the range compression, in which the reference chirp (having high fidelity with the transmitted signal) is cross-correlated with the received echo in each PRI. This process of matched-filtering applied to a linear frequency modulated rectangular pulse results in a sinc centered at the time-position of the reflector, as shown in Figure 2.2(b). The time (range) resolution of the received echo is given by the width of the main lobe and is equal to $1/\text{bandwidth}$. An undesired effect of the range-compression processing is the generation of the sidelobes, which may mask the peak power from subsurface reflectors. In order to reduce the sidelobe levels, a weighting window (such as hanning or hamming) is used at the cost of increasing the width of the main lobe, and thus also reducing the range resolution [139]. The windowing parameters are selected such that the sidelobe level (with respect to the peak) after suppression is lower than the radar dynamic range (expected ratio of peak surface to subsurface power), and the main lobe widening is lower than required range resolution.

The next important step is the Doppler processing, that improves the ability of the radar to resolve the targets in the horizontal direction (i.e. the along-track resolution). The along-track resolution is proportional to the beamwidth (antenna length/wavelength). Since RSs operate at long wavelengths, a narrow beamwidth can be produced only using a very long antenna, which cannot be mounted on a satellite platform for mechanical

reasons. However, by exploiting the movement of the radar along the track, a long antenna array can be synthesized, by considering pulses transmitted at consecutive along-track positions. In this process of synthetic aperture radar (SAR) focusing, the integrated echoes from the synthetic aperture are aligned in phase as if they are received at the synthetic antenna at the same time.

There are several well-established techniques used for SAR focusing of RSs (e.g. [94, 80, 83]). The key steps are: (1) the estimation of the Doppler parameters (bandwidth and centroid) by reconstructing the along-track geometry of acquisition using surface topography data, (2) the generation of the azimuth reference function, (3) the transformation of the echoes to the Doppler frequency domain using the Doppler parameters, (4) the correction for range migration of echo samples received from same target position, (5) the azimuth compression by cross-correlation between the migration-corrected echoes and the azimuth reference function, and (6) the transformation of the data to time domain. The accuracy of the focusing depends on the uncertainties in the target surface topography and the platform telemetry. Thus, the synergy of the RS data with other on-board instruments (such as altimeter) can be important for precise processing.

Sources of noise and mitigation techniques

Depending on the propagation environment, the processing chain may also include the suppression of surface clutter, the corrections for ionospheric distortions, the alignment of the echoes to the surface topography (correction for the variations in the receiving window opening time) and the removal of spurious frequencies [1]. As compared to airborne sounders, the data from planetary sounders suffer from higher noise levels, propagation loss and surface clutter. The processing (range and Doppler compression) greatly improves the data quality in terms of the SNR and the signal-to-clutter ratio (SCR). The residual speckle noise present in the radargrams can be reduced by denoising techniques [49]. The problem of clutter is more challenging since it can result in an unrecoverable loss of information on the subsurface echoes arriving at the same time as the surface clutter. Moreover, the off-nadir surface clutter may be incorrectly identified as a subsurface reflection (since it appears below the nadir surface echo), thus leading to misinterpretation of the radargrams. In order to prevent the ambiguous interpretation of surface clutter as a subsurface reflector, techniques have been developed to discriminate the surface echoes in the radargrams. The most commonly used technique involves simulating the surface response using available topographic information within the footprint of the radar [122, 132, 31]. By co-registering the cluttergram (simulated clutter radargram) with the acquired radargram, the non-matching reflections can be attributed to the target subsurface. However, this approach is dependent on the availability of high resolution digital elevation models (with horizontal spacing lower than the wavelength of the radar).

Recently, other techniques exploiting the electromagnetic properties of the signal have been exploited to discriminate between the clutter and the subsurface response. These approaches require instrument design level implementations. One approach is based on using two antennas with different pointing directions - one towards nadir, and the other in the orthogonal direction to collect echoes from off-nadir surface reflections. The signal received by the second antenna is used to detect and cancel the clutter in the echoes received by the nadir-pointing antenna [123]. Another approach proposes the use of two antennas separated by a baseline (similar to interferometric SAR systems) [29]. The phase distribution of the subsurface echoes and the clutter are expected to be different. Thus, by estimating the phase difference of the echoes at the two antennas, the clutter can be discriminated. An alternative approach proposes the exploitation of the different polarization signatures of nadir and off-nadir echoes for circularly polarized waves [128].

A recent interesting approach draws inspiration from the clutter discrimination capabilities of big brown bats [24] and exploits the analogies between sonar (used by the bats) and radar detection strategies. This approach requires the radar to operate at multiple frequencies that are well-separated in the spectrum, or can also be implemented by splitting the available large bandwidth into sub-bands. The signal at the higher frequencies is attenuated more significantly during propagation through the subsurface, while the lower frequencies suffer less attenuation. On the other hand, the strength of the clutter echo (propagating only through the free-space) is independent of the frequency. Thus, a simple ratio of the received power at the different frequencies can help to discriminate the clutter.

Besides the clutter, the RS signal propagation through the ionosphere can also degrade the quality of the radargram. Since the refractive index of the ionospheric plasma is frequency-dependent, it results in dispersion of electromagnetic waves. The RS signal is affected in three ways: (1) phase distortion, (2) attenuation in the signal power, and (3) Faraday rotation of the linearly polarized plane wave. The degree of these distortion effects can be modeled as a function of the electron density profile, the collision frequency and the magnetic field strength (more details in Section 3.2.2). Mitigating the effects of the ionosphere requires the accurate prediction of the distortion using the best-fit models of the ionospheric parameters.

Several techniques have been developed to solve for the unknown ionospheric distortion. One such approach is based on the Front Surface Reflection technique [133], in which the surface response is matched with the ideal chirp, first compensating for the system and surface frequency responses (which can be modeled using the radar equation and on-board calibration). The compensated surface response is matched with theoretical estimates of the ionospheric attenuation and phase distortions to obtain the best fit bulk parameters of the ionosphere. This technique was significantly improved and applied to the MARSIS

data in a more recent approach in which the surface echoes in the radar response are also positioned accurately using data from an altimeter [95]. In the improved approach, the phase distortion caused by the ionosphere is represented as a Taylor series expansion consisting of the increasing powers of $1/\text{frequency}$. The coefficients of each term depend on the ionospheric parameters and are obtained so as to maximize the signal amplitude of the surface reflection. The optimization explores the ionospheric parameter-space that is defined based on the expected electron density profile. A similar but more rapid approach based on an autofocus correction algorithm was applied to the SHARAD signals [21]. Here, the parameters of the phase function are optimized using a gradient search algorithm to maximize the image sharpness. More recently, it was found that for RSs operating at low-frequency and large bandwidth, Legendre orthogonal polynomials were more effective for compensating large distortions as compared to the previously used Taylor series expansion [138].

In all the cases, the accuracy of the correction techniques depends on the accuracy of estimation of the ionospheric parameters. From the predicted distortion, the phase correction term is obtained, which is then multiplied to the spectrum of the received signal, to remove the phase distortion caused by the ionosphere. This step is generally applied prior to the range compression. In general, as a by-product of the ionospheric mitigation, an accurate inversion of the ionospheric parameters is also obtained.

The processed radargram (i.e. the Level 1 data), generated at the ground segment, are then disseminated to the scientific community for extraction of high-level scientific information. The radargrams are stored in the form of a matrix of the complex voltage (amplitude and phase). Each column of the matrix represents one position along the track and the rows represent the individual time samples of each echo. In this thesis, we will refer to the columns of the radargram as radar traces and to the rows as samples.

2.3.3 High-level processing

Qualitative interpretation of radargrams

Radargrams must be analyzed and interpreted to derive information about the target. Geological interpretation of the radargrams typically involves inferring the geometry of the target, its composition, and its geophysical properties such as porosity, temperature profile, presence of volumetric debris and impurities. This information is obtained by analyzing the properties of the radar response of the target. The first step in this direction is to visually interpret the radargrams and extract their basic characteristics, to obtain qualitative information about the target. In particular, signal peaks in a radar trace provide information about the high-contrast dielectric discontinuities in the subsurface (see Figure 2.1). Since the power is attenuated exponentially with depth, the reflections from deeper subsurface have lower echo strength. Thus, the nature of the subsurface

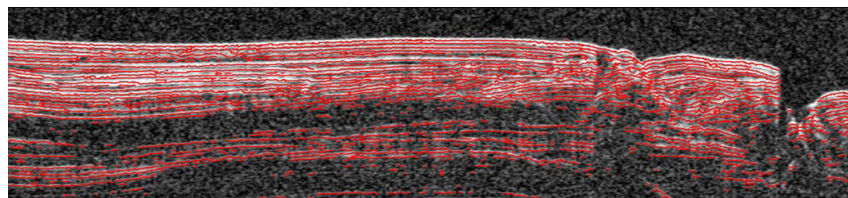
medium is inferred by examining in parallel the characteristics of the received echo such as: (1) the time-delay between successive reflections, (2) the strength of the reflected echo, (3) the statistical properties of the samples [48], and (4) the spatial relationships between different reflections [74]. Furthermore, the interpretation from a single radargram is validated by looking for consistent interpretations from adjacent radar tracks, target geological models and other ancillary datasets [122].

Automatic target detection algorithms

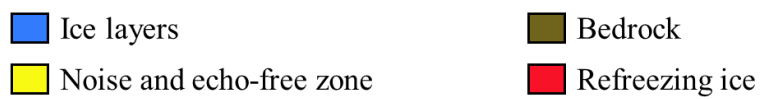
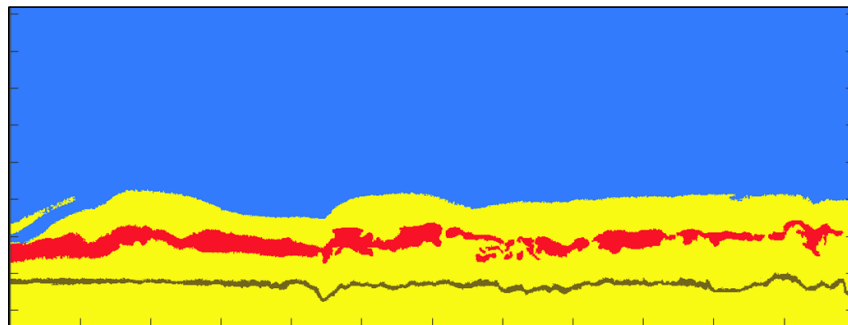
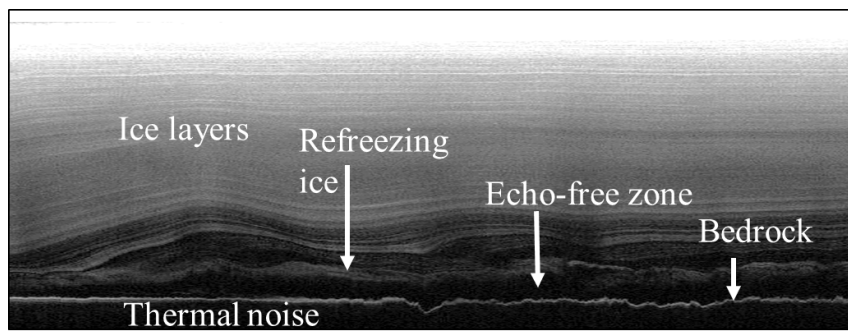
Visual interpretation of the radargrams can be time-consuming and is affected by a subjective bias. Several automatic techniques have been developed for extracting geophysical information from the airborne and planetary RS data. Some examples are:

1. Extraction of the properties of the ice layers as vectors with attributes of position, width and radar contrast, using Steger filter [49, 157, 51]
2. Estimation of layer thickness, the presence of seawater, sediments, marine ice, and crevasses [116, 56]
3. Detection of any linear reflectors [23]
4. Segmentation of the radargram into regions representing stratified reflectors, basal reflection, noise and the echo-free zone [75, 48]
5. Automatic mapping of subglacial lakes in Antarctica by modeling the electromagnetic signature of the lakes' ice-water interfaces [110, 76]
6. Mapping of basal refreezing of melt-water and upwarping of basal layering [43]
7. Detection of targets with complex geomorphology, such as lava tubes by forward modeling the radar response using simulators [27, 42]

RS data have significantly contributed to the understanding of an important class of subsurface targets that are characterized by stratigraphic variations in dielectric properties, which appear as nearly horizontal quasi-parallel layers in the radargrams. Automatic feature detection algorithms have been developed for characterizing the layers in the North Polar Layered Deposits (NPLD) on Mars from SHARAD radargrams. Freeman et al. have flattened the layers with respect to the surface pixels to reduce the effect of local slope and have applied filtering, thresholding and morphological processing [51]. Ferro et al. extracted the layers as vectors with attributes of position, width and radar contrast, using Steger filter [49]. However, these methods are efficient in detecting only horizontal interfaces. Carrer et al. proposed an improved method for detecting linear features in general using local scale hidden Markov model and the Viterbi algorithm [23] (see Figure 2.3(a)).



(a)



(b)

Figure 2.3: Examples of algorithms for automatic target detection in RS data. (a) Linear dielectric interface detection [23]. (b) Segmentation of ARS data into layers, bedrock, echo-free zone, thermal noise and refreezing ice [43].

The radargrams acquired over the polar areas of the Earth and Mars are rich in information, and comprise of several regions characterized by different radar signatures. Ferro et. al. analyzed the statistical characteristics of these different regions to define subsurface feature maps of the Mars NPLD [48], which were then used to segment the radargram into regions corresponding to no returns, low returns, weak layers, strong layers and basal returns. Ilisei et. al. extended this idea further by introducing other features related to the range to the targets and their textural properties and using supervised classification algorithms based on support vector machines to automatically classify Antarctica radargrams into layers, bedrock, echo-free zone and noise [75]. Recently, Donini et. al. further extended this supervised segmentation algorithm to also map basal refreezing units. These represent zones of local refreezing of melted water at the base of ice-sheets, which cause an upwarping of the lower layers and appear as diffused scatterers in the ARS data [43] (see Figure 2.3(b)).

The ice-water interface is another important class of targets detectable by RSs due to the high dielectric contrast between the two media. Ilisei et. al. proposed an automatic technique to map regions of liquid water ponded at the base of ice-sheets, i.e. subglacial lakes [76] in East Antarctica radargrams. These targets appear as linear specular reflections having highly correlated basal waveforms between adjacent radar traces. The authors defined a set of features representing the basal power and its statistical properties, the shape of the basal waveform and its correlation between adjacent columns, and the basal topography. These were used as input to a support vector machine based automatic algorithm that classified each radar trace into lakes and non-lakes.

In some cases, RS data of specific targets are not available at present but they will be acquired in future missions. In these cases, automatic data analysis algorithms can be developed with the help of simulated radargrams. Donini et. al. exploited this possibility by developing an algorithm for automatic lava tube detection using simulated radargrams as reference. The algorithm is based on the extraction of linear features, followed by their evaluation based on a fuzzy inference system to detect the ground, the ceiling and the floor of the lava tubes [42].

2.4 RS instruments: past, present and future

The importance of radar sounding techniques in providing a complete three-dimensional information of the target has been well-recognized in the scientific community. Ground penetrating radars are commonly used for field surveys to detect buried objects. To enhance area coverage of these instruments, RSs mounted on airborne platforms have been used for regional-scale mapping of Antarctica and Greenland (e.g. [36, 141]). In the past two decades, several RS instruments have been designed and launched for planetary ex-

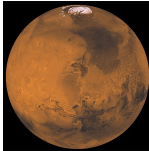






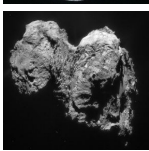





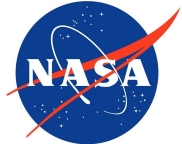
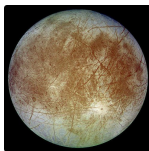
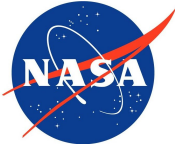

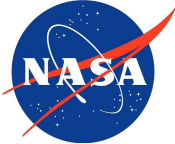
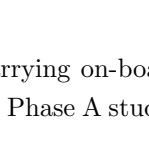
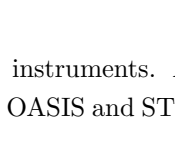

	Radar Sounder	Mission	Target	Developed by	
2003	MARSIS	Mars Express			
2006	SHARAD	MRO			
2007	LRS	SELENE Kaguya			
...					
2014	CONCERT	ROSETTA			
...					
2018	SRS	EnVision			
2019					
2022	RIME	JUICE			
...					
2025	REASON	Europa Clipper			
2032	SRS launch	EnVision			
!!!	OASIS, STRATUS	Earth-orbiting satellite			

Figure 2.4: Past and future satellite missions carrying on-board RS instruments. Among these instruments, SRS (highlighted in red) is currently in the Phase A study, and OASIS and STRATUS (highlighted in green) have been proposed.

ploration and several others have been selected for scheduled missions in the near future. These instruments have demonstrated the capability of detecting subsurface structures and layers that no other sensor can detect. Figure 2.4 shows the list of the past, present and future RS instruments designed for planetary exploration (some of these missions have been studied but not yet approved). The design of the future instruments leverages the heritage of the past and currently operating RSs. Furthermore, the data available from existing RSs can be used, with appropriate adaptation, for predicting the performance of the scheduled RSs. In the following, we briefly review these state-of-the-art planetary RSs in terms of the mission carrying the instrument, its scientific objectives and the main design parameters.

2.4.1 MARSIS

The Italian Space Agency (ASI)'s Mars Advanced Radar for Subsurface and Ionosphere Sounding (MARSIS) [122] is the RS instrument on-board European Space Agency (ESA)'s Mars Express orbiter, which was launched in 2003 and activated in June 2005. The goal of MARSIS is to perform subsurface sounding of the Martian crust up to several kilometers. Apart from subsurface sounding, MARSIS is also designed for ionospheric sounding and large-scale surface altimetry. It can operate at four central frequencies, i.e. 1.8, 3, 4 and 5 MHz with a bandwidth of 1 MHz, resulting in a range resolution of 150 m in free-space. The 1.8 and 3 MHz bands are used for night-side operation, while the 4 and 5 MHz bands are used for day-side operation to minimize distortions caused by the ionosphere. Synthetic aperture processing is performed on-board using three Doppler channels and the complex spectrum of the signal in the frequency domain is down-linked. On-ground processing involves transforming the signal to time domain and correcting for phase-distortions due to the ionosphere.

The main transmitting and receiving antenna is a 40 m long dipole oriented orthogonal to the direction of motion. A secondary monopole antenna is also included, and is oriented vertically in order to receive off-nadir echoes. MARSIS radargrams revealed the first-ever subsurface image of the Mars NPLD, which provided evidence for the presence of ice-rich Martian polar caps [122]. Further, a 250 km diameter buried impact basin was also discovered in Chryse Planitia mantled by low-loss ice-rich material [152]. Even a decade after the launch of MARSIS, the radar continues to reveal crucial features of Mars, such as the recently discovered first evidence of extra-terrestrial liquid water in the form of a 20 km wide subglacial lake at a depth of about 1.5 km below the South Polar Layered Deposits (SPLD) [107].

2.4.2 SHARAD

The ASI's Shallow Radar (SHARAD) [139], on-board the Mars Reconnaissance Orbiter (MRO), is the second Martian subsurface radar and complements MARSIS' deep probing capability with high resolution shallow probing data. With a 10 m dipole antenna, SHARAD operates at a central frequency of 20 MHz with a bandwidth of 10 MHz. This results in a range resolution of 15 m in free-space and an expected penetration up to several hundred meters. A key feature of the SHARAD data is the achievement of "high fidelity" signal reconstruction in terms of minimum distortions and low sidelobes. This is achieved by (1) minimizing on-board processing, and (2) minimizing analog electronics, such as baseband conversion. The down-linking of nearly raw data (possible due to high data-rate of MRO) allowed the precise processing of the SHARAD radargrams and further improvement of the processing-chain over time [35].

Similar to MARSIS, the data from SHARAD resolved several scientific debates regarding the composition, formation and evolution of interesting geological features on Mars. For example, SHARAD provided evidence that the lobate debris aprons in the mid-latitudes are primarily composed of ice [124]. Complementing the MARSIS detection of the base of the polar layered deposits, SHARAD resolved the details of the layering, thus supporting stratigraphic and palaeoclimatic studies [121]. The capability of RSs in detecting the geological past was demonstrated by the detection of the stratigraphic horizon between the younger surface sediments of the Vastitas Borealis Formation and the buried Hesperian volcanic plains [19]. Thus, through orbital acquisitions, SHARAD and MARSIS provide a global subsurface mapping of the Mars shallow crust.

2.4.3 Radar sounding of the Moon

The first ever RS experiment to perform sounding measurements from orbital platform was the Apollo 17 Lunar Sounder Experiment (ALSE), on-board the Command and Service Module of the Apollo 17 orbiter in 1971 [120]. The technology available at that time allowed recording of the analog signals in a film. ALSE was a chirped radar operating at three frequencies, i.e. 5, 15 and 150 MHz with the goal of mapping subsurface layering on the Moon. At the wavelength of 60 m, ALSE detected 2 subsurface horizons in Mare Serenitatis at depths of 0.9 km and 1.6 km, respectively, and another horizon in Crisium at a depth of 1.4 km [114]. Due to the poor range resolution of 1200 m (free-space), ALSE did not detect any evidence of layering in the lunar crust.

Following in the heritage of the Martian RSs and leveraging the advancements in digital electronics, the Lunar Radar Sounder (LRS) [106] was launched on-board Japan Aerospace Exploration Agency (JAXA)'s Selenological and Engineering Explorer (SELENE) Kaguya spacecraft in 2007, with the aim of detecting buried regolith layers at a range resolution

of 75 m. The LRS operates at a central frequency of 5 MHz with a frequency sweep from 4 to 6 MHz, at a $2\pi \times 10^{10} \text{ rad/s}^2$ sweep rate of angular frequency. For an expected loss tangent of 0.006 of lunar regolith, LRS can achieve a penetration up to 5 km. Due to the absence of ionosphere on the Moon, the signal is not affected by dispersion. There are 4 units comprising the antenna system resulting in two dipoles X and Y. LRS can operate in several modes, such as using X for transmission and Y for reception and vice versa, or in monostatic mode using either X or Y and a transmitter-receiver switch. The echo signal can be down-linked in time domain, or as power spectrum after on-board Fourier transform (to reduce the data-rate).

One of the scientific objectives of LRS is to find evidence of stratification in the nearside Maria at depths of several hundred meters below the surface. In this context, the data from LRS revealed buried regolith layers that accumulated in the lunar geological past and were subsequently mantled by mare basalts [105]. Multiple layers were detected in Mare Imbrium, Crisium and Oceanus Procellarum. The estimated dielectric properties of these regions from the radar profiles are consistent with the Apollo measurements. However, the reflectors detected by ALSE were not detected by LRS, possibly due to the different capabilities of the two instruments.

2.4.4 CONSERT

Following the success of the lunar and the Martian sounders, subsurface exploration of distant planetary bodies began to gain interest. At the end of a decade-long cruise, ESA's Rosetta mission entered into orbit of the comet 67P/Churyumov-Gerasimenko. The mission carried on-board the bi-static Comet Nucleus Sounding Experiment by Radiowave Transmission (CONSERT) [79] radar and the lander Philae with the aim of investigating the internal structure of the comet nucleus, and providing information about its evolution and formation in the early solar system. Unlike Mars or the Moon, comet 67P is a small body with diameter of the order of a few kilometers. This required a mission-specific unique design of the CONSERT radar.

The conventional design and acquisition geometry of RSs was modified to a bi-static configuration such that the Rosetta orbiter and the Philae lander both carried identical pairs of transmitting and receiving antennas operating at a central frequency of 90 MHz with a bandwidth of 10 MHz. Due to the relative movement between the orbiter and the comet, an occultation geometry is obtained that allows the signal to propagate through the comet nucleus during transmission and reception between the orbiter and the lander. By estimating the time delay and the amplitude of the signal, the bulk dielectric permittivity of the comet can be predicted, thus providing insights into its composition. The accuracy of the prediction would depend on the accuracy of the relative position of the lander and

the orbiter. Unfortunately, due to multiple bounces after landing, there was initially a high uncertainty in the position of Philae.

However, extensive studies on the possible hypotheses of the dielectric properties of the comet were conducted prior to the mission [66], which helped to resolve this unexpected problem. It is well-known that the permittivity is a function of porosity, composition, temperature, internal structure and scale of potential heterogeneities in the comet. 3D simulations of the radar signal were carried out considering a wide range of values of these parameters. These values were obtained from laboratory measurements of the comet-analog dust-ice-void mixtures. Upon the misplacement of the lander, another parameter was added to the set of unknowns, i.e. the position of the lander. The simulated values of time delay and amplitude were matched with the obtained observations from CONSERT. This helped in constraining the lander's location to within an area of 21 x 34 sq.m and ascertaining the average permittivity of the comet nucleus as 1.27. The dust/ice ratio was constrained to the range 0.4-2.6 and the porosity to the range 58%-75%. The CONSERT instrument on-board the Rosetta mission demonstrated the usefulness of creating a database of dielectric measurements and radar simulations in preparation for complex missions.

2.4.5 Radar sounding of the Jovian icy moons

Recently there has been a growing scientific interest in the outer planet satellites. These moons around the gas giants (Jupiter and Saturn) are composed of volatiles such as methane and water, which hint at the possibility of past or present life or habitability. The satellites of Jupiter i.e. Ganymede, Callisto and Europa are composed of water-ice. In the past, data from Voyager and Galileo missions detected magnetic fields around Ganymede, hinting at the possibility of a vast body of liquid water ocean below the ice crust. These missions also imaged the surface of these Galilean moons, showing interesting geo-morphological features such as bands, multi-ringed basins, palimpsests, paterae, and sub-parallel ridges and troughs [57]. Understanding how and why the icy moons have such diverse geological features is the key to understanding the dynamic history of the solar system and the evolution and interior dynamics of the Jovian system. The successful heritage of the previous RS missions, the high penetrability of low-temperature ice and the need for a direct subsurface evidence of liquid water has motivated the selection of two RS instruments in the upcoming Jovian missions.

The JUper ICy moons Explorer (JUICE) [57] is the first large-class mission chosen as part of the ESA's Cosmic Vision 2015-2025 program. The JUICE mission is aimed at studying the Jovian system and investigating potential habitable zones in the Jovian satellites. The Radar for Icy Moon Exploration (RIME) [18], is the RS on-board the

JUICE and will be the first instrument to profile the subsurface of the outer planet moons. RIME will operate at a central frequency of 9 MHz with a bandwidth of 1 MHz or 2.8 MHz. It is optimized for penetration up to 9 km through ice. For the three moons, data will first be acquired in multiple-flybys, which will be followed by an insertion into a circular orbit at an altitude of 500 km (nominal phase) around Ganymede. Thus, RIME will provide a global coverage of its principle target, i.e. Ganymede.

The scientific objectives of RIME are: (1) to characterize the structure of the ice shell and the distribution of subsurface water; (2) to understand the formation of surface features; (3) to search for past and present activity; and (4) to determine the global composition, distribution and evolution of surface materials. RIME would contribute to these objectives by profiling the subsurface to detect geological horizons or interfaces at which there is significant contrast in dielectric permittivity [18]. A minimum on-board processing will be applied to the data, such as presumming up to a factor of 8 and digital sampling, thus enabling robust data processing in the ground segment.

The other RS to explore the subsurface of the Jovian moons, especially Europa, is Radar for Europa Assessment and Sounding: Ocean to Near-surface (REASON) [12] approved on-board NASA's Europa Clipper mission. Europa is the smallest and the most active icy moon of Jupiter. There are evidences of interesting geodynamic processes occurring on its near-surface region, resulting in geological features such as plumes and ice diapirs. Due to the shallow expected depth of the putative ocean on Europa, the detectability of the ice-ocean interface is more probable than on the other icy moons. However, due to its proximity to Jupiter, the high intensity of the Jovian emissions does not allow orbital sounding of Europa. Thus, Europa Clipper would operate as a fly-by centric mission, acquiring the subsurface profiles over multiple fly-bys. The goal of REASON is to investigate the habitability of Europa by subsurface sounding of its ice-shell. REASON is a dual frequency (9 MHz and 60 MHz), multi-channel radar, enabling concurrent deep and shallow probing. A minimum on-board processing will be performed taking advantage of the fly-by centric configuration in order to apply robust on-ground processing [96].

2.4.6 Subsurface sounding of Venus

Venus, our closest neighbour, is an interesting planetary target for radar sounding. The presence of optically dense clouds blanketing the planet requires the use of radar to observe its surface and thus to study its geological characteristics. Previous missions carrying SAR instruments (Magellan and Venus Express) [134, 143] have provided radar images of the Venusian surface revealing the complexity of the surface topography, the globally random distribution of craters (indicating that the entire planet's surface has the

same age), the possibility of active volcanism, and the presence of extensively long lava flow channels. This poses many intriguing questions about the history and the present-day geological activity on Venus. With the goal of addressing these objectives, the EnVision [154] is shortlisted as one of the candidates for ESA's fifth medium class mission (M5) in its Cosmic Vision science programme, with a planned launch date in 2032.

One of the instruments on-board EnVision is the Subsurface Radar Sounder (SRS), which will be the first instrument to provide direct subsurface measurements of Venus. SRS will examine the presence of layering in the modified craters, search for buried craters and geological features, constrain the three-dimensional structure of complex targets such as the tesserae and estimate the volume of flow units. The instrument will operate in the range 9 - 30 MHz (the central frequency is yet to be selected) with about 60% fractional bandwidth. SRS is in the preliminary design phase, i.e. the instrument parameters are being analyzed for the selection based on the mission requirements and the expected target properties.

2.4.7 Earth observation radar sounders

We have seen so far that there have been several RSs orbiting different planetary bodies to study the subsurface characteristics of the shallow subsurface. Interestingly, there is no such orbiting RS for Earth observation yet. This is mainly due to the challenge of allocating the electromagnetic spectrum required for RSs for Earth-observation and the propagation through the ionosphere. From the perspective of radar sounding, the areas of interest are the regions having hyper-arid conditions (minimum of liquid water in the shallow crust). This is because liquid water has high electrical conductivity, and thus does not allow penetration of electromagnetic waves through them. Thus, the target areas include the dry equatorial deserts and the polar ice caps.

Subsurface sounding in the polar caps has been successfully demonstrated by the airborne campaigns [141, 117, 36]. The radargrams from these campaigns have revealed the complex stratigraphy of the englacial layering, which can be interpreted to understand the past climatic history of the Earth. The dynamic processes in the ice-sheets, such as the basal melting and refreezing, the presence of subglacial lakes and the rate of the seaward ice-flow have also been predicted using the airborne radar sounder (ARS) data (e.g. [6, 118]). In the desert regions, several interesting geological features can be buried under layers of loose sand. These include buried craters, faults and stratigraphic horizons. More importantly, the scarcity of water resources in arid deserts demands the search for shallow ground-water aquifers. Radar sounding can be successfully exploited to map the locations of potential aquifers and buried geological targets. To this purpose, there have also been airborne campaigns for subsurface profiling of arid areas (e.g. [64, 115]).

The scientific value of subsurface observations over the polar region, demonstrated by the ARSs, has motivated the proposal of an Earth-orbiting radar sounder (EORS) that can provide greater coverage in space and time with higher feasibility compared to the ARSs. In this direction, recently, Bruzzone et. al. proposed the SaTellite Radar sounder for eArTh sUbsurface Sensing (STRATUS) [16] and Heggy et. al. proposed the Orbiting Arid Subsurface and Ice Sheet Sounder (OASIS) [67] missions for subsurface observations of the Earth. Since the signal has to propagate through the Earth's ionosphere, the central frequency of the radar should be greater than the ionospheric cut-off, which varies by geographical location and the solar zenith angle. A RS operating at 45 MHz will be able to propagate through the ionosphere with minimum distortions [50]. At this frequency, the EORS signal will be able to penetrate through 4-5 km of ice and a few hundred metres of desert sand. The other instrument and acquisition geometry parameters need to be selected based on the detection requirements of different targets. Nevertheless, an EORS is feasible and can greatly support the scientific community from the perspective of studying the effects of climate change and water resources management.

2.5 Conclusions

In this chapter, we have briefly explained the principles of radar sounding from orbital platforms and their applications to planetary exploration. The basic terminologies used in the context of radars are introduced. In Section 2.2, the principles of the radar acquisition process have been presented, beginning with the transmission of the signal, the reception of the reflected echoes, and the electromagnetic interaction between the target and the radar signal. Section 2.3 has described the sequential processing of the received echoes on-board, in the ground segment before distributing to the users of the data and processing of the radargrams for scientific analysis. Section 2.4 has provided a historical overview of the past, current and possible future RS instruments, briefly mentioning the technical challenges and scientific breakthroughs achieved by each.

Chapter 3

Radar response simulation and performance assessment techniques

This chapter reviews the state-of-the-art techniques for the simulation of the radar response and the performance assessment of the RS. These techniques are discussed from the perspective of the different requirements in different phases of the mission design. First, we present the techniques for modeling the acquisition scenario in terms of the target properties and the environmental factors. Then, we review the techniques for performance assessment.

3.1 Introduction

The development of a RS within the framework of a mission is based on two-fold requirements. First, it is necessary to realistically model the unknowns in the acquisition process, i.e. the target and the environmental conditions. Second, the RS needs to be designed by selecting the appropriate instrument, orbit and data processing parameters so as to maximize the scientific returns from the mission. As the mission design phase evolves, the design parameters are selected with increasing accuracy based on detailed modeling of the target and the environment. Accordingly, the performance assessment also generally evolves to be more precise and detailed in terms of complexity as the mission development progresses. This scenario is schematically illustrated in Figure 3.1.

Typically, the sequence of steps followed (not rigorously followed in all missions) in the development of RSs for planetary exploration are outlined in Figure 3.2. The proposal of a RS for the mission is based on prior knowledge of the likelihood of subsurface dielectric interfaces in the shallow crust of the planetary body. This knowledge is used to identify the science targets for radar sounding. Next, the feasibility of detecting these targets is demonstrated by a preliminary study of the RS performance in the expected acquisition

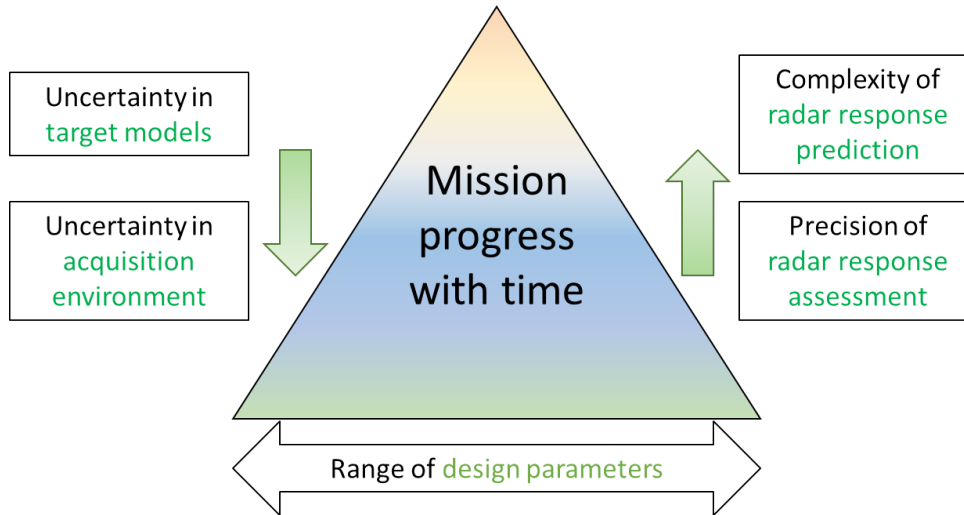


Figure 3.1: Schematic representation of the general scenario with respect to the design of the RS, the modeling of the target and the environment, and the required precision in the performance assessment with the progress of the mission

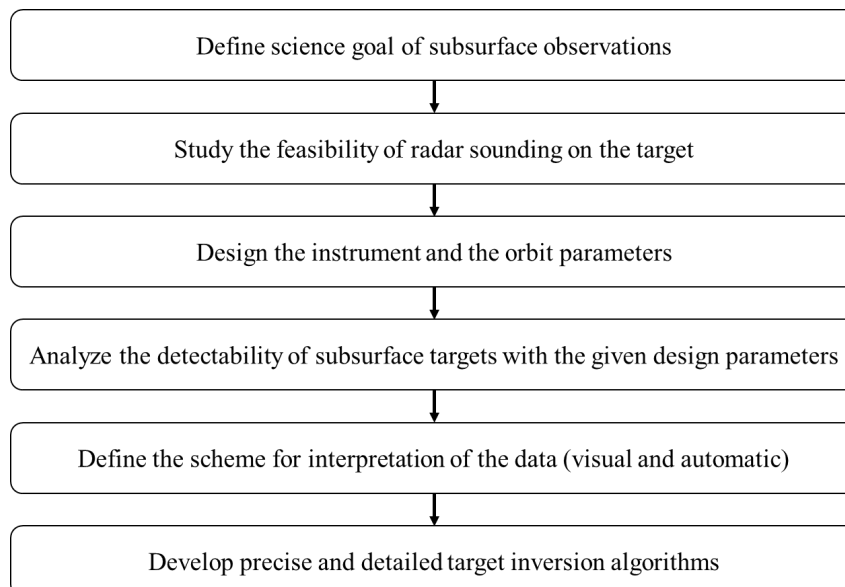


Figure 3.2: Requirements in different phases of mission design

scenario. This is used to guide the selection of the instrument and orbit parameters to ensure that the scientific requirements of the mission can be achieved. At an advanced design phase, the detectability of the different subsurface targets is analyzed in detail. This is helpful in choosing an optimum operations sequence to maximize the scientific returns from high priority targets. Once the data have been acquired, the focus is on defining schemes for extracting valuable scientific information, which involves visual and automatic interpretation of the data. In the long term, the archives of the RS data are used by the scientific community from time to time to improve their inversion and to better constrain the target properties.

In this chapter, we review the techniques for modeling the target and the environment in Section 3.2. The state-of-the-art performance assessment techniques are reviewed in Section 3.3, highlighting various approaches to the simulation of the RS data. Finally, Section 3.4 summarizes the main conclusions of the chapter.

3.2 Modeling the acquisition scenario

In this section, we describe the techniques used in modeling the unknowns in the acquisition process, which are the key inputs to the performance assessment of the RS. The main inputs to be modeled are the target, the background noise and the electromagnetic obstacles in the propagation path (e.g. the ionosphere). The accuracy of the models is the degree to which they represent realistic acquisition conditions on the target scenarios.

3.2.1 Target modeling

The first step in modeling the target is to understand its geological and geophysical properties. The next step is to translate this understanding into a simplified representation that is valid in the context of the investigated RS. Thus, the target models are defined by - (1) the subsurface components having sizes greater than the wavelength of the radar, (2) the dimension bounds given by the antenna footprint and the penetration capability of the RS, and (3) the interfaces represented by a significant dielectric contrast. The target electromagnetic interaction, which is the basis of this translation, is briefly described in Section 2.2.3.

The information required for modeling the target comes from the current knowledge inventory of the planetary body. The fact that a mission is being planned to explore the planetary body indicates that there are gaps in this knowledge that will be filled by the data acquired by the mission. In such a scenario, the detailed models of the targets are affected by subjective bias. This bias is broadly reduced by modeling in three ways:

1. *Theoretical models of the target:* A common approach is based on geological interpretation of the surface images of the targets obtained from the previous missions.

The surface expression is the first evidence for the subsurface structure. Understanding why a particular morphology appears on the surface, correlating it with the other morphologies in the region, and finally mapping it on a global context, helps in predicting the characteristics of a given target. An example is the interpretation of the pedestal crater morphology on Mars to arrive at the models of ejecta related emplacement [61].

2. *Mechanical models of the target:* In a less subjective approach, the available global knowledge of the planetary body (e.g. the size, distance from the sun, surface morphology) is combined with the current understanding of the processes in the solar system (e.g. impacts, volcanic eruption, tectonics, mass wasting, planetary differentiation) and the laws of physics (stresses and strains in common planetary materials) to simulate the mechanics of the processes that lead to the formation of a particular target. The mechanical models of the target may be represented using a finite element approach to the evaluation of the deformations for a given crustal material and a set of external forces. The mechanical models are validated by comparing the simulated deformations with the observations from surface images. An example is the modeling of the extension of the ice-shell of Ganymede to derive structural models of the grooved terrain [10].
3. *Analog-based models of the target:* Another simple and effective technique is based on searching for geological features with similar morphology as the target, but at a location that is more easily accessible. This idea has been well-exploited in the field of comparative planetary geology, wherein geological features on distant planetary bodies are explained by studying their terrestrial analogs. Of course the differences in the two cases need to be carefully analyzed, especially in terms of the scale, the materials and the magnitude of the forces. For example, the formation and structure of the ripple-ringed Valhalla basin on Callisto is explained using the genesis models of ice cauldrons in Iceland having a similar ringed morphology [155].

The target models have two main components: (1) the geometry, describing the shape of the dielectric interfaces, and (2) the geo-electrical properties of the space bounded by these interfaces. These components will be described in detail in the next two subsections.

Target geometry modeling

One of the most favorable targets for radar sounding is the one having a stratified geometry, i.e. the target can be modeled by a set of nearly parallel horizontal layers. The parameters of the stratified models are the shape (topography) of the interfaces and the spacing between them. The surface is the first stratigraphic interface and its

statistical properties are crucial for understanding the detectability of the subsurface layers. The surface topography can be obtained from digital elevation models obtained from laser altimeters [145], stereo cameras [98], interferometric SAR [126], differential global positioning system, or by exploiting the parallax shift between two images (stereo-viewing geometry) [82].

For a preliminary assessment of the scattering from surfaces, the 3D topography is not required. Instead, a few statistical parameters characterizing the surface are sufficient. Assuming a scale-dependent fractal surface, two important surface parameters are the Allan deviation of heights ζ and the slope ψ , given by [20]:

$$\zeta = \zeta_0 \left(\frac{\Delta x}{\Delta x_0} \right)^{\mathbf{H}} ; \psi = \psi_0 \left(\frac{\Delta x}{\Delta x_0} \right)^{\mathbf{H}-1} \quad (3.1)$$

where Δx_0 is the horizontal scale at which ζ_0 and ψ_0 are estimated (typically the resolution of the digital elevation model used for estimating the parameters). Δx is the scale at which we wish to estimate these parameters (typically the wavelength of the RS signal). \mathbf{H} is the Hurst coefficient, which ranges from 0 to 1 and is estimated by linear regression of the variogram, i.e. the plot of the square of the Allan deviation vs the horizontal scale. The fractal models of the surface are not only useful for estimating the surface backscatter coefficient, but also for synthesizing realistic parametric surfaces.

In the stratified model, the subsurface layers are generally the buried older terrains, whose surface exposures are perhaps visible at other locations on the planetary body. Stratigraphic and age-relationship analysis is used to determine the age of the different surface geological units [113, 137]. Thus, the subsurface topography can also be generated similarly to the surface using the fractal concepts or digital elevation data available for the exposed older units.

More realistic and complex types of target models consider the presence of volume inclusions between two layers [84]. The population of the inclusions is generally modeled using a power law size distribution [20], whose parameters may also vary with the depth (e.g. the density of rock debris may decrease with depth due to compaction). Examples of volume distributed components are rock debris, pockets of water, void spaces and fractures [68, 81]. However, the modeling of the volume inclusions and the estimation of the volume scattering losses is a relatively new field with a huge scope for future developments.

Target geo-electrical modeling

For different materials, laboratory and field measurements have been conducted to derive empirical relations that estimate the dielectric properties at different physical conditions (e.g. [66, 65, 119]). The complex permittivity of a pure material (ϵ_{pure}) is given

by the Debye equation [38]:

$$\epsilon_{pure} = \epsilon_{\infty} + \frac{(\epsilon_{static} - \epsilon_{\infty})}{1 + j2\pi f_c \tau_{debye}} - j \frac{\sigma_{e-}}{2\pi f_c \epsilon_0}, \quad (3.2)$$

where ϵ_{static} and ϵ_{∞} are the Debye parameters of low and high frequency permittivity, respectively, τ_{debye} is the relaxation time at the frequency (f_c) of the radar, σ_{e-} is the inelastic scattering of free charge carriers by the material, and ϵ_0 is the permittivity of free space. The Debye parameters depend on the temperature and the material. Thus, the temperature profile as a function of depth z can be translated into the complex dielectric profile of the pure material $\epsilon_{pure}(z)$.

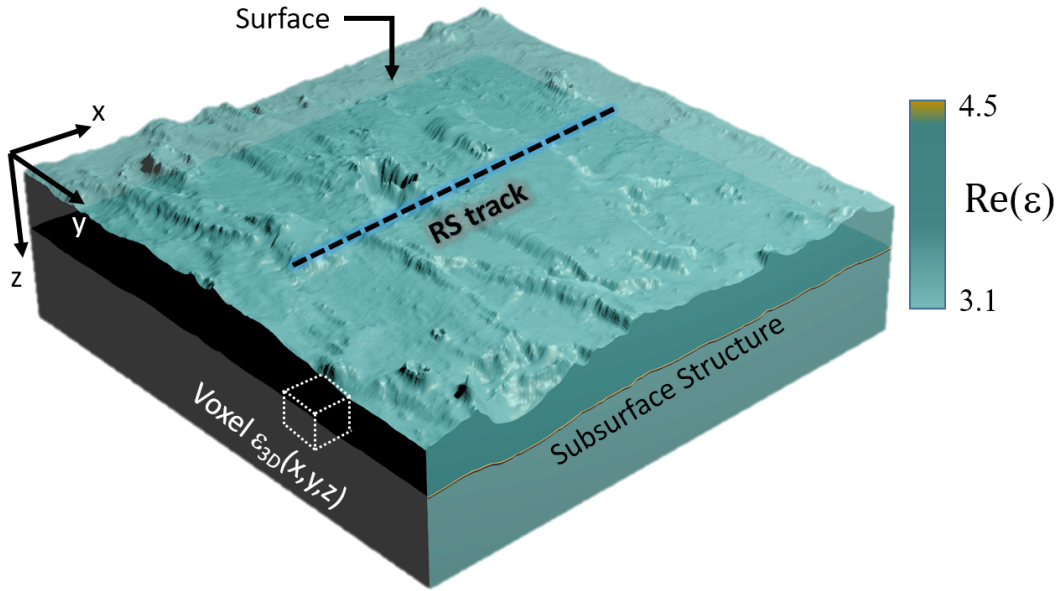


Figure 3.3: Example of 3D geo-electrical model representing the complex permittivities $\epsilon(x, y, z)$ for every quantitative cell (voxel).

In reality, planetary surfaces are mixed with voids and solid impurities having different dielectric permittivities. If the fraction of the impurities is significantly lower than the bulk pure material, the effective permittivity of the impure material can be computed using the mixing formula [142]. Thus, the impurity and the porosity (fraction of voids) profiles can be translated into the effective permittivity profile $\epsilon_{eff}(z)$.

The knowledge of these geophysical properties, such as the temperature, the porosity and the impurity profiles, is known at a more global or regional scale. The global dielectric profile is integrated with the target geometrical modeling to generate the local geo-electrical models. In this way, the dielectric properties of each structural component of the target is defined. Figure 3.3 shows an example of a local geo-electrical model of

a possible pedestal crater on Ganymede. The interface labeled as ‘Subsurface Structure’ represents a dielectric discontinuity between the crater’s ejecta blanket and the underlying bedrock. This has to be subjectively modeled, assuming a global dielectric profile $\epsilon_{eff}(z)$ and introducing the appropriate dielectric contrast to represent the discontinuity. Examples of geo-electrical models for different planetary targets can be found in [65, 68].

Thus, the knowledge of the target can be translated into the complex 3D geo-electrical model $\epsilon_{3D}(x, y, z)$, which describe the real and imaginary permittivity at every position (x, y, z) in the target space, where x and y are the along-track and cross-track directions of the RS, respectively and z is the depth. Depending on the capabilities of the simulators, the 3D geo-electrical model requires to be simplified. For 3D electromagnetic simulators, $\epsilon_{3D}(x, y, z)$ is discretized into volumetric finite elements, or voxels, as shown in Figure 3.3. For multi-layered simulators, the model is represented as uniformly triangulated layers that describe the main dielectric interfaces.

3.2.2 Environment modeling

Ideally, the RS should receive electromagnetic waves only from the target. In addition, the received signal is affected by the white Gaussian thermal noise generated by the receiver electronics, which depends on the noise temperature of the receiver and the bandwidth. However, the receiver also collects noise from the environment coming from various sources of high intensity radio emissions. This background noise may interfere with the detectability of the useful target signal and further reduce the SNR. Moreover, obstacles in the propagation path, such as the ionosphere may degrade the quality of the radar response in various ways. Thus, it is important to model the characteristics of the acquisition environment in order to select RS parameters than can overcome the signal degradation caused by these factors.

Radio emissions

Spaceborne RS signals are invariably affected by the isotropic galactic cosmic microwave background (CMB) emissions that have a peak intensity in the microwave frequencies (160 GHz). The galactic noise temperature resulting from these emissions has been measured using half-wave dipoles in the polar regions of the Earth [22]. The plot of the galactic noise temperature as a function of the frequency is shown in Figure 3.4. The power of the galactic noise P_{cmb} is proportional to the noise temperature T_{cmb} and the bandwidth B of the receiver and is given by:

$$P_{cmb} = k_{Boltzmann} B T_{cmb} \quad (3.3)$$

where $k_{Boltzmann}$ is the Boltzmann constant.

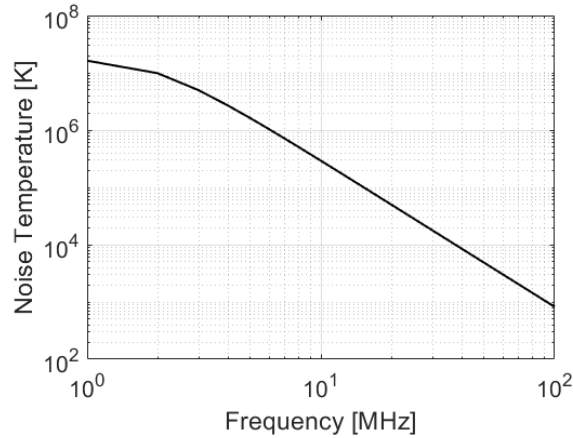


Figure 3.4: Frequency-dependent galactic noise temperature [22]

For acquisitions in the outer planetary systems, the high intensity Jovian radio emissions are another important source of noise. Jupiter emits thermal (which depend on its temperature) and non-thermal radiations, which are composed of 4 different frequency components. Among them, for example, the Decametric radiation (3-40 MHz) coincides with the operating frequency of planned orbiting RSs RIME and REASON. It has been found that the electromagnetic interaction between Io's plasma torus and Jupiter's magnetosphere triggers bursts of Decametric emissions, implying that some of the RS acquisitions in the Jovian system may be severely affected and degraded by these emissions. Recent data from the NASA's Juno mission provide deeper insights into the nature of these emissions that will support, in the future, the modeling of the Jovian radio noise [92]. Similarly, the acquisitions in the inner planetary systems, especially close to the sun, are likely to be affected by radio emissions from the sun.

Apart from the noise power of the radio emissions, another important parameter of the noise is its statistical distribution. The galactic noise and the receiver thermal noise are generally modeled as having a Gaussian distribution. After envelope detection, the in-phase and quadrature components (Gaussian distributed) are transformed in a signal amplitude with Rayleigh distribution. This theoretical output is confirmed by experiments on the statistical properties of the free-space region of planetary radargrams (between the surface and the first sample) [48]. However, the statistical distribution of the sporadic Jovian noise and the solar radio noise cannot be assumed to be Gaussian and need further analysis. The noise power of the radargram P_n is obtained by replacing T_{cmb} by the equivalent noise temperature T_{eq} of all the sources of noise in (3.3).

Ionospheric parameters

The analysis of the ionospheric distortion and the plasma frequency is important for designing the central frequency of the RS. The plasma frequency f_{plasma} in Hz is given by [133]:

$$f_{plasma} = 8.98\rho_e \quad (3.4)$$

where ρ_e is the electron density per cubic meter. The frequency-dependent complex refractive index η of the ionosphere depends on the plasma frequency, the frequency components of the RS signal f and the electron-neutral collision frequency ν , and is given by [133]:

$$\eta^2 = 1 - (2\pi f)^2(2\pi f_{plasma})^2 - i\omega\nu \quad (3.5)$$

Thus, the electron density profile and the collision frequency are key parameters required for assessing the effects of the ionosphere. Furthermore, at low frequencies the magnetic field intensity and the direction of the magnetic field vector also contribute significantly to the refractive index. The electron density profile at low solar zenith angles is described by the Chapman's model [30], which has two parameters - the maximum electron density and the scale height of the atmosphere. These parameters are obtained by fitting the measurements of the electron density profiles by magnetometers and electron reflectometers at different solar zenith angles and ionospheric columns. The density also varies with solar activity, and thus measurements at different times during an 11-year solar cycle are needed for better characterization. On the Earth, detailed measurements of the ionosphere are available from the international reference ionosphere [50]. Similarly, the magnetic field parameters are obtained by analyzing the measurements provided by magnetometer instruments.

3.3 Performance assessment of radar sounders

At the beginning of the mission it is not required to have detailed analysis of the scenarios but the necessary performance assessment to design the main RS parameters. This is used to define the rough boundary conditions on the parameters that mainly affect the performance. To this purpose, the preliminary performance assessment is focused on evaluating a number of commonly used metrics related to simple models of the target, the environmental factors, and the design parameters. These metrics assume the propagation of the electromagnetic waves to be one-dimensional, i.e. only in the nadir direction, and through a target having homogeneous dielectric properties. Thus, the preliminary performance assessment is computationally simple and requires only basic knowledge of the target.

However, in the advanced phases of development of the RS instrument, it is necessary to analyze in detail the realistic target properties. To this end, simulation techniques are

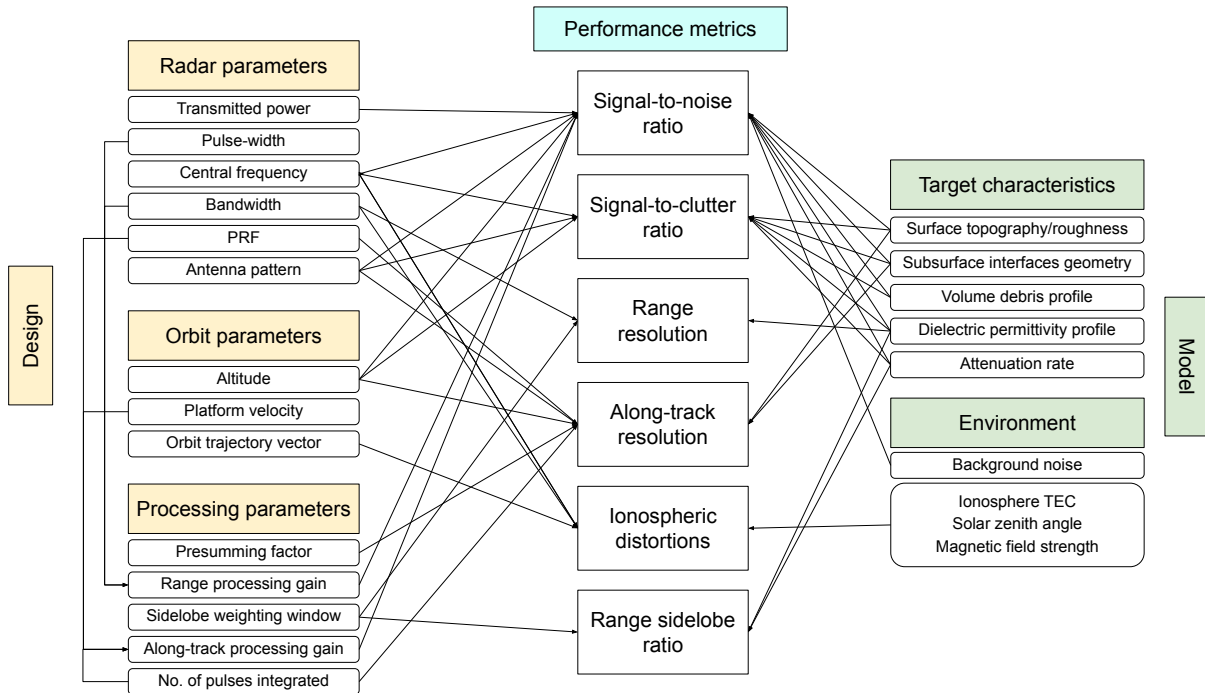


Figure 3.5: Schematic representation of radar performance evaluation.

widely used for detailed performance assessment of the RS. There are several simulators, capable of handling different target models, ranging from simple flat layers to multi-layered and finally volumetric 3D models. In this section, we first review the state-of-the-art techniques for preliminary performance assessment and then we present the approaches to the RS simulations.

3.3.1 Preliminary performance assessment

The preliminary performance is evaluated in terms of metrics representing the quality of the radar response. Figure 3.5 shows a schematic representation of the most commonly used performance metrics and their relationship with the design parameters and model properties. A quick glance at the inter-connectivity reveals that the central frequency, the bandwidth, the antenna pattern and the platform altitude are among the most critical design parameters that significantly affect the radar performance. The definition and estimation of the performance metrics are briefly presented below.

Signal-to-noise ratio

The received signal power backscattered from the target is given by the radar equation [144]. This power should be above the system and background noise at the receiver in order to detect the target. The ratio of the received signal power to the noise level is

the signal-to-noise ratio (SNR) metric. Figure 3.5 shows that SNR is a crucial metric that accounts for a large number of model and design parameters. Thus, estimating the SNR has been the most commonly used technique for assessing the detectability of the target. Due to the large number of variables involved and the uncertainties in the models, a pragmatic approach to the evaluation of the SNR relies on first estimating the link budget at the surface (*SurfSNR*), which depends largely on the instrument parameters. The *SurfSNR* for an incoherent scattering is given by[15]:

$$SurfSNR = \frac{P_t G^2 \lambda^2 \sigma_s(\theta)}{(4\pi)^3 (2H)^4 P_n} G_{range} G_{alt} \quad (3.6)$$

The *SurfSNR* depends on:

radar instrument parameters:

transmitted power P_t ,

antenna gain G ,

wavelength of the transmitted signal λ ,

processing parameters:

range processing gain G_{range} ,

along-track processing gain G_{alt} ,

orbit parameters:

platform altitude H , and its possible variation during the orbit

the effect of the environment:

environmental noise power P_n , that depends on the equivalent noise temperature of all sources at the receiver,

the effect of the target:

radar cross-section $\sigma_s(\theta)$, that depends on the radiation incidence angle θ , the antenna footprint illuminating the ground, the Fresnel power reflection coefficient at the surface, the surface topography, and the central frequency of the radar.

The processing gains are given by:

$$G_{range} = t_{pulse} B; \quad G_{alt} = \frac{\sqrt{2\lambda H} f_{PRF}}{v_s} \quad (3.7)$$

where t_{pulse} is the pulse-width, B is the bandwidth of the transmitted signal, v_s is the velocity of the platform, and f_{PRF} is the pulse-repetition frequency. These gains can be obtained by applying appropriate processing techniques.

As the signal propagates through the target subsurface, the power budget at the surface progressively decreases due to attenuation losses and scattering from multiple interfaces encountered by the wave along its path. The resulting SNR of a subsurface reflector is computed similar to the surface SNR. However, the surface radar cross-section is replaced

by the subsurface radar cross-section. Also, the losses in the subsurface are accounted in the SNR with additional terms related to the reflectivity at each interface and the attenuation coefficient, which depend on the target dielectric profile.

Apart from the attenuation and scattering losses, the presence of volume debris in the subsurface (such as pockets of water and boulders of diameter comparable to the wavelength of the radar) results in volume scattering losses. Furthermore, the roughness of the interfaces at the scale of the radar wavelength results in additional loss in the coherency of the signal, reducing the SNR even further.

The SNR calculation can be used to predict the penetration depth, which helps to define the achievable science objectives of the mission. The penetration depth is obtained by evaluating the SNR at different depths below the surface and comparing it with the sensitivity of the radar (i.e. the SNR margin required for discriminating between the signal and the noise). The farthest depth at which the evaluated SNR is above the SNR margin is reported as the maximum penetration capability of the RS.

Signal-to-clutter ratio

The reflections from off-nadir surface structures can potentially mask the nadir subsurface target reflections in radargrams. The signal-to-clutter ratio (*SCR*) of the reflection from the subsurface interface is given by [15]:

$$SCR = \frac{\Gamma_{SS}}{\sigma_s(\bar{\theta})}; \quad \bar{\theta} \approx \sqrt{\frac{2z\sqrt{\text{Re}(\epsilon)}}{H}}, \quad (3.8)$$

where Γ_{SS} is the wave propagation factor (combined effect of reflection, transmission and attenuation) of the subsurface, z is the depth of the subsurface reflector, H is the height of the platform, $\text{Re}(\epsilon)$ is the real dielectric permittivity of the medium, and $\bar{\theta}$ is the off-nadir radiation incidence angle contribution to the clutter interfering with the subsurface. Thus, the SCR metric is useful in designing the central frequency, the antenna pattern and the platform altitude of the radar. The accuracy of the SCR evaluation relies on the accurate modeling of the surface topography and roughness characteristics (see Section 3.2).

The radar cross-section of the surface is evaluated within the footprint of the antenna. Consider a dipole antenna of length L_a oriented along the track. The along-track antenna footprint size is dependent on the beam-width, while in the across-track direction, the footprint size depends on the radius of the planetary body ρ_{planet} . The along-track ρ_{alt} and across-track ρ_{act} footprint sizes are given by [15]:

$$\rho_{alt} = \frac{H\lambda}{L_a}; \quad \rho_{act} = \rho_{planet} \left\{ \pi - \sin^{-1} \left(\frac{\rho_{planet}}{H + \rho_{planet}} \right) \right\} \quad (3.9)$$

However, in reality the echoes coming from large off-nadir angles are too weak to contribute to the SCR. For smooth (flat) surface, the coherent scattering is assumed to be contributed by the first Fresnel zone, which therefore defines a more realistic definition of the footprint size in both along and across-track directions. The diameter of the Fresnel zone (D_F) is given by[15]:

$$D_F = \sqrt{2\lambda H} \quad (3.10)$$

In case of rough surfaces, the scattering is incoherent and the pulse-limited footprint better represents the along and across-track footprint size. The diameter of the pulse-limited footprint is given by:

$$D_{pl} = 2\sqrt{\frac{cH}{B}} \quad (3.11)$$

Thus, the realistic footprint sizes are nearly circular (i.e. similar for along and across-track directions) for smooth or rough surfaces. Also, they depend only on the design parameters, i.e. the central frequency, the bandwidth, and the height of the platform.

The surface backscatter coefficient is estimated from the probability distribution of the surface slopes. Several models for surface scattering are described in [20]. The type of scattering model depends on the statistical properties of the surface at the scale of RS wavelength. For the large-scale roughness, the scattering is evaluated using the Kirchhoff approximation of the phase and the principles of geometric optics, which assumes the surface to be a gently curving dielectric interface. The scattering caused by small-scale roughness which is superimposed on the large-scale undulations can be evaluated using the Small Perturbation Method. Scattering from surfaces characterized by a wide range of roughness scales can be evaluated using the Integral Equation Method [84]. A popular technique for many planetary RS assessment is based on the Hagfors' model, which is applicable to gently-undulating surfaces having a Gaussian distribution of surface heights [60].

Range resolution and sidelobe ratio

The minimum distance between two consequent reflectors positioned along the range that can be discriminated by the radar gives the range resolution performance metric. In case of frequency modulated radar signal, the vertical (range) resolution depends on the bandwidth and is given by:

$$\Delta r = \frac{c}{2B\sqrt{\text{Re}(\epsilon)}} \quad (3.12)$$

where c is the speed of light in vacuum and $\text{Re}(\epsilon)$ is the real dielectric permittivity of the medium. As described in Section 2.3, the range compression improves the range resolution, at the cost of generating sidelobes in the signal. The ratio of the peak to the sidelobe power level defines the sidelobe ratio performance metric, also known as radar

dynamic range (RDR). The sidelobe ratio should be lower than the expected power level of the subsurface echoes (normalized with respect to the surface), to ensure detectability of the target. This is achieved by applying a sidelobe weighting window to the range compressed signal. A consequence of the sidelobe weighting is the enlargement of the main-lobe of the signal peak, and thus a reduction in the range resolution by a factor equal to the degree of enlargement. Thus, the weighting window parameters are selected on the basis of the sidelobe level requirement and the maximum allowable loss of range resolution.

Along-track resolution

In the absence of any processing applied to the radargrams, the achievable along-track resolution is given by the footprint size, described by (3.9), which is in the order of a few kilometers. However, it can be significantly improved by synthetic aperture (SAR) processing, as described in Section 2.3. If the Doppler processing exploits the full phase history of the signal, i.e. a fully focused processing, the maximum theoretical along-track resolution ρ_{alt}^f considering echoes coming from the first Fresnel zone is given by:

$$\rho_{alt}^f = \frac{\sqrt{\lambda H}}{2\sqrt{2}} \quad (3.13)$$

In reality, the quality of the focused radargrams, in terms of processing gain and along-track resolution, depends on the accuracy of the processing algorithm. This further depends on the integration time, i.e. the number of pulses integrated to obtain the echo corresponding to one resolution cell, and the accuracy of estimation of the Doppler bandwidth and centroid. Furthermore, the synthetic aperture processing works only if the PRF is higher than the Doppler bandwidth, and thus the Doppler spectrum is sampled without aliasing. Thus, the along-track resolution is a requirement that affects the design of the central frequency, PRF, platform height and platform velocity.

Ionospheric distortions

Radar sounding of planetary bodies that are enveloped by an ionosphere suffers from distortions in the signal. The ionosphere reflects back signal having a frequency lower than the plasma frequency. This cut-off frequency depends on the total electron count (TEC), which varies with the solar activity, the solar zenith angle and the location. Thus, the plasma frequency defines the lower limit to the central frequency of the RS. In particular, for solar zenith angle less than 100° , i.e. for day-side acquisitions, even with a frequency higher than the cut-off, the signal can be significantly distorted. The distortion results in loss in the peak power, polarization distortion due to Faraday rotation, delay in the propagation, phase dispersion, refraction and loss of coherence time [50]. The attenuation in dB/km α_{iono} of the signal power during propagation through the ionosphere depends

on the electron density ρ_e , collision frequency ν and the RS signal frequency components f , and is given by [133]:

$$\alpha_{iono} = 4.61 \times 10^4 \rho_e \nu (2\pi f)^2 + \nu^2 \quad (3.14)$$

The phase distortion affects all the frequency components in the signal by varying degrees, and thus degrades the range resolution ideally obtainable by auto-correlation with the transmitted chirp. The phase shift in radian ($\Delta\phi$) caused by the ionosphere is given by [133]:

$$\Delta\phi = 4\pi f c \int \text{Re}(\eta - 1) dz \quad (3.15)$$

where c is the speed of light in vacuum, η is the complex refractive index of the ionosphere given by (3.5). The integration is carried out over the entire depth of the ionosphere in the space through which the signal propagates for a given pulse.

As described in Section 2.3, the ionospheric correction term is obtained from the modeling of the ionospheric parameters using techniques described in Section 3.2. However, there may be residual distortions in the corrected signal due to errors in the estimated ionospheric parameters. Scuccato et. al. describe three performance metrics for analyzing the quality of the ionospheric compensated radar response: (1) peak to sidelobe ratio, (2) ratio of the peak power of ionospheric corrected signal to that of the one not affected by ionosphere, and (3) resolution loss factor comparing the width of the main lobe of the signal with and without the ionosphere [138]. The metrics are evaluated for a given central frequency, bandwidth and pulse-width of the RS signal, and varying the TEC, the maximum electron density, the magnetic field strength and the solar activity scenarios. Such analysis is useful in selecting the central frequency and to search for optimum acquisition windows in which the ionosphere does not drastically affect the data quality.

3.3.2 Radar sounder simulation techniques

The main limitation of the preliminary performance assessment techniques is that they do not account for many important effects like the large antenna footprint, which significantly affects the clutter performance. Also, the 3D structures of the target surface and subsurface interfaces are not considered. These limitations are addressed in the detailed analysis of the target detectability, using advanced techniques for simulating the radar response. Depending on the complexity of the assessment required, different simulators are used for generating an A-scan or the full radargram. Some of the common RS simulators and the applications for which they were used are briefly described below.

1D wave propagation simulators

The simplest RS simulators consider a plane-wave propagation of the electromagnetic waves only in the range direction. The target model for such 1D simulators assumes

horizontal and parallel interfaces having homogeneous dielectric permittivities between them. These simulators are the basis for the SNR performance metric described in the previous section. In particular, the simulators evaluate the Fresnel coefficients of reflection and transmission, the time delay between successive interfaces, and the attenuation in the medium.

Prior to the launch of the Mars RSs, Leuschen et. al. developed a simulator for supporting the performance assessment of MARSIS and SHARAD. The first-order simulations proposed by them were based on one-dimensional plane-wave propagation assuming the subsurface media to be composed of N perfectly flat layers. The received power was evaluated using the Friss transmission formula [148]. The transmitted waveform was represented in frequency domain and the target amplitude response for each subsurface layer was simulated.

In the post mission phase, the simulation of the one-dimensional wave propagation was used to confirm the evidence of the subglacial lakes in Mars' South Polar Layered Deposits (SPLD) from the MARSIS radargrams [107]. The target was modeled as a three layered plane parallel stratigraphy (free-space, a homogeneous layer representing the SPLD, and the basal material beneath the SPLD). The ratios of the global reflection coefficients of the surface and basal interfaces were recursively simulated for every frequency and considering a range of dielectric properties. The complex permittivity of the SPLD layer was derived from mixtures of water ice and dust in various proportions and temperatures to constrain the range of permittivity values of the basal material. The high values of the inverted basal permittivity indicated that the basal material is water-saturated or composed of layers of liquid water.

Single layer surface clutter simulators

Another class of simulators consider the spherical propagation of the electromagnetic waves and estimates the radar response of the surface (i.e. the clutter response) of the target within the antenna footprint. The Facet method was developed and applied to evaluate the surface backscattered power by MARSIS using a coherent clutter simulator [99]. In the Facet method, the surface is modeled as a series of planar facets that are tangential to the actual surface. Each facet is treated as an antenna illuminated by the RS electromagnetic wave. The distance of the facet to the RS can be evaluated from the surface elevation and the acquisition geometry parameters, and is used to simulate the time delay and the phase of the received echo. The power backscattered by the facets (which depends on surface Fresnel reflectivity, and the orientation and size of the facets) is integrated in the frequency domain, based on Huygens principle, to simulate the received power from the surface. The Facet method is suitable for surfaces that are relatively smooth at the scale of the RS wavelength.

The Facet method was also used by Choudhary et. al. for incoherently simulating the cluttergram of SHARAD, but by evaluating the backscattered power using the radar equation [31]. The gain and the radar cross-section of each facet were evaluated based on the effective area and the radar incidence angle. A radar footprint radius of 45 km was considered for integrating the returned power from the facets, assuming the surface reflectivity to be diffused, in order to maximize the detected clutter.

Another incoherent clutter simulator for SHARAD used a purely geometrical approach to the generation of the cluttergrams [132]. In this approach, instead of facets, each MOLA elevation sample is represented as a point scatterer. The incoherent backscatter coefficient is computed for each scatterer at each position of the spacecraft over a length equal to the synthetic aperture. Since the radar response of the point appears in multiple range positions due to range cell migration, these responses are incoherently summed into a single cell. The response of the terrain, simulated at each along-track position of the spacecraft, is concatenated to form a matrix, which is convolved with the 2D ideal SAR impulse response to obtain the simulated cluttergram.

Recently, a coherent clutter simulator CLUSIM [77] has been developed for the Mars RSs. CLUSIM models the surface by projecting the Mars Orbiter Laser Altimeter (MOLA) elevation data onto a plane tangential to the sub-spacecraft point, thus neglecting the effect of the curvature of the planet. The topographic variations are then interpolated using cubic spline interpolation for a uniformly spaced rectangular grid on the tangential plane. The simulated cluttergram is generated by integrating the reflections from the modeled surface using the Kirchhoff integral (which is valid for large rough surfaces). A novel feature of CLUSIM is its aperture synthesis capability, which is obtained by an additional integral over the spacecraft coordinates for a distance equal to twice the synthetic aperture length. The simulator was used to test the impact of the clutter on the performance of an existing ionospheric phase correction algorithm.

Multi-layer subsurface simulators

Apart from the clutter response, the need to simulate the subsurface is recognized in order to resolve the ambiguities in the interpretation of the acquired radargrams. The initial attempts to simulate the subsurface were based on evaluating the incoherent subsurface backscattered power. The previously described first-order 1D simulator considering N flat layers developed by Leuschen et. al. was further extended to a higher order simulator considering N rough layers [84]. The geometric optics approximation was used to evaluate the backscatter from the N layers as a function of the incidence angle. The computation was simplified by first evaluating the response of a point scatterer and then convolving the response with the 2D surface topographic variations.

A more recently developed subsurface simulator for SHARAD (SHARSIM) [146] was

also based on incoherent subsurface response evaluation. SHARSIM evaluates the subsurface backscattering based on the radar equation, and by modeling each layer using the Facet method, similar to the clutter simulator proposed by Choudhary et. al. [31]. In addition, the scattering caused by small-scale roughness within each facet is computed using the Hagfors model and assuming a Gaussian distribution of topographic heights. This requires the facet size to be much larger than the wavelength of SHARAD, which is easily satisfied by using the data from MOLA.

A more accurate subsurface simulation is provided by coherent multi-layered simulators, which solve the actual propagation of the electromagnetic field using Huygen's principle. Thus, they are also able to simulate the phase of the radar signal [9, 46]. Kobayashi et al. developed a simulator for the lunar radar sounder and presented an analytical solution of the electric field variation with range [78], assuming the Kirchhoff approximation. However, the exact analytical solution, although provides accurate computation of the fields, also results in very high computational requirements. Fa et al. attempted to simplify this approach by replacing the analytical solutions by a numerical solution based on the ray tracing principles of geometric optics, along with Kirchhoff's approximation of rough surface scattering for a two-layer model [46]. In this approach, the magnitude and direction of the transmitted and backscattered wave vectors are computed using Snell's law. This simulator was used in the preparation for the Chang-E Chinese lunar radar sounding project.

Berquin et. al. proposed another computationally efficient coherent simulator that relies on the analytical solutions of the scattered electromagnetic fields by solving Huygen-Fresnel's equations and evaluating the phase contribution of each facet based on a linear phase approximation [9]. The surface is modeled as triangular facets having size larger than the wavelength of the RS, thus enabling the subsurface simulations of realistic planetary targets with computational efficiency, while not compromising the accuracy.

Recently, a multi-layer coherent RS simulator (MRS) [53] has been developed that, similar to [46], computes the electric field propagation through the multiple layers of the subsurface using the ray-tracing principles of geometric optics. Similar to [9], it evaluates the phase contribution of each facet based on the linear phase approximation and calculates the total received field by solving the Stratton-Chu integral. The MRS simulator has been applied to the analysis of active and passive sounding performance of RIME for the Jovian icy moons [53].

Volumetric 3D simulators

One of the most powerful RS simulation techniques is the Finite Difference Time Domain (FDTD) [158] method that simulates the electromagnetic field for the entire subsurface volume. It is capable of using detailed 3D models of the subsurface, which are

subdivided into small 3D elementary cells (voxels). It involves a numerical solution of the differential form of the Maxwell equations for wave propagation. Since FDTD works in the time domain, it allows for the representation of the input signal by the actual transmitted waveform. Moreover, being a 3D simulation technique, it allows flexibility in modeling the target geometry, the material dielectric properties and the radar parameters. Thus, FDTD allows to accurately model the radar parameters and the volume scattering caused by distributed subsurface scatterers, however at a very high computational cost.

The FDTD based simulation approach has been applied in diverse fields such as for military applications of GPR [14], for airborne RSs [52], for the GPR experiment on NETLANDER for Mars [32], to characterize volcanic terrains on Mars for MARSIS and SHARAD [65], and to constrain the composition of the Comet 67P [81]. In recent studies, the approach has been used to predict the capability of RIME in detecting the brittle-ductile interface, deep fractures, brine lenses and the subsurface ocean [68].

3.4 Conclusions

In this chapter, we have reviewed the state-of-the-art techniques for performance assessment of RSs. In the introduction, we have described the general scenario of planetary missions and described how the requirements evolve with the progress of the mission. Section 3.2 reviews the techniques for modeling the target and the environment, which are the unknowns in the acquisition process and important inputs to the performance assessment. Section 3.3 describes the simulation and performance assessment approaches, beginning with computationally simple metrics, followed by clutter simulators, multi-layered simulators and 3D volumetric simulators.

**Part II: Proposed methods for
simulation and analysis of
radargrams**

Chapter 4

An approach to the simulation of RS radargrams based on geological analogs

As described before, conventional radar sounder simulation techniques, based on solving the propagation of the electromagnetic waves, require detailed subjective models of the target, are computationally intensive, and yet produce radargrams that are not often realistic. In this chapter¹, we propose a novel simulation approach that exploits the data available from existing RSs in geologically analogous terrains, to produce realistic simulations of the investigated RS target. The approach is demonstrated using three case studies for different possibilities of the analog and the investigated scenarios. The validation of the simulated radargrams with actual data demonstrates the effectiveness of the proposed approach.

4.1 Introduction

In the previous chapters, we have described the importance of simulation techniques in supporting RS missions. Without the aid of simulators, interpretation of RS data can be challenging since the response of subsurface geometries is a combined effect of the orientation of the dielectric interfaces [18] with respect to the radar's nadir looking geometry; the dielectric properties of the medium; volume scattering due to porosity and heterogeneities in natural media, and clutter due to surface roughness. These factors are not easy to model and hence their effect on the radar response cannot be intuitively understood. To facilitate the interpretation of the radargrams, and further, to develop data analysis schemes for automatic interpretation of RS data, it is necessary to forward

¹Part of this chapter appears in

Thakur, Sanchari, and Lorenzo Bruzzone. "An Approach to the Simulation of Radar Sounder Radargrams Based on Geological Analogs." IEEE Transactions on Geoscience and Remote Sensing (2019).

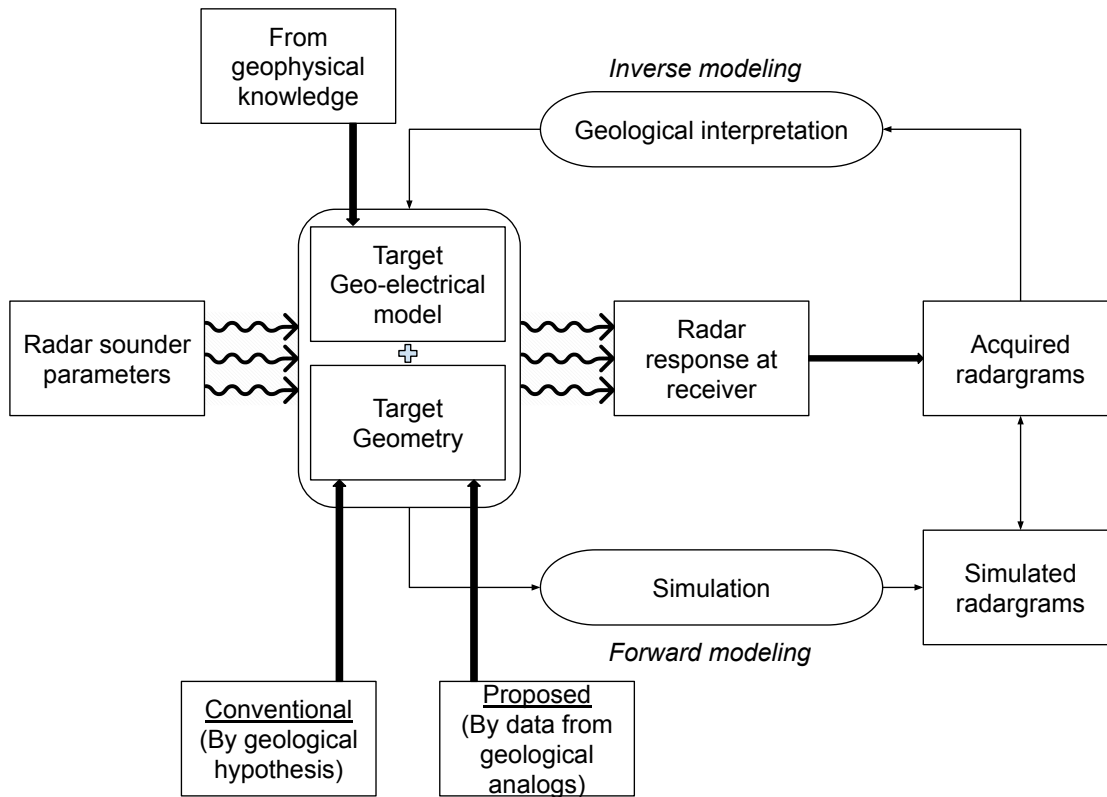


Figure 4.1: Flowchart describing the RS acquisition process and its relation with simulation and geological interpretation.

model the subsurface through simulations.

While interpretation of radargrams is an inverse modeling problem in which the underlying geo-electrical model is inferred, electromagnetic simulation is a forward modeling approach for predicting the radar response of a subsurface target (Figure 4.1). State-of-the-art simulation techniques (described in Section 3.3.2) involve: (1) modeling the target geometry and geo-electrical properties (see Section 3.2), (2) simplifying the target models according to the capabilities of the simulator, and (3) solving for the electromagnetic field propagation through the target.

Although the conventional simulation techniques accurately compute the electromagnetic interaction of the RS signal with the subsurface medium, they are based on subjective assumptions about the target and thus require detailed knowledge of the planetary body. For targets for which high resolution surface images are not available, this task can be challenging and affected by uncertainties. Moreover, the interpretation of the surface images cannot provide a complete knowledge of the actual subsurface scenario, which includes heterogeneities caused by small-scale structures. These heterogeneities cannot be

realistically translated into the input geo-electrical models used by the conventional simulators. Hence, the simulated radargrams do not realistically represent the real acquired radargrams.

In this chapter, we propose an alternative approach to the simulation of radargrams. This approach aims to reduce the bias in the target geometry modeling by leveraging the data available from existing RSs. In particular, the approach uses data acquired over geological features having similar surface expressions as the target of interest. These features with similar surface expressions are referred to as geological analogs. Since the surface expression is an indicator of the subsurface structure of a geological feature, the radargram available over the geological analog can be used to predict the subsurface signature of the class of target under investigation. In this approach, we simulate the radargrams starting from the data acquired over the geological analogs, and reprocess them to account for the differences between the analog and the investigated radar parameters and target subsurface properties. The main contribution of this chapter is twofold: (1) modeling the geo-electrical properties of the investigated target using its geological analog, and (2) reprocessing and adapting the radar parameters of different RS instruments. The simulated radargrams, obtained by the proposed approach represent the radar response of the analog feature to the investigated RS parameters, assuming that the analog occurs on the investigated planetary body.

The chapter is organized as follows. Section 4.2 describes the previous studies involving geological analogs in planetary exploration. Section 4.3 describes the details of the proposed methodology and Section 4.4 presents three cases demonstrating the proposed approach. The first two cases validate the method by comparing with existing RS data. The third case is a real-world application of this approach for predicting the performance of RIME. Section 4.5 presents the conclusions.

4.2 Geological analogs in planetary exploration

Analyses of terrestrial analogs are an integral part of planetary science and space exploration. Analogs are used for interpretation of data acquired by space-missions, for design of future missions and in the field of comparative geology for understanding the processes of formation of planetary features [85, 55, 91, 93, 58, 5]. Analog sites were selected or created artificially to train astronauts for lunar field surveys and to test-drive rover missions [85]; in the field of astrobiology to test life detection instruments [86] and in the field of space mission planning for the Mars Science Laboratory mission, which landed the rover Curiosity [69].

Recently, GPR investigations of terrestrial analogs have been used for the SHARAD and MARSIS missions. Basaltic terrains on Earth that are compositionally similar to

certain volcanic provinces on Mars were used for dielectric characterization and evaluation of scattering losses prior to and also during the SHARAD and MARSIS missions. Surveys and field measurements were conducted at the North Amargosa Desert, Nevada [62] and Idaho [63] to evaluate the depth of penetration achievable in Martian volcanic terrains at different frequency bands.

The dielectric signatures and scattering losses due to subsurface heterogeneities in the ice-rich terrain and volcanic terrains on Mars have been quantified by resistivity and GPR measurements of temperate permafrost in Fairbanks, Alaska [13] and the Bishop Tuff volcanic terrain in California [59], respectively. These terrestrial investigations helped in estimating the SHARAD attenuation parameters.

Although the use of analogs provides a more realistic picture of challenges posed by real planetary surfaces and subsurfaces, these studies have not addressed the possibility of simulating the data of scheduled missions using data available on the analogs. This is a very important opportunity for improving our capability to predict radargrams captured in complex scenarios by using real data as starting points for simulations. However, this poses methodological challenges that should be properly addressed in order to generate adequate analog-based simulations leveraging the large amount of data available for the Earth, the Moon and Mars.

4.3 Methodology

4.3.1 Notation and terminology

In this section, we introduce the nomenclature used in this chapter to refer to different components of the proposed approach (Figure 4.2). The RS instrument and the planetary body for which we are interested in simulating the radargrams are referred to as the *Investigated RS* and the *Investigated planetary body*, respectively. On the surface of the investigated planetary body the interesting features often with unusual geomorphology, unknown processes of formation, and subsurface structure are referred to as the *Investigated surface and subsurface features*.

Target refers to the physical object that interacts with the radar signal (the analog target interacts with the analog RS, while we are interested in simulating the interaction of the investigated target with the investigated RS). The *target* is described by the *Target models* in terms of geo-electrical properties and the geometry. Geophysical properties of the planetary body, such as composition, temperature and porosity can be translated into the *geo-electrical parameters* of the target models. The *geo-morphological parameters* (i.e. the target geometry) is difficult to model for an unknown feature, and therefore, for the geomorphology we propose to derive it from the *analog surface and subsurface features*. These are identified as geological features on the *analog planetary body* that have

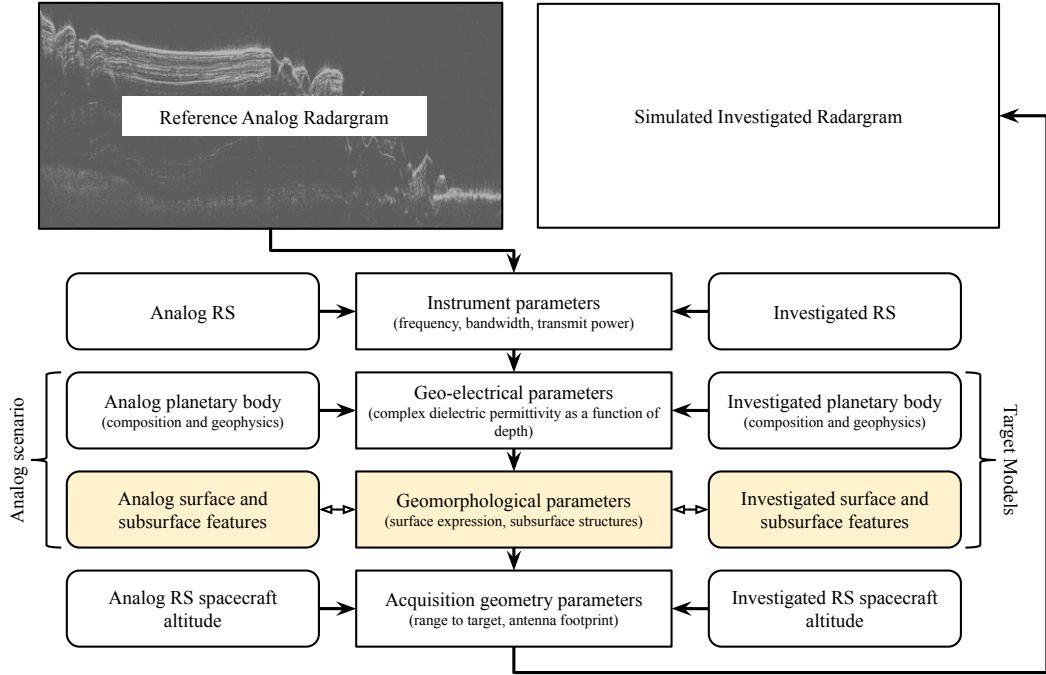


Figure 4.2: Nomenclature of the variables describing the analog and the investigated acquisition scenarios.

a similar surface expression as the *investigated surface features*, and for which radargrams are available and acquired by the *analog RS*.

In the proposed approach, we start from the available radargrams acquired over the *analog features*, referred to as the *reference analog radargram*. From this radargram, we aim to borrow the surface and subsurface geomorphology. Then we model expected differences in the investigated radargram in terms of instrument parameters, geo-electrical parameters and acquisition geometry parameters through a set of corrections, as presented in Table 4.1 and described in the next section. The final resulting *simulated investigated radargram* represents an approximation (under the considered assumptions) of the *real investigated radargram*.

4.3.2 Assumptions

The proposed approach is based on assumptions of similarity between the analog and the investigated scenarios, which should be clearly understood. Of course in cases where these assumptions can be weakly satisfied the simulation results should be carefully analyzed. The considered assumptions are as follows:

Geometrical similarity

We assume that the geometry of the investigated features, i.e. the shape and position of the dielectric interfaces, are similar to the surface and subsurface structure of the

Table 4.1: Main effects of radar and target parameters on the radargram

Difference between the analog and target scenarios	Effect on RS response	Correction applied
Spacecraft altitude	Propagation loss	Signal magnitude correction
Subsurface geo-electrical properties	Attenuation loss, interface reflectivity	
Transmit power, wavelength, antenna gain	Received echo power	
Receiver noise figure, Environment	Noise power	Noise correction
Receiver bandwidth, geo-electrical properties	Vertical resolution	Bandwidth correction
Real dielectric permittivity	Delay time of the echoes	Time correction
Sampling frequency	Time resolution	
Antenna footprint, PRF, spacecraft altitude	Along-track resolution	Along-track resolution correction

analog features. This assumption is based on the fact that similarity in geomorphology is caused by similar deformational stresses and homologous temperatures on different planetary bodies in the solar system [33]. However, the scale i.e. the physical dimension of the analog and the investigated features may be different, which is not addressed by the proposed approach.

Noise similarity

We assume that noise is additive and not signal dependent, i.e. it affects all echo samples in the same way. The difference between the noise power levels of the analog and investigated instruments can be added stochastically, assuming that the investigated radargram has the same underlying noise statistical distribution as the analog radargram. Noise is due to different sources, such as the CMB (which is present in data acquired from orbital RS, but is absent in case of airborne RS). Furthermore, the noise characteristics depend on the processing scheme applied to the raw radargrams, which is assumed to be indifferent in the proposed analysis.

Geo-electrical models

When working with non-terrestrial analogs, direct measurements of the subsurface are not available. Thus, the geo-electrical models of both the analog and the investigated targets are based on the current state-of-the-art prediction of the properties of the subsurface. However, as will be demonstrated in the next section, the simulations produced by the proposed approach are not very sensitive to the uncertainty in the input geo-electrical models.

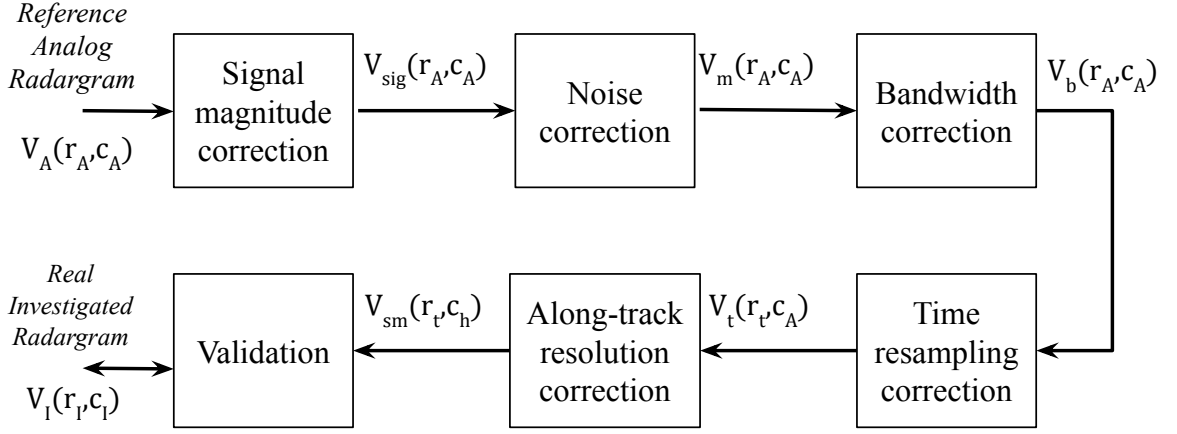


Figure 4.3: Methodology flowchart along with the notation used to represent the radargram and its row and column indices at each step.

Topography and surface roughness

Surface topography widely varies across planetary surfaces. Surface roughness, within the antenna footprint, affects the surface clutter visible in planetary radargrams. Modeling the clutter requires high resolution digital elevation models of the target, which is not always available for less-explored planetary bodies. For wider applicability of the proposed method, we assume the clutter contribution is the same in the analog and investigated scenarios.

4.3.3 Target models

The reference analog radargram, with N_{r_A} rows (samples) and N_{c_A} columns (radar traces), is given by $V_A(r_A, c_A)$, where V_A refers to the radargram complex received echo for each index (r_A, c_A) , such that $r_A = 1, 2, \dots, N_{r_A}$ and $c_A = 1, 2, \dots, N_{c_A}$. The radar traces represent the echoes sampled in the along-track direction and the samples in each radar trace represent the sampling in time (range) of the received echo. The subscript A is used to refer to variables related to the analog scenario, while I is used for the investigated scenario. Figure 4.3 shows the sequence of corrections along with the notation used to represent the radargram and its row and column indices at each step.

We construct the geometry of the target geo-electrical models by delineating the interfaces visible in the reference analog radargram and assigning the corresponding complex dielectric permittivities for the cells between the interfaces (Figure 4.4). The free-space propagation zone above the surface (detected using [48]) is used for extracting the noise samples for estimating the statistical properties of noise in the radargrams. A number of techniques are available for detecting linear or connected dielectric interfaces (e.g.

[23, 47]). For simplicity, we have visually delineated the other interfaces for the results presented in this chapter.

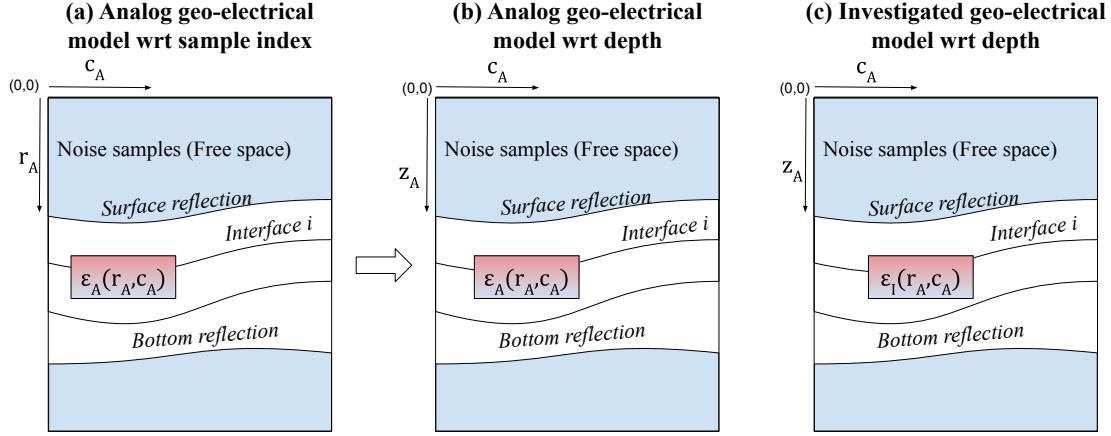


Figure 4.4: Geo-electrical modeling for the analog-based simulation approach: (a) Geo-electrical model of the analog scenario developed from the reference analog radargram, where each cell represents the time delay of the echo samples. The number of cells of the geo-electrical model is equal to the number of samples in the reference analog radargram. (b) Conversion of time to depth using the analog geo-electrical model. (c) Geo-electrical model of the investigated scenario assuming the same geometry as the analog model, but considering the complex dielectric permittivities of the investigated subsurface features.

The depth $z(r_A, c_A)$ from the first cell (shown as (0,0) in Figure 4.4) to each cell (r_A, c_A) , depends on the speed of propagation of the radar signal through the subsurface, which in turn depends on the analog geo-electrical model $\epsilon_A(r_A, c_A) = \text{Re}\{\epsilon_A(r_A, c_A)\} + j \text{Im}\{\epsilon_A(r_A, c_A)\}$ and is given by:

$$z(r_A, c_A) = \sum_0^{r_A} \frac{c\Delta t_A}{2\sqrt{\text{Re}\{\epsilon_A(r_A, c_A)\}}}, \quad (4.1)$$

where c is the speed of light in vacuum, and Δt_A is the uniform sampling time of the analog RS. Due to the assumption of geometrical similarity, the same depth is also associated with the investigated geo-electrical model $\epsilon_I(r_A, c_A)$ and the corresponding complex permittivities are chosen from the literature for the investigated subsurface feature.

From the complex geo-electrical models, we derive the wave propagation factor $\Gamma(r_A, c_A)$ quantifying the echo power received from each cell, given by:

$$\Gamma(r_A, c_A) = R(r_A, c_A) \prod_{m=0}^{r_A-1} \frac{[1 - R(m, c_A)]^2}{L^2(m, c_A)}, \quad (4.2)$$

where $R(r_A, c_A)$ is the interface reflection coefficient between the cells r_A and $r_A + 1$ and is given by:

$$R(r_A, c_A) = \left| \frac{\sqrt{\epsilon(r_A, c_A)} - \sqrt{\epsilon(r_A + 1, c_A)}}{\sqrt{\epsilon(r_A, c_A)} + \sqrt{\epsilon(r_A + 1, c_A)}} \right|^2. \quad (4.3)$$

The attenuation in power $L^2(r_A, c_A)$ of the wave as it propagates through the subsurface depends on the wavelength (λ), the geo-electrical model and the depth, and is given by:

$$L(r_A, c_A) = \exp\left(\frac{-2\pi}{\lambda} \int_0^z \sqrt{\frac{\text{Re}(\epsilon)}{2} \sqrt{1 + \left(\frac{\text{Im}(\epsilon)}{\text{Re}(\epsilon)}\right)^2} - 1} dz\right), \quad (4.4)$$

The wave propagation factors of the analog radargram $\Gamma_A(r_A, c_A)$ and the investigated radargram $\Gamma_I(r_A, c_A)$ calculated using (4.2) to (4.4) are used as parameters for the signal magnitude correction, as described in the next section.

4.3.4 Analog-based approach to the simulation of investigated radargrams

Signal magnitude correction

The wave propagating through the subsurface medium is backscattered at interfaces that have a significant contrast in dielectric properties. Thus, the backscattered signal is restricted to a few echo samples. On the contrary, during propagation through medium allowing pure transmittance or absorption, like those associated with the free space, homogeneous layers or deeper subsurface beyond the penetrability of the RS, only the thermal noise and cosmic background noise are received. We propose a correction to the signal component of the received radargram echo magnitude based on the radar equation [144]. Note that some of the available radargrams, such as that of MARSIS and SHARAD are not absolutely calibrated for the actual received power. For the cases I and II presented in the next section in which we validate the simulation results by comparing with real investigated radargrams, it is necessary to apply a minimum relative calibration with respect to the investigated radargram.

The analog signal power $P_{r,A}(r_A, c_A)$ backscattered from the target and received at the sensor of a monostatic radar antenna mainly depends on the analog RS parameters, i.e. the transmitted power $P_{t,A}$, the antenna gain G_A and the wavelength λ_A of the transmitted pulse. The corresponding parameters of the investigated RS are $P_{t,I}$, G_I and λ_I , respectively. For a known analog and investigated RS, these parameters are available.

The power also depends on the acquisition geometry, in particular, the range to the scatterer. The range is the sum of spacecraft altitude (defined with the surface as the datum) and the depth to the subsurface scatterer from the surface. Since the spacecraft altitude is much greater than the depth, we approximate the range to be equal to the spacecraft altitude ($H_A(c_A)$ and $H_I(c_A)$), which can vary in the along-track direction.

These can be determined from the spacecraft orbit parameters and must be resampled to match the number of radar traces (N_{c_A}) of the analog radargram. The power depends also on the aforementioned wave propagation factor and in general, is given by:

$$P_r(r_A, c_A) = \frac{P_t G^2 \lambda^2 \Gamma(r_A, c_A)}{(4\pi)^3 (2H(c_A))^4} \quad (4.5)$$

The signal power received by the investigated RS ($P_{r,I}(r_A, c_A)$) is estimated by considering the parameters of the analog and investigated scenarios described above, and is given by:

$$\frac{P_{r,I}(r_A, c_A)}{P_{r,A}(r_A, c_A)} = \frac{P_{t,I} G_I^2 \lambda_I^2 H_A(c_A)^4 \Gamma_I(r_A, c_A)}{P_{t,A} G_A^2 \lambda_A^2 H_I(c_A)^4 \Gamma_A(r_A, c_A)} \quad (4.6)$$

Note that (4.5) and (4.6) are applicable to the signal part of the received echo. However, the radargram contains both the signal and the noise components. To correctly apply these equations, we need to identify the samples in which the signal dominates over the noise. To detect these samples, we threshold the radargram to the peak noise floor N_T (measured from the radargram), to obtain a binary signal-noise image $v(r_A, c_A)$ given by:

$$v(r_A, c_A) = \begin{cases} 1; & P_{r,A}(r_A, c_A) > N_T \\ 0; & P_{r,A}(r_A, c_A) \leq N_T \end{cases} \quad (4.7)$$

In reality, the signal is not present in isolated samples but is spread over neighboring range samples, corresponding to the range resolution. To account for that, the binary signal-noise image $v(r_A, c_A)$ is low-pass filtered using a Gaussian kernel of standard deviation σ_{kernel} . Here σ_{kernel} can be chosen based on the ratio between the range resolution and the range sample spacing of the analog radargram, while the size of the Gaussian filter can be chosen as $\Omega = \lceil 2\sigma_{kernel} \rceil + 1$. The resulting smoothed signal-noise image is represented as $\kappa(r_A, c_A)$. Finally, the estimated signal magnitude corrected radargram $V_{sig}(r_A, c_A)$ is obtained as:

$$\begin{aligned} |V_{sig}(r_A, c_A)| &= \sqrt{P_{r,I}(r_A, c_A) \kappa(r_A, c_A)} + \\ &|V_A(r_A, c_A)| (1 - \kappa(r_A, c_A)) \end{aligned} \quad (4.8)$$

Noise correction

Noise is stochastically present in all samples of the radargram. As described in Section 3.2.2, the noise power level of the investigated radargram $P_{n,I}$ can be estimated from the equivalent noise temperature $T_{eq,I}$, the receiver bandwidth B_I and the Boltzmann constant $k_{Boltzmann}$, given by:

$$P_{n,I} = k_{Boltzmann} B_I T_{eq,I} \quad (4.9)$$

In the noise correction step, the difference between the mean noise power level of the analog $P_{n,A}$ and the investigated $P_{n,I}$ is stochastically added to the signal magnitude corrected radargram, assuming that the noise distribution of the investigated radargram is the same as that of the analog radargram. As explained in Section 3.2.2, the noise samples in planetary RS data follow Rayleigh distribution with parameter equal to the mean power of the noise samples. We obtain the mean noise power of the analog radargram $P_{n,A}$ by maximum likelihood fitting of Rayleigh distribution to the analog noise samples. The magnitude of the radargram after applying noise correction is obtained as:

$$|V_m(r_A, c_A)| = |V_{sig}(r_A, c_A)| + \frac{Z}{\max\{Z\}} (\sqrt{P_{n,I}} - \sqrt{P_{n,A}}) \quad (4.10)$$

where Z refers to $N_{r_A} \times N_{c_A}$ randomly drawn Rayleigh distributed samples with parameter $P_{n,A}$. The maximum value of the random samples $\max\{Z\}$ is used to normalize the stochastic component to avoid considering the analog noise power twice.

Bandwidth correction

There are two possible scenarios with respect to the bandwidth of the radar signal. The bandwidth of the analog instrument (B_A) can be either greater or smaller than that of the investigated instrument (B_I). The first case requires decreasing the bandwidth. This correction applied to the magnitude corrected radargram $V_m(r_A, c_A)$ requires removing the the windowing function used in the processing of the radargram for sidelobe suppression, transforming each radar trace to the frequency domain and then applying a low pass filter with a cutoff frequency equal to the bandwidth of the target instrument.

The second case is more challenging because it requires to apply a super-resolution by predicting the increased bandwidth in the frequency domain. We propose the autoregressive linear prediction to extrapolate the signal, as described in [127]. In this method, the radargram is transformed into the frequency domain, the windowing function is removed and additional frequency samples are forward and backward predicted using linear prediction. Note that increasing the resolution of the radargram cannot be intended as an increase in the information content. A RS operating at a higher bandwidth will be able to resolve finer dielectric layers that another sounder operating with a lower bandwidth cannot. Of course the information content that is not existing in the analog radargram cannot be artificially created by the proposed approach. Hence, a bandwidth increase will mainly increase the sharpness of the simulated radargram and make it comparable to that of the investigated radargram, without presenting additional subsurface information, which is not available in the reference analog radargram.

After applying the bandwidth correction, it is necessary to ensure that the integral of the power spectrum is not changed. Let $S_m(\omega_m)$ and $S_{bw}(\omega_b)$ represent the frequency spectrum of the radargram before and after bandwidth change (increase or decrease), respectively, where ω_m and ω_b represent the frequency support of the corresponding radargrams. The Fourier magnitude of the bandwidth corrected signal compensated for the change in power due to the correction process can be obtained as:

$$|S_b(\omega_b)| = \sqrt{|S_{bw}(\omega_b)|^2 \frac{\int_{\omega_m} |S_m(\omega_m)|^2 d\omega_m}{\int_{\omega_b} |S_{bw}(\omega_b)|^2 d\omega_b}} \quad (4.11)$$

The phase spectrum of the power-compensated bandwidth-corrected magnitude $|S_{b,I}(\omega_b)|$ is taken to be the same as that of the reference analog radargram and transformed back to the time domain to obtain the bandwidth corrected radargram $V_b(r_A, c_A)$. Note that the bandwidth correction step is related to the vertical resolution and not the sampling frequency of the investigated instrument. Hence, in this step, the number of radar traces and samples remains the same as that of the reference analog radargram.

Time resolution correction

The time delay $\tau_{sm}(r_A, c_A)$ of the backscattered echo from the reflector at depth z is the total time required for the echo to travel through the medium described by the investigated geo-electrical model $\epsilon_I(r_A, c_A)$, given by:

$$\tau_{sm}(r_A, c_A) = \int_0^z \frac{2\sqrt{\text{Re}\{\epsilon_I(r_A, c_A)\}}}{c} dz \quad (4.12)$$

$\tau_{sm}(r_b, c_A)$ describes the time support of the samples of the radargram $V_b(r_A, c_A)$. We uniformly sample each radar trace of this radargram at time instants specified by the sampling frequency of the investigated instrument, resulting in the time resolution corrected radargram $V_t(r_t, c_A)$, where $r_t = 1, 2, \dots, N_{r_t}$ represents the row indices after time resolution correction. For the resampling, we use the nearest neighbor interpolation without applying an anti-aliasing filter for removing high frequencies prior to resampling. As expected, this interpolation minimizes effects on the statistical distribution of the noise samples, as we have also confirmed through experiments.

Along-track resolution correction

The antenna footprint of the RS represents the area from which signal is backscattered to the receiver. The across-track footprint affects the signal to clutter ratio of the radargram and, as discussed in Section 4.3.2, is not accounted for in the proposed approach. The along-track footprint size determines the azimuth resolution of the radargram and is improved by synthetic aperture processing.

Let ΔX_A and ΔX_I represent the post-processing along-track spacing between radar traces of the analog and the investigated radargrams, respectively. The along-track resolution correction is performed by the nearest neighbor interpolation leading to either up-sampling, if $\Delta X_I < \Delta X_A$ or down-sampling, if $\Delta X_I > \Delta X_A$. The time resolution corrected radargram $V_t(r_t, c_A)$ is positioned along the track at distances given by the along-track distance support:

$$X_A = 0, \Delta X_A, 2\Delta X_A, \dots, (N_{c_A} - 1)\Delta X_A \quad (4.13)$$

Each row of the radargram $V_t(r_t, c_A)$ is sampled at the distances given by the query vector:

$$X_I = 0, \Delta X_I, 2\Delta X_I, \dots, (N_{c_h} - 1)\Delta X_I, \quad (4.14)$$

where $N_{c_h} = N_{c_A} \frac{\Delta X_A}{\Delta X_I}$. The final simulated radargram magnitude after applying all the aforementioned corrections is given by $V_{sm}(r_t, c_h)$.

4.4 Case studies: Application of the proposed approach

4.4.1 Taxonomy of combinations of analog and investigated scenarios

In this section, we present possible analog and investigated acquisition scenarios that would require the application of the different steps of the proposed approach. In general, the reprocessing method depends on the choice of the analog feature and instrument. Table 4.2 presents the possible taxonomy of the analog and the investigated scenarios, the advantages and limitations of the choice of the geological analog, and the applicable specific details of the proposed approach in each case.

In this section, we demonstrate the proposed approach for three case studies for orbital RSs. The first two cases are used for validating the proposed approach by comparing the simulated radargrams with the real data of the investigated scenario. The first case study represents the most ideal application for the proposed approach, in which the analog RS data is available for the investigated target. This eliminates the need for choosing analog geological features and also minimizes the uncertainty in the assumption of the analog geo-electrical model. This is the case of same targets but different RS instruments, wherein the instrument parameters govern the reprocessing approach. The second case study is the most general scenario in which different analog and investigated instruments operate on different planetary bodies with different geo-electrical properties. Hence, we use this case to demonstrate the effect of the corrections requiring the target models.

The third case is a real-world application of the proposed approach to the prediction of the radargrams of an ongoing RS mission, RIME. The third case shows how the proposed

Table 4.2: Taxonomy of cases for application of the proposed analogs approach

Characteristics	Analog	Investigated	Reprocessing method	Application
Platform	Orbital	Orbital	bandwidth increase /decrease, time resampling only dependent on Δt_I	Performance assessment for scheduled missions on planetary bodies with existing orbital RS data (e.g.SHARAD and MARSIS)
Observation target	Same planetary body			
Bandwidth	Low /High	High /Low		
Penetration depth	Deep /Shallow	Shallow /Deep		
Platform	Airborne	Orbital	signal magnitude correction dependent on target attenuation, noise correction (add P_{cmb}), bandwidth decrease, time resampling only dependent on Δt_I	Future orbital missions for which airborne acquisitions exist or can be acquired easily (e.g. using airborne RS on Earth to simulated future Earth orbiting RS)
Observation target	Same planetary body			
Bandwidth	High	Low		
Platform	Airborne	Orbital	signal magnitude correction dependent on ϵ_A and ϵ_I , noise correction (add P_{cmb}), bandwidth decrease, time resampling dependent on ϵ_A and ϵ_I	Planning future orbital RSs taking advantage of terrestrial analogs of the planetary features (e.g. using airborne RS on Earth to simulate SHARAD or RIME data)
Observation target	Different planetary bodies			
Bandwidth	High	Low		
Platform	Orbital	Orbital	signal magnitude correction dependent on ϵ_A and ϵ_I , noise correction (contribution from radio noise sources), bandwidth increase /decrease, time resampling dependent on ϵ_A and ϵ_I	Future RS targets on planetary bodies having geological analogs on other planetary bodies within the coverage of the existing RSs (e.g. using analog SHARAD, MARSIS, LRS to simulate RIME and REASON)
Observation target	Different planetary bodies			
Bandwidth	Low /High	High /Low		

approach can be used to interpret and predict the RIME response for a combination of instrument and target hypotheses. The parameters of the instruments used in the case studies are presented in Table 4.4.

Table 4.4: Instrument parameters of the existing and scheduled RSs used for demonstrating the proposed approach

Characteristics	RIME (HRO/LRO)	SHARAD	MARSIS	LRS
Mission	JUICE	MRO	MEX	SELENE (Kaguya)
Central frequency (MHz)	9	20	1.8, 3, 4, 5	5
Bandwidth (MHz)	HRO-2.8 LRO-1	10	1	2
Spacecraft altitude (km)	500	280	800	100
Two-way time resolution (μ s)	0.1667	0.075	0.7143	0.32
Sampling frequency (MHz)	12	26.67	2.8	6.25
Transmit power (W)	10	10	5	753
Antenna gain (dB)	1	1	2.1	2.1484
Penetration depth (km)	4-9	0.1 - 1	0.5 - 5	5
Along-track resolution (m)	300-1000	300-1000	5000-9000	600
Free-space vertical resolution (m)	HRO-50 LRO-150	24	150	75

We have qualitatively analyzed the simulation results by visually comparing the reference analog, the simulated and the real investigated radargrams for cases I and II and by plotting the average radar trace. For statistical interpretation, we have used the histograms of the full radargram magnitudes. The signal samples are relatively lower in number than the pure noise samples and are seen as the right tail of the full image histograms. The noise samples appear in the mode of the histograms.

For quantitative estimation of the similarity between the simulated and the real investigated radargrams, we have used the mutual information (MI) measure [140, 39]. The MI between two variables is a measure of the reduction in uncertainty in the prediction of one variable, given the knowledge of the other variable. High values of MI between two radargrams, i.e. high similarity, indicates that one can be predicted from the other.

4.4.2 Case I: Same observation target with different instruments

The first case addresses the scenario in which RS acquisitions are available over the investigated planetary body but with an instrument having different parameters as that of the investigated RS. As an example of this case, we consider the North Polar Layered Deposits (NPLD) on Mars as the investigated geological feature. The aim is to simulate

the data acquired by MARSIS, which is the investigated RS, using SHARAD as the analog RS. For simulating the MARSIS radargram over the area of interest, we select the reference analog radargram as the SHARAD data acquired at a central frequency of 20 MHz with a bandwidth of 10 MHz [139] on the orbit 1848101. Note that this case is interesting uniquely for validating the methodology as the real MARSIS radargram is available to serve as the reference validation data. To this purpose, we have identified a real MARSIS radargram from the same region of Mars (Figure 4.5), which was acquired at a central frequency of 5 MHz with a bandwidth of 1 MHz on the orbit track 3668.

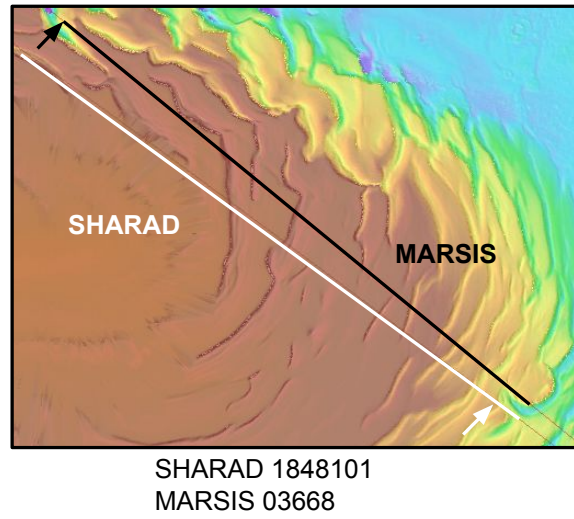


Figure 4.5: Case I: Ground tracks for the analog SHARAD radargram 1848101 and the investigated MARSIS radargram 3304 over the Mars North Polar Layered Deposits. The arrows indicate start of the radargram.

The NPLD comprises of layers, which are expected to be composed of water ice, dry ice, silicate inclusions and CO_2 -clathrates representing the climatological history of the Mars polar caps. Below the layers, the bedrock is expected to occur at a depth of 1 - 2 km. Here we have considered a two layered geo-electrical model as follows [100]:

- Layer 1 (Bulk ice): $\text{Re}(\epsilon) = 3.15$, $\tan\delta = 6.3 \times 10^{-4}$
- Layer 2 (Bedrock): $\text{Re}(\epsilon) = 8.8$, $\tan\delta = 1.7 \times 10^{-2}$

In this case, the analog and investigated target geo-electrical models are the same. However, the attenuation factors - $L_A(r_A, c_A)$ and $L_I(r_A, c_A)$ are dependent on the central frequency and hence affect the signal magnitude correction step. Figure 4.6 shows the soft threshold $\kappa(r_A, c_A)$, obtained by applying the Gaussian filtering to the noise threshold. Comparing with the binary signal-noise image obtained after thresholding, we can see that $\kappa(r_A, c_A)$ is close to 1 where the signal component is dominating, whereas it decreases to 0

where only noise is present in the radargram (e.g. above the surface and below the deepest subsurface reflector). Bandwidth of the investigated RS is lower than that of the analog RS, thus bandwidth reduction is required. The range samples are down-sampled to the sampling frequency of MARSIS in the time resolution correction step, without requiring the geo-electrical model. The number of radar traces is also down-sampled to match the lower along-track resolution of MARSIS.

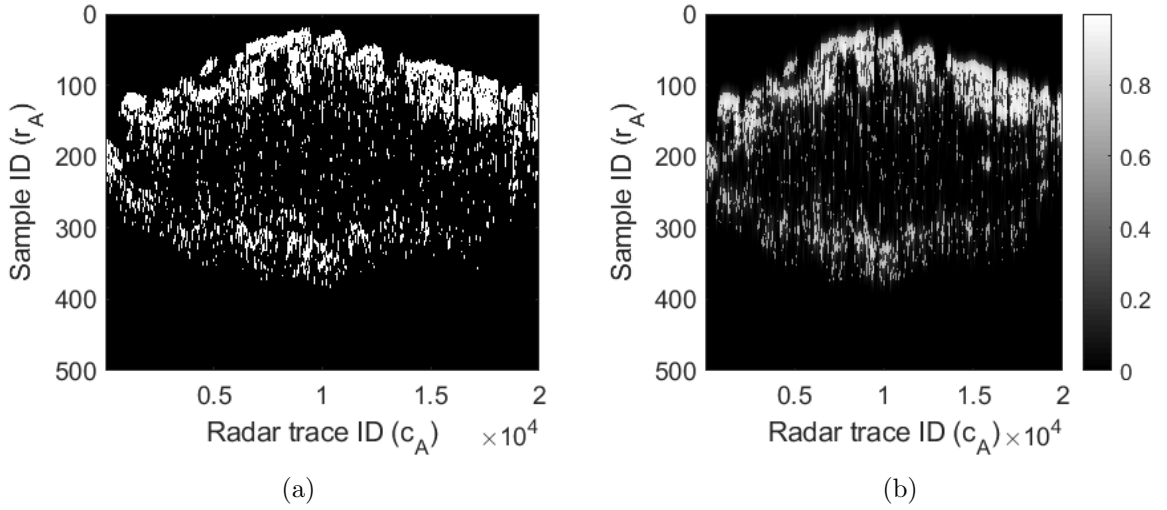


Figure 4.6: Example of signal magnitude correction (Case I). (a) Binary signal-noise image $v(r_A, c_A)$; (b) Gaussian filtered signal-noise image $\kappa(r_A, c_A)$ used in the signal magnitude correction.

Figure 4.7 shows the reference SHARAD, the simulated radargram and the real MARSIS radargrams for comparison. Figure 4.7(b) shows the plot of the average magnitude of the radar traces occurring within the yellow bars in (a), (c) and (d). The magnitude is normalized with respect to the noise level in the analog SHARAD radar trace and is plotted against depth.

The first observation here is that the simulated and the real MARSIS radargrams have the same number of samples and radar traces, as a result of the time sampling correction and the along-track resolution correction. At this resolution, we can see that the geometry of the NPLD feature is visually similar in the simulated and the real radargrams, than in the reference analog radargram. Similarity is observed in terms of (1) the relative strength of the subsurface reflectors with respect to the surface, which is an effect of the attenuation correction, (2) the range resolution and (3) the signal to noise ratio.

From the radar trace plot, we can identify four noteworthy reflections. The cyan line represents the surface. The green line represents the base of the layers, which appears as a single prominent peak in the simulated and the real radargrams. Between the surface

and the base, finer layers are visible in the analog SHARAD radargram, which are also seen in the simulated radargram as a subtle peak between the cyan and the green line. The blue line represents the strong return from the basal (ice-bedrock) interface. It is visible as a sharp peak in the simulated radar trace and a broader peak in the real MARSIS radar trace. Due to shallow penetration of SHARAD, the deeper and stronger subsurface reflector (magenta line) detected by MARSIS was not detected by SHARAD, and therefore, also not seen in the simulated radargram.

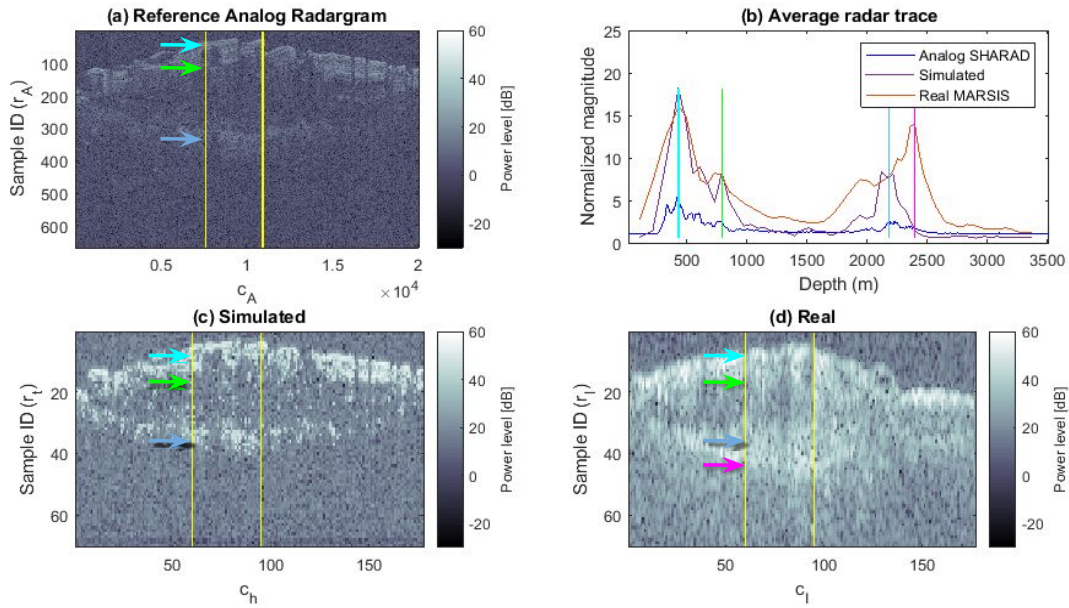


Figure 4.7: Case I: (a) Reference analog radargram SHARAD 1848101; (b) Average radar trace plot of simulated and real radargrams for the radar traces indicated in yellow in (a), (c) and (d); (c) Simulated radargram; (d) Real investigated radargram MARSIS 3304.

Statistically, the validation of the simulated radargram can be done by comparing the full-image histograms of the analog, the simulated and the real radargrams, as shown in Figure 4.8. There is a good match in the mode (representing the noise samples) as well as the right tail (representing the signal samples) of the simulated and real radargrams. Table 4.5 presents the values of MI. We can see that the MI of the real MARSIS radargram with respect to the simulated radargram is higher than the one with respect to the reference analog radargram. This shows that the processing applied to the reference analog radargram is necessary to produce simulated radargrams that are more similar to the actual investigated one.

In this example, we have assumed a simplified two-layered geo-electrical model to represent the NPLD. This model does not accurately describe the complex stratigraphy

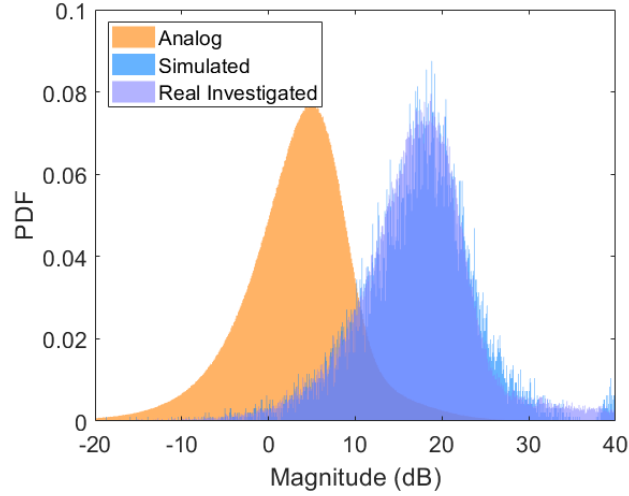


Figure 4.8: Case I: Histograms showing the probability density plots of the magnitudes of the reference analog radargram (SHARAD 1848101), the simulated radargram and the real investigated radargram (MARSIS 03668).

Table 4.5: Case I: Value of the mutual information for the case of SHARAD to MARSIS

	Real investigated radargram
Reference analog radargram	2.3973
Simulated investigated radargram	5.8873

of the polar ice on Mars. This does not affect the shape or spacing between the subsurface layering observed in the simulated radargram, but may have minor effects (of the order of a few dB) on the attenuation factor used in the signal magnitude correction step.

This case study represents the scenario in which available radargrams can be used to predict the performance of a scheduled mission for the same planetary body. This could typically be useful for future Moon, Mars and terrestrial RS missions.

4.4.3 Case II: Different observation targets with similar instruments

The second case addresses the issue of simulating the data of the investigated scenario using radargrams available over a different planetary body. The aim here is to leverage the wider database of currently available radargrams on all planetary bodies to get an understanding of how the features may look like in the real investigated radargrams, accounting for two main differences in the analog and investigated scenarios: (1) the difference in the composition of the two planetary bodies, and (2) the difference in the parameters of the two instruments. In this case, the simulated radargram represents the hypothetical data acquired by the investigated RS over the analog feature, assuming that

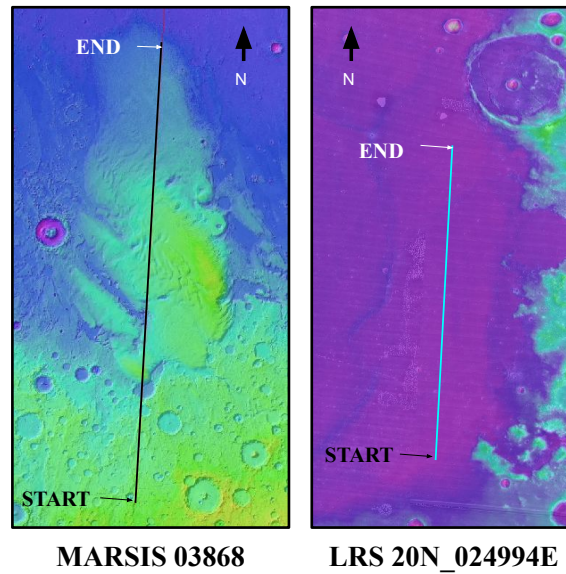


Figure 4.9: Case II: Ground tracks for the investigated MARSIS radargram 03868 over the Medusae Fossae Formation and the reference analog radargram LRS_SAR05KM.C.20N_024994E over the lunar Mare Serenitatis.

it occurs on the investigated planetary body.

Inter-planetary geological analogs are identified in the comparative planetary geology literature. These are also documented by the International Astronomical Union (IAU), which categorizes planetary features based on similarity in geomorphology. For unexplored paradigms, surface morphology is the most suitable criterion for identifying analogs. Similarity in surface expression is an indirect evidence of similarity in subsurface structure and hence in the possible RS response. For well-explored planetary surfaces, with a large amount of data available, identifying the analogs based on the genesis of the features that have similar surface expression can refine the choice of the analogs.

As an example of this case, we have identified the equatorial Medusae Fossae formation (MFF) on Mars as the analog of the Mare Serenitatis on the Moon. The selection criteria takes advantage of the well-understood genesis of the selected analog feature from the substantial availability of data. It should be noted that unlike the previous case, the observation targets are different, but they represent similar relative structure of the interfaces. Hence we cannot obtain a direct correspondence between the simulated and the real radargrams, but we can use this example to qualitatively interpret the simulated radargrams.

In this example, we investigate the data acquired by MARSIS using the LRS as the analog RS. We have selected the analog as the MARSIS radargram acquired at the central frequency of 3 MHz with a bandwidth 1 MHz in the orbit 03868 passing over the MFF. For

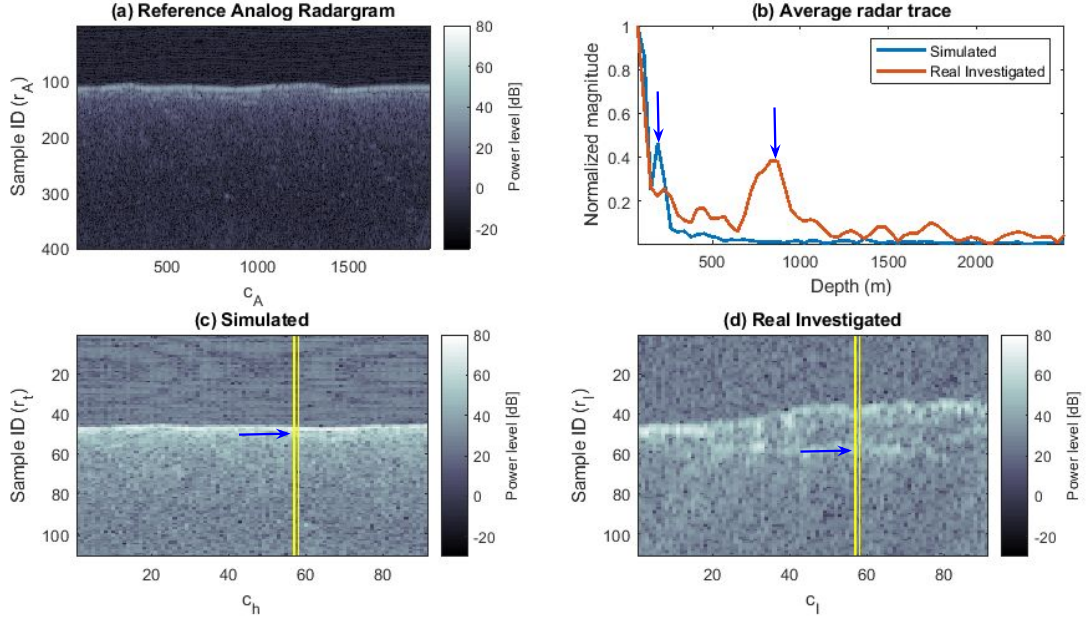


Figure 4.10: Case II: (a) Reference analog radargram LRS_SAR05KM_C_20N_024994E, (b) Average radar trace plot of the simulated and real radargrams for the radar traces indicated in yellow in (c) and (d), (c) Simulated radargram, (d) Real investigated radargram MARSIS 03868.

validation, we use LRS_SAR05KM_C_20N_024994E, as the real investigated radargram. Figure 4.9 shows the ground tracks of the analog and investigated RS.

These geological terrains are analogs in the sense that both comprise of a nearly flat two-layered geo-electrical structure. The basal unit (bedrock in case of Mars or consolidated regolith in case of the Moon) is overlain by a fill material with contrasting dielectric properties. The Mare Serenitatis comprises of 350 meters of mare basalts overlying the lunar regolith layers below. We have created a two-layer analog geo-electrical model as follows [105]:

- Layer 1 (mare basalts): $\text{Re}(\epsilon) = 4$, $\tan\delta = 10^{-3}$
- Layer 2 (lunar regolith): $\text{Re}(\epsilon) = 6.09$, $\tan\delta = 10^{-2}$

On the other hand, the composition of MFF deposits is debatable and could be volcanic ash, eolian sediments or ice-rich material with possible thickness between 0.5 to 2.5 km. In this study we have considered the investigated geo-electrical model as follows [151]:

- Layer 1 (ice-rich mantling): $\text{Re}(\epsilon) = 2.9$, $\tan\delta = 2 \times 10^{-3}$
- Layer 2 (bedrock): $\text{Re}(\epsilon) = 8$, $\tan\delta = 6 \times 10^{-3}$

In this case, since the targets are different, the signal magnitude correction step requires the geo-electrical models. The bandwidth of LRS is twice that of MARSIS, thus requiring

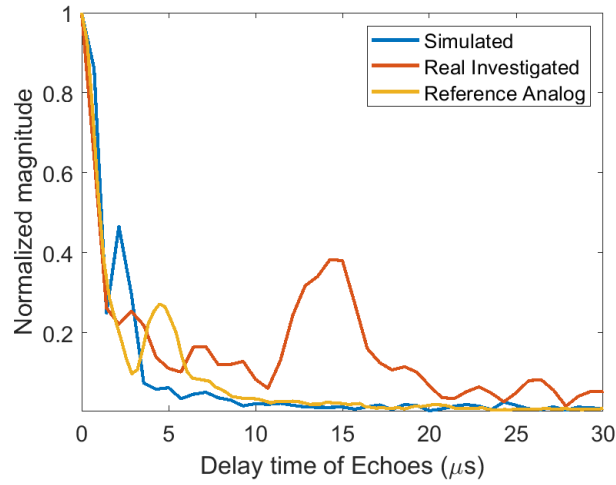


Figure 4.11: Case II: Normalized average magnitude of the simulated, real investigated and reference analog radar traces indicated in yellow in Figure 4.10, plotted against delay time.

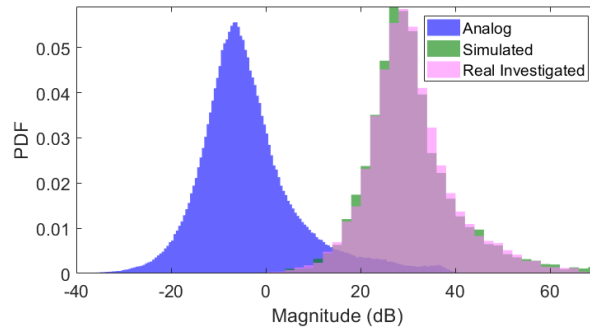


Figure 4.12: Case II: Histograms showing the normalized probability distributions of the magnitudes of the reference analog (LRS 20N.024994E), the simulated and the real investigated radargrams (MARSIS 03868).

bandwidth reduction. The delay time corresponding to the investigated echo samples are calculated using the MFF geo-electrical model. These echo samples are resampled to the sampling frequency of MARSIS. The along-track resolution of LRS (600 m) is finer than that of MARSIS (about 5.5 km), requiring a down-sampling of the number of radar traces.

Figure 4.10 show the analog, the simulated and the real investigated radargrams. As an effect of the analogs processing, the signal to noise ratio of the simulated radargram is similar to the real radargram. Similarity is also observed in the relative strength of the subsurface reflection with respect to the surface in the average radar trace plot (Figure 4.10(b)). Note that the analog and the investigated features have different surface topography and the thickness of the subsurface layer. Hence, the subsurface peak in

Table 4.6: Case II: Value of the mutual information for the case of LRS to MARSIS

	Real Investigated radargram
Reference analog radargram	4.5159
Investigated simulated radargram	6.6826

the simulated and the real radar traces do not coincide, representing the difference in geometry. The aim of this approach is not to scale the geometry of the analog feature to match that of the investigated scenario since in a real application, such level of detail about the investigated feature is not expected to be known a priori.

Another effect of the processing is to align the echoes to the delay time of the investigated scenario using the geo-electrical models. Figure 4.11 shows the analog, the simulated, the real radar traces plotted against the delay time. The simulated subsurface peak is closer to the surface than the analog. This is because the MFF real permittivity ($\text{Re}(\epsilon_A) = 2.9$) is lower than that of the Moon ($\text{Re}(\epsilon_A) = 4$), hence the waves travel faster in the investigated subsurface. Also, the relative strength of the subsurface echo of the simulated and the real scenario are more similar than that of the analog echo. This is a result of the attenuation, transmission and reflection factors in the signal magnitude correction step, using the analog and the investigated geo-electrical models.

A statistical comparison of the histograms shows that the real investigated signal and noise magnitudes are more similar than that of the analog (Figure 4.12). Table 4.6 shows that the MI of the real radargram is higher with respect to the simulated than the reference analog radargram, thus confirming that the simulated radargram is more similar to the real MARSIS radargram as a consequence of the processing. Because of the difference in geometry of the features, and therefore the lack of one-to-one correspondence between the simulated and the real radargrams, the value of MI is not significantly large.

It can be observed that the simulated radargrams appear sharper than the real investigated radargrams (Figure 4.7 and Figure 4.10). This is due to the use of the nearest neighbor down-sampling, which produces minimum distortion to the statistical properties, but can affect the local smoothness. The correction for the differences in the Doppler filtering and the sidelobe suppression technique can also make the simulated radargram appear more similar to the real one. However, if needed the proposed approach can be easily extended to incorporate these steps.

This case has two main applications. The first is when no RS data are available for the investigated planetary body. This approach can be used to predict the appearance of the radargrams and to support development of the processing-chain of the actual investigated radargrams. An example of this application is presented in the next case study. The

second application is when RS data are available on the investigated planetary body. In this case, the approach can be used to isolate the basic structure of the geological feature, normalizing the effects of the composition and the RS instrument. This will support comparative geological studies of different planetary features.

4.4.4 Case III: Future missions on unexplored observation targets

The previous two cases allowed a qualitative and quantitative validation of the proposed approach by comparing with real radargrams of the investigated scenario. In this case study, we present an application of the approach to a real-world scenario, i.e. for investigating the radar response of RIME [18]. RIME has three programmable modes of operation:

1. High resolution orbit (HRO) using a bandwidth of 2.8 MHz for detailed observation of the shallow subsurface (resolution ~ 30 m in ice)
2. Low resolution orbit (LRO) using a bandwidth of 1 MHz for deep penetration (resolution ~ 140 m in ice)
3. High resolution flybys with high data rate for deep probing with high vertical resolution

The JUICE spacecraft will be inserted into orbit around Ganymede at a nominal altitude of 500 km, where RIME will operate with the HRO or the LRO modes [18].

In this study, we demonstrate that the proposed approach is an effective tool to test different hypotheses on the RS and target characteristics. Here we consider four different combinations of the two RIME modes and two predominant geo-electrical models of the RIME targets. Furthermore, we also demonstrate that this technique allows the translation of the geophysical properties to a finely resolved geo-electrical profile varying with depth, a feature that is computationally highly demanding in case of multi-layer simulators and is a powerful element of the 3D EM simulators.

The investigated feature is the Acheleous pedestal crater located in the north polar region of Ganymede. We have identified an analog of the Acheleous crater as a pedestal crater in the southern hemisphere of Mars for which data is available from the SHARAD radargram 782801. Figure 4.13(a) shows the analog RS ground track, while (b) shows a hypothetical track of RIME for an equivalent orientation on the investigated feature.

We consider a two-layered analog geo-electrical model [101]:

- Layer 1 (pedestal ejecta deposits composed of water-ice and silicates mixture): $\text{Re}(\epsilon) = 2.3$, $\tan\delta = 6.3 \times 10^{-3}$
- Layer 2 (JSC Mars 1 consolidated regolith): $\text{Re}(\epsilon) = 4.9$, $\tan\delta = 1.757 \times 10^{-2}$

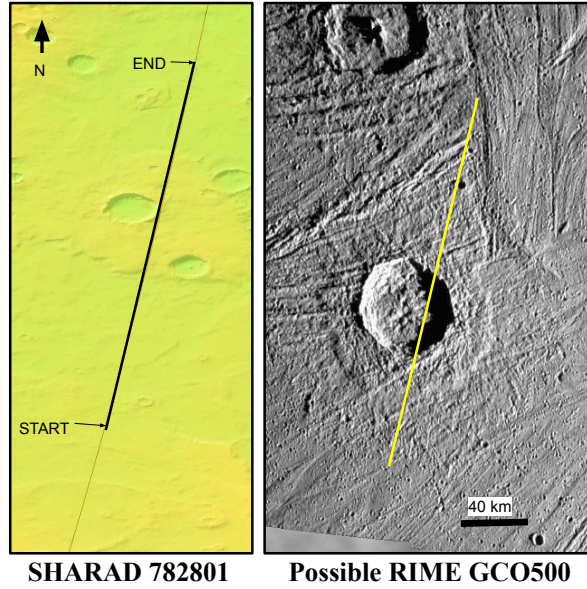


Figure 4.13: Case III: (a) Ground tracks for the analog radargram SHARAD 782801 over a pedestal crater on Mars. (b) The surface image of the investigated feature on Ganymede (Creator credit: NASA/JPL/DLR PIA01660). The yellow line represents a hypothetical acquisition track of RIME that resembles the relative orientation of the analog RS track.

The pedestal craters on Ganymede are characterized by freshly excavated ejecta deposits, similar to the Martian craters [70]. Images from Galileo and Voyager missions revealed two broad types of terrains on Ganymede: bright terrain (BT), which is composed of younger and cleaner ice, and dark terrain (DT), which is composed of older dusty ice. The investigated geo-electrical models for the BT and DT are defined as a function of temperature, porosity and dust fraction profile, as described in [68], and will be elaborated in the later chapters. The depth resolution of the BT and DT profiles corresponds to the range sampling interval of the analog instrument. In order to represent the base of the pedestal deposits, we assume a dielectric discontinuity in the otherwise continuous BT and DT profiles, by introducing a contrast equal to 0.8 units in the real permittivity between the pedestal deposit (lower permittivity) and the base (higher permittivity), to resemble the relatively pure ejecta ice. Figure 4.14 shows the real dielectric permittivity of the resulting geo-electrical model of the DT.

The four combinations representing possible investigated scenarios studied here are:

1. BT model for acquisition in the HRO mode
2. DT model for acquisition in the HRO mode
3. BT model for acquisition in the LRO mode

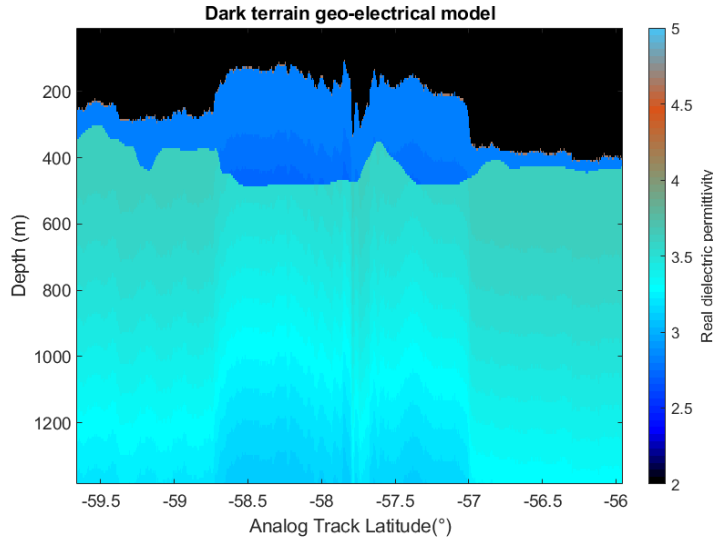


Figure 4.14: Case III: Dark terrain geo-electrical model used as input for the proposed approach. Each cell represents the depth-dependent real dielectric permittivity corresponding to the Ganymede DT geo-electrical model.

4. DT model, for acquisition in the LRO mode

Note that in all the cases we do not model the difference of surface roughness that can be expected in the different scenarios.

The instrument parameters of RIME are reported in Table 4.4. Similar to Case II, the signal magnitude correction requires the reflection and transmission factors and the attenuation loss derived from the analog and the investigated geo-electrical models. RIME will acquire on the anti-Jovian side to avoid the effects of the Jupiter radio noise [17]. Thus we do not consider this noise level in the simulations. The corrections for bandwidth and time resolution follow the same routine as described for Case II. The along-track resolution of the analog and the investigated instruments are similar. Hence, along-track resolution correction is not required.

Figure 4.15 shows the box-plot and Figure 4.16 shows the full-image histograms of the magnitudes of the analog and the four simulated radargrams. We can see that the variance of the noise weakly increases by decreasing the bandwidth as seen from the histograms' modal probabilities. On the other hand, the right tail, corresponding to the signal part of the radargram, does not show significant differences between the different combinations. This is because the loss tangents, corresponding to the BT and DT models, are not significantly different.

Figure 4.17 shows the simulated and the reference analog radargrams. Since the sampling frequency of both the modes is 12 MHz, we see the same number of samples in all

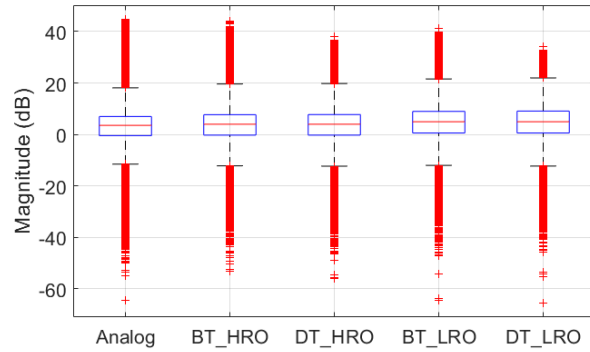


Figure 4.15: Case III: Boxplot of the analog radargram and the simulated RIME radargrams for different parameter combinations. ‘Analog’ is the reference SHARAD radargram, ‘BT’ refers to the bright terrain geo-electrical model, ‘DT’ refers to the dark terrain geo-electrical model, ‘HRO’ refers to the HRO mode and ‘LRO’ refers to the LRO mode.

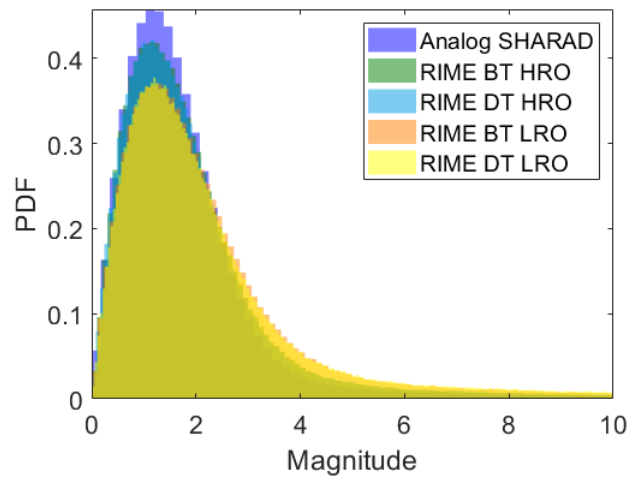


Figure 4.16: Case III: Histograms showing the normalized probability density functions of the magnitudes of the reference SHARAD radargram and the simulated RIME radargrams.

the four simulated radargrams, which are less than the analog (with sampling frequency of 26.67 MHz). Visually the reduction in vertical resolution in the LRO mode is easily observed. The geo-electrical model results in the subsurface reflectors being pushed towards or away from the surface, depending on whether $\text{Re}\{\epsilon_I\}$ is lower or higher than $\text{Re}\{\epsilon_A\}$, respectively. Figure 4.18 shows the average magnitude of the radar traces within the region of the radargrams bounded by the yellow vertical lines.

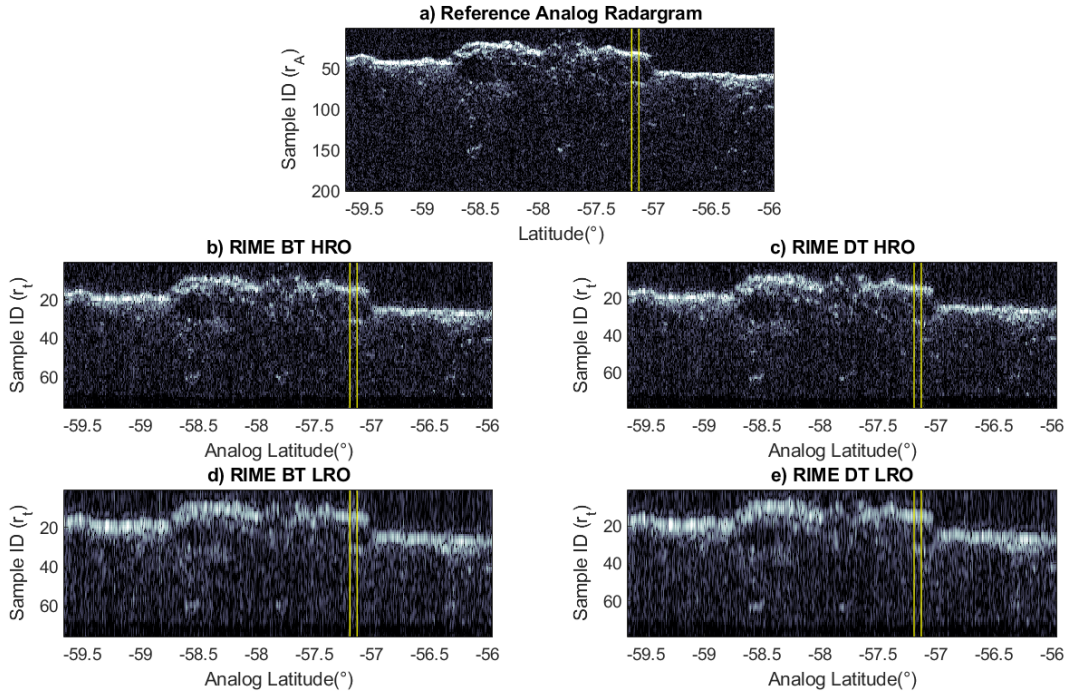


Figure 4.17: Case III: (a) Reference analog radargram SHARAD 782801, (b) simulated RIME radargram for the High resolution orbital (HRO) mode, for the bright terrain (BT) geo-electrical model, (c) simulated RIME radargram for the HRO mode for dark terrain (DT) geo-electrical model, (d) simulated RIME radargrams for Low resolution orbital (LRO) mode, for BT model, (e) simulated RIME radargrams for LRO, for DT model.

As expected, the time delay of the reflector from the surface depends only on the geo-electrical model, as can be seen with the co-occurring peaks in the radar traces for the same geo-electrical models. However, the effect of the bandwidth can be seen in the vertical resolution - the LRO mode radar traces are broader than the corresponding HRO mode ones, which are broader than the analog. In order to clearly observe the effect of the geo-electrical hypotheses, we have created hypothetical geo-electrical models as follows:

1. Mars pedestal crater two layer model:

- Layer 1 $\epsilon_A = 6 + 0.0145j$

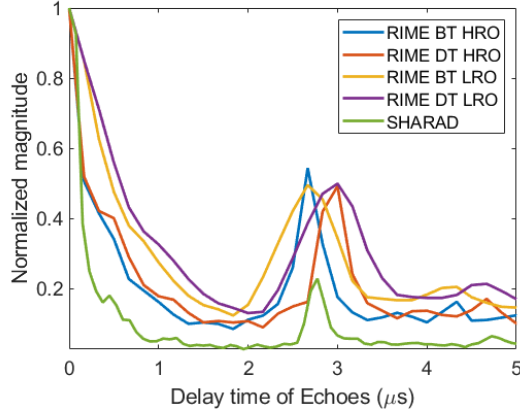


Figure 4.18: Case III: Average radar trace magnitude normalized with respect to the surface (for the radar traces indicated in yellow in Figure 4.17), plotted against time delay.

- Layer 2 $\epsilon_A = 6.9 + 0.0861j$
2. BT model changed from depth dependent dielectric profile to a two layer model:
 - Layer 1 $\epsilon_I = 2 + 0.0011j$
 - Layer 2 $\epsilon_I = 3 + 0.0011j$
 3. DT model changed from depth dependent dielectric profile to a two layer model:
 - Layer 1 $\epsilon_I = 4 + 0.0034j$
 - Layer 2 $\epsilon_I = 3 + 0.0034j$

Figure 4.19 shows the average radar trace plot for the hypothetical geo-electrical models. The vertical lines 1, 2 and 3 correspond to the BT, DT and analog models, respectively. Since the real dielectric permittivity of BT is smaller than that of DT (which is smaller than that of the analog), the signal travels fastest in the BT case (therefore shortest delay time) and slowest in the analog case (therefore longest delay time). The other observation regards the height of the peaks. The BT model, having the lowest loss tangent, has the lowest attenuation and therefore the highest normalized magnitude of the subsurface reflection. On the contrary, the analog model has the highest loss tangent and attenuation factor, and therefore has the lowest strength of the subsurface reflection among the three models.

This case demonstrates that the proposed approach effectively represents the instrument and target properties in the simulated radargrams, thus enabling the interpretation of the simulations in the context of the investigated scenario.

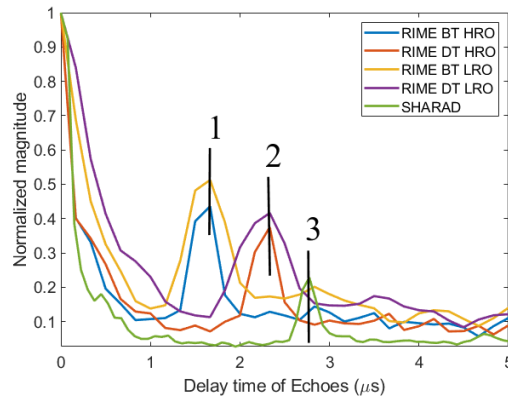


Figure 4.19: Case III: Average radar trace magnitude normalized with respect to the surface (for the radar traces in the region of the radargram marked in yellow in Figure 4.17) plotted against delay time of the echo with respect to the surface. This plot refers to the hypothetical geo-electrical model assumed for the analog and investigated scenario to demonstrate the effectiveness of the time resolution correction.

4.5 Conclusions

In this chapter, we have presented a novel approach to the simulation of RS data using existing radargrams acquired over geological analogs of the investigated targets. In this approach, we start from the reference analog radargram and minimize the difference between the variables of the acquisition process using a series of corrections. The applicability of the method is demonstrated and validated by two case studies - (1) using SHARAD radargrams as analogs and simulating the MARSIS radargrams for the same target on Mars, and (2) using LRS radargrams on the Moon as an analog for simulating the MARSIS radargram of a similar feature on Mars. Finally, we demonstrate an application to the simulation of RIME acquisitions, in which the radargram acquired by SHARAD on a pedestal crater on Mars is used to predict the radargrams to-be-acquired by RIME over a pedestal crater on Ganymede. A real application of the proposed approach to RS simulations would imply testing different possibilities of the instrument and target characteristics and this has been demonstrated in the third case by considering four combinations of RIME acquisition modes and Ganymede subsurface geo-electrical models.

Figure 4.20 provides a comparison between the proposed approach and conventional electromagnetic simulators. The proposed approach is highly computationally efficient in terms of speed and memory requirements. This allows for more combinations of instrument and subsurface hypotheses of the investigated scenario to be tested in reasonable time and in a more realistic way. Although this approach also requires the input geo-electrical models, the simulation output is less sensitive to the uncertainty in the models.

Approaches to Simulation of Radargrams

Conventional Electromagnetic
Simulators

Analogs Approach

Limitations	Strictly forward modeling approach	Starting from real radargrams	Benefits
	Requires detailed knowledge of target characteristics	Subsurface geometry borrowed from analog	
	Requires time-demanding computation of the electromagnetic interaction with the geo-electrical model (constrained by the size of the simulation cell)	Complex electromagnetic interactions already accounted, since simulation starts from real radargrams and hence more close to realistic	
Benefits	Greater control on the penetration capability and the achievable resolution	Details of the target model constrained by radar capabilities of the analog RS	Limitations
	Flexibility to model all possible subsurface hypotheses of the targets	Subsurface hypotheses of the analog introduces uncertainty	

Figure 4.20: Comparison between conventional and proposed simulation approaches

It offers a feasible workaround for incorporating volume scattering in the simulation, thereby producing more realistic radargrams.

However, the knowledge of preliminary planetary geology is required for the first steps of identifying the analogs of the investigated targets, which can be done following the steps described in Case II. Furthermore, the assumption of geometric similarity is not completely true because, ideally, no planetary features in the universe can be identical to each other. However, it should be noted that the aim of the simulation is not to reproduce the investigated radargram, but to understand the detectability of subsurface features and their appearance in the radargrams. To this aim, the mismatch in geometry does not hinder the applicability of the method.

A limitation of this approach is that the simulated radargrams are constrained by the information acquired by the analog instrument and the raw data processing-chain. For instance, we expect greater penetration and more subsurface features in the case of RIME than in the case of SHARAD as the subsurface medium of the icy moons is more radar transparent. Thus, the radargrams simulated by the proposed approach starting with SHARAD represent only the shallow subsurface of the icy moons and should be used complementary to the conventional simulators. These give more control on the geometry and depth, but lack in a realistic representation of the subsurface scenario.

The proposed approach can be applied to RS missions at various stages of their development. A unique application is in the post-mission phase, where the approach can be

useful for scientific studies in the field of comparative geology, which are currently largely restricted to analyses of high-resolution optical images and digital elevation models of the planetary features. The strong influence of the radar parameters and the difference in composition of different planetary bodies makes it unmanageable to directly compare radargrams of similar features on different targets. The proposed approach provides a tool to isolate the effect of the instrument and the global composition of the planet to observe the structural differences between features and thus perform scientific studies.

Chapter 5

An approach to the generation and analysis of databases of simulated RS data for performance prediction and target interpretation

In the previous chapters, we have explained the importance of simulations in understanding the complex interaction between the large number of variables involved in the acquisition process. However, to adequately exploit the strength of the RS simulators, it is necessary to systematically generate a large database of radar responses representing the acquisition scenario. In this chapter¹, we present an approach to the generation of databases of geo-electrical models and simulated radargrams corresponding to combinations of different hypotheses on the acquisition variables. Further, we describe techniques for analyzing the generated databases for supporting the performance assessment of the RS and the interpretation of the radargrams. Experimental results are presented for the RIME detectability of the Ganymede pedestal craters, described in the previous chapter.

¹Part of this chapter appears in

Thakur, Sanchari, Andrea Vettor, and Lorenzo Bruzzone. "Analysis of Subsurface Hypotheses through Simulation of RIME Radargrams Based on Available Analogous Data." IGARSS 2019-2019 IEEE International Geoscience and Remote Sensing Symposium. IEEE, 2019.

and

Thakur, Sanchari, and Lorenzo Bruzzone. "An approach to the generation and analysis of databases of simulated radar sounder data for performance prediction and target interpretation." IEEE Transactions on Geoscience and Remote Sensing (in review).

5.1 Introduction

The objective of a RS can be defined at two levels of scientific requirements on the mission. At the primary level, the RS must be able to meet the mission requirements on the detectability of the targets. A target can be detected if it is larger than the RS range and along-track resolutions, and the power received from it is above the noise and the sidelobe levels, and is distinguishable from clutter. At the secondary level, the RS must be able to deliver scientifically valuable information about the targets. Thus, the target composition, geological structure, and geophysical properties should be invertible from the RS data. Prior to the inversion, it is necessary to understand the level of detail (resolution) to which the RS can detect the target properties.

For the fulfilment of these objectives, the full understanding of the related radar response and its performance assessment is of fundamental importance. A comprehensive scheme for RS performance evaluation is presented in [15], which estimates the radar penetration capability as a function of the target and the instrument characteristics. This requires modeling (i) the surface statistical properties; (ii) the subsurface structure, composition and roughness; (iii) the environmental noise; and (iv) the instrument parameters. A robust implementation of this scheme requires both a detailed modeling of the target surface and subsurface characteristics, and a study of the quality of the corresponding radargrams, which can be achieved by using RS simulators.

In this chapter, we propose an approach to the understanding of the complex relationships between the acquisition scenario and the corresponding radar response by exploiting the capabilities of RS simulators (Figure 5.1). To this purpose, we define the acquisition scenario in terms of the sounder, the acquisition geometry and the target variables. For each variable, we identify a set of possible hypothesis values expected during the acquisition. Then, we create combinations of different hypotheses to represent a set of possible acquisition scenarios.

Next, we select the geo-electrical variables and generate the geo-electrical models, which are important inputs to the simulator. A prior analysis of the geo-electrical models can help in simplifying the understanding of the target hypotheses. For each combination, we first generate the geo-electrical model and use it to simulate the radargrams using an appropriate simulator. Thus, we obtain a database of the models and of the radargrams for the defined acquisition scenarios. Each geo-electrical model and simulated radargram is linked to the corresponding combination of hypotheses on the geo-electrical variables and all the acquisition variables, respectively. This allows one to relate the interpretation of the radar response with the corresponding target properties.

In this contribution, we also present an approach to the systematic analysis of the databases of radar responses to support the evaluation of the RS acquisitions in terms

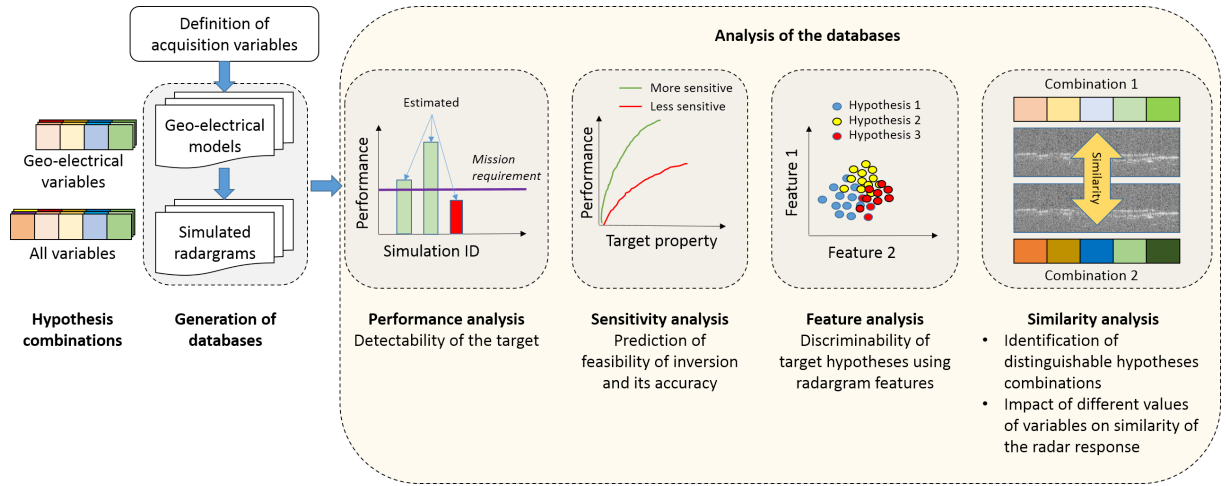


Figure 5.1: Conceptual illustration of the proposed approach to i) the generation of databases of geo-electrical models and simulated radargrams and ii) the analysis of the databases for supporting RS missions in terms of performance prediction and target detection understanding.

of (i) the detection performance on the targets, and (ii) the ability of interpreting and identifying the underlying target hypotheses from the RS data. The database of simulated radargrams can be used to test whether the subsurface targets are detectable under different acquisition scenarios. The proposed approach evaluates the target detectability by applying performance metrics to the simulated radargrams and matching them with the science requirements, as shown in Figure 5.1. The approach also consists in evaluating the sensitivity of the RS to small changes in the target properties. This can be used to predict the feasibility of inverting the particular target properties and the accuracy of inversion.

Moreover, the databases can be analyzed to understand which combinations of variables produce significantly distinguishable radar responses. The proposed approach includes a novel technique to identify the combinations of target properties that produce discriminable radar response. This is achieved by estimating the similarity between pairs of radargrams corresponding to different combinations of target hypotheses. This analysis yields two-fold information: (i) the identification of the combinations of target properties that produce significantly distinguishable radargrams, and (ii) the understanding of the variables that have a significant impact on the radar response, irrespective of the values of the other variables. The analysis of the database is also applied to the features extracted from the simulated radargrams to assess their separability for different acquisition hypotheses.

This chapter is organized in six sections. Section 5.2 presents a comparison between the various RS simulation techniques, including the proposed approach based on analogs

(presented in Chapter 4) in order to guide the selection of an appropriate simulator for generating the databases. Section 5.3 describes the proposed technique for generating databases of geo-electrical models and simulated radargrams for a range of possible acquisition hypotheses. Section 5.4 describes the general approach to the analysis of the databases for performance, feature and similarity analysis that can be used for any RS mission. Section 5.5 demonstrates the application of the proposed method to the assessment of the databases for a selected RIME target on Ganymede. Section 5.6, draws the conclusions of this contribution.

5.2 Comparison between different simulation techniques

Table 5.1: Comparison of available simulation techniques

Simulation technique	Multi-layer coherent RS simulator (MRS) [54]	FDTD based simulator [68]	Analog-based simulator
Method	Ray-tracing following Snell's law	Finite difference solution of Maxwell's equations in time domain	Reprocessing analog radargrams by matching instrument and target properties
Geo-electrical models	Triangulated layers at different depths	3D models defined by voxels representing complex permittivities	Derived from the analog radargrams by reprocessing the properties of the target scenario
Instrument parameters	Signal waveform, antenna footprint	Plane wave approximation, near zone field collection	Dependent on the analog waveform
Computational performance (using Intel Core i-3 CPU@3.70 GHz)	Parallel implementation of radar traces - 16 GB RAM, 16 h per radar trace	98 TB RAM, 500 days per radargram of orbital track-length	Negligible RAM, 20 seconds per radargram of orbital track-length

Different simulation techniques have different requirements, in terms of the inputs, memory and computation time. They are also suitable for different applications. Table 5.1 discusses three recent simulation techniques that have been used for RIME simulations, and highlights the key differences between them, in terms of the method, computational performance, and the inputs. Apart from these, there are also other simulators (e.g. [84, 88, 132, 46]) that have been used for RS missions, depending on the application required, and their specific advantages and limitations.

The electromagnetic simulators (Multi-layer coherent radar sounder simulator (MRS) and FDTD based) allow the modeling of the actual transmitted pulse, thus providing accurate representation of the signal characteristics. Due to its capability of handling 3D models, the FDTD based simulator is useful when studying unusual planetary targets, which can be represented by spatially varying geo-electrical models. However, this is limited by the computation time required, making it unrealistic to simulate radargrams for too many subsurface hypotheses. The MRS produces coherent simulated radargrams, giving the advantage of analyzing the phase response of the subsurface target. However, it only operates on layered target-models and thus targets with complex 3D geometries cannot be simulated.

The analog-based simulator resolves the need for subjective modeling of the subsurface target, by assuming that the subsurface geomorphology of the target is similar to that of its geological analog. It preserves the characteristics of real radargrams, such as noise statistics, volume scattering, and interface roughness, which are challenging to model with the electromagnetic simulators. Thus, this gives the opportunity to use the analog-based simulated radargrams for developing automatic target detection algorithms, which can be implemented on the real data, with minor adaptations. However, the penetration depth and the waveform characteristics are constrained by the characteristics of the analog instrument.

5.3 Proposed Approach: Construction of the database

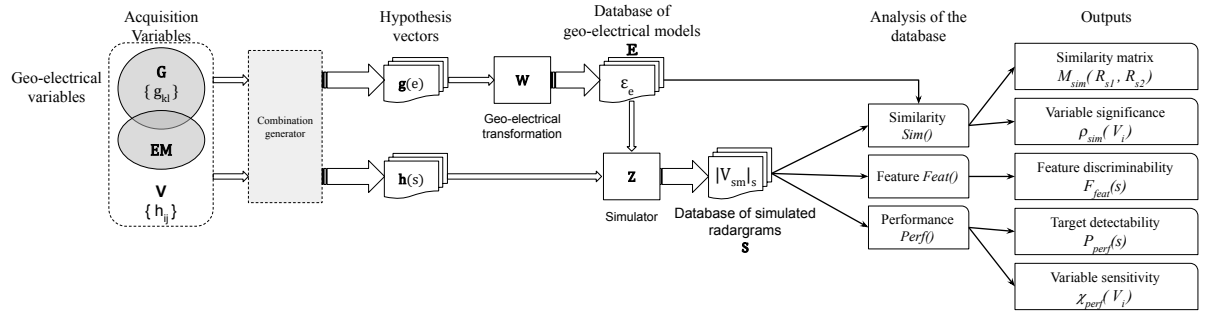


Figure 5.2: Flowchart of the procedure for database generation and analysis. The figure also shows the notation used in the chapter.

In this section, we describe a methodology for constructing a database representing the acquisition scenario of a RS. Figure 5.2 shows the steps of this methodology, which are illustrated in detail in the following subsections. The resulting databases of geo-electrical models and simulated radargrams are valuable assets for assessing the performance, modeling the relationship between different acquisition variables, and understanding the in-

interpretability of the actual radargrams. To this purpose we introduce techniques for analyzing the database for extracting this information in the next section.

5.3.1 Definition of the acquisition scenarios

The first step in the proposed approach is the selection of the target of interest within the coverage of the RS being studied. For the selected target, we make an inventory of the current geological knowledge that can be translated into the geo-electrical properties of the target. This knowledge is used to define the geo-electrical variables that describe the target properties, such as composition, structure, and porosity. The target geo-electrical properties also depend on certain instrument parameters, such as the central frequency of the transmitted signal.

Let $\mathbf{G} = \{\overline{G}_k\}, k = 1, 2, \dots, N_g$ be the set of N_g geo-electrical variables, in which each variable is denoted by \overline{G}_k . The variable \overline{G}_k can take the hypothesis values belonging to the set $\{g_{k,l}\}$, defined by:

$$\overline{G}_k = \{g_{k,l}\} = \{g_{k,1}, g_{k,2}, \dots, g_{k,m_k}\}, \quad (5.1)$$

where the index $l = 1, 2, \dots, m_k$ identifies the l^{th} out of the m_k hypothesis values that the geo-electrical variable \overline{G}_k can take. The geo-electrical variables are translated into the complex dielectric permittivities defined in a 3D space representing the target. The radar response is simulated as a function of the geo-electrical models and other electromagnetic variables such as the instrument parameters (e.g. central frequency, bandwidth) and the orbit parameters (e.g. orbit altitude).

Let \mathbf{EM} denote the set of the electromagnetic variables. Then the super-set of all acquisition variables is defined as $\mathbf{V} = \mathbf{G} \cup \mathbf{EM}$. We define $\mathbf{V} = \{\overline{V}_i\}, i = 1, 2, \dots, N_a$ as the set of N_a acquisition variables, in which each variable is denoted by \overline{V}_i . The acquisition variable \overline{V}_i takes a set of plausible hypotheses values given by:

$$\overline{V}_i = \{h_{i,j}\} = \{h_{i,1}, h_{i,2}, \dots, h_{i,n_i}\}, \quad (5.2)$$

where n_i refers to the number of selected plausible hypothesis values for the variable \overline{V}_i , the index i identifies the i^{th} variable and the index $j = 1, 2, \dots, n_i$ corresponds to j^{th} hypothesis of the variable \overline{V}_i . The simulated radargrams are related to the acquisition variables \mathbf{V} , whereas the geo-electrical models are related to the geo-electrical variables \mathbf{G} .

5.3.2 Database of geo-electrical models

Next, we create combinations of the hypotheses values of each variable to use as inputs to the geo-electrical model and the simulator. We assume that the acquisition variables

are independent, i.e. the hypothesis value of one variable does not depend on the values of the other variables. Therefore, the real acquisition scenario can be represented by all possible combinations of the hypothesis values for the different acquisition variables. This is true in general. However, in cases where the acquisition variables are not independent (e.g. for bandwidth dependent on the central frequency), the proposed approach is still applicable by eliminating some of the invalid combinations.

For the geo-electrical variables \mathbf{G} , each unique combination is represented by the index e . The variable values corresponding to each combination are stored in an N_g -element geo-electrical hypothesis vector $\mathbf{g}(e)$ given by:

$$\mathbf{g}(e) = [g_{1,l(e,1)}, g_{2,l(e,2)}, \dots, g_{k,l(e,k)}, \dots, g_{N_g,l(e,N_g)}],$$

$$e = 1, 2, \dots, N_e, N_e = \prod_{t=1}^{N_g} m_t \quad (5.3)$$

where N_e is the total number of combinations, and the index $l(e, k)$ corresponds to the value of the k^{th} variable for the e^{th} combination.

The geo-electrical models for the e^{th} combination are given by $\epsilon_e = \mathcal{W}[\mathbf{g}(e)]$. The transformation function $\mathcal{W}()$, applied to the geo-electrical hypotheses vector $\mathbf{g}(e)$ estimates the dielectric properties (mainly the real and imaginary parts of the permittivity) and depends on the type of the planetary material. The transformation $\mathcal{W}()$ can be achieved using the techniques for geo-electrical modeling described in Section 3.2.

The knowledge of the 3D geo-electrical model $\epsilon_{3D}(x, y, z)$ should be translated to an appropriate representation, depending on the simulator to be used. In particular, for the analog-based simulator, the along-track profile of the model $\epsilon_{3D}(x, z)$ is discretized at the pixel size of the analog radargram, while the cross-track variation $\epsilon_{3D}(y, z)$ is assumed to be the same as the analog. Thus, the geo-electrical models ϵ_e are generated for the e^{th} combination of geo-electrical hypotheses to obtain the database of geo-electrical models $\mathbb{E} = \{\epsilon_e\}$.

5.3.3 Database of simulated radargrams

Similar to the combinations of geo-electrical variables, we create N_s unique combinations of all the acquisition variables. For each unique combination s , we create an N_a -element simulation hypothesis vector $\mathbf{h}(s)$, given by:

$$\mathbf{h}(s) = [h_{1,j(s,1)}, h_{2,j(s,2)} \dots h_{i,j(s,i)}, \dots, h_{N_a,j(s,N_a)}],$$

$$s = 1, 2, \dots, N_s, N_s = \prod_{t=1}^{N_a} n_t \quad (5.4)$$

where $j(s, l)$ is the index corresponding to the the value of the i^{th} acquisition variable of the s^{th} combination.

The simulator computes the 2D radargram $V_{sm}(r_I, c_I)$, whose magnitude is given by $|V_{sm}|_s(r_I, c_I) = \mathcal{Z}[\mathbf{h}(s)]$ for the s^{th} combination index, using the simulation function $\mathcal{Z}()$. Recall that c_I refers to the column index and r_I refers to the row index of the simulated radargram of the investigated RS. For simplicity, the radargram will henceforth be denoted as $|V_{sm}|_s$ without explicitly mentioning the row and column indices.

The definition of the function $\mathcal{Z}()$ depends on the choice of the simulator. This usually involves computation of the electromagnetic interaction between the RS instrument parameters, orbit parameters and the geo-electrical models. In the previous section, we described several simulation techniques. In this contribution, we use the analog-based method described in Chapter 4 for producing the database of simulated radargrams. We choose this method because of the computational efficiency and the ability to produce realistic radargrams. Therefore, by simulating the radargrams $|V_{sm}|_s$ for each hypotheses combination, we obtain the database of simulated radargrams $\mathbb{S} = \{|V_{sm}|_s\}$.

5.4 Proposed approach: Analysis of the databases

In this section, we describe an approach to analyze the databases of the geo-electrical models \mathbb{E} and the simulated radargrams \mathbb{S} in terms of (a) the detection performance of the RS under different acquisition scenarios, (b) the hypotheses discrimination ability of features extracted from the simulated radargrams, and (c) the degree of similarity between the radargrams and between the geo-electrical models produced by different hypotheses.

5.4.1 Performance analysis

For supporting the design of the RS, the database \mathbb{S} can be used to identify the hypotheses that meet the science requirements of the mission. For each radargram $|V_{sm}|_s$ we calculate the performance measure $P_{perf}(s) = Perf(|V_{sm}|_s)$. Different performance measures can be defined by the function $Perf()$, depending on the science requirement to be tested. Here some examples of performance functions are provided.

- *Subsurface signal to noise ratio (SSNR)*: The ratio of the peak subsurface power to the background noise level for the radar traces containing the subsurface echo ($P_{SSNR}(s)$). This should be higher than the SNR margin of the RS for detectability.
- *Subsurface to surface ratio (SSR)*: The ratio of the peak subsurface power to the peak surface power for the radar traces containing the subsurface echo ($P_{SSR}(s)$). This should be higher than the requirement on the dynamic range (i.e. the minimum side-lobe ratio) for the detectability of the subsurface above the sidelobes of the surface reflection.

- *Surface signal to noise ratio (SurfSNR)*: The ratio of the peak surface power to the background noise level for the radar traces containing the subsurface echo ($P_{SurfSNR}(s)$). This should be higher than the SNR margin of the RS for detectability.
- *Probability of subsurface detection (Pd)*: The conditional probability of detecting distributed subsurface targets ($P_{Pd}(s)$). This is estimated as the ratio of the number of pixels above the noise level in the simulated radargrams to that expected in the subsurface region.

The performance analysis can also be used for estimating the sensitivity of the RS to small changes in the hypothesis values of a variable. The sensitivity can be used to define the detectable resolution of the variable, i.e. the precision up to which the variable value can be inverted from the acquired radargram. We define the sensitivity of the RS to the variable \bar{V}_i for the performance function $Perf()$ by:

$$\chi_{perf}(\bar{V}_i) = \frac{\partial P_{perf}(s)}{\partial h_{i,j}(s,i)} = \frac{\partial Perf\{\mathcal{Z}[\mathbf{h}(s)]\}}{\partial h_{i,j}(s,i)} \quad (5.5)$$

The practical implementation of the sensitivity estimation for the variable \bar{V}_i can be done by selecting a set of hypothesis vectors such that only the values of \bar{V}_i are varying while the other variables are fixed to constants. The sensitivity is then estimated by calculating the slope of the $P_{perf}(s)$ versus the hypothesis values $h_{i,j}(s,i)$ plot.

5.4.2 Feature analysis

The database of simulated radargrams can also be used to support the development of automatic radargram interpretation schemes. One of the key steps in the automatic interpretation algorithms is the extraction of radargram features that can discriminate the different characteristics of the targets. In this analysis, we define feature extraction functions $Feat()$ that derive a set of single-valued features $F_{feat}(s) = Feat(|V_{sm}|_s)$ for each radargram. In general, features can be defined for each pixel or radar trace of the radargram.

In this contribution, we use three of the performance measures SSR, SSNR and Surf-SNR, as power-based features. Since the analysis performed on the features is different from the performance analysis, we refer to these by the notation $F_{SSR}(s) = P_{SSR}(s)$, $F_{SSNR}(s) = P_{SSNR}(s)$, and $F_{SurfSNR}(s) = P_{SurfSNR}(s)$.

The feature $F_{SSR}(s)$ represents the loss in power during propagation up to the subsurface. It depends on the attenuation in the medium at the RS frequency. The feature $F_{SSNR}(s)$ represents the power received from the subsurface interface. It depends on the dielectric contrast at the interface, the attenuation up to the subsurface and the power

of the transmitted signal. The feature $F_{SurfSNR}(s)$ depends on the surface scattering properties (e.g. roughness, dielectric permittivity) and the power incident on the surface.

In addition to the power-based features, we define a time-based feature *Time to subsurface (SST)*, i.e. the average time delay between the surface and subsurface echo calculated from the radar traces containing the subsurface echo ($F_{SST}(s)$). This feature is related to the bulk real part of the permittivity between the surface and subsurface and depends on the central frequency of the RS signal.

We perform a discriminant analysis on the extracted features to test which variables are separable. For each variable \bar{V}_i , we create clusters of the combination indices, one for each hypothesis value $h_{i,j}$, i.e. for each cluster the variable \bar{V}_i takes the values $h_{i,1}, h_{i,2}, \dots, h_{i,n_i}$, respectively. Let the corresponding set of clusters of features be defined by $\mathbf{C}_i = \{C_{i,1}, C_{i,2}, \dots, C_{i,n_i}\}$, such that $C_{i,j} = \{F_{feat}(s_{i,j})\}$ is the cluster of features representing the case in which the variable $\bar{V}_i = h_{i,j}$ and other variables assume all their respective hypotheses values and so on.

The feature discriminant analysis is performed using the simple analysis of variance (ANOVA) technique [135]. Using this technique we test the null hypothesis that the clusters of features corresponding to different hypothesis values of a variable belong to the same population. ANOVA estimates the ratio of the distances between the cluster means to those within the cluster. This test statistic follows F-distribution. For the set of clusters \mathbf{C}_i , we calculate the p-value, i.e. the probability of obtaining a test statistic greater than the estimated one if the null-hypothesis was true. If the calculated p-value is smaller than the significance level (here assumed to be 0.01), the null hypothesis is rejected. This means that the feature can significantly discriminate the different hypotheses of the variable \bar{V}_i . This information can be used for selecting discriminating features suitable for the automatic interpretation algorithms.

5.4.3 Similarity analysis

Another important aspect of the radar response to be analyzed is the similarity of the geo-electrical models and the full simulated radargrams to each other. To this purpose, we consider every pair of geo-electrical models ($\epsilon_{e1}, \epsilon_{e2}$) from the database \mathbb{E} and compute the degree of similarity between them. In this case, the similarity measures are applied to complex data. Thus, the real $\text{Re}[\epsilon_e]$ and imaginary $\text{Im}[\epsilon_e]$ parts of the geo-electrical models ϵ_e are compared separately. Similarly, we compare pairs of radargrams ($|V_{sm}|_{s_1}, |V_{sm}|_{s_2}$) (having the same dimension) from the database \mathbb{S} . Due to the large dynamic range of the radargram values, these are converted to decibels for this analysis. Thus, we obtain the

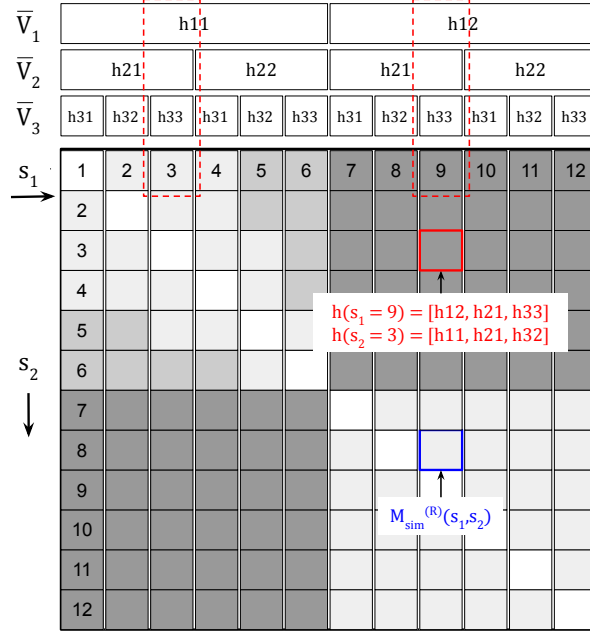


Figure 5.3: Example of a sorted similarity matrix considering 3 acquisition variables $\bar{V}_1, \bar{V}_2, \bar{V}_3$ and the corresponding hypotheses.

following similarity values:

$$\begin{aligned}
 M_{sim}^R(s_1, s_2) &= Sim(|V_{sm}|_{s_1}, |V_{sm}|_{s_2}), s_1, s_2 \in s, \\
 M_{sim}^{Re(\epsilon)}(e_1, e_2) &= Sim(\text{Re}[\epsilon_{e_1}], \text{Re}[\epsilon_{e_2}]), e_1, e_2 \in e, \\
 M_{sim}^{Im(\epsilon)}(e_1, e_2) &= Sim(\text{Im}[\epsilon_{e_1}], \text{Im}[\epsilon_{e_2}]), e_1, e_2 \in e \quad (5.6)
 \end{aligned}$$

The function $Sim\{I_1, I_2\}$ measures the pixel-to-pixel similarity between the two matrices I_1 and I_2 . For simplicity, in this discussion we will refer to the geo-electrical models and radargrams as images, represented by I_1 and I_2 . Here we describe four well known similarity measures that can be used in the proposed approach.

- *Mutual information (MI)*: The measure of the joint entropy, i.e. the information obtainable for the image I_1 , given the other image I_2 [39, 140]. We use the normalized MI value given by:

$$M_{MI}(I_1, I_2) = \frac{mi(I_1, I_2)}{\sqrt{mi(I_1, I_1)mi(I_2, I_2)}}, \quad (5.7)$$

where $mi()$ computes the value of the mutual information as given by [39] and previously used in Chapter 4. The normalized MI ranges from 0 (completely different images) to 1 (completely identical, i.e. $I_1 = I_2$). Mutual information captures the spatial relationship between pixels. High MI values occur for image pairs having

similar structure and neighbourhood pixel intensities. Mutual information is not affected by the absolute value of the reflected signal and hence it is not affected by calibration issues of the radargrams.

- *Correlation (COR)*: The measure of pixel-to-pixel correlation between the two images, given by

$$M_{COR}(I_1, I_2) = \frac{(I_1 - \bar{I}_1) \cdot (I_2 - \bar{I}_2)}{\sigma(I_1)\sigma(I_2)}, \quad (5.8)$$

where \bar{I}_1 and \bar{I}_2 are the global mean values, $\sigma(I_1)$ and $\sigma(I_2)$ are the standard deviation values of the two images, and the dot operator implies the inner product of the terms in the parentheses. The correlation captures similarity in terms of structure, and is not sensitive to the relative pixel intensities.

- *Structural similarity index (SSIM)*: The measure of image similarity in terms of contrast, structure and the pixel intensity [150], given by:

$$M_{SSIM}(I_1, I_2) = \frac{[2\bar{I}_1\bar{I}_2 + q_1][2\sigma(I_1)\sigma(I_2) + q_2]}{[\bar{I}_1^2 + \bar{I}_2^2 + q_1][\sigma^2(I_1) + \sigma^2(I_2) + q_2]}, \quad (5.9)$$

where q_1 and q_2 are constants that depend on the dynamic range (DR) of the images. In this analysis, $q_1 = (0.01 \times \text{DR})^2$ and $q_2 = (0.03 \times \text{DR})^2$. SSIM compares the shape of the objects in the two images, independent of the scale.

- *Difference (DIF)*: The average pixel-to-pixel difference between the two images. If the difference is 0, the two images are identical, and if it is close to 0, the images are very similar. We specifically use the difference values to identify the trivial cases of hypotheses that result in exactly identical geo-electrical models.

From the perspective of RS, low values of similarity (i.e. low MI, SSIM and COR, and high DIF) between pairs of simulated radargrams or geo-electrical models are interesting. These pairs indicate combinations that can add new information, whereas the pairs having high similarity would contain similar information. The similarity measures are used to define similarity matrices and to study quantitatively the variable significance.

Similarity matrix

The similarity values of the geo-electrical models are stored in the form of $N_e \times N_e$ matrices, and those of the radargrams in $N_s \times N_s$ matrices. The row and column indices of the matrix correspond to the combination index $(e_1, e_2) \in e$ for the geo-electrical models and $(s_1, s_2) \in s$ for the simulated radargrams. These matrices are symmetrical, since $M_{sim}(I_1, I_2) = M_{sim}(I_2, I_1)$. For better visualization, the matrices are plotted as a gray-scale square image (each pixel corresponding to one element of the matrix). The diagonal

elements of the MI, COR and SSIM matrices are 1 and the pixel intensity is proportional to the similarity value. Thus bright pixels at the diagonal represent the highest similarity, and the dark pixels represent low similarity. The diagonal elements of DIF matrices are 0 and the bright pixels represent high difference i.e. low similarity.

In the interpretation of these matrices, we consider a variable to be dominant over other variables, if changing the values of this variable changes significantly the radargram properties (i.e. results in image pairs having very low similarity), irrespective of the values of the other variables. Figure 5.3 shows a schematic representation of a hypothetical 12×12 similarity matrix of the simulated radargrams. Above the first row, the three acquisition variables are displayed in the order in which the combinations are generated: $\bar{V}_1 = \{h_{1,1}, h_{1,2}\}$, $\bar{V}_2 = \{h_{2,1}, h_{2,2}\}$, and $\bar{V}_3 = \{h_{3,1}, h_{3,2}, h_{3,3}\}$. The value in the cell (s_1, s_2) is the similarity measure between $|V_{sm}|_{s_1}$ and $|V_{sm}|_{s_2}$. For instance, the red cell represents the similarity between the radargrams $R_9 = \mathcal{Z}[\mathbf{h}(9)]$ and $R_3 = \mathcal{Z}[\mathbf{h}(3)]$. The hypothesis values for the hypothesis vectors $\mathbf{h}(9)$ and $\mathbf{h}(3)$ can be read from the labels above the matrix (dotted red boxes).

For the ease of interpretation, the sequence of the variables $\bar{V}_1, \bar{V}_2, \bar{V}_3$ should be selected in such a way that the bright pixels are clustered close to the diagonal and the darker shades are clustered off-diagonal. A suitable order of the variables that gives an interpretable and sorted matrix has to be selected by trial-and-error. The matrix in Figure 5.3 is an example of a sorted matrix since similar intensity pixels are clustered together. In this case, \bar{V}_1 is the dominant variable. Further, since no clear pattern is observed corresponding to the changes in the hypothesis values of \bar{V}_2 and \bar{V}_3 , this implies that the other two variables are not dominant.

Note that the dominance of an acquisition variable depends on its hypothesis values. It is recommended to perform this analysis in two stages. First perform a preliminary analysis considering a small number of sharply different values of the hypotheses and identify the dominant and non dominant variables. Next, repeat the database generation and variable analysis for a redefined set of hypotheses. For this second stage, the dominant variables should be studied in detail by choosing finer intervals of the hypothesis values, while the hypotheses of the non dominant variables should be minimized.

Variable significance

The similarity matrices provide a qualitative way to visualize the entire database. However, to compare the similarity values for different variables and determine an estimate of the variable significance, we need a more quantitative approach. The goal of this quantitative analysis is to estimate the average similarity between pairs of images whose hypotheses differ for only one of the variables, while the values for all the other variables are the same. This average similarity is the estimate of the significance of the variable

that has the differing hypotheses. Note that low values of the variable significance, corresponding to low average similarity implies that changes in the variable value significantly affect the radargram or geo-electrical model.

To compute the significance of the geo-electrical variable $\overline{G}_t \in \mathbf{G}$ using the similarity between the geo-electrical models, we select the pairs of combination indices (e_1, e_2) such that only the value of \overline{G}_t is different between the corresponding hypothesis vectors $\mathbf{g}(e_1)$ and $\mathbf{g}(e_2)$. Let W_t denote the set of these pairs of combination indices, satisfying the condition:

$$(e_1, e_2) \in W_t \text{ if } g_{k,l}(e_1) \neq g_{k,l}(e_2), \forall k = t, \\ g_{k,l}(e_1) = g_{k,l}(e_2), \forall k \neq t \quad (5.10)$$

For the database of geo-electrical models \mathbb{E} , the set W_t has $N_q = \binom{m_t}{2} \frac{N_e}{m_t}$ elements, where m_t is the number of hypotheses of \overline{G}_t . The significance score $\rho_{sim}^{\text{Re}(\epsilon)}(\overline{G}_t)$ and $\rho_{sim}^{\text{Im}(\epsilon)}(\overline{G}_t)$ of the geo-electrical variable \overline{G}_t , in terms of the real and imaginary parts of the geo-electrical models, respectively, is defined as:

$$\rho_{sim}^{\text{Re}(\epsilon)}(\overline{G}_t) = \frac{1}{N_q} \sum_{(e_1, e_2) \in W_t} \text{Sim}(\text{Re}[\epsilon_{e_1}], \text{Re}[\epsilon_{e_2}]), \\ \rho_{sim}^{\text{Im}(\epsilon)}(\overline{G}_t) = \frac{1}{N_q} \sum_{(e_1, e_2) \in W_t} \text{Sim}(\text{Im}[\epsilon_{e_1}], \text{Im}[\epsilon_{e_2}]) \quad (5.11)$$

Similarly, for estimating the significance of the variable $\overline{V}_t \in \mathbf{V}$, we select pairs of combination indices (s_1, s_2) such that only the value of \overline{V}_t is different between the corresponding hypothesis vectors $\mathbf{h}(s_1)$ and $\mathbf{h}(s_2)$. Let U_t denote the set of these pairs of combination indices, satisfying the condition:

$$(s_1, s_2) \in U_t \text{ if } h_{i,j}(s_1) \neq h_{i,j}(s_2), \forall i = t, \\ h_{i,j}(s_1) = h_{i,j}(s_2), \forall i \neq t \quad (5.12)$$

For the database \mathbb{S} , the set U_t has $N_p = \binom{n_t}{2} \frac{N_s}{n_t}$ pairs of combination indices, where n_t is the number of hypotheses of \overline{V}_t . We define the significance score $\rho_{sim}(\overline{V}_t)$ of the variable \overline{V}_t using the similarity functions $\text{Sim}()$ as

$$\rho_{sim}(\overline{V}_t) = \frac{1}{N_p} \sum_{(s_1, s_2) \in U_t} \text{Sim}(|V_{sm}|_{s_1}, |V_{sm}|_{s_2}) \quad (5.13)$$

The higher the $\rho_{sim}(\overline{V}_t)$ score for MI, COR and SSIM, the lower is the significance of the variable \overline{V}_t . This is because the corresponding radargrams or the geo-electrical models have higher similarity to each other, even though the hypothesis values of \overline{V}_t are changing. On the other hand, the higher the $\rho_{DIF}(\overline{V}_t)$ score, the higher is the significance of the variable.

5.5 Experimental results

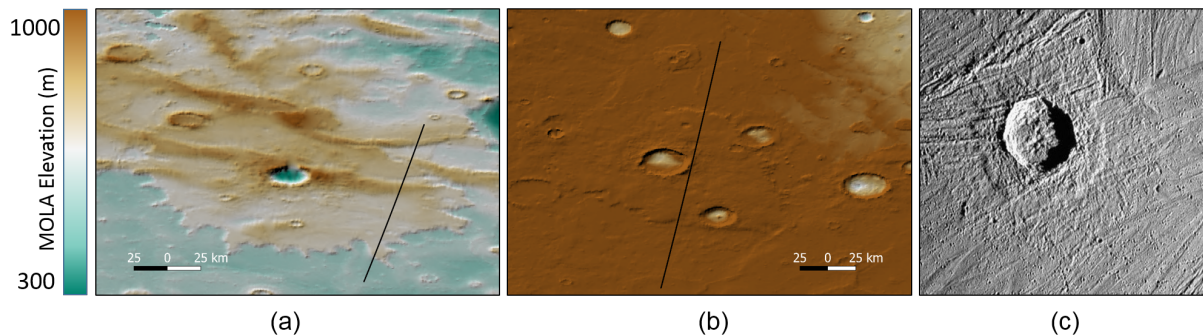


Figure 5.4: Selected Mars analog features of the Ganymede pedestal craters: (a) Mars pedestal crater (P1) and SHARAD ground-track 0748401, (b) another Mars pedestal crater (P2) and SHARAD ground-track 0782801, and (c) the Acheleous crater on Ganymede (credit-NASA/JPL/DLR).

In this section, we demonstrate the proposed approach for RIME [18]. The surface of Ganymede is riddled with craters of diverse geomorphologies, a deeper insight into which can reveal the geological history of the moon. For the demonstration of the proposed approach, we have selected an important target on Ganymede, i.e. the pedestal craters, which were introduced in Section 4.4.4 (Case III). Due to the availability of SHARAD radargrams on Mars-analog pedestal craters and the absence of detailed knowledge of these targets required for subjective geo-electrical modeling, the analog-based method is used for the analysis. Here we present a part of the selected geological hypotheses for the target. However, with this approach, all possible hypotheses can be tested on different targets.

5.5.1 Construction of the databases

The pedestal craters on Ganymede are fresh impact craters, about 6 - 89 km in diameter [70]. Their morphology is characterized by a raised pedestal ejecta with sharp scarp-like brims, similar to Mars pedestal craters [101]. However, unlike the multi-lobed Mars pedestal craters, the ones on Ganymede are formed on an ice-rich volatile crust, and are usually single lobed. The pedestal craters postdate the bright grooved terrain and hence are found within both the terrain types. The detectable subsurface target is the interface between the pedestal ejecta and the underlying substrata. The interface is visible as a horizontal reflector below the pedestal, and is nearly parallel to the surface.

Definition of the acquisition scenario

For the pedestal craters, we define a set of 9 acquisition variables and their corresponding hypothesis values, as listed in Table 5.2. The acronyms used in this chapter

for these variables are given in brackets alongside. The bandwidth variable represents the two programmable bandwidths in two of the operation modes of RIME: HRO at 2.8 MHz, for detailed profiling of shallow targets, and LRO at 1 MHz; for deep probing at low resolution. We consider the two hypotheses on the nominal orbit altitude of the JUICE spacecraft from Ganymede surface, i.e. 500 km during the nominal mission phase, and possibly down to 200 km post the nominal phase.

Table 5.2: Example of acquisition variables and the corresponding hypotheses for the Ganymede pedestal crater target

Acquisition variables $\{\bar{V}_i\}$	Hypothesis values $\{h_{i,j(i)}\}$
Geometry	{P1, P2}
Bandwidth (B) (MHz)	{2.8, 1}
Spacecraft altitude (H) (km)	{500, 200}
Surface temperature (Ts)	{80, 100, 120}
Scale height (Th)	{cb, cs}
Void fraction (Vfn)	{0.01, 0.1, 0.2}
Impurity profile (Impf)	{BT, DT}
Structure (Str)	{cont, discontin}
Contrast (Cntr)	{-0.8, 0.8}

The geometry variable represents the possible geomorphology of the pedestal crater. It depends on the shape of the crater with respect to the orientation of the RS track. In this analysis, we consider two analog radargrams (P1 and P2, see Figure 5.4), as two possible hypotheses of the geometry variable. The important geophysical properties are the temperature profile, the void fraction and the dust-fraction profile (impurity). Ganymede geothermal temperature $T(z)$ at depth z is described by [68]:

$$T(z) = T_s e^{(z/Th)} \quad (5.14)$$

This depends on the surface temperature (T_s), which varies between 80 K and 120 K, from the equator to the poles. We have considered three hypotheses for T_s , i.e. 80 K, 100 K and 120 K. The other parameter controlling the slope of the temperature profile is the scale height (Th). For an ice thickness of 10 km, we assume two hypotheses: (1) ‘cb’, i.e. a constant base temperature such that the temperature at a depth of 10 km is 130 K irrespective of the surface temperature, or (2) ‘cs’ i.e. a constant slope profile with the base temperature increasing proportionately with the surface temperature, given by:

$$Th = \begin{cases} \frac{10}{\ln(130/T_s)}, & \text{if } \text{cb} \\ \frac{10}{\ln(130/120)}, & \text{if } \text{cs} \end{cases} \quad (5.15)$$

The pure ice dielectric permittivity $\epsilon_{pure}(z)$ is calculated using the temperature profile $T(z)$. Due to global-scale tectonic activity on Ganymede, the shallow ice is porous, i.e. mixed with voids. For the void fraction, we consider three hypotheses: $Vfn = \{0.01, 0.1, 0.2\}$. Impact processes contaminate the shallow ice-crust with dust impurities, which are present in higher concentration for older terrains. As described in Chapter 4, the two hypotheses of the impurity profiles of the bright terrains (BT) and the dark terrains (DT) on Ganymede are described by [68]. The effective permittivity $\epsilon_{eff}(z)$ of the terrain-scale crustal ice on Ganymede is calculated using the mixing formula.

The structure variable represents the nadir profile of the ejecta interface. We consider two hypotheses for the structure: (1) ‘cont’ (continuous) i.e. extending beyond the visible interface, to the full length of the radargram, or (2) ‘discont’ (discontinuous), i.e. present only where it is visible in the radargram. In the Mars analog, the pedestal base represents a compositional discontinuity, predicted to have a dielectric contrast of 0.9 in the real permittivity of the two layers. Here we consider two hypotheses of the contrast variable for Ganymede geo-electrical models, i.e. 0.8 and -0.8. The value of the contrast is a constant factor (± 0.8) added to the pedestal layer, after computing the terrain-scale effective permittivity $\epsilon_{eff}(z)$.

Databases of geo-electrical models and simulated radargrams

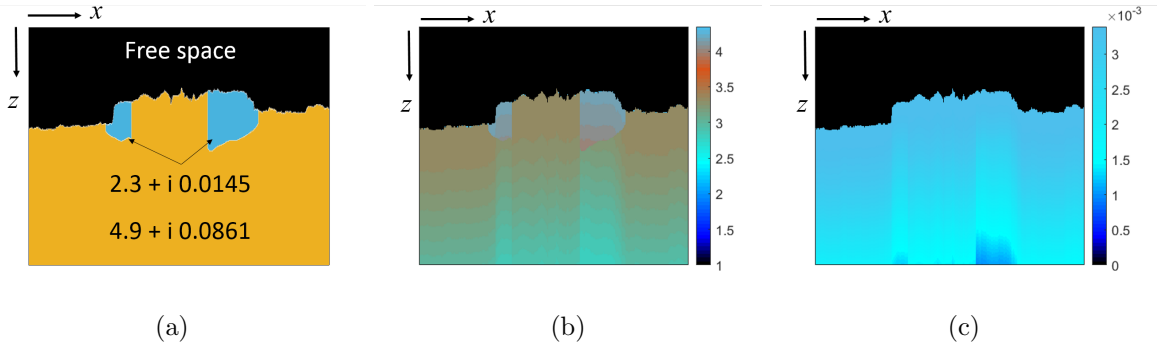


Figure 5.5: Example of geo-electrical models: (a) P2 Mars analog geo-electrical model, (b) P2 real part of the geo-electrical model $\text{Re}[\epsilon_{144}]$, (c) P2 imaginary part of the geo-electrical model $\text{Im}[\epsilon_{144}]$.

All possible combinations of the hypothesis values of the 9 acquisition variables result in 1152 simulated radargrams, equally split between each geometry P1 and P2. In the following analysis, we will treat these as two different databases corresponding to each analog radargram. Thus, in both cases the cardinality of \mathbb{S} is 576. We do this division to compare the results of both pedestal craters independently. Similarly, the hypotheses combinations of the 6 geo-electrical variables (not including geometry) result in two databases of geo-electrical models \mathbb{E} containing 144 models each.

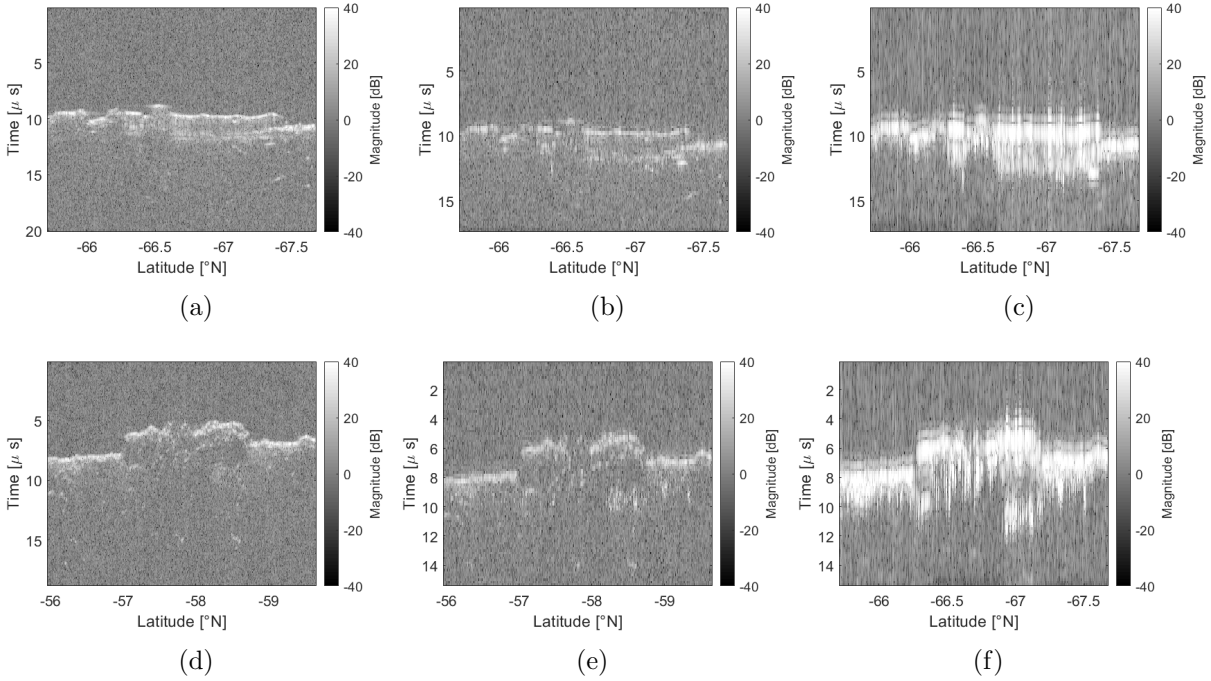


Figure 5.6: Example of simulated radargrams: (a) P1 analog SHARAD radargram, (b) P1 simulated radargram $|V_{sm}|_1$, (c) P1 simulated radargram $|V_{sm}|_{576}$, (d) P2 analog SHARAD radargram, (e) P2 simulated radargram $|V_{sm}|_1$, (f) P2 simulated radargram $|V_{sm}|_{576}$.

Figure 5.5 shows examples of the real and imaginary parts of the geo-electrical models of the pedestal crater P2 for the combination index $e = 144$. The corresponding hypothesis vector is $\mathbf{g}(144) = [T_s = 120, T_h = cs, V_{fn} = 0.2, Impf = DT, Str = \text{discont}, Cntr = 0.8]$. Figure 5.5(a) shows the analog geo-electrical model, as described in [101]. Figure 5.5(b) shows the real part and (c) shows the imaginary part of the RIME input geo-electrical model. In this example, the structure is discontinuous, i.e. the subsurface is assumed to be present only where it is visible in the analog radargram (Figure 5.6(d)). The contrast value of 0.8 at the pedestal base is clearly visible in the real part the geo-electrical model. The imaginary part is dependent mainly on the geophysical variables. However, a minor effect of the structure is also visible, since it affects the analog model, and thus controls the time-to-depth conversion.

Figure 5.6 shows examples of the analog and the simulated radargrams of P1 (a - c) and P2 (d - f). The radargrams correspond to the combination indices $s = 1$ (Figure 5.6(b) and (e)) and $s = 576$ (Figure 5.6(c) and (f)). The corresponding hypothesis vectors are $\mathbf{h}(1) = [B = 2.8, H = 500, T_s = 80, T_h = cb, V_{fn} = 0.01, Impf = BT, Str = \text{cont}, Cntr = -0.8]$ and $\mathbf{h}(576) = [B = 1, H = 200, T_s = 120, T_h = cs, V_{fn} = 0.2, Impf = DT, Str = \text{discont}, Cntr = 0.8]$. Note that the difference in spacecraft height is apparent on

the SNR of the surface and subsurface interfaces. The effect of bandwidth is seen in the resolution and decrease in the sharpness of the radargrams (c) and (f) compared to (b) and (e), respectively. The sampling frequency of RIME is 12 MHz for both the HRO and LRO modes, and thus the time axis for the two pairs of simulated radargrams are the same. However, note that due to higher real permittivity of the DT, the subsurface echo is slightly delayed in time, in case of (c) and (f), compared to (b) and (e), respectively. Next, we present the quantitative comparison of the effects of the different hypotheses on the geo-electrical models and the simulated radargrams.

5.5.2 Analysis of the databases

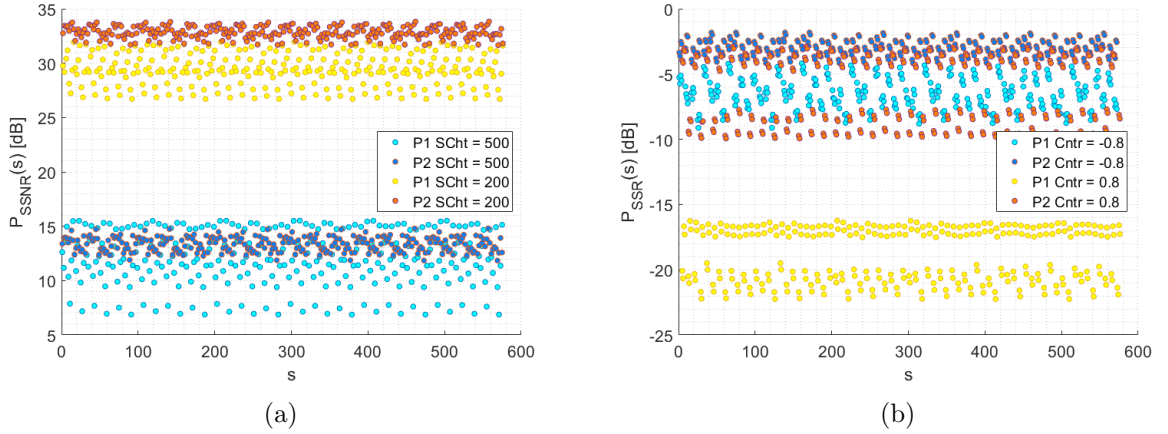


Figure 5.7: Plot of the performance measures of each simulated radargram for the pedestal craters P1 and P2: (a) subsurface signal to noise ratio (SSNR), clustered by the spacecraft height variable (b) subsurface to surface power ratio (SSR), clustered by the contrast variable.

Performance analysis

We apply the performance analysis on the databases of the two pedestal craters, for each of the 576 simulated radargrams. Since the subsurface peak can be clearly identified, we select the radar traces containing the subsurface echoes and calculate the two performance measures - subsurface signal to noise ratio $P_{SSNR}(s)$ and surface to subsurface ratio $P_{SSR}(s)$. The plots of the two performance estimates versus the combination index of the simulated radargrams are shown in Figure 5.7(a) and (b).

The worst and best case $P_{SSNR}(s)$ for P1 are 5 dB and 33 dB, respectively, while for P2, they are 12 dB and 35 dB, respectively. Thus, allowing a SNR margin of at least 5 dB, we see that in all the cases, the pedestal base will be detectable within the sensitivity of RIME. Similarly, the worst and the best case $P_{SSR}(s)$ for P1 are -23 dB and -4 dB, respectively, while for P2 they are -4 dB and -1 dB, respectively. Thus, the $P_{SSR}(s)$ is

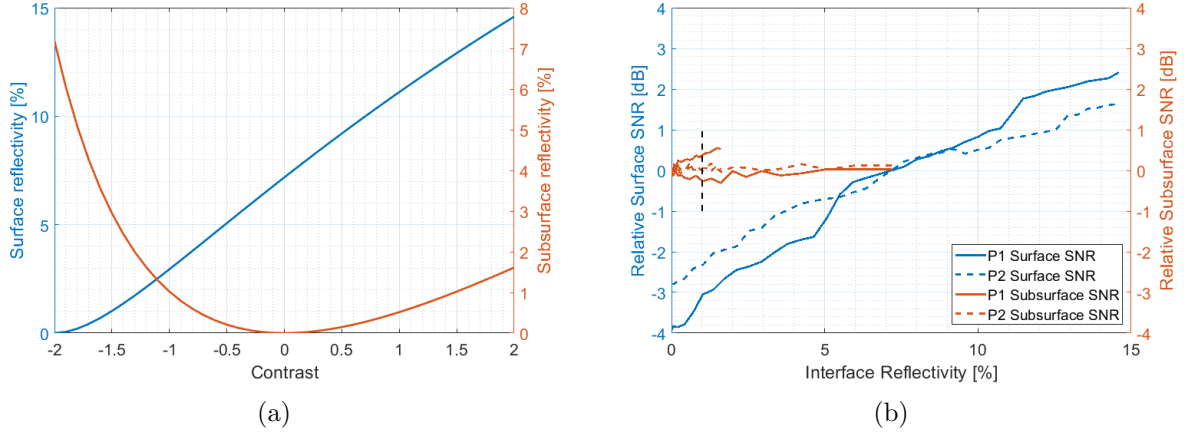


Figure 5.8: RIME sensitivity to the contrast variable: (a) surface and subsurface reflectivity versus contrast, (b) relative surface and subsurface SNR versus reflectivity.

better than the minimum sidelobe requirement of -55 dB, ensuring the detectability of the pedestal base above the sidelobes of the surface echo. Moreover, both the pedestal craters show similar pattern of $P_{SSNR}(s)$ and $P_{SSR}(s)$, thus confirming that the detectability is consistent for different geometries of pedestal craters.

Next, we estimate the sensitivity $\chi_{SSNR}(\text{Cntr})$ and $\chi_{SurfSNR}(\text{Cntr})$ of the subsurface and surface SNR, respectively, to the contrast variable (Cntr). For this analysis, we generate another database \mathcal{S}' considering a single acquisition variable, i.e. the contrast. In this case, $\text{Cntr} = \{-2, -1.9, -1.8, \dots, 1.9, 2\}$ are the hypothesis values of the contrast, thus resulting in 41 simulated radargrams. Although, the contrast is more closely related to the physical scenario, a more interpretable quantity from a radar perspective is the interface reflectivity. The reflectivity at the two interfaces, i.e. the surface reflectivity R_S and the subsurface reflectivity R_{SS} , can be related to the contrast by:

$$R_{SS} = \left| \frac{\sqrt{\epsilon_b + \text{Cntr}} - \sqrt{\epsilon_b}}{\sqrt{\epsilon_b + \text{Cntr}} + \sqrt{\epsilon_b}} \right|^2, \quad R_S = \left| \frac{\sqrt{1} - \sqrt{\epsilon_b + \text{Cntr}}}{\sqrt{1} + \sqrt{\epsilon_b + \text{Cntr}}} \right|^2 \quad (5.16)$$

where ϵ_b is the average complex permittivity of the substrata, below the pedestal.

Figure 5.8(a) shows the relationship between the contrast and the reflectivity, expressed in percentage and calculated assuming $\epsilon_b = 3$. The contrast values correspond to a surface reflectivity between 0% - 15% and subsurface reflectivity between 0% - 8%. The surface reflectivity increases monotonically with the contrast, since the real permittivity of the top layer increases with increase in the contrast. On the other hand, subsurface reflectivity decreases as the absolute magnitude of the contrast decreases, and is 0% for 0 contrast.

For this analysis, we use a modified version of the SSNR and SurfSNR performance

measures, referred to as relative surface SNR and relative subsurface SNR. Since, the SNR depends on the dielectric contrast and the interface roughness, it is necessary to isolate the contribution of the contrast to the SNR. Thus, the relative surface and subsurface SNR values are computed by calibrating them to 0, corresponding to the 0 contrast. Figure 5.8(b) shows the plot of the relative surface and subsurface SNR versus the interface reflectivity. The range of variability of the subsurface SNR is much lower than that of the surface. In particular, for P2, the subsurface SNR changes very subtly with the reflectivity. Note the trend in relative subsurface SNR with increasing interface reflectivity. In this case, as the contrast increases, both the surface and the subsurface reflectivity increase. However, since the increase in surface reflectivity is higher than the increase in the subsurface reflectivity, the net effect is a significant decrease in the power reaching the subsurface. Thus, we observe two values of subsurface SNR (a higher and a lower) for the same value of subsurface reflectivity, corresponding to a lower and a higher surface reflectivity, respectively.

Table 5.3 reports the sensitivity scores $\chi_{SSNR}(\text{Cntr})$ and $\chi_{SurfSNR}(\text{Cntr})$ of the contrast to the two performance measures. The result further confirms that the P2 subsurface SNR is less sensitive to the contrast compared to P1. Since the ground-track of P1 does not contain any clutter from the crater-pit and the subsurface interface is specular and prominent, the sensitivity to the contrast is higher.

Table 5.3: Sensitivity analysis of the contrast variable using the database of simulated radargrams (S')

Sensitivity [dB/Cntr]	P1	P2
$\chi_{SSNR}(\text{Cntr})$	0.1651	-0.0116
$\chi_{SurfSNR}(\text{Cntr})$	1.7048	1.1450

Note that, in the analog-based method, this analysis is biased by the uncertainty in our knowledge of the Mars analog geo-electrical models. Moreover, the analog SHARAD radargrams are not calibrated in power but the relative power between the samples is correctly represented. Hence we use the relative SNR instead of the absolute power. The dielectric contrast value is one of the main factors needed for detecting subsurface interfaces. Other factors contributing to the reflected power, such as volume scattering caused by distributed subsurface scatterers, depend on the morphology of the targets. In the analog-based simulation method, the effects of the volume scattering are preserved. From this analysis we conclude that the pedestal base is detectable due to volume scattering, which is evident from the low sensitivity to the dielectric contrast.

Table 5.4: Feature analysis of the database of simulated pedestal crater radargrams: p-values of the ANOVA test

Considered features		Ts	Th	Vfn	Impf	Str	Cntr	B	H
$F_{SST}(s)$	P1	0.803	1	7E-7	8E-7	0.098	0.514	4E-61	0.729
	P2	0.939	0.983	1.8E-10	2.5E-13	0.193	1E-214	0.845	0.516
$F_{SSNR}(s)$	P1	0.999	0.993	0.943	0.724	0.615	0.594	0.119	0
	P2	0.994	0.999	0.994	0.262	0.0081	0.0086	0.007	4E-294
$F_{SurfSNR}(s)$	P1	0.998	0.996	0.867	0.474	0.233	2E-81	2E-4	1E-84
	P2	0.993	0.999	0.848	0.388	2E-6	5E-20	0.031	4E-160
$F_{SSR}(s)$	P1	0.999	0.988	0.903	0.168	0.027	0	1.8E-4	0.323
	P2	0.996	0.999	0.660	0.005	5E-29	1E-87	0.828	0.153

Feature analysis

The four radargram features (time to subsurface, surface SNR, subsurface SNR and subsurface to surface ratio) described in Section 5.4 are extracted for the 576 simulated pedestal crater radargrams of the two pedestal craters P1 and P2. The p-value of the ANOVA applied to the variable-specific clusters of the features are reported in Table 5.4. The cells highlighted in purple represent the p-values below the significance level, i.e., these features can discriminate the corresponding variable. The red cell corresponds to a p-value equal to 1, which means that the SST feature is equal for all hypotheses of the scale height. Indeed, all the feature values are highly similar for different hypotheses of scale height and surface temperature, as one can see by the p-values nearly equal to 1.

On the other hand, SST can be used to distinguish the hypotheses values of void fraction and impurity profile, and this is consistent for both the pedestal craters. The contrast can be distinguished by the surface SNR and SSR, as also seen in Figure 5.7(b). The features SSR, SSNR and SurfSNR discriminate the structure, while SSR can discriminate the impurity profile of P2. The spacecraft height strongly influences the SNR, due to the inverse square relationship between the propagation loss and the range to the target. Thus, the subsurface and surface SNR are very different for the two hypotheses of spacecraft altitude, as also seen in Figure 5.7(a). The influence of bandwidth on the features differs for P1 and P2. This is expected, since the resolution required to discriminate different geo-morphological units can vary.

Similarity analysis using similarity matrix (qualitative results)

The similarity analysis is carried out using the four similarity measures (Mutual Information, Structural Similarity Index, Correlation and Difference) described in Section 5.4. For each of the two pedestal craters we analyze the similarity between the real and

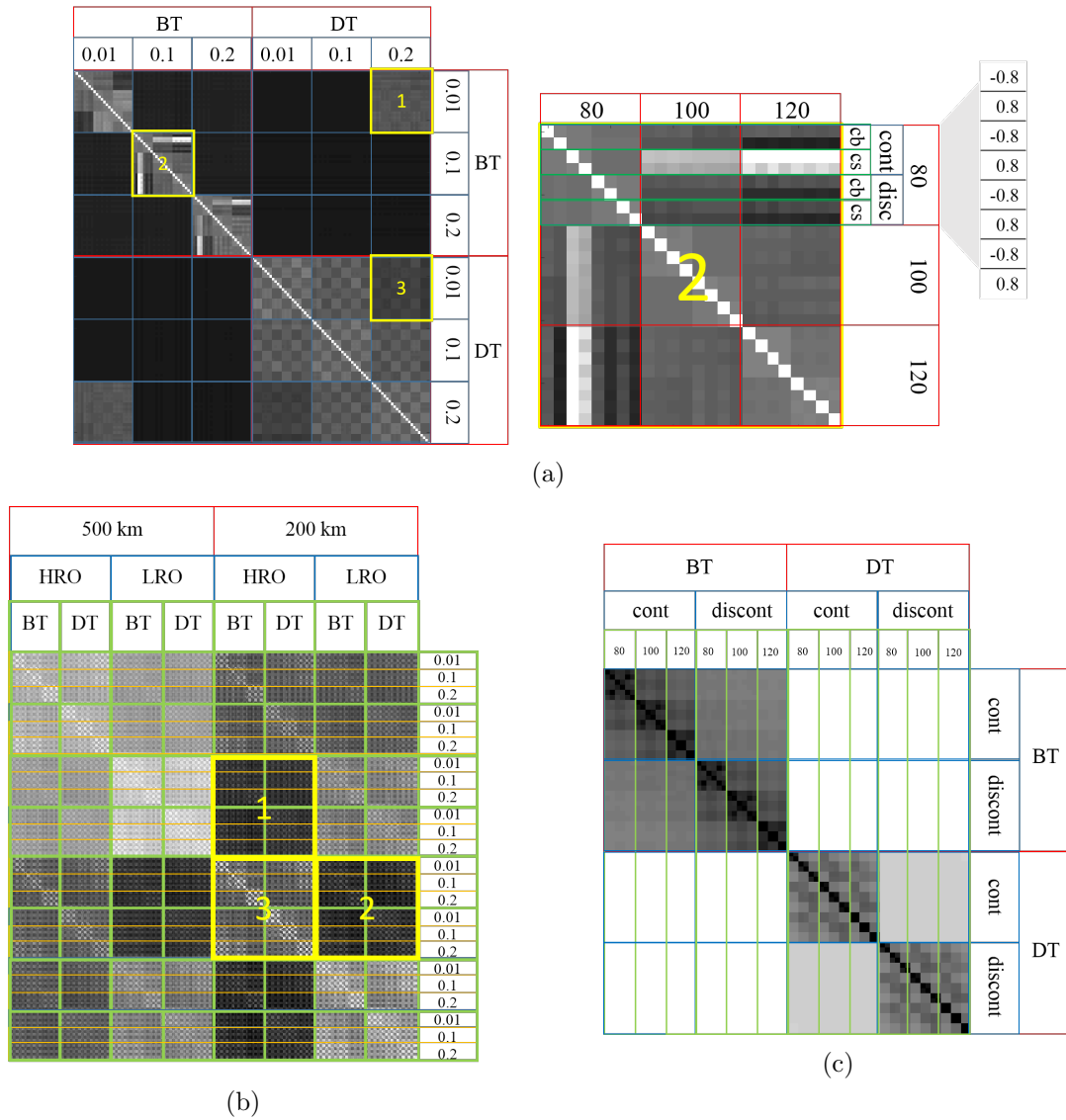


Figure 5.9: Example of similarity matrices generated from the pedestal crater database: (a) the Mutual Information similarity matrix of the real part of the geo-electrical models of P1 (the image on the right is the magnification of the square labelled 2 in the left image), (b) the Correlation similarity matrix of the simulated radargrams of P2, (c) the Difference similarity matrix of the imaginary part of the geo-electrical models of P2.

the imaginary parts of the geo-electrical models, and between the simulated radargrams. Thus, we generate sixteen 144 x 144 and eight 576 x 576 similarity matrices. The acquisition variables are sorted such that the similarity matrix reveals visually interpretable patterns of the complex relationship between the hypotheses (Figure 5.3). In this section, we present some examples of the similarity matrices obtained for the RIME databases.

Figure 5.9(a) shows the similarity matrix for the real part of the geo-electrical models of the pedestal crater P1, computed using the MI measure. In this matrix, the geo-electrical variables are in the order $\{\overline{G}_1 = \text{Impf}, \overline{G}_2 = \text{Vfn}, \overline{G}_3 = \text{Ts}, \overline{G}_4 = \text{Str}, \overline{G}_5 = \text{Th}, \overline{G}_6 = \text{Cntr}\}$. In this case, the impurity profile appears to be the dominant variable, i.e. the real permittivities in the BT are very different from those in the DT. Within the bright terrain, the void fraction is dominant, represented by the bright cells along the diagonal and the dark cells off-diagonal. However, within the DT, the effect of void fraction is less prominent and the similarity decreases gradually away from the diagonal.

The similarity matrix also reveals combinations of hypotheses that compensate the effect on the real permittivity. The yellow cells 1 and 3 represent an example of such compensation. On the one hand, cell 1 corresponds to different impurity profiles (BT and DT), and different void fractions (0.2 and 0.01). On the other hand, cell 3 corresponds to different void fractions, while the impurity profile is the same. Intuitively, one may think that similarity values in cell 3 are higher than the cell 1, but we can observe that the reverse is true. This occurs since higher porosity leads to lower permittivity, while higher impurity (in case of DT) leads to higher permittivity of the ice, thus compensating the value of the effective permittivity. A careful examination of the similarity matrix reveals complex interdependence between the different hypotheses. The image on the right of Figure 5.9(a) shows the magnification of the cell 2, representing the hypotheses of BT, with a void fraction of 0.1. We can see that the surface temperature is a non-dominant variable. However, the structure and the scale height are dominant for certain combinations of the other variables, at different surface temperatures. Such information from the similarity matrices has important implications in the inversion of the underlying geology. For illustration, let us consider two pedestal craters occurring in the BT, one in the polar regions ($T_s = 80$ K) and one in the mid-latitudes ($T_s = 120$ K). Let us assume that from the acquired radargrams, the permittivities corresponding to the two scenarios are extracted and the MI between the real permittivities is found to be very high. Using the similarity matrix we can infer that the pedestal crater in the polar region has a continuous structure, the scale height corresponds to constant base temperature, and the void fraction is high (0.1 - 0.2).

Figure 5.9(b) shows the similarity matrix for the simulated radargrams of the pedestal crater P2, computed using the COR measure. In this matrix, the acquisition variables

are in the order $\{\bar{V}_1 = H, \bar{V}_2 = B, \bar{V}_3 = \text{Impf}, \bar{V}_4 = \text{Vfn}, \bar{V}_5 = \text{Ts}, \bar{V}_6 = \text{Th}, \bar{V}_7 = \text{Str}, \bar{V}_8 = \text{Cntr}\}$. The matrix is noisier than the previous one, due to the complex relationships between the different variables and the radar response. As expected, the instrument parameters are the dominant ones, since they are designed to facilitate the acquisition of more informative radargrams. The interpretation of the effects of the instrument parameters is obvious, and thus we use this as a means to qualitatively validate the proposed approach. For example, the cell 1 represents the pairs of radargrams corresponding to spacecraft height 200 km and bandwidth 2.8 MHz, and spacecraft height 500 km and bandwidth 1 MHz. These pairs have significantly low correlation, whereas the complementary pairs (1, 200) and (2.8, 500) have a higher value of correlation. This is in agreement with the expectations, since the radargram quality is enhanced at higher bandwidth (2.8 MHz) and lower altitude (200 km), while the quality is significantly degraded at lower bandwidth (1 MHz) and higher altitude (500 km).

The yellow cell 2 shows that at 200 km altitude, bandwidth is strongly dominant, possibly because the SNR is much higher, thus enhancing the effect of the resolution. Within the HRO mode other hypotheses are relatively more dominant compared to within the LRO mode. This is justified since the shallow reflectors of the pedestal craters require higher range resolution to be detected. The variations within the yellow cell 3 represent the effect of the geo-electrical variables. The dominant geo-electrical variables inferred from Figure 5.9(a), i.e. impurity profile and porosity, are also dominant in cell 3, and the compensation at the off-diagonal corner is also observed. However, compared to the real part of the geo-electrical models, the impurity profile has less impact on the similarity between the simulated radargrams.

Figure 5.9(c) shows the similarity matrix for the imaginary part of the geo-electrical models of the pedestal crater P2 computed using the Difference measure. In this matrix, the geo-electrical variables are in the order $\{\bar{G}_1 = \text{Impf}, \bar{G}_2 = \text{Str}, \bar{G}_3 = \text{Ts}, \bar{G}_4 = \text{Vfn}, \bar{G}_5 = \text{Th}, \bar{G}_6 = \text{Cntr}\}$. The darker values (lower DIF) correspond to higher similarity. In this case, the impurity profile is a dominant variable. Irrespective of the other variables, changes in the impurity profile significantly affect the imaginary permittivity values. Furthermore, within the BT, surface temperature is also a dominant variable. Since the BT is composed of relatively pure ice, the imaginary permittivity has strong dependence on the temperature profile. On the other hand, within the DT, structure is a dominant variable. Since the impurity profile of the DT changes rapidly with depth, the effect of structure on depth is dominant on the DT imaginary permittivity.

Similarity analysis using variable significance (quantitative results)

We estimate the variable significance score as the average similarity between pairs of hypothesis vectors differing only in the variable of interest, based on (5.13), and (5.11).

Table 5.5: Estimation of variable significance using similarity analysis

Similarity measures			Ts	Th	Vfn	Impf	Str	Cntr	B	H
COR	GEO- REAL	P1	1.00	1.00	0.99	0.99	0.98	0.95		
		P2	1.00	1.00	0.99	0.99	0.98	0.92		
	GEO- IMAG	P1	1.00	1.00	1.00	0.97	0.99	1.00		
		P2	1.00	1.00	1.00	0.93	0.99	1.00		
	SIM	P1	0.97	0.99	0.87	0.85	0.85	0.80	0.73	0.88
		P2	0.98	0.99	0.84	0.81	0.79	0.83	0.74	0.84
SSIM	GEO- REAL	P1	1.00	1.00	0.99	0.98	0.95	0.94		
		P2	1.00	1.00	0.99	0.98	0.96	0.94		
	GEO- IMAG	P1	1.00	1.00	1.00	0.98	1.00	1.00		
		P2	1.00	1.00	1.00	0.98	0.99	1.00		
	SIM	P1	0.92	0.98	0.64	0.59	0.60	0.59	0.24	0.73
		P2	0.94	0.99	0.53	0.47	0.50	0.64	0.23	0.65
MI	GEO- REAL	P1	0.85	0.97	0.46	0.19	0.79	0.98		
		P2	0.95	0.96	0.52	0.16	0.41	0.68		
	GEO- IMAG	P1	0.89	0.98	0.91	0.13	0.70	1.00		
		P2	0.89	0.98	0.92	0.11	0.65	1.00		
	SIM	P1	0.82	0.97	0.40	0.37	0.31	0.61	0.15	0.46
		P2	0.86	0.99	0.33	0.28	0.32	0.45	0.12	0.50
DIF	GEO- REAL	P1	0.01	6E-4	0.3634	0.5418	0.8073	1.6		
		P2	0.012	8E-4	0.3634	0.5418	1.3009	1.6		
	GEO- IMAG	P1	5E-6	2E-7	7E-6	0.0023	1E-4	0		
		P2	5E-6	2E-7	7E-6	2E-3	1E-4	0		
	SIM	P1	40	15	54	56	59	63	60	55
		P2	44	20	62	64	75	68	65	65

Table 5.5 reports the estimated values of the variable significance for the RIME acquisition variables, for the real and imaginary parts of the geo-electrical models and the simulation databases of the pedestal craters P1 and P2.

Note that the variable significance is nearly consistent between the two pedestal craters. Moreover, there is consistency between the variable significance estimates obtained from the geo-electrical models and the corresponding the simulated radargrams. This confirms that the method is producing reliable results. Among the variables, surface temperature and scale height are the least significant, and result in very similar geo-electrical models, and therefore simulated radargrams. This is true for all the similarity measures, thus indicating that these two variables have low significance in terms of the effect of shape, size and relative intensities on the simulated radargrams and the geo-electrical models.

The bandwidth, impurity profile, contrast and structure have higher variable significance in terms of the simulated radargrams. Contrast and structure depend on the pedestal geometry, thus resulting in differing variable significance for P1 and P2, particularly using the MI measure. Void fraction and the temperature profile have negligible effects on the shape (SSIM) and skeletal structure (COR) of the imaginary permittivity, and thus they are also not significant for the simulated radargrams, when compared to the impurity profile.

5.5.3 Discussion

The selected target, i.e. the pedestal craters, represents a class of shallow distributed subsurface scatterers. These targets are important for understanding the formation of unique geomorphologies on the icy moons. The results of the performance analysis indicates that the subsurface response from the pedestal base is detectable in all the considered acquisition scenarios. Analysis of RIME sensitivity to the dielectric contrast indicates that the surface power is more sensitive to small changes in the value of the contrast, as compared to the subsurface power. The sensitivity is also dependent on the morphology of the pedestal craters. Analysis of the radargram features revealed that surface to subsurface time can be used to distinguish the void fraction and the impurity profile. The surface SNR and the surface to subsurface power ratio can distinguish the interface dielectric contrast.

The similarity matrices indicate that the composition (impurity profile, contrast and void fraction) and the structure are dominant, while the temperature profile is a non-dominant variable. The matrices also show the compensation effect of different hypotheses, resulting in very similar geo-electrical models or simulated radargrams. Further, complex relationships between different variables can be interpreted, such as within the BT the hypotheses of void fraction and scale height are invertible, if we can constrain the surface temperature and the structure using other ancillary datasets. Thus, the similarity matrices can provide means for cross-validating and synergizing the information derived from different instruments on-board the JUICE. Analysis of variable significance further confirm that surface temperature and scale height are the least significant variables, whereas impurity profile and structure are more significant ones. Analogs for the deeper targets, such as the putative subsurface ocean or shallow brine lenses are difficult to find within areas covered by existing RSs, since such targets are unique to the icy moons. For the analysis of these deep and unique targets, the electromagnetic simulators are more useful.

5.6 Conclusion

In this chapter, we have presented an approach to the generation and analysis of a database of RS responses. The proposed approach is based on: (i) selecting a target of interest, (ii) defining the possible scenarios during acquisition over a given target, (iii) generating databases of geo-electrical models and simulated radargrams corresponding to the various acquisition scenarios, and (iv) analyzing the generated databases. The databases can be analyzed in a number of ways, depending on the goal of the study. We have described three main analysis techniques: (a) similarity analysis (to understand the net effect of combinations of different hypotheses on the geo-electrical models and the simulated radargrams), (b) performance analysis (for testing the detectability of the subsurface response), and (c) feature analysis (for testing the ability of the radargram features to discriminate different hypotheses of the acquisition variables).

The proposed approach is adaptive to modifications in the acquisition variables, the hypotheses, the choice of the simulation technique, the performance measures, the features and the similarity measures. It can be used for any RS mission at any stage of its development. During the RS design phase, the method can be used to support the definition and selection of the RS parameters. A database can be created by considering a range of feasible instrument parameters and the target properties we are interested to detect. Then the performance analysis can be conducted on the database to identify the best parameters that satisfy the scientific requirements of the mission for the majority of the target hypotheses. During the mission phase, the proposed approach can be used for planning operations, by choosing the right combinations of programmable parameters for each specific target. This can be done by analyzing the similarity matrices for different targets.

During the post-acquisition phase, the database can be used for supporting the inversion of the acquired radargrams. The underlying hypothesis vector corresponding to the acquired radargram can be retrieved by querying into the database using content based image retrieval techniques (e.g. [40]). This can be done by matching the acquired radargrams with the simulated radargrams, using appropriate similarity measures selected using the similarity analysis. After successful completion of the mission, in the data archiving phase, this method can be used for managing and organizing archives of available data.

During the scientific interpretation and data analysis phase, the proposed approach can support the development of automatic interpretation algorithms. Currently there are numerous techniques for automatic interpretation of subsurface targets using radargram features. These features can be used as the feature extraction functions $Feat()$ in the proposed analysis for supporting the adaptation of the existing algorithms to the data from the new RS mission.

We have presented an application of the proposed method to a selected RIME target (pedestal crater) on the Jovian moon Ganymede using the analog-based simulation approach. Two different pedestal crater morphologies are considered to understand the consistency of the approach for the interpretation of different targets of the same type. The created database of geo-electrical models and simulated radargrams revealed interesting relationships between the geophysical hypotheses and the RIME response. The database was also used to estimate the RIME detection performance and sensitivity to changes in the dielectric contrast at the subsurface interface. The results are very promising and demonstrate the usefulness of the proposed approach to systematically provide valuable information for supporting RS missions.

Currently we are applying the proposed approach to a long-term development of an extensive database of RIME responses, representing all the interesting targets within the RIME coverage and scientific objectives. This include many other targets modeled using i) different simulators in tandem, ii) other geological and geophysical hypotheses relevant to the Jovian moons, iii) the incorporation of the Jovian noise and surface clutter in the analysis of the RIME performance, and iv) the analysis of the discriminability of other radargram features.

**Part III: Performance assessment of
future radar sounder missions**

Chapter 6

Performance assessment of RIME: subsurface sounding of the Jovian icy moons

The Jovian icy moons show evidences of unique tectonic structures that can reveal significant information about the characteristics of their ice-shells. Subsurface data acquired by RIME is expected to resolve the geological and geophysical properties of these unique features. This chapter¹ presents the performance assessment of RIME in detecting subsurface targets on the Jovian moon Ganymede, in particular the geophysical profiles of the dark terrain and the bright terrain, and the brittle-ductile interface below the grooved bright terrain. To analyze the radar response of these complex targets, we exploit the capability of the FDTD simulator in dealing with 3D geo-electrical models. A novel contribution of this application is the multi-level interpretation of complex target geometries, i.e. by analyzing both the radar response of individual components of the model and that of their realistic spatial arrangement.

6.1 Introduction

Subsurface investigation of the Jovian icy moons is expected to disclose interesting information on the Jovian system. To provide a key for interpretation for the real acquired data, simulations of different possible scenarios on Ganymede are necessary. Most simulations studies consider targets with significant dielectric contrast. However, many geological targets on Ganymede are expected to appear as distributed subsurface scatters

¹Part of this chapter appears in Sbalchiero, Elisa, Sanchari Thakur, and Lorenzo Bruzzone. "3D radar sounder simulations of geological targets on Ganymede Jovian Moon." Image and Signal Processing for Remote Sensing XXV. Vol. 11155. International Society for Optics and Photonics, 2019.

that contribute to volume scattering in the radargrams.

An interesting target representing diffused basal scattering is the pedestal crater, in which the base represents the ejecta deposited over the area surrounding the impact site. In Chapter 4 and 5, we have briefly presented applications of the proposed approaches to the simulation and performance assessment of RIME, considering the pedestal craters on Ganymede as the target of interest. The analog-based simulation was used in both the cases. In presenting the case studies, we have briefly introduced the principal geophysical models of Ganymede, which depend on the two globally identified terrain types, i.e. the bright and the dark terrain. Moreover, the effect of the temperature profile on the geo-electrical models, and therefore on the simulated radar response was found to be negligible. However, the pedestal craters represent a class of shallow targets, for which a large variation in the geophysical profiles is not expected. In fact, none of the existing RSs have achieved a penetration depth of 9 km that RIME aims to achieve, primarily due to the inhibiting conditions on their target planetary bodies. In this context, the analysis of the impact of the geophysical profiles on the RIME radar response needs to be studied using electromagnetic simulators that allow more flexibility in modeling the target.

Another aspect of the Ganymede targets is that many of them are unique to the icy moons, and thus their geological analogs have not been found or not previously detected by RSs. An example of such an important subsurface target is the brittle-ductile interface (BDI), which is expected to be present below the grooved bright terrain and represents the transition between brittle ice on the top and ductile ice below. The BDI is characterized by a set of sub-parallel normal faults of thickness that is much smaller than the RIME wavelength. The inclined geometry, the sub-parallel nature and the low contrast between the fault-fill and the background ice makes it difficult to intuitively understand their radar response, and therefore to interpret these targets from the radargrams. The 3D compositional and structural variations in the grooved bright terrain faults cannot be represented accurately using a multi-layered model, thus making the MRS simulator less suitable for this application.

To this end, the FDTD based volumetric 3D simulations are found to be the most suitable approach to the simulation of the RIME response to the BDI and the variations in the geophysical profiles. A recent study has applied FDTD simulations to five global geo-electrical models of Ganymede, Callisto and Europa [68]. The study analyzed the subsurface detectability of (1) the grooved bright terrain and the furrow system of the dark terrain on Ganymede, (2) the double ridges and the chaos terrain on Europa, and (3) the knobs on Callisto.

In this chapter, we present an approach to the performance assessment of RIME based on 3D modeling, followed by electromagnetic simulations of selected icy moon targets

using the FDTD simulation technique. This analysis is an extension of the study presented in [68] to further support the RIME data interpretation by analyzing interesting tectonic RIME targets on Ganymede, in terms of the detectability of expected subsurface features. In particular, we define an approach to analyze the target models at two levels. First, the contribution of individual features is analyzed, varying their geometry and composition to understand how the measured fields vary accordingly. Second, a more realistic geological arrangement of a combination of subsurface features is considered. The Ganymede targets analyzed are: 1) the dark terrain regolith, 2) the bright terrain dielectric profile up to 9 km, and 3) the grooved bright terrain. For the grooved bright terrain characterized by the domino-style tilt-block faults, the radar response is expected to reveal the BDI. Thus, in this case, we analyze the detectability of the faults, first at an individual level, and then considering the full model of the grooved bright terrain.

The chapter is organized as follows. Section 6.2 describes the experimental setup of the FDTD simulations, focusing on modeling the simulation inputs and simulating the RIME radargrams. Section 6.3 presents the experimental results and their interpretation for the selected RIME targets. Finally, Section 6.4 discusses the implications of the simulation results on the detection performance of RIME.

6.2 Methodology for performance assessment

Figure 6.1 summarizes the main steps of the simulation workflow used in the proposed approach. The first step is to define the geological and geophysical characteristics of the target models. These are then translated into the geometry and dielectric properties defining the geo-electrical models to be simulated. The other inputs to the simulator include the instrument parameters of RIME. In the next step, we setup the FDTD simulator according to the definition of the inputs. Since FDTD is not a conventional RS simulator, the general setup needs to be adapted to simulate RS radargrams. Finally, the electric field computed by the simulator is processed to obtain the simulated radargrams. These steps are described as follows.

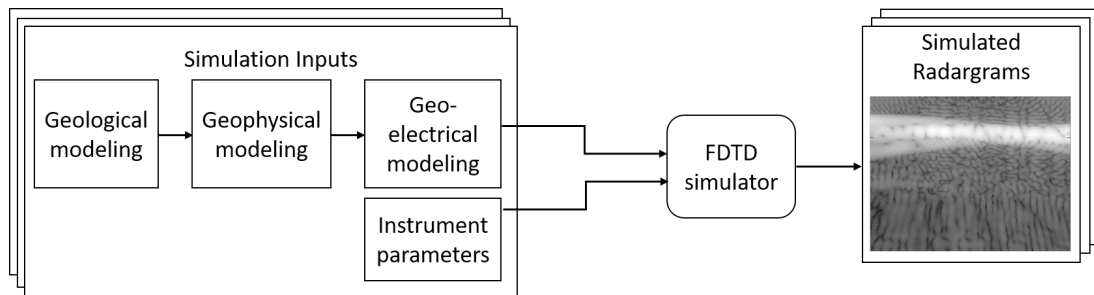


Figure 6.1: Flowchart of the FDTD simulation workflow for the performance assessment of RIME.

6.2.1 Target geo-electrical modeling

Geological hypotheses

Figure 6.2 shows an image of three common geological terrains on Ganymede characterized by different geometries, brightness and therefore, inferred to have different stratigraphic ages and possibly tectonic histories. The dark terrain (DT) occurs over one-third of the surface and is characterized as a dust-rich, heavily cratered and furrowed ancient region, which appears dark in the optical images. This region is divided and cross-cut by relatively younger and ice-rich swaths of the bright terrain (BT), which are about 10 - 100 km wide, having a bright appearance. The formation of the two terrains could be explained by a range of possible tectonic and volcanic models, supported by evidences of complex extensional features [111].

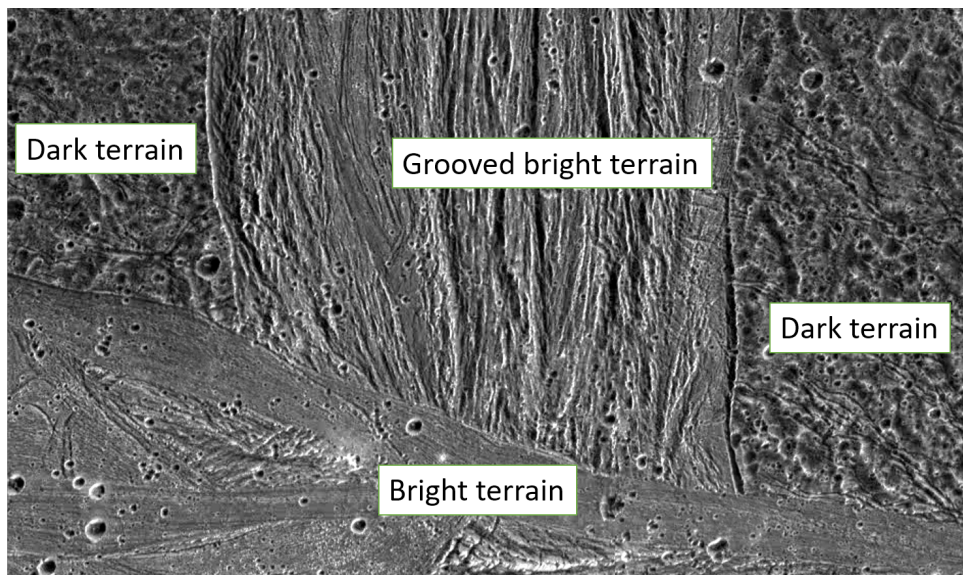


Figure 6.2: Galileo image of Ganymede showing the dark terrain cross-cut by swaths of the smooth and the grooved bright terrain. (Image credit: NASA/JPL)

The DT is composed of a thin dust-rich dark layer overlaying an ice-rich basal material. RIME can provide direct evidence of the presence of this thin regolith layer by detecting the dielectric discontinuity representing the transition from the dust-rich to the ice-rich basal material. The BT is expected to be formed by tectonic evolution of the DT, followed by further tectonic or volcanic resurfacing of the fractured crust.

Within the bright terrain, two types of geometries are observed: (1) lanes of very low surface roughness (indicated by the label 'Bright terrain' in Figure 6.2), (2) relatively rougher wide swaths comprising of linear sub-parallel structures (indicated by the label 'Grooved bright terrain'). The grooved bright terrain is characterized by multiple super-imposed wavelengths of deformation, and hundreds of kilometers of alternating ridges and

troughs, possibly caused by a tilt-block style of normal faulting. These perhaps represent fracturing in the brittle ice-shell. Therefore, the concurrent depths of the tilt-block faults can be used to infer the relic depth to the BDI [111]. These faults could be detected in RIME radargrams as a diffused reflection near the BDI.

In order to study these geological hypotheses, we have selected some interesting targets on Ganymede for understanding their detectability by RIME. These are listed in Table 6.1. The first hypotheses considers two simple models for the DT regolith and the BT in order to study how significant is the effect of the variation of dielectric properties on the radar response. The second hypothesis considers the grooved bright terrain at two levels: (1) contribution of individual faults, varying their geometry and composition, to understand how the measured fields vary accordingly; and (2) combined response of a set of tilt-block faults, to understand the detectability of the BDI.

Table 6.1: Proposed analysis for the RIME test cases of the geological features on Ganymede. The parameters of the baseline test case used as reference for the individual fault comparison are highlighted in bold.

Geological feature	Hypothesis tested	Value
Dark terrain regolith	Regolith thickness	[50,100] m
Bright terrain	Dielectric profile	Varying with depth Constant
Grooved bright terrain	Individual faults: dip angle thickness composition geometry	[30, 60] [°] [3 ,6] m 20%void , 100% void planar , listric
	Full brittle-ductile interface	[60 [°] , 3m, 20% void, planar geom- etry]

Here, we consider three important structural properties of faults that can influence their radar response: (1) the dip angle, (2) the thickness, and (3) the geometry, as shown in Figure 6.3. The dip angle determines the orientation of the fault with respect to the horizontal. The thickness of the fault determines the detectability by the radar at the wavelength of the signal and the vertical resolution in ice. The two common normal fault geometries, planar and listric considered here, also determine the orientation of the interface with respect to the radar. The full-scale grooved bright terrain model is of particular interest, since the complex interaction of a block of normal faults may reveal the BDI in the RIME radargrams, which may be not exposed from individual fault responses.

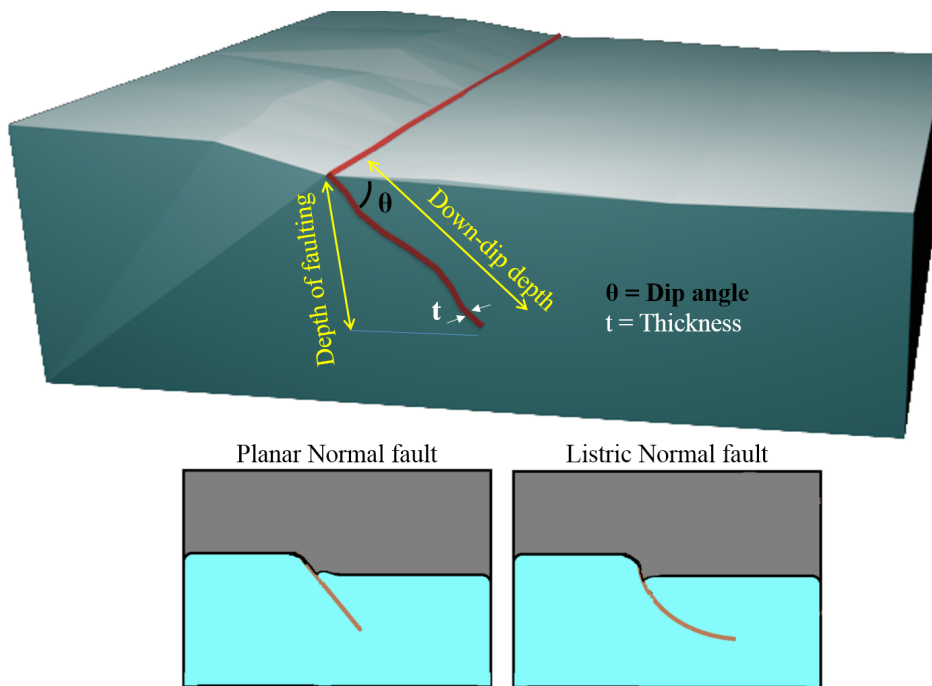


Figure 6.3: Grooved bright terrain: geological models of the faults, showing the parameters defining the hypotheses and the two fault geometries considered.

Geophysical hypotheses

In this analysis, we consider the three main properties of Ganymede's BT and DT, i.e. temperature, void fraction and impurity profiles, which were described in the RIME case study presented in Chapter 5. In this case, we consider a geothermal profile having a base temperature of 130 K and the surface temperature of 120 K [68], as shown in Figure 6.4(a). The void fraction is taken as 0.1 and is assumed to be constant with depth, due to the low temperature variation in the ice-shell of Ganymede. Figure 6.4(b) reports the impurity profiles (modeled assuming a sigmoidal curve) in terms of dust-mass fraction and note that the dust is particularly relevant in case of the DT. We define the thickness of the regolith as the depth at which the impurity profile drops below half of its maximum value. We assume two hypotheses on the thickness, i.e. 50 m and 100 m. Below the regolith cover, the DT profiles follow the quasi-linear decreasing trend of the BT impurity profile. These geophysical models are translated into the complex geo-electrical models. In particular, the complex permittivity of pure ice, derived using Debye's equations, is combined with impurities using the Rayleigh multiphase mixing formula for spherical scatterers [68].

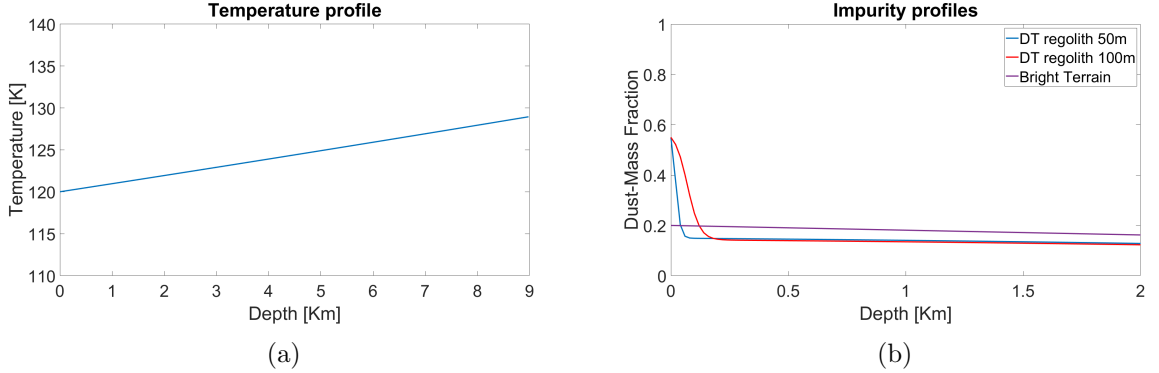


Figure 6.4: Geophysical profiles of Ganymede: (a) temperature profile, (b) impurity profile.

Geo-electrical models

For the DT, we studied two simple models discretized as flat layers having thickness of 20 m. The discretization step has been chosen in order to represent the small regolith thickness (50 m and 100 m). The resulting real permittivity varies in the range 2.8 - 3.63, as it can be noticed in the models reported in Figure 6.5(a). The corresponding imaginary permittivity varies in the range 0.8×10^{-4} - 3.3×10^{-3} . The thickness of the regolith decides how rapidly the permittivity values decrease with depth in the two different cases.

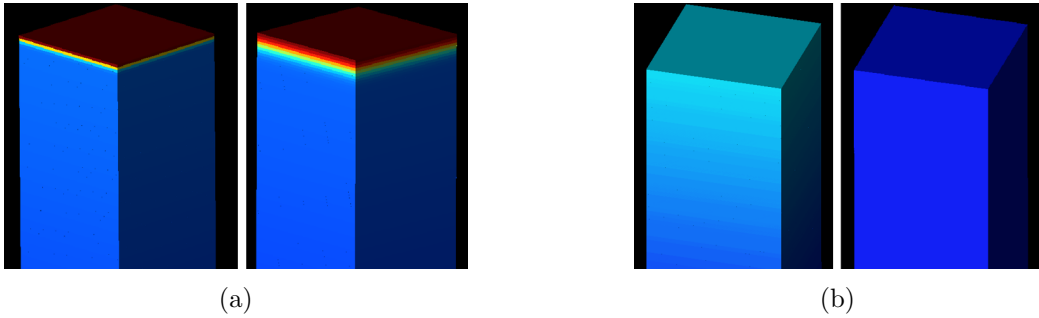


Figure 6.5: 3D geo-electrical models of Ganymede: (a) Dark terrain regolith with depth of 50 m (left) and 100 m (right), (b) Bright terrain layered (left) and constant dielectric profile (right).

To understand the overall effect of the gradual variation of both the real and imaginary permittivities in the BT, we tested it against the hypotheses of homogeneous ice dielectric permittivity. We simulated two simple cases for the BT, i.e. a gradually varying layered dielectric profile and a constant profile. Both models consist of a flat surface but for the first case the dielectric profile has been discretized into 100 m thick layers, while for the second case a single layer is considered. The obtained models are reported in Figure 6.5(b), where one can notice that the real permittivity assumes values in the range 2.8 - 3.09 for the layered profile, while the imaginary part varies in the range 1.6×10^{-4} -

1.09×10^{-3} . Note that the ice becomes increasingly transparent for radar penetration with increasing depth. For the alternate hypothesis of constant dielectric profile, we average the permittivity of the layered profile and obtain 2.9 for the real part and 6.18×10^{-4} for the imaginary one.

For the grooved bright terrain models, we generate the surface by the superposition of the topographic wavelengths, estimated from high resolution Galileo images [112]. The profile of the grooved terrain $A(x)$ is a function of the long and short topographic wavelengths (λ_L and λ_S , respectively), and the corresponding amplitudes (A_L and A_S , respectively). The surface topography can be formulated as:

$$A(x) = A_L \cos(2\pi x/\lambda_L) + A_S \text{square}(2\pi x/\lambda_S), \quad (6.1)$$

where the *square()* function generates a square wave, with a given periodicity. The topographic wavelengths are related to the deformational stresses and the mechanical properties of the crust at the time of deformation. Ideally, the real Ganymede surface is best described by considering multiple superimposed wavelengths. Hence, we add the contributions of a number of long and short wavelengths to define a realistic grooved bright terrain surface. The tilt-block faults of 1 meter depth and a given thickness, dip angle and composition are added to the grooved terrain at the edge of the grooves. For the full-scale model, the fault properties are randomly selected assuming a Gaussian distribution centered around the hypothesis value. A profile representation of the full grooved terrain model is shown in Figure 6.6.

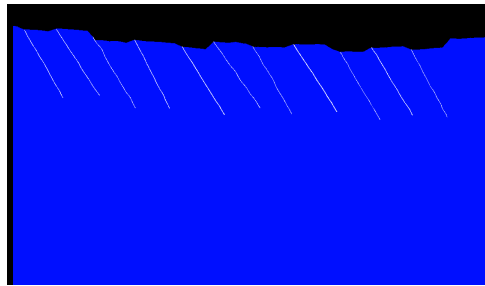


Figure 6.6: Model of full grooved bright terrain with BDI

The first subsurface feature we consider is the individual fault. In order to isolate the effect of the fault geometries, the shallow ice-shell was modeled using a uniform dielectric permittivity, as previously defined for the constant BT profile. The faults are assumed to be composed of 20% voids in a host material of pure ice, resulting in $\epsilon = 2.5851 + j1.0747 \times 10^{-14}$. The hypothesis of fault made of pure void space (i.e. 100% voids) has also been tested for comparison. Also for the full grooved bright terrain we consider a homogeneous ice-shell, with faults composed of 20% voids in a host material

of pure ice.

In all the models, a random roughness, with mean height 50 m, is added to all the flat faces. For the individual faults analysis, we define a baseline case which is used as reference for the comparison with the other cases. Moreover, to identify the contribution of the subsurface, for each model we also simulate a *cluttergram*, i.e. only the surface model without the subsurface features.

6.2.2 FDTD simulation approach

As briefly introduced in Section 3.3.2, the FDTD method is based on the solution of Maxwell's equation in the time domain. With this technique, the simulation space is discretized into Yee cells [158] and accordingly, time is discretized into timesteps, where one timestep is the time needed for the wave to travel inside a single cell. Each cell is assigned with a material defined in terms of complex permittivity. The electric and magnetic fields are computed at each cell location by solving the Maxwell's equations. It is therefore clear that the accuracy of the computation depends on the size of the cells. First, the cell size is chosen according to the scenario under investigation and should strictly be at least one-tenth of the smallest wavelength in the medium. For the models considered in this analysis, we use a uniform cell size of 1.5 m, which satisfies the constraint for both the bright and the dark terrain, and results in a timestep equal to ~ 2.89 ns.

Simulation space

The collection of all the Yee cells defines the simulation grid. The across-track dimension of the simulation space is fixed at 120 m for all the models. This is justified since the model does not vary in the across-direction for the cases studied here. Instead, the along-track dimension varies depending on the test case. For the simple models of DT and BT, we are interested in understanding the power loss as a function of the permittivity, which is only varying with depth. Thus, the along-track dimension is set to a relatively small value of 600 m. For the individual fault analysis, the along-track dimension is chosen as 2.7 km, to guarantee that the faults are within the grid boundaries. For the full-scale models, we simulate 6 km along-track dimension to account for a more realistic arrangement of the features. The simulation space includes 3 km of free space above the surface of each model. Moreover, in order to avoid artefact reflections coming from the bottom of the simulation grid, the depth of the simulation space is taken to be larger than the depth to be analyzed. This ensures that the artefact echoes will not interfere with the subsurface feature of interest. The simulation time is set in order to stop the simulation before the collection of such artefacts.

Boundary conditions

Artefacts may arise in the outer boundaries of the simulation space because field values at each cell depend on neighboring field values and at the boundaries they may be incorrectly calculated. The discontinuities all around the simulation space are seen as real interfaces and result in reflection of the propagating wave. To avoid these phenomena the employment of boundary conditions becomes a powerful instrument to reduce simulation noise. For this work, ten Perfectly Matched Layers (PML) are used as boundary conditions. A PML is an artificial layer, placed at all outer boundaries of the simulation grid, and acts as an absorbing material. Increasing the number of PMLs increases the absorption on the outer boundaries, at the expense of an increase in the memory requirement for the simulation. The number of PML layers should be set to at least ten [129].

External Excitation

We consider the wave incident to the surface as in far field and thus we chose a plane wave as the external excitation in the simulations, polarized in the along-track direction. The waveform of the external excitation is based on the RIME linear frequency-modulated chirp. For the simulations, we use a compressed and shortened chirp of $12 \mu s$ pulse-width, instead of the actual RIME chirp of $100 \mu s$ pulse-width. This choice drastically reduces the computation time required for the simulation. Figure 6.7(a) shows the waveform used for the simulation in the time domain, while Figure 6.7(b) shows its spectrum compared to that of the actual compressed RIME chirp. Note that the spectrum are same up to a power level of -60 dB, below which the simulation waveform has higher sidelobes.

In order to validate our choice, we carried out simulations with the actual RIME chirp and with the simulation waveform compressed chirp. The two cases produced similar results in terms of correct position of the subsurface echo and its power level with respect to the surface echo.

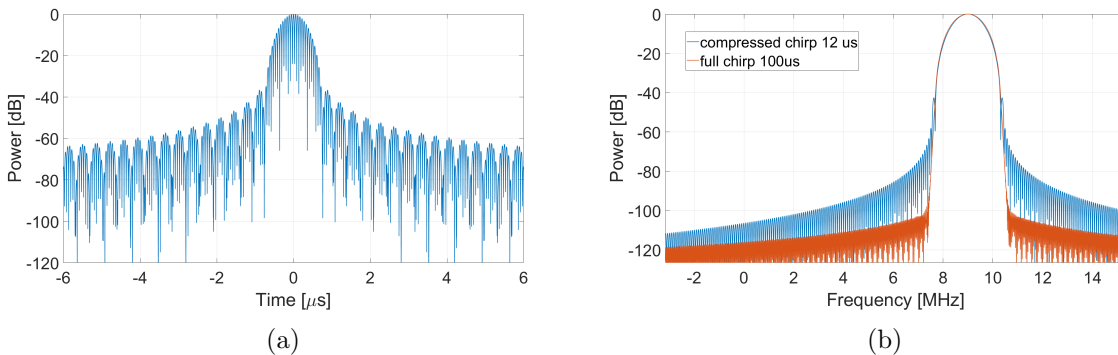


Figure 6.7: Input RIME waveform for FDTD simulations: (a) the compressed chirp with $12 \mu s$ pulsewidth, 3 MHz bandwidth and modulated at 9 MHz, (b) spectrum of the compressed chirp.

Solution of Maxwell's equations

The solution of Maxwell's equations through FDTD can be performed with two techniques depending on the field formulation, i.e. the pure scattered field formulation or total/scattered field formulation. With the first method, scattered fields are computed over the entire simulation space, while with the second method the simulation space is subdivided into two regions: an internal one, where total fields are computed, and an external one where only the scattered ones are estimated. The boundary between the two regions is located eight cells from the boundaries of the simulation space. The total/scattered field formulation should be preferred when working with user-defined waveforms, as in our case, in order to obtain correct results.

Receivers

To simulate the behaviour of the spacecraft motion, we sample the total electric field at each timestep using near-zone point sensors placed at ~ 2 km above the surface, with 10 m along-track spacing between them. When sampling the total field, the point sensors measure both the transmitted wave and the reflected one. This means that the round-trip time from the sensors to the surface should be larger than the pulse-width of the transmitted waveform, in order to separate the transmitted and the reflected fields. Note that we did not place point sensors within 15 cells from the grid boundaries, in order to not sample the field in the boundary region and to keep some margin from the boundaries.

Radargram formation

Once the simulation is completed, we create the simulated radargram by concatenating the signal acquired by the point sensors. Since we are interested in analyzing the backscattered signal, we consider the sampled signal from below the reflected surface echo, thus removing the transmitted wave and also some artifacts due to the boundaries of the simulation space. Then, the received signal is demodulated and normalized with respect to the surface echo. The radargram is obtained as a two-dimensional image in which each column represents the signal sampled by successive point sensors placed along-track.

In this method, we have the following assumptions:

1. Background noise is present in the actual acquisition but is not modeled here. This can be added to the simulated radargrams in post-processing.
2. For the simple models of DT regolith and BT dielectric profile, the effect of surface clutter is not accounted, since the objective is to study the effect of the dielectric variation.
3. The actual RIME antenna footprint is 2-10 km. However, due to computational constraints we use a smaller footprint.

- The simulated radargrams represent a far-field acquisition but not the actual platform altitude of RIME.

6.3 Experimental results

The results of the FDTD simulations are presented as follows. For the simple models of the DT regolith and BT dielectric profiles, we present the average simulated radar trace power normalized to the surface power as a function of depth. For the individual fault analysis and the full-scale models, we present both the average normalized radar trace power and the simulated radargrams. As described in Section 3.3.1, the power level of the sidelobes of the sinc defines the radar dynamic range (RDR), which is used as an indicator of detectability while analyzing the results. The RIME chirp has an RDR of -55 dB. Subsurface echoes that are below the RDR cannot be detected. In all the plots of the radar traces, the RDR is plotted as a horizontal green line.

6.3.1 Bright and dark terrain geo-electrical profiles

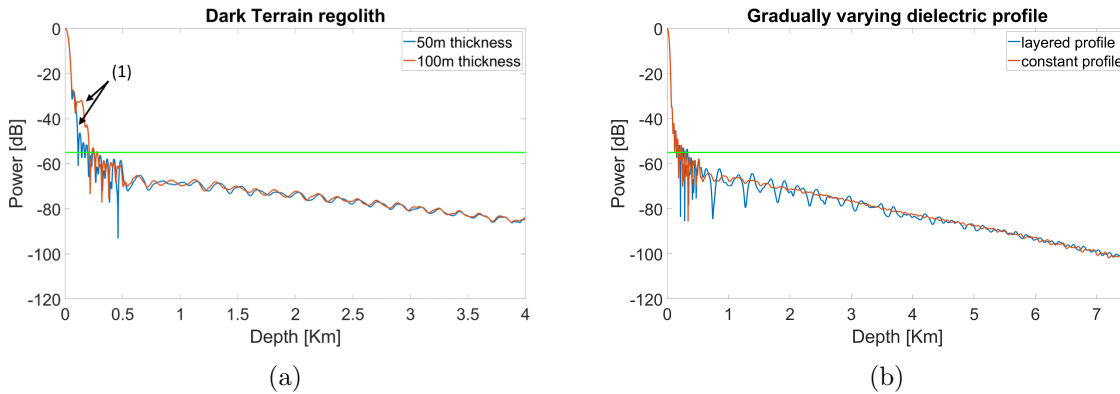


Figure 6.8: Simulated normalized radar trace power for the dark and bright terrains: (a) Dark terrain: regolith 50 m and 100 m deep, (b) Bright terrain: gradually varying layered and constant dielectric profile.

In Figure 6.8, the average normalized radar trace in both cases for the DT regolith models are reported. The two models represent different thicknesses of the regolith layer. We observe a sharp drop in power at the depth corresponding to the thickness of the regolith, indicated by arrows (1) in Figure 6.8(a). The reflections from the regolith layer are above the RDR. Thus, the presence of the regolith and its thickness can be detected from the RIME radar trace plots.

Figure 6.8(b) shows the normalized radar traces of the BT for the layered and constant dielectric profile cases. We observe that there is no significant difference between the two profiles. Previous RIME simulations considered layered profiles for the BT dielectric

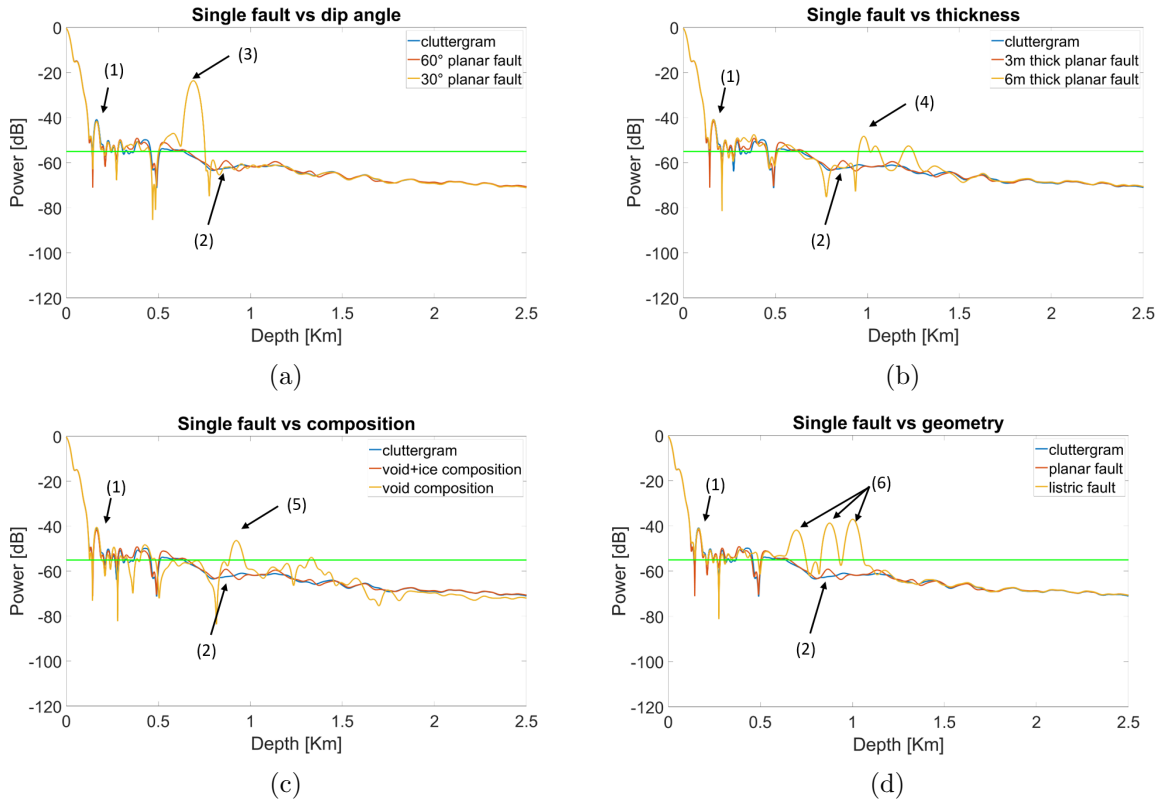


Figure 6.9: Grooved bright terrain - average normalized radar traces of individual fault under different hypotheses, compared to the cluttergram and the baseline case: (a) varying dip angles, (b) varying thickness of the fault, (c) varying composition of the material filling the fault, and (d) varying the geometry of the fault.

properties [68], thus making the models more complex. Our results show that the trend of the two profiles are similar, even though they differ at small scale. For analysis of the detectability of these geophysical variations, the layered representation can be useful. For the purpose of this work, the final goal is the detectability of the subsurface features. Thus, the BT dielectric profile can be assumed to be constant, for isolating the reflections from subsurface targets. Hence, for the subsequent simulations, we use the constant profile for the BT.

6.3.2 Grooved bright terrain: radar response of individual faults

For the grooved bright terrain, we first consider the different hypotheses of the individual faults reported in Table 6.1. Figure 6.9 shows the average normalized radar traces of the individual fault analysis, while Figure 6.10 shows the simulated radargrams. For understanding the effect of changing a hypothesis, we simulate the baseline case (plotted in red), while for discriminating the subsurface reflections from surface clutter, we

consider the cluttergram (plotted in blue). For the baseline case fault, the dip angle is 60° , the thickness is 3 m, the fault is composed of 20% void and 80% pure ice, and has planar normal geometry. The echoes indicated by arrows (1) in Figure 6.9 and Figure 6.10 appear to be the reflections from the surface and the off-nadir clutter. Figure 6.10(a) shows the cluttergram for all the cases. Arrow (2) in Figure 6.9 shows the weak echo response of the subsurface in the baseline case; the corresponding radargram is shown in Figure 6.10(b).

Figure 6.9(a) shows the effect of changing the fault dip angle from 60° to 30° , indicated by arrow (3). The 30° fault produces a stronger reflection with respect to the baseline case, since the low dip-angle faults are more orthogonal to the incoming plane wave, compared to the steeper 60° fault. This is also confirmed by arrow (3) in Figure 6.10(c). Since the fault dips to the right, the strong reflection is offset to the right of the radargram. This information can help in inferring the strike plane of the fault.

Figure 6.9(b) reports the effect of changing the thickness of the individual fault from 3 to 6 m, indicated by arrow (4). In this case, the subsurface feature produces a slightly stronger echo with respect to the baseline case. This is also confirmed in the simulated radargram of Figure 6.10(d), where the subsurface appears with a stronger echo power.

Figure 6.9(c) shows the effect of varying the composition of the individual fault from 20% to 100% of void, indicated by arrow (5). The subsurface echo is stronger with respect to the baseline due to the increase in dielectric contrast between fault and background. In this case, the subsurface echo is even stronger than that of varying thickness, meaning that composition can affect more strongly the received echo. Figure 6.10(e) shows this effect on the simulated radargrams. The high contrast between the fault material and the background ice results in the reflection indicated by Arrow (5), which is spread over many radar traces and time samples.

Figure 6.9(d) reports the effect of varying the geometry of the fault from planar normal to listric normal, indicated by arrow (6). The echo is strongly above the RDR, due to the geometry of the fault, which results in being almost orthogonal to the direction of propagation of the wave, causing a higher specular component. This is visible also in the simulated radargram in Figure 6.10(f), where the response of the fault is spread over different range positions due to the geometry of the fault. Averaging the power over different range lines results in multiple echoes at different range positions in the normalized radar trace seen in Figure 6.9(d).

Comparing all the cases, we see that the surface clutter level is not compromising the detectability of the subsurface echo. Except for the baseline case, the subsurface echo is above the RDR. In particular, the strongest echoes are collected in the 30° fault and the listric fault, indicating that the geometry of the target has strong effect on the radar

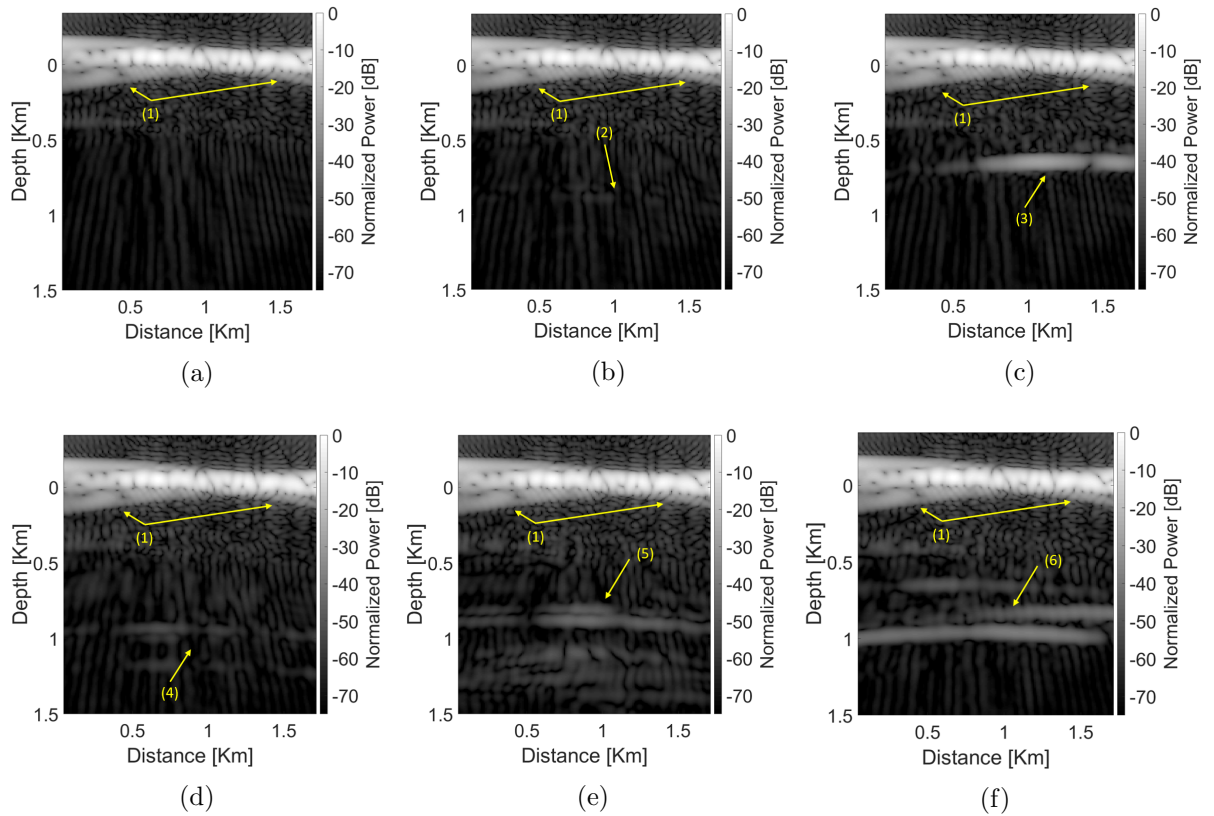
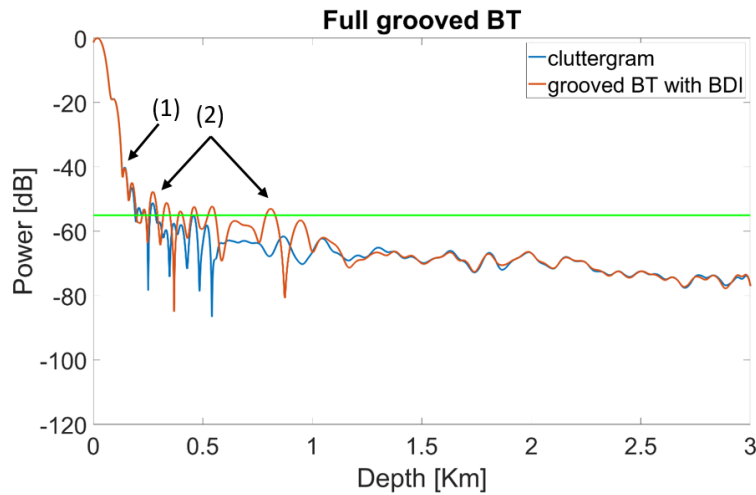


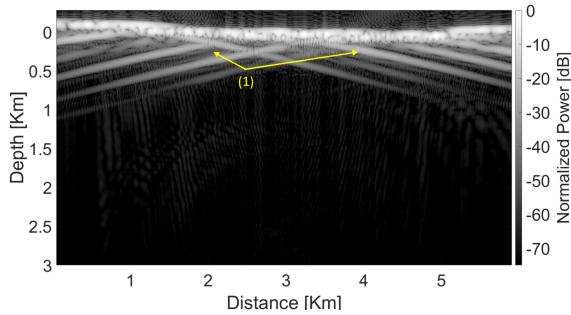
Figure 6.10: Grooved bright terrain - simulated radargrams of individual faults under different hypotheses (parameters different from the baseline case are pointed out in bold): (a) response of only the surface (cluttergram), (b) simulated radargram corresponding to geometry: planar normal fault; dip angle: 60° ; thickness: 3 m; composition: 20%void and 80% pure ice - **baseline case for faults**, (c) simulated radargram corresponding to geometry: planar normal fault; **dip angle: 30°** ; thickness: 3 m; composition: 20%void and 80% pure ice, (d) simulated radargram corresponding to geometry: planar normal fault; dip angle: 60° ; **thickness: 6 m**; composition: 20%void and 80% pure ice, (e) simulated radargram corresponding to geometry: planar normal fault; dip angle: 60° ; thickness: 3 m; **composition: 100% void**, and (f) simulated radargram corresponding to **geometry: listric normal fault**; dip angle: 60° ; thickness: 3 m; composition: 20%void and 80% pure ice.

performance. For faults with 60° dip angle, we see that the strongest detectable echo is produced with 100% void composition. For the ice-rich faults, a larger thickness produces a relatively stronger echo. The baseline case of 60° dip angle, 3 m fault thickness, 20% void composition and planar normal geometry produces the weakest echo, which is below the RDR.

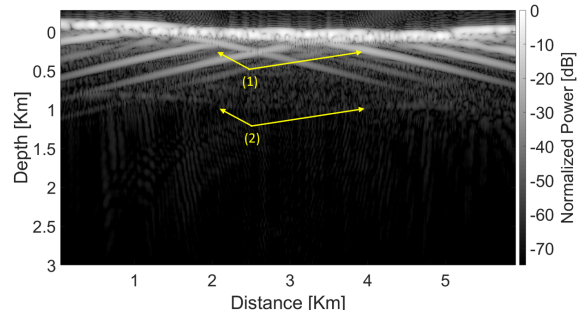
6.3.3 Grooved bright terrain: detectability of the brittle-ductile interface



(a)



(b)



(c)

Figure 6.11: Grooved bright terrain - FDTD results of the full model: (a) average normalized radar trace, (b) simulated cluttergram, (c) simulated radargram.

Figure 6.11 shows the effect of a realistic combination of individual faults, i.e. the full-scale grooved BT model. Figure 6.11(a) shows the average normalized radar trace of the cluttergram plotted in blue, while that of the full grooved BT is plotted in orange. The simulated cluttergram is shown in Figure 6.11(b), and the simulated radargram of the full model is shown in Figure 6.11(c). Arrow (1) indicates the surface clutter, which is present in both normalized radar traces, while arrows (2) indicates the subsurface reflection of

the BDI. The subsurface echo is slightly above the RDR. The contribution due to the BDI appears at a depth of 1 km below the surface, indicating the depth up to which the faults extend. Note that the echo of the individual baseline case fault was below the RDR but the complex interaction of a block of normal faults reveals the presence of the BDI above the detectable range. The detectability could be further improved using focusing techniques. The full BDI was modeled using the parameters of the worst case of detection performance on individual faults. In realistic scenarios, a combination of different fault characteristics is expected to increase the detection performance of the BDI.

6.4 Discussions and Conclusions

In this section, we presented an approach based on FDTD simulations to estimate the detection performance of RIME on interesting targets on Ganymede. To this purpose, we identified three interesting targets: 1) the dark terrain regolith, 2) the bright terrain dielectric profile and 3) the grooved bright terrain. For the dark terrain regolith we tested two hypotheses on the thickness of the regolith layers. The results show that the regolith produces a strong detectable near-surface reflection, which increases with the thickness. For the bright terrain, we studied the effect of depth-varying dielectric profile, as a function of temperature and impurity profiles, in comparison to a constant ice-shell dielectric permittivity. The results show that the effect of the gradually varying layered dielectric profile produces a radar response comparable to the constant one. For the purpose of isolating the subsurface feature, in this study we used a constant dielectric profile. Depending on the final goal, this result can support future RIME simulations by simplifying the geo-electrical modeling of Ganymede.

For the grooved bright terrain, we conducted the analysis in two levels. First, we analyzed the effect of varying the dip angle, thickness, composition and geometry of the individual normal faults expected in the grooved bright terrain, in order to understand the impact on the radar response. We compared the average normalized radar traces and radargrams of the different cases to the cluttergram and the baseline case. The results show that for most of the cases the subsurface reflection is detectable above the clutter level and the RDR. Furthermore, geometry and dip angle are the most significant factors affecting the strength of the subsurface echo. Moreover, increasing the void fraction and thickness values improves the detectability. Second, we studied the overall effect of a realistic arrangement of tilt-block normal faults to understand the detectability of the BDI. The set of faults was modeled using the parameters of the worst case of detectability (identified to be the baseline case from the individual fault analysis). The results indicate that the combined effect of the faults, which were not detectable individually, produces a detectable BDI.

Chapter 7

Performance assessment of a radar sounder for Earth observation: subsurface sounding of the polar ice caps

A radar sounder for Earth observation of the polar regions from a satellite platform can immensely support the continuous monitoring of the cryosphere in the framework of climate change. This chapter¹ presents the performance assessment of an Earth orbiting radar sounder in detecting different subsurface targets in the polar ice. To this purpose, we take advantage of the data available from airborne radargrams and reprocess them using the analog-based simulation approach, described in Chapter 4. The analysis of the simulated radargrams is used to guide the design of the EORS, in particular for the selection of the antenna gain.

7.1 Introduction

The polar ice-sheets of the Earth are important elements of the cryosphere that affect the global climate change and the sea-level rise. A number of cryo-hydrodynamic processes occurring at the base of the ice-sheets affect the stability and sea-ward flow of the ice. Direct measurement and imaging of the ice-sheet down to the base is essential for studying these processes and modeling the stability of the ice-sheets. This can be appropriately achieved by profiling the ice using RSs. Considering the need of RS data for imaging the

¹Part of this chapter appears in

Donini, Elena, Sanchari Thakur, Francesca Bovolo, and Lorenzo Bruzzone. "Assessing the Detection Performance on Icy Targets Acquired by an Orbiting Radar Sounder." In 2019 IEEE International Geoscience and Remote Sensing Symposium, pp. 997-1000. IEEE, 2019.

polar ice caps, several airborne radar sounder (ARS) campaigns have been conducted in Antarctica and Greenland [141, 97, 36]. As briefly introduced in Section 2.4.7, relevant scientific returns have been obtained from the data acquired by these campaigns, such as: (1) estimation of the thickness of the ice sheets, (2) analysis of the englacial layering, (3) detection of subglacial lakes [159], (4) analysis of basal flow regime [136], and (5) identification of basal refreezing [7]. However, these acquisition campaigns are expensive and time-consuming. Thus, the data are collected in one-time campaigns with local coverage to study specific phenomena, and repeat-pass acquisitions are not available. Due to the use of different instruments, the data quality also varies between the different campaigns. Moreover, the use of airborne platforms for radar sounding introduces artefacts in the radargram due to the movement of the aircraft.

A RS on-board an Earth-orbiting satellite platform can address these limitations posed by the airborne campaigns by providing homogeneous data quality with uniform and multi-temporal coverage of the Earth. However, at orbiting altitudes RSs are subjected to a number of performance limiting factors. The large distance between the RS and the target requires the use of lower carrier frequency, which constraints the bandwidth to a smaller value, resulting in poorer range resolution compared to ARSs. The large distance also results in higher propagation losses, larger antenna footprint, and therefore lower signal to clutter ratio. Moreover, the signal has to propagate through the Earth's ionosphere and is affected by the galactic noise, while sounding from satellite platforms. These factors can further degrade the range resolution and the subsurface SNR.

We have mentioned in Section 2.4.7 some of the studies that have proposed an EORS, operating in the HF band [16, 67, 50]. These studies were aimed at demonstrating the feasibility of detecting the subsurface targets in the polar ice by radar sounding from an orbital platform. The main challenge in the performance assessment of these targets is the high variability and uncertainty in their dielectric properties with depth and distance. The preliminary performance assessment techniques (described in Section 3.3.1) are based on a homogeneous dielectric model and therefore do not accurately estimate the scattering effects of complex targets such as the englacial layering. The electromagnetic simulators can provide accurate estimations but they require detailed models of the ice-sheet targets. Ice-core drilling can provide extensively detailed models of the ice, but they are generally limited to a depth of a few meters and sparse spatial sampling.

The other source of information for the target models is the data available from the airborne campaigns. This is a richer source due to (1) the availability of a large database of available ARS data from the multiple campaigns, (2) the widespread and full-depth coverage of the Antarctic and Arctic ice-sheets, and (3) the similarity with the actual radar signatures of complex cryospheric targets. The ARS data can be leveraged for

the simulations of the EORS data using a special case in the taxonomy of the possible applications of the analog-based simulation approach (Table 4.2). In this case, the analog and the investigated targets are the same, i.e. the Earth's polar ice caps. The ARS is the analog instrument, while the EORS is the investigated one.

In this chapter, we apply the analog-based approach to the performance assessment of an EORS, by simulating the radargrams generated by reprocessing available ARS data. Since the EORS is in the proposal phase, the goal of the assessment is to demonstrate the feasibility of the RS instrument. We have selected two targets for the analysis that are crucial for many of the scientific goals of an Earth observing sounding mission, i.e. the basal interface and the englacial layering. We aim to identify the instrument design that maximizes the detectability of these two targets in different regions of the cryosphere, i.e. the grounded ice, the floating ice and the subglacial lakes, occurring in the two major polar cryosphere systems, i.e. Antarctica and Greenland. In particular, we focus on the design of the antenna gain that maximizes the SNR of the resolvable layers and allows penetration up to the base of the ice.

The chapter is organized as follows. Section 7.2 describes the performance assessment method based on a minor adaptation of the analog-based simulation approach and the definition of performance metrics describing the detectability of the basal interface and the englacial layering. Section 7.3 presents the experimental results obtained by analyzing the simulated radargrams of the selected targets. Section 7.4 discusses the results and provides a critical analysis of the proposed performance assessment scheme.

7.2 Methodology for performance assessment

The methodology for the assessment of an EORS is represented schematically in Figure 7.1. We begin by defining the parameters of the EORS and the ARS, the noise parameters and the ARS radargram acquired over the target of interest. For each variable instrument parameter, one simulated EORS radargram is produced by following the analog-based simulation approach (described in detail in Chapter 4). In this technique, the analog radargram is reprocessed by applying a series of steps that model the differences in the acquisition scenarios of the analog and the investigated RSs. In the more general case, the analog and the investigated targets are assumed to be occurring on different planetary bodies. However, in the present application, the target represented by the analog ARS is exactly the same as the investigated one. Thus, we present a modification to the generalized analog-based simulation approach by minimizing the subjective assumptions on the target geo-electrical profile. Following this, we describe the approach to the performance assessment by analyzing the simulated radargrams.

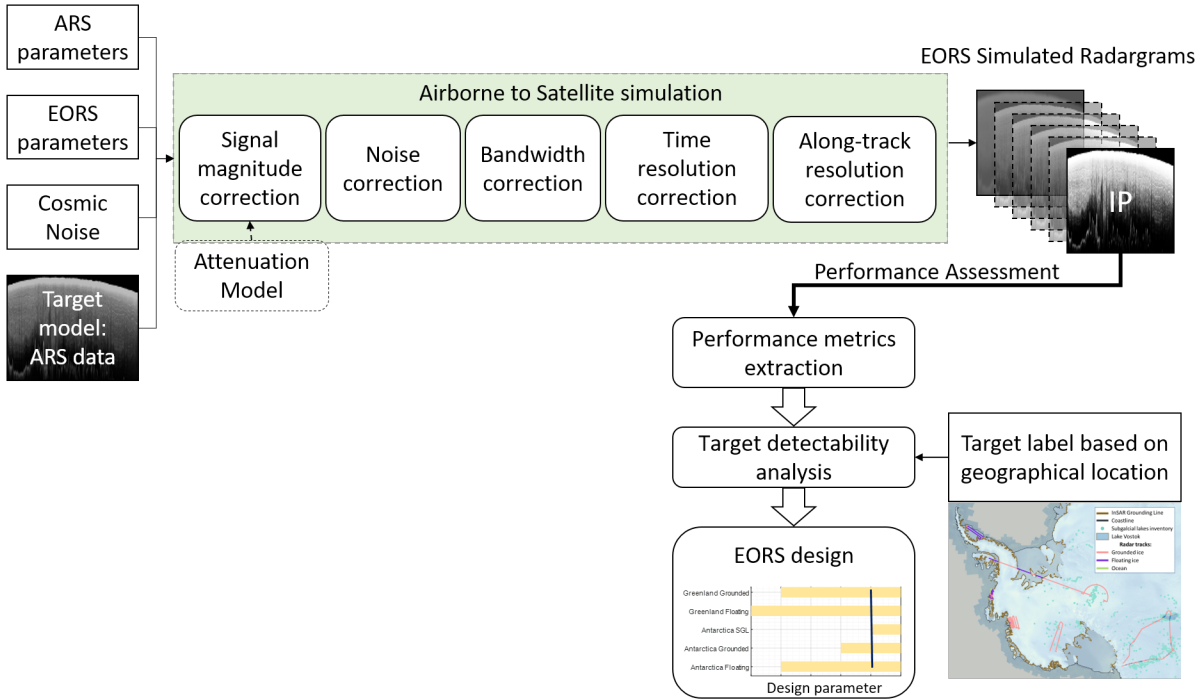


Figure 7.1: Flowchart of the proposed methodology

7.2.1 Modified analog-based simulation approach

The complex dielectric permittivity profile of the polar ice depends on several factors such as the presence of impurities mixed with ice (e.g. dust, ash, rocks, salts, acids), the crystal orientation fabric of the ice, the thermal gradient, and the distribution of melt-zones. The high variability of these factors over unknown spatial scales and the lack of geophysical models to translate them to the corresponding electrical properties makes it difficult to subjectively define the dielectric profile of the ice. In the proposed simulation approach, we leverage the target representation in the ARS data and reduce the subjective modeling to the following basic assumptions:

1. The dielectric profile (i.e. position of the dielectric interfaces and the complex permittivity values) of the ice target is the same at the frequencies of the ARS and the EORS.
2. The change in the complex permittivity with depth is not substantial over small distances (of the order of a few tens of meters).

Note that the assumptions of the analog-based simulation approach are also applicable (recalled here for ease of understanding). The performance of the simulated radargram (penetration and resolution) is constrained by the detection capability of the ARS. The

effects of clutter at the EORS footprint and the ionospheric distortions are not addressed by the simulations. These can be addressed in separate studies using well-established techniques [132, 131], and their effects can be mitigated (Section 2.3.2). The radar echo processing techniques applied to the ARS and possibly applicable to the EORS are likely to be different due to the differences in the acquisition scenarios. The simulations also do not account for the differences in the echo processing techniques. In addition to the general steps of the simulation approach, the correction for the frequency-dependent attenuation profile is introduced in the signal magnitude correction step. The details of the modification to the analog-based simulation approach are as follows.

Recalling the signal magnitude correction step, the attenuation up to an interface at depth z is given by [119]:

$$L^2(z) = \exp\left(f_c \frac{4\pi}{c\sqrt{2}} \int_0^z \sqrt{\sqrt{\text{Re}(\epsilon)^2(z) + \text{Im}(\epsilon)^2(z)} - \text{Re}(\epsilon)(z)} dz\right) \quad (7.1)$$

where f_c is the central frequency of the RS, c is the speed of light in vacuum, and $\text{Re}(\epsilon)$ and $\text{Im}(\epsilon)$ represent the real and imaginary parts of the complex dielectric permittivity profile, respectively. Let us define the target attenuation constant as:

$$\alpha(z) = \frac{4\pi}{c\sqrt{2}} \int_0^z \sqrt{\sqrt{\text{Re}(\epsilon)^2(z) + \text{Im}(\epsilon)^2(z)} - \text{Re}(\epsilon)(z)} dz \quad (7.2)$$

Thus, we obtain $L^2(z) = \exp[-f_c \alpha(z)]$. Based on the assumption that the complex dielectric permittivity does not vary significantly with the RS frequency, we can assume that $\alpha(z)$ of the analog and the investigated targets is approximately similar. Moreover, the target reflectivity profile $\rho(r_A, c_A) = R(r_A, c_A) \prod_{m=0}^{r_A-1} [1 - R(m, c_A)]^2$, also depends on the complex dielectric permittivity, and therefore is also assumed to be approximately similar for the ARS and the EORS. However, the dielectric profile is unknown, and therefore it is not possible to directly evaluate the wave propagation factor given by (4.2). We overcome this in the following way.

Let us consider the received power variation $P_{r,A}(r_A, c_A = c_o)$ over a given radar trace c_o . Hereafter, for simplicity, we refer to the single radar trace as $P_{r,A}(c_A)$. Let $\gamma_A(z)$ be the natural log-transform of $\Gamma_A(r_A, c_A = c_o)$. Combining (4.2), (7.1) and (7.2), $\gamma_A(z)$ can be represented as:

$$\gamma_A(z) = \ln\{\rho(r_A, c_A)\} - f_{c,A} \alpha(z) \quad (7.3)$$

Due to the heterogeneous nature of cryosphere targets, the dielectric profile changes with depth in a way that cannot be estimated easily. However, we assume that for a small thickness (the order of a few resolution cells), the dielectric profile is locally constant. This is generally true at RS wavelengths, since the sensitivity of the RS to small changes in the

dielectric profile depends on the bandwidth, which is relatively lower for long wavelength RSs. By applying the log-transformation, $\gamma_A(z)$ can be estimated from the ARS received power and the known instrument parameters and is given by:

$$\hat{\gamma}_A(c_A) = \ln \left[P_{r,A}(c_A) \frac{(4\pi)^3 (2H_A)^2}{P_{t,A} G_A^2 \lambda_A^2} \right] \quad (7.4)$$

Based on the assumption of the locally constant dielectric profile, we can estimate $\hat{\alpha}(z)$ as the piece-wise slope of $\hat{\gamma}_A(z)$ profile, applying the time-to-depth transform. In practice, we extract the $\hat{\alpha}(z)$ profile by applying a moving average function to $\hat{\gamma}_A(z)$. The approximate estimation of the corresponding profile of the EORS is therefore given by:

$$\hat{\gamma}_I(z) = \hat{\gamma}_A(z) + (f_{c,I} - f_{c,A})\hat{\alpha}(z) \quad (7.5)$$

The exponential of $\hat{\gamma}_I(c_A)$ for all the radar traces gives the approximate EORS wave propagation factor $\Gamma_I(r_A, c_A)$. Substituting in (4.6), the corrected received power, followed by the corrected signal magnitude of the simulated radargrams is obtained.

Note that at the flying altitude of the ARS, the data are not affected by the galactic noise. However, sounding from a satellite platform is subjected to the isotropic CMB. We evaluate the Rayleigh distributed galactic noise power, whose parameter is evaluated for an equivalent noise temperature at the EORS frequency, using the measurements reported in [22].

7.2.2 Analysis of the performances of the EORS

The next step after the simulations is the assessment of the performance of the EORS (Figure 7.1). To this purpose, we define metrics that represent the detection performance of the targets and extract them from the simulated radargrams. The metrics are compared to the mission requirements in order to analyze the detectability of the targets. The parameter that maximizes the detectability of the targets in all the different regions of the cryosphere is recommended for the design of the EORS. The ARS data is also used to define the detection requirements, since the performance of ARS is expected to be higher than the EORS due to its proximity to the target.

In this analysis, we extract two metrics representing the detectability of englacial layering and the basal interface. The metrics are estimated for each radar trace c_h of the simulated radargrams, and associated to the corresponding geographical location (latitude and longitude). The type of ice-target at a given geographical location is determined from ancillary data (described in the next subsection), and a label is assigned to each target. Thus, each radar trace is associated with a target label T and is represented as $c_h^{(T)}$. The metrics evaluated at each radar trace are grouped based on the target labels, to analyze the detection performance of each target type.

Layer detection performance

The ice-sheets and ice-shelves are characterized by linear reflectors nearly parallel to the surface, formed by seasonal accumulation and ablation of snow. The dielectric interfaces representing the englacial layers are known to have a strong contrast and a horizontal aspect. This information is well-known and used in the literature for automatic detection of the layers [23]. The first step in extracting the layer detection performance metric is the identification of the radargram pixels corresponding to layer interfaces. Due to the large number of airborne radargrams to be analysed in this work, we formulate a computationally simple and general layer detection algorithm. The algorithm consists of two main steps: (1) defining the layer detectability requirement from the ARS data, and (2) comparing the EORS layer detection with the requirement to estimate the layer detection metric. For defining the requirement, the algorithm extracts the location of the layers from the input ARS data and resamples them to the required resolution of the EORS.

First, we apply an order 4 symlet and a 2-level wavelet decomposition for denoising the ARS radargram. Next, the horizontal edges are extracted from the denoised data as the 2-level horizontal wavelet decomposition detail component, which is segmented into a binary edge image by histogram thresholding [108]. In order to enhance the horizontal connectivity of the layers, morphological closing operation is performed on the binary edge image, followed by connected component analysis, to remove isolated speckle reflections due to the coherent nature of radar data. The morphologically refined binary edges (edge mask) are compared pixel-by-pixel to the original ARS data. The edge locations for which the corresponding ARS pixel intensity is below the noise threshold (estimated from the free-space noise region of the radargram) are removed from this binary edge mask. The noise-checked edge mask is resampled to the dimensions of the simulated radargram (using the sampling and along-track correction step of the analog-based simulation approach) to obtain the layer requirement mask.

Now, the layer requirement mask is compared pixel-by-pixel to the simulated radargram to create a binary detected layers image. This image has the value 1 at pixels for which the layer requirement mask is 1 and the simulated radargram intensity is above the simulated noise threshold, and has 0 elsewhere. Let c_h denote the index of the radar traces of the simulated radargrams. For each radar trace, the layer detection performance metric $\vartheta_L(c_h)$ is given by the ratio of the total number of detected layers in the radar trace to the total number of the required ones (given by the layer requirement mask). Thus, the metric $\vartheta_L(c_h)$ represents the fraction of detectable layers per radar trace.

However, reliable scientific interpretation of the radargrams requires that the layer detection be significantly high across the different radar traces. Since different types

of ice targets represent different geophysical conditions in the englacial layering (e.g. thermal gradient, ice-sheet velocity, salinity), we analyze the detectability of the layers separately for the radar traces corresponding to each target type. The variation of the layer detectability across the radar traces is represented by the variable $N_{c_h}^{(T)}(\vartheta_L)$, which we define as the fraction of the total number of radar traces belonging to the target T for which the layer detection metric is higher than ϑ_L . The plot of ϑ_L vs $N_{c_h}^{(T)}(\vartheta_L)$ can be understood as a cumulative probability distribution of the metric ϑ_L for each target type.

The cumulative plot varies for different targets and the variable instrument parameter. Since the goal is to identify the feasible range of instrument parameters that maximizes the detectability for all types of targets, we need to project the information from the cumulative plot on to the instrument parameter vs target type parameter-space. This requires us to define a reasonable value of the metric ϑ_L and the cumulative fraction of radar traces $N_{c_h}^{(T)}(\vartheta_L)$ which should be satisfied by the design. To avoid introducing any bias due to subjective assumption on these requirements, we consider all possible pairs of ϑ_L and $N_{c_h}^{(T)}(\vartheta_L)$ and map the detectability on to the parameter-space. The instrument parameter range that satisfies the detectability for all the target types is reported for each pair of ϑ_L and $N_{c_h}^{(T)}(\vartheta_L)$. The table of the feasible range of instrument parameters can then be used by the design engineers to arrive at the optimum trade off between the design challenges and the science requirements of the mission.

Basal interface detection performance

The basal interface at the bottom of the ice-cover is important for estimating the thickness of the ice-sheets and the ice-shelves, and identifying the basal flow regime. The basal interface in cryosphere radargrams may represent the contact between ice and bedrock (for grounded ice), ice and saline water (for floating ice), or ice and fresh water (for subglacial lakes). Each of these targets represent different basal interface reflectivity and roughness characteristics, and can strongly influence the detectability.

Similar to the approach for extracting the layers, we extract the position of the basal interface as the last reflection in the ARS radargrams. We define the basal interface requirement vector, which has the value 1 if the basal interface is detectable in the ARS data, and 0 elsewhere. Next we check the SNR of the samples at the corresponding position of the basal interface in the simulated radargram, to extract the basal interface detection metric $\vartheta_B(c_h)$ for every radar trace c_h . If the SNR is above a margin and the basal requirement vector has the value 1, $\vartheta_B(c_h)$ takes the value 1. The metric is grouped by the target label. For each target and instrument parameter, the basal interface detectability is estimated in terms of the percentage of radar traces detectable in the simulated radargrams ($\vartheta_B(c_h^T) = 1$), given that they are also detectable in the corresponding ARS data (basal requirement vector also has a value 1).

Table 7.1: Proposed EORS [16] and ARS [141] parameters

Parameter	EORS	ARS
Central frequency f_c (MHz)	45	195
Bandwidth B (MHz)	10	30
Altitude H (km)	500	2 - 4
Transmitted power P_t (W)	200	1050 W
One-way antenna gain G (dB)	[4.3 - 30]	6
Along-track resolution (m)	300	30
Sampling frequency (MHz)	45	111

7.3 Experimental results

In this section, we present the experimental results obtained by applying the proposed approach to a selected set of ARS radargrams acquired the representative cryosphere targets. First we describe the dataset and the ARS and EORS instruments. Next we present the results of the EORS simulations and performance assessment of the EORS. We also present the interpretation of the results to support the selection of the EORS instrument parameter.

7.3.1 Description of the inputs

We consider an EORS with parameters similar to the one proposed by [16] and [67]. The ARS radargrams are taken from the database provided by the Centre for Remote Sensing of the Ice-Sheets (CRESIS), acquired by the airborne Multi-channel Coherent Radar Depth Sounder (MCoRDS) [141].

Table 7.1 lists the parameters of the ARS and the proposed EORS systems. The 45 MHz central frequency of the orbiting RS is suitable for the scientific requirements of subsurface sounding in icy areas [16]. Although, currently the International Telecommunication Union (ITU) does not allocate this frequency for Earth observation, its allocation is included in the preliminary agenda of the 2023 World Radiocommunication Conference. Also, it provides a good balance between the penetration capability, the range resolution, the surface roughness, and the ionospheric effects [67]. In particular, a signal with central frequency of 45 MHz and bandwidth of 10 MHz may propagate through the ionosphere under specific conditions and be able to image the cryosphere subsurface. Although these effects are not modeled in the proposed method, note that they may be present in the real radargrams even after compensation.

The transmitted power and the antenna gain can be varied, depending on the require-

ments and feasibility. At the frequency of 45 MHz, the equivalent CMB temperature is estimated to be 6320 K, and for a bandwidth of 10 MHz, the mean cosmic noise power is obtained as -120.6 dB. In this experiment, we consider six different values of the product $P_t G = \{52, 55, 57, 60, 62, 65\}$ dB, corresponding to transmitted power $P_t = 200$ W and the one-way antenna gain equal to $\{4.3, 10, 15, 20, 25, 30\}$ dB. Thus, in this experiment, the variable instrument parameter is given by the product $P_t G$.

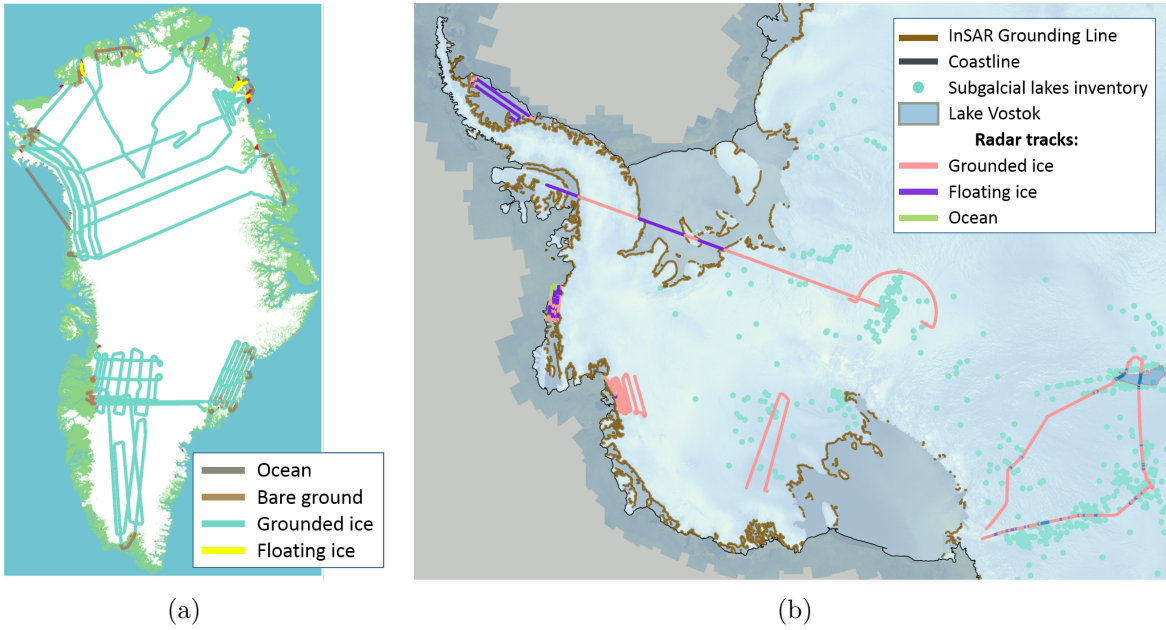


Figure 7.2: Selected ARS radargram tracks labelled by the type of target: (a) in Greenland, (b) in Antarctica.

The ARS tracks are selected in Antarctica and Greenland over grounded ice, floating ice and subglacial lakes (only in Antarctica). Figure 7.2 shows the locations of the ARS tracks of the input radargrams used in this analysis. The five target labels T for the different target types are determined with the help of several ancillary datasets available for Earth's polar regions. For Greenland, the MEaSURE's Greenland Ice Mapping Project (GIMP) ice, ocean and grounded-ice masks are used [72, 73]. For Antarctica, the Norwegian Polar Institute's Quantarctica package [90] is used to identify the target labels, which consists of the grounded ice and the floating ice boundaries dataset [71, 130]. The subglacial lakes are labelled using the subglacial lakes inventory [156, 11] and the demarcated boundary of the Vostok lake [147]. Note that the selected ARS dataset has a total track of 135,000 km, of which about 130,000 km is expected to have a detectable basal interface in the ARS data.

7.3.2 Simulated EORS radargrams

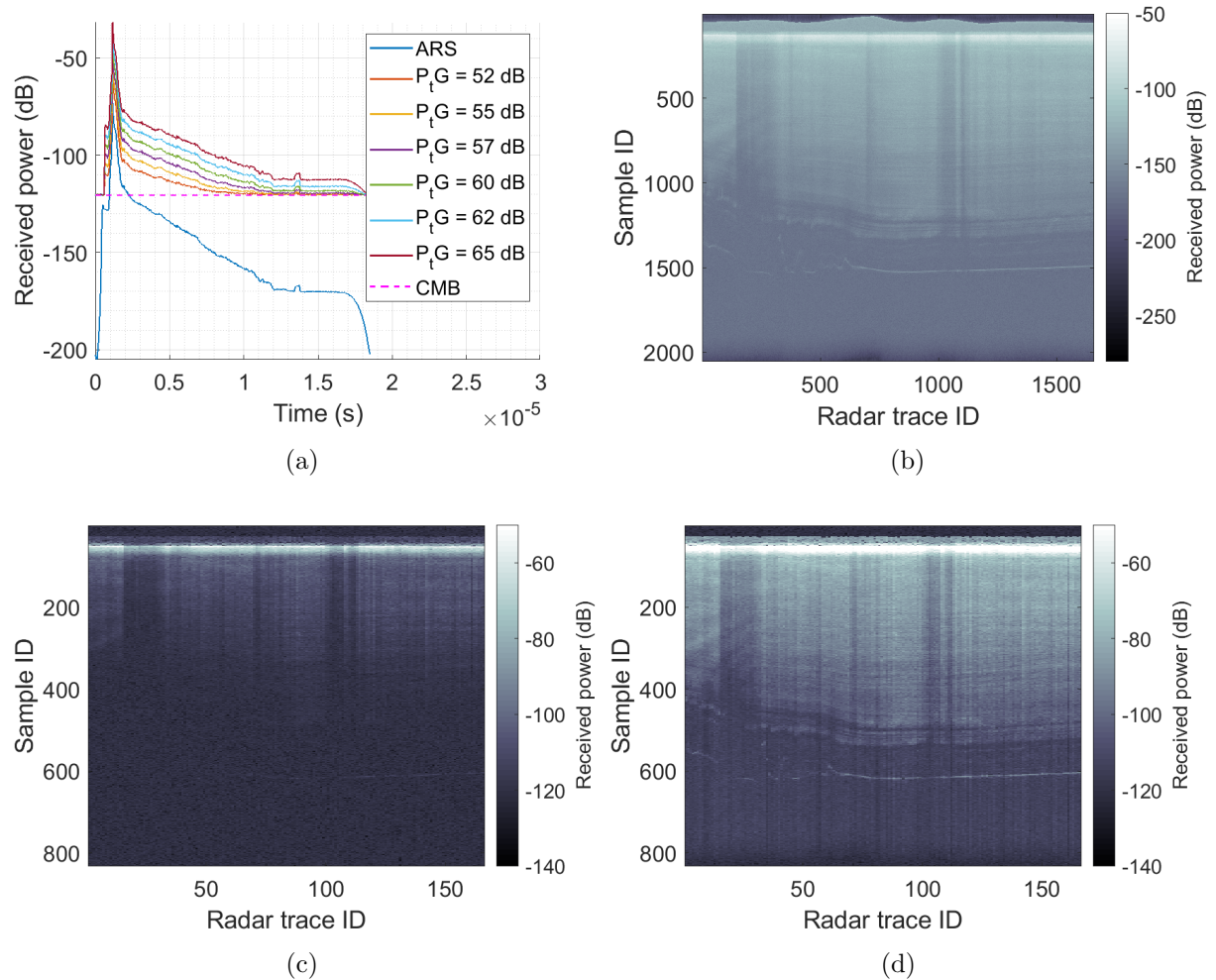


Figure 7.3: Examples of simulated radargrams and average radar trace plots corresponding to the ARS data 20131127_01_041 in East Antarctica. (a) Average radar trace plot of the ARS data and the EORS simulated radargrams for different values of $P_t G$, (b) the ARS radargram, (c) the simulated EORS radargram for $P_t G = 52$ dB, (d) the simulated EORS radargram for $P_t G = 65$ dB.

Figure 7.3(a) shows the average radar trace plots of the simulated radargrams corresponding to the selected values of $P_t G$, in comparison with the ARS radar traces. The effect of the power correction step in modifying the slope of the radar trace power, as a function of the EORS frequency is clearly visible. Further, the effect of noise correction resulting in the noise floor nearly matching the CMB level can also be observed. Figure 7.3(b-d) show examples of the input ARS radargram and the simulated radargrams for two extreme values of the selected $P_t G$ parameter. Visually we can see that increasing the $P_t G$ increases the detectability of the layers and the basal interface.

7.3.3 Layer detection performance

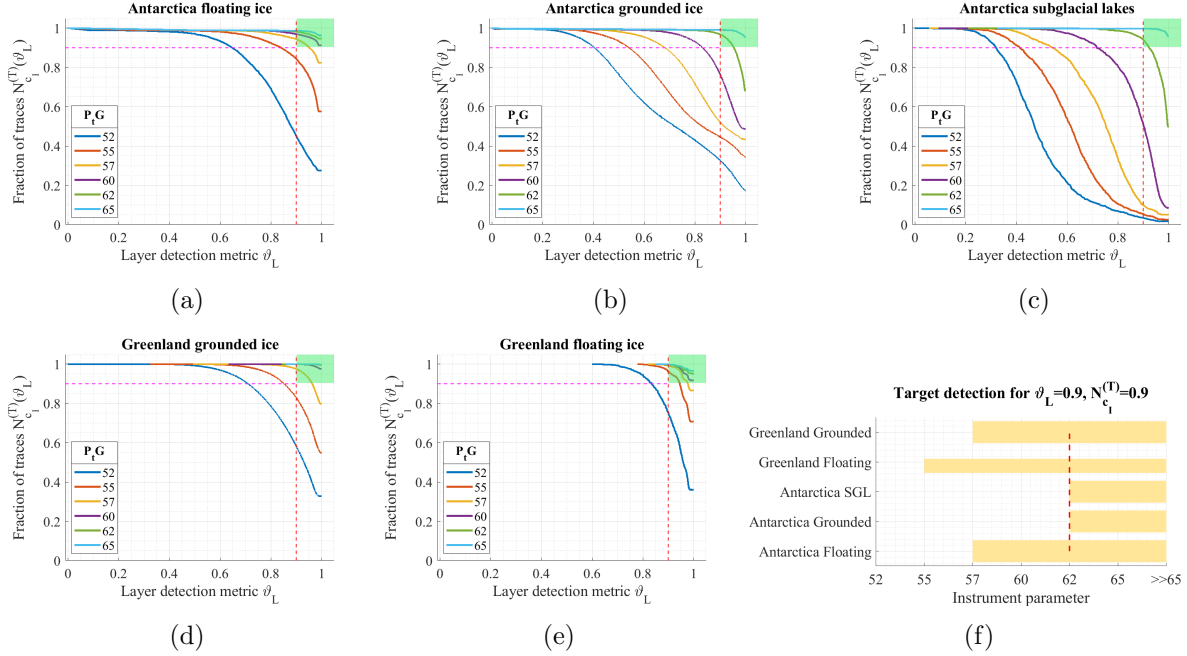


Figure 7.4: Results of the layer detection performance for different types of targets and values of P_tG . Cumulative probability distribution of the layer detection metric ϑ_L vs the fraction of radar traces having the metric greater than ϑ_L , for the target types: (a) Antarctica floating ice, (b) Antarctica grounded ice, (c) Antarctica subglacial lakes, (d) Greenland grounded ice, and (e) Greenland floating ice. For each target, we identify the instrument parameters that result in the value of detection metric greater than 0.9 (red dashed vertical line), which is satisfied by at least 0.9 of all the radar traces (magenta dashed horizontal line). The region of the cumulative distribution plots that satisfy these conditions is highlighted in the green box. The range of feasible instrument parameters obtained from each target's cumulative frequency plots are represented by the yellow bars in (f). The red dashed vertical line in (f) corresponding to $P_tG = 62$ dB indicates that, for the given conditions on the metric and the radar traces, the feasible P_tG should be greater than 62 dB for the detectability of all the five targets.

Figure 7.4(a-e) shows the cumulative probability distribution of the layer detection metric for each type of target. The horizontal axis shows the fraction of detected layers in each radar trace ϑ_L , while the vertical axis shows the fraction of radar traces for which the metric is greater than ϑ_L , i.e. $N_{c_h}^{(T)}(\vartheta_L)$. We see that the curve shifts towards the top right corner with the increase in the P_tG value, indicating an improvement in the performance. The plots show that the targets in Greenland have higher detection performance compared to those in Antarctica.

The information from the cumulative plots are projected on to the instrument parameter vs target type parameter-space for each pair of ϑ_L and $N_{c_h}^{(T)}$. Figure 7.4(f) shows an example of the projection for $\vartheta_L = 0.9$, shown by red dashed vertical lines in Figure

		Cumulative fraction of radar traces																						
		0.00	0.05	0.10	0.15	0.20	0.25	0.30	0.35	0.40	0.45	0.50	0.55	0.60	0.65	0.70	0.75	0.80	0.85	0.90	0.95	1.00		
Layer detection metric	0.00	52	52	52	52	52	52	52	52	52	52	52	52	52	52	52	52	52	52	52	52	52		
	0.05	52	52	52	52	52	52	52	52	52	52	52	52	52	52	52	52	52	52	52	52	>65		
	0.10	52	52	52	52	52	52	52	52	52	52	52	52	52	52	52	52	52	52	52	52	>65		
	0.15	52	52	52	52	52	52	52	52	52	52	52	52	52	52	52	52	52	52	52	52	>65		
	0.20	52	52	52	52	52	52	52	52	52	52	52	52	52	52	52	52	52	52	52	52	>65		
	0.25	52	52	52	52	52	52	52	52	52	52	52	52	52	52	52	52	52	52	52	52	>65		
	0.30	52	52	52	52	52	52	52	52	52	52	52	52	52	52	52	52	52	52	52	52	55	>65	
	0.35	52	52	52	52	52	52	52	52	52	52	52	52	52	52	52	52	52	52	55	55	55	>65	
	0.40	52	52	52	52	52	52	52	52	52	52	52	52	52	52	52	52	55	55	55	55	57	>65	
	0.45	52	52	52	52	52	52	52	52	52	52	52	52	52	55	55	55	55	55	55	57	57	>65	
	0.50	52	52	52	52	52	52	52	52	52	52	52	52	52	55	55	55	55	55	57	57	57	60	>65
	0.55	52	52	52	52	52	52	55	55	55	55	55	55	55	55	55	57	57	57	57	60	60	>65	
	0.60	52	52	52	52	52	55	55	55	55	55	55	57	57	57	57	57	57	57	60	60	60	>65	
	0.65	52	52	52	52	55	55	55	55	57	57	57	57	57	57	57	57	60	60	60	60	60	>65	
	0.70	52	52	52	55	55	55	57	57	57	57	57	57	57	57	57	60	60	60	60	60	62	>65	
	0.75	52	52	55	55	57	57	57	57	57	57	57	60	60	60	60	60	60	60	60	62	62	>65	
	0.80	52	52	55	57	57	57	57	60	60	60	60	60	60	60	60	60	60	60	62	62	62	>65	
	0.85	52	52	57	57	60	60	60	60	60	60	60	60	60	60	60	62	62	62	62	62	62	>65	
	0.90	52	55	60	60	60	60	60	60	60	60	60	62	62	62	62	62	62	62	62	62	65	>65	
	0.95	52	57	60	60	60	62	62	62	62	62	62	62	62	62	62	62	62	62	65	65	65	>65	
1.00	52	57	62	62	62	62	62	62	62	62	65	65	65	65	65	65	65	65	65	65	65	>65		

Figure 7.5: Feasible instrument parameter value for detectability of all cryosphere targets for different conditions on the layer detection metric and the cumulative fraction of radar traces. The red box identifies the requirements represented in Figure 7.4. The values in the matrix indicate the lower limit of the instrument parameter.

7.4(a-e), and $N_{c_h}^{(T)} = 0.9$, shown by magenta dashed horizontal lines in Figure 7.4(a-e). For ease of understanding, the region of the cumulative plots satisfying these two conditions is marked by a green box. For example, for the Antarctica subglacial lakes and grounded ice, the green box contains the plots corresponding to P_tG equal to 62 and 65. This implies that the P_tG should be at least 62 dB for the detection of these targets, as represented by the yellow bars in Figure 7.4(f). For the detectability of all the targets, P_tG should be greater than or equal to 62 dB, indicated by the minimum of the range for each target (red dashed vertical line in Figure 7.4(f)).

However, depending on the scientific objectives of the mission and the feasibility of obtaining the desired P_tG value, there may be a need to determine a right trade-off between the requirements and the instrument design. Thus, we present the feasible P_tG for all possible pairs of cumulative fraction of radar traces $N_{c_h}^{(T)}$ and layer detection metric ϑ_L , shown in Figure 7.5. Note that by increasing the P_tG over 65 dB results in marginal

improvement in the performance. For the EORS design considered here, having P_tG less than or equal to 65 dB, nearly all the layers can be detected in up to 95% of the radar traces. A P_tG value over 62 dB is a good trade-off in terms of the layer detection performance.

7.3.4 Basal interface detection performance

Table 7.2: Basal interface detection performance (in percentage) for different targets

Target	Instrument parameter P_tG [dB]					
	52	55	57	60	62	65
Antarctica floating ice	99.9	99.9	99.9	99.9	99.9	99.9
Antarctica grounded ice	86.8	93.5	97.3	99.3	99.8	99.9
Antarctica subglacial lakes	54.5	78.0	91.1	98.5	99.7	99.8
Greenland floating ice	99.9	99.9	99.9	99.9	99.9	99.9
Greenland grounded ice	83.2	93.7	99.4	99.7	99.7	99.7

For each target, Table 7.2 shows the basal interface detection performance for the different targets. The reported values are the percentage of radar traces detectable in the simulated radargrams given that they are detectable in the ARS data. The cells highlighted in purple show the combinations of instrument and target for which the basal interface is detectable in more than 99% of the radar traces. The detection performance is relatively lower for the subglacial lakes since these targets represent the deepest basal interfaces in the polar ice radargrams (up to 4.5 km in some cases). However, the assessment presented here shows that EORS having the P_tG product greater than or equal to 62 dB will be able to detect more than 99.7% of the subglacial lake basal interfaces. Note that the floating ice of Antarctica and Greenland have a very high percentage of the radar traces representing basal detectability, irrespectively of the P_tG value. Thus, the thickness of the ice-shelves in Antarctica and the floating ice-tongues in the Greenland grounding zone can be detected in nearly all the radar traces.

7.4 Discussions and Conclusions

In this chapter, we have presented the application of the analog-based simulation approach to the assessment of a RS for an Earth observation mission over the polar regions. We have presented a modification to the analog-based method in order to adapt it for the special case in which the analog and the investigated targets are the same, in this case the subsurface of the polar ice. The simulated radargrams are assessed by performance

metrics that quantify the detectability of the englacial layering and the basal interface. The proposed approach to the assessment of the EORS is demonstrated using a large number of ARS radargrams over subglacial lakes, grounded ice and floating ice in Greenland and Antarctica. The simulations are performed for different values of the instrument parameter, in this case the product of the transmitted power and the one-way antenna gain. The results show that the detection performance over all the targets is maximized for the P_tG product greater than or equal to 62 dB.

Recently, a distributed radar sounder [23] architecture has been proposed, which is based on the deployment of an array of small satellite sensors in a suitable orbital flying configuration. Such an architecture allows the synthesis of very large antenna apertures, thereby significantly improving the along-track resolution, the clutter performance and the SNR. In particular, the SNR of such a system depends on the antenna gain and transmitted power of individual sensors, and the total number of sensors. Therefore, the performance analysis presented in this chapter can support and simplify the design of the distributed architecture for an EORS.

Apart from the target dielectric properties, the off-nadir clutter and the Earth's ionosphere are very critical performance limiting factors that need to be considered for designing the EORS. Recently, there have been independent studies on the clutter performance [131] and the ionospheric effects [50, 138] to guide the design of the EORS. The clutter performance can be integrated into the proposed analysis, by complementing it with the simulation of the cluttergram over the selected ARS tracks. The masking of the englacial layering by the off-nadir clutter should be considered for evaluating the actual layer detection performance. However, for the design of the EORS, the clutter analysis is typically used to constrain the central frequency, and does not significantly influence the antenna gain. Regarding the ionosphere performance, the loss of signal strength during propagation through the ionosphere may reduce the estimated layer and basal interface detectability, which would require a higher value of the antenna gain than the value predicted in this analysis. We have tested the integration of the ionosphere simulations into the proposed simulation approach using the complex range-compressed ARS data acquired by the POLARIS [36] instrument. However, similar to the clutter performance, the ionospheric properties are used to guide the design of the central frequency and the bandwidth, and therefore do not have significant influence on the P_tG parameter.

The simulated radargrams generated by the proposed method can also be used to test the adaptability of automatic target detection algorithms developed for the ARS data to the EORS case. In Section 2.3.3, we have briefly described some of the well-established data analysis algorithms that are used to segment the ARS profiles into different target regions [75], to detect subglacial lakes [76], to map the englacial layering [28] and to

classify basal refreezing units [43]. In preparation for the scientific interpretation of the acquired EORS in its advanced phases of development, the proposed simulation approach can be used to adapt the existing algorithms for applications to the EORS radargrams.

Chapter 8

Conclusions

This chapter concludes the dissertation by presenting an overall discussion of the thesis, a brief overview of the novel contributions, and the related critical analysis. Moreover, we propose possible future developments of the works.

8.1 Overall importance of the thesis

In this thesis, we have presented four novel contributions to the field of RS simulations and performance assessment. The contributions highlight the importance of using simulations for supporting planetary missions carrying RS instruments, especially for performance evaluation, design and data interpretation. In this context, the thesis emphasizes the relevance of an accurate modeling of the target, which is the most important element in the acquisition process. The target is not only the object of the scientific analysis but also the factor limiting the detection performance. An important aspect of the target that is often ignored by conventional simulators is the volume scattering contribution to the radar response. The proposed simulation techniques have proven to be better equipped for incorporating the volume scattering effects in the simulated radargrams. Conventional techniques for evaluating the performance are based on a homogeneous and flat target model, and therefore tend to overestimate or underestimate the performance with a large margin. On the contrary, the proposed approaches based on realistic target modeling can narrow the error margin in the estimated performance, thus supporting a more efficient design of the instruments.

It is noteworthy that the proposed approaches are versatile as they can be easily adapted to any RS instrument developed for past, present or future missions, targeting subsurface observations of any planetary body. The approaches have different properties that can be adapted to different scientific requirements of the missions on the detectability of the target subsurface interfaces. These requirements determine the most suitable simulator and the performance metrics to be used for the specific application.

The proposed simulation approaches produce realistic radargrams that have similar characteristics as the real acquired data. As a consequence, the simulated data can be systematically archived in a database organized on the basis of the modeled target hypotheses. These databases can then be used to significantly improve the accuracy as well as the efficiency of extracting relevant scientific information from the data acquired during the mission according to an inversion process.

8.2 Novel contributions

In Chapter 4, we have described a simulation approach that is based on reprocessing the RS data available on geological analogs of the investigated target. The simulated radargrams are obtained by correcting for the differences in the instrument and orbit parameters as well as the target geo-electrical properties. The geometries of the prominent dielectric interfaces are assumed to be the same in the investigated and the analog targets. We have also identified the taxonomy of the cases in which the proposed approach can be applied, and demonstrated it on two of these cases. In the first case, the considered analog and investigated RSs are mounted on orbital platforms and the target is the same planetary body. We simulated the MARSIS data using the SHARAD radargrams acquired over the same region of Mars. The second case considers satellite-mounted RSs for which the analog is derived from a different planetary body. This case is demonstrated using the simulation of MARSIS data over the MFF on Mars, by reprocessing the LRS data over a lunar analogous stratified target. A good agreement was found between the simulated and real investigated MARSIS radargrams in both the cases, thus validating the proposed approach. A third case study is illustrated for simulating the RIME data over the Ganymede pedestal craters using analog SHARAD radargrams over the Mars pedestal craters. The results show that the approach has promising applications for future missions. It is worth noting that the approach can also be applied to existing and past missions, for supporting scientific studies in the field of comparative planetary geology. A comparison between the simulation time of the analog-based simulator and that of the conventional electromagnetic simulators shows that the proposed approach is much faster, thus allowing the simulation of a large number of radargrams.

In Chapter 5, we have presented an approach to the generation and analysis of databases of simulated RS data for performance prediction and target interpretation. This proposed approach is independent of the choice of the simulator and outlines the general steps to be followed for systematically organizing the complex task of simulating a large database of radar responses representing the possible scenarios expected during the acquisition. The strategy adopted in this approach involves the definition of a set of possible target geological and geophysical hypotheses, the translation of the hypotheses into possible geo-

electrical models, and the simulation of the radargrams corresponding to these models. The database of geo-electrical models and simulated radargrams thus obtained are analyzed in terms of: (1) the detectability of the subsurface echo, (2) the ability to distinguish between different hypotheses combinations, (3) the sensitivity of the RS to the acquisition variables, and (4) the separability of radargram features. The proposed approach can be easily extended to include other types of analysis, such as the design of the instrument parameters or the detectability of targets in the presence of external sources of noise. The method is illustrated using the analog-based simulations of RIME for the Ganymede pedestal craters, considering different target hypotheses on the geometry, temperature profile, impurity profile, structure and the dielectric contrast, as well as the design parameters - bandwidth and spacecraft altitude. The analysis revealed that for shallow pedestal craters, the temperature profile does not have any significant effect. The similarity analysis showed that certain variables have a strong influence on the discriminability of the hypotheses of other variables. For example, for the real part of geo-electrical models, the different hypotheses of the void fraction can be distinguished if the acquisitions are in the bright terrain, while in the dark terrain the differences are not very significant. In general, the proposed approach can be used at different phases of RS missions, by analyzing different acquisition variables to cater to the specific requirements.

An interesting application of the aforementioned approach is presented in Chapter 6 for the performance assessment of RIME in detecting complex targets on Ganymede, in particular the BDI below the grooved bright terrain. The BDI is an example of a distributed subsurface scatterer composed of a set of sub-parallel normal faults, which produce diffused volume scattering in the radargrams. The most suitable simulation technique to analyze the detectability of the BDI is the FDTD simulator, which takes as input detailed 3D geo-electrical models of the target. However, the high computational requirement of FDTD inhibits the full-scale simulation of all possible hypotheses on the target. In the thesis, we have presented a novel approach to resolve the complex target into the individual scatterers (in this case the faults) and analyzed their detectability by changing their geometry, composition, dip angle, and thickness. This gave us a preliminary idea of the relative performance for the individual hypotheses. Then, in the next level of analysis, we simulated the full-scale model corresponding to the baseline case (the most probable set of hypotheses). The results show that the BDI is detectable for the full-scale model corresponding to the baseline case, while the subsurface reflection of the individual baseline case fault is below the RDR, and hence not detectable. Such inferences are non-intuitive and demonstrate the strength of the FDTD based simulation technique.

The application of performance assessment approaches based on simulations to the design of RSs is relatively new to this field. In this regard, the last contribution of the thesis

(described in Chapter 7) has illustrated a design-oriented application of the proposed approaches. The application consists in a feasibility study of radar sounding of the polar ice caps from a satellite-mounted platform (EORS). In this case, the targets occur in a well known area and we have data available from existing airborne RS campaigns. This presents an opportunity to exploit another case in the taxonomy of the possible applications of the analog-based simulation, in which the analog and the investigated targets are the same (the polar ice caps), although the analog instrument is mounted on an aircraft. We took advantage of this relatively low uncertainty in the knowledge of the investigated target to study the other variables in the acquisition process, i.e. the instrument parameters. In order to further minimize the subjective assumptions on the target properties, we have adopted a minor modification to the proposed analog-based simulation approach by reprocessing the ARS data and generating the EORS radargrams. The performance assessment of the simulated EORS data has focused on analyzing the detectability of two major polar ice targets, i.e. the englacial layering and the basal interface. The ARS tracks were grouped into 5 target categories, namely the subglacial lakes, the grounded ice and the floating ice in Antarctica, and the grounded and the floating ice in Greenland. The database of simulated radargrams has been generated for combinations of the target categories and six possible values of the antenna gain. The analysis has been used to identify the system gain that maximizes the detection of the layers and the basal interface in all the target categories. As mentioned in Chapter 7, the design of the EORS based on novel RS architectures, such as the distributed sounder, can benefit from this analysis. Furthermore, the simulated radargrams can be used to test the adaptability of the existing ARS data analysis algorithms to the EORS case.

8.3 Discussion and critical analysis

The approaches proposed in the thesis have some limitations that should be properly understood for a correct use of them. The reliability of the analog-based simulation depends on both the availability of analog data and the fidelity between the subsurface geometry of the analog and the investigated targets. Moreover, the physical size of the analog and investigated geological features and the scale of surface roughness may be different. When analogs on different planetary bodies are considered, the ambiguities in the knowledge of the analog geo-electrical properties introduce uncertainty in the radar response. Furthermore, the upper limit to the detection performance of the investigated RS is constrained by the analog RS performance, in particular, the range resolution and the penetration depth. We recommend using analog RSs having deep penetration capability for investigating deep targets, and high resolution analog RSs for investigating small-scale details in the investigated targets. Note that the clutter in the investigated simulated data

corresponds to the antenna footprint and the surface roughness characteristics of the analog scenario. Similarly, the volume scattering contribution depends on the RS wavelength and the size distribution of the scatterers. If available, the analog instrument should be chosen as similar as possible to the investigated instrument, to improve the accuracy of the simulation.

In the context of the analysis of databases of radargrams, the accuracy of the proposed approach depends on the fidelity of the simulated radargrams to the acquired RS data. For the same hypotheses on the acquisition scenario, the simulated radargrams may differ depending on the limitations and capabilities of the different simulators. Similarly, the fidelity of the geo-electrical models to the actual target properties depends on the accuracy of our understanding of how the physical properties translate to the dielectric characteristics at the frequency range of the RS. The representativeness of the database to the real acquisition scenario also depends on the depth of our knowledge of the target, which is usually affected by uncertainties in the case of planetary exploration. The reliability of the database analysis can be enhanced by using different simulation techniques in tandem for the same target, and by supporting the geo-electrical modeling with laboratory measurements of the dielectric properties of the expected target material in the temperature range of the planetary body and the frequency range of the RS.

Regarding the use of simulation approaches based on FDTD, they present the challenge of drastically increasing the computational time and memory requirement with the increase in the size of the simulation space. In the analyzed case of RIME application, the simulations are not able to realistically represent: (1) the power received by RIME from the platform height of the JUICE spacecraft, and (2) the clutter from the real footprint size of RIME. The issue regarding the received power can be resolved by propagating the complex electromagnetic field sampled by the point sensors to the real altitude of the RIME receiver. However, the simulation of the across-track clutter even for targets as deep as 1 km is not feasible in a realistic time. For the same reason of computational complexity, it is not practical to use, as external excitation, the frequency-modulated chirp signal due to the large pulse-width (which requires a greater separation between the point sensors and the target model, thereby increasing the dimensions of the simulation space). In the thesis, we mitigated this problem by using the compressed chirp, which introduces minor differences in the sidelobe level.

Regarding the performance assessment of the EORS, the proposed approach focuses mainly on the effects of the target dielectric properties. However, the design of the EORS should also consider the effects of the off-nadir clutter and the Earth's ionosphere, which are very critical performance limiting factors. These can be easily integrated into the proposed performance assessment approach, as mentioned in Chapter 7, to guide the selection

of the central frequency and the bandwidth. Moreover, we have assumed the complex dielectric permittivity profile to be constant at the different frequencies of the ARS and the EORS, which may introduce minor errors in the estimated performance. This needs to be verified by laboratory experiments and possibly supported by field measurements in Antarctica and Greenland.

8.4 Future work

This section presents some of the possible future developments of the thesis. The analog-based simulation approach presented here takes as input processed analog radargrams and produces processed simulated radargrams. This impedes the use of the simulated data for supporting the development of the full processing chain. Furthermore, the effects of different processing applied to the analog and the investigated data cannot be corrected. An improved version of the analog-based simulator can be developed by reprocessing the raw complex analog radargram to take into account the differences in the unprocessed echo characteristics, to simulate the raw investigated data.

Another possible extension of the thesis is the development of an integrated simulator that combines the advantages of the realistic target models from the analogs and the accurate representation of the signal characteristics from the electromagnetic simulators. A possible solution can involve inversion of the analog radargram to extract the analog geo-electrical model. This can be used to support the modeling of the investigated target, by changing the dielectric permittivity and scaling the geometry of the analog model. The analog-inspired target models can be further improved by integration with the available surface elevation data of the investigated target, and addition of other dielectric interface that are not expected in the analog scenario. The investigated geo-electrical models thus generated can be used by electromagnetic simulators to produce more accurate and better controlled radar response.

The generation and analysis of the database of geo-electrical models can be improved with the help of laboratory measurements of the dielectric properties of planetary materials, at different temperatures and frequencies. In particular, the geo-electrical modeling of the RIME targets can be made more reliable if the subjective assumptions are replaced by dielectric measurements of low temperature ice mixed with dust and expected ionic compounds.

The proposed techniques can be applied to the development of future RS missions (e.g. RIME, REASON, and SRS), to the proposal of new RS instruments (e.g. EORS), and to the design of novel RS systems (e.g. the distributed RS [26]). For instance, recently simulations have been used to study the feasibility of a RS for lunar lava tubes detection [27]. RS data can be acquired over the terrestrial lava tubes (e.g. Surtshellir in Iceland)

and the analog-based simulation approach can be used to simulate the data for the lunar lava tube sounder.

The approach based on similarity analysis between radargrams can be extended to improve the inversion of the data from existing RSs on Mars and the Moon. For a given RS data (from SHARAD, MARSIS or LRS), this can be achieved by simulating the radargram of the corresponding track by considering a range of expected target hypotheses. The simulated data having the best match with the acquired one can be back-traced to retrieve the underlying geo-electrical model, and to obtain (by inversion) the corresponding geophysical and geological properties.

Bibliography

- [1] G Alberti, S Dinardo, S Mattei, C Papa, and MR Santovito. SHARAD radar signal processing technique. In *2007 4th International Workshop on, Advanced Ground Penetrating Radar*, pages 261–264. IEEE, 2007.
- [2] AP Annan. GPR—History, trends, and future developments. *Subsurface sensing technologies and applications*, 3(4):253–270, 2002.
- [3] AP Annan and SW Cosway. Ground penetrating radar survey design. In *5th EEGS Symposium on the Application of Geophysics to Engineering and Environmental Problems*, pages cp–210. European Association of Geoscientists & Engineers, 1992.
- [4] AP Annan and JL Davis. Impulse radar sounding in permafrost. *Radio Science*, 11(4):383–394, 1976.
- [5] VR Baker and DJ Milton. Erosion by catastrophic floods on Mars and Earth. *Icarus*, 23(1):27–41, 1974.
- [6] RE Bell et al. Influence of subglacial geology on the onset of a West Antarctic ice stream from aerogeophysical observations. *Nature*, 394(6688):58, 1998.
- [7] RE Bell, K Tinto, I Das, M Wolovick, W Chu, TT Creyts, N Frearson, A Abdi, and JD Paden. Deformation, warming and softening of Greenland’s ice by refreezing meltwater. *Nature Geoscience*, 7(7):497, 2014.
- [8] RC Benson, RA Glaccum, and MR Noel. *Geophysical techniques for sensing buried wastes and waste migration*. Environmental Monitoring Systems Laboratory, 1983.
- [9] Y Berquin, A Herique, W Kofman, and E Heggy. Computing low-frequency radar surface echoes for planetary radar using Huygens-Fresnel’s principle. *Radio Science*, 50(10):1097–1109, 2015.
- [10] MT Bland, WB McKinnon, and AP Showman. The effects of strain localization on the formation of Ganymede’s grooved terrain. *Icarus*, 210(1):396–410, 2010.

-
- [11] DD Blankenship, SP Carter, JW Holt, DL Morse, ME Peters, and DA Young. Antarctic subglacial lake classification inventory. *Boulder, Colorado USA, National Snow and Ice Data Center*, 2009.
- [12] DD Blankenship, WB Moore, DA Young, and ME Peters. Radar Imaging of Europa’s Subsurface Properties and Processes: The View from Earth. In *AGU Fall Meeting Abstracts*, 2007.
- [13] J Boisson, E Heggy, SM Clifford, K Yoshikawa, A Anglade, and P Lognonné. Radar sounding of temperate permafrost in Alaska: Analogy to the Martian midlatitude to high-latitude ice-rich terrains. *Journal of Geophysical Research: Planets*, 116(E11), 2011.
- [14] JM Bourgeois and GS Smith. A complete electromagnetic simulation of a ground penetrating radar for mine detection: Theory and experiment. In *Antennas and Propagation Society International Symposium, 1997. IEEE., 1997 Digest*, volume 2, pages 986–989. IEEE, 1997.
- [15] L Bruzzone, G Alberti, C Catallo, A Ferro, W Kofman, and R Orosei. Subsurface radar sounding of the Jovian moon Ganymede. *Proceedings of the IEEE*, 99(5):837–857, 2011.
- [16] L. Bruzzone et al. STRATUS-SaTellite Radar sounder for eArth sUb-surface Sensing. *Final Report to STRATUS Project, Italian Space Agency*, 2018.
- [17] L Bruzzone, JJ Plaut, G Alberti, DD Blankenship, F Bovolo, BA Campbell, D Castelletti, Y Gim, A-M Ilisei, W Kofman, et al. Jupiter icy moon explorer (JUICE): Advances in the design of the Radar for Icy Moons Exploration (RIME). In *Geoscience and Remote Sensing Symposium (IGARSS), 2015 IEEE International*, pages 1257–1260. IEEE, 2015.
- [18] L Bruzzone, JJ Plaut, G Alberti, DD Blankenship, F Bovolo, BA Campbell, A Ferro, Y Gim, W Kofman, G Komatsu, et al. RIME: Radar for Icy Moon Exploration. In *Geoscience and Remote Sensing Symposium (IGARSS), 2013 IEEE International*, pages 3907–3910. IEEE, 2013.
- [19] B Campbell, L Carter, R Phillips, J Plaut, N Putzig, A Safaeinili, R Seu, D Biccari, A Egan, and R Orosei. SHARAD radar sounding of the Vastitas Borealis Formation in Amazonis Planitia. *Journal of Geophysical Research: Planets*, 113(E12), 2008.
- [20] BA Campbell. *Radar remote sensing of planetary surfaces*. Cambridge University Press, 2002.

-
- [21] BA Campbell, NE Putzig, LM Carter, and RJ Phillips. Autofocus correction of phase distortion effects on SHARAD echoes. *IEEE Geoscience and Remote Sensing Letters*, 8(5):939–942, 2011.
- [22] HV Cane. Spectra of the non-thermal radio radiation from the galactic polar regions. *Monthly Notices of the Royal Astronomical Society*, 189(3):465–478, 1979.
- [23] L Carrer and L Bruzzone. Automatic enhancement and detection of layering in radar sounder data based on a local scale hidden Markov model and the Viterbi algorithm. *IEEE Transactions on Geoscience and Remote Sensing*, 55(2):962–977, 2017.
- [24] L Carrer and L Bruzzone. Solving for ambiguities in radar geophysical exploration of planetary bodies by mimicking bats echolocation. *Nature communications*, 8(1):2248, 2017.
- [25] L Carrer, R Croci, and L Bruzzone. A robust on-board tracking technique for spaceborne radar sounders. In *2015 IEEE International Geoscience and Remote Sensing Symposium (IGARSS)*, pages 1064–1067, July 2015.
- [26] L Carrer, C Gerekos, F Bovolo, and L Bruzzone. Distributed Radar Sounder: A Novel Concept for Subsurface Investigations Using Sensors in Formation Flight. *IEEE Transactions on Geoscience and Remote Sensing*, 57(12):9791–9809, 2019.
- [27] L Carrer, C Gerekos, and L Bruzzone. A multi-frequency radar sounder for lava tubes detection on the Moon: Design, performance assessment and simulations. *Planetary and Space Science*, 152:1–17, 2018.
- [28] L Carrer, Land Bruzzone. Automatic enhancement and detection of layering in radar sounder data based on a local scale hidden Markov model and the Viterbi algorithm. *IEEE Transactions on Geoscience and Remote Sensing*, 55(2):962–977, 2016.
- [29] D Castelletti, DM Schroeder, S Hensley, C Grima, G Ng, D Young, Y Gim, L Bruzzone, A Moussessian, and DD Blankenship. Clutter detection using two-channel radar sounder data. In *2015 IEEE International Geoscience and Remote Sensing Symposium (IGARSS)*, pages 1052–1055, July 2015.
- [30] S Chapman. The absorption and dissociative or ionizing effect of monochromatic radiation in an atmosphere on a rotating earth part II. Grazing incidence. *Proceedings of the physical society*, 43(5):483, 1931.

-
- [31] P Choudhary, JW Holt, and SD Kempf. Surface Clutter and Echo Location Analysis for the Interpretation of SHARAD Data From Mars. *IEEE Geoscience and Remote Sensing Letters*, 13(9):1285–1289, Sep. 2016.
- [32] V Ciarletti, B Martinat, A Reineix, JJ Berthelier, and R Ney. Numerical simulation of the operation of the GPR experiment on NETLANDER. *Journal of Geophysical Research: Planets*, 108(E4), 2003.
- [33] GC Collins, WB McKinnon, JM Moore, RT Nimmo, Fand Pappalardo, LM Prockter, and PM Schenk. Tectonics of the outer planet satellites. *Planetary Tectonics*, 11:264, 2009.
- [34] JB Coon, JC Fowler, and CJ Schafers. Experimental uses of short pulse radar in coal seams. *Geophysics*, 46(8):1163–1168, 1981.
- [35] R Croci, R Seu, E Flamini, and E Russo. The SHallow RADar (SHARAD) Onboard the NASA MRO Mission. *Proceedings of the IEEE*, 99(5):794–807, May 2011.
- [36] J. Dall et al. ESA’s polarimetric airborne radar ice sounder (POLARIS): Design and first results. *IET Radar, Sonar & Navigation*, 4(3):488–496, 2010.
- [37] JL Davis, AP Annan, G Black, and CD Leggatt. Geologic sounding using low-frequency radar. In *SEG Technical Program Expanded Abstracts 1985*, pages 5–7. Society of Exploration Geophysicists, 1985.
- [38] PJW Debye. *Polar molecules*. Chemical Catalog Company, Incorporated, 1929.
- [39] J Delpiano. Fast mutual information of two images or signals. *Mathworks Central File Exchange*, 2015.
- [40] B Demir and L Bruzzone. Hashing-Based Scalable Remote Sensing Image Search and Retrieval in Large Archives. *IEEE Transactions on Geoscience and Remote Sensing*, 54(2):892–904, Feb 2016.
- [41] LT Dolphin, WB Beatty, and JD Tanzi. Radar probing of Victorio Peak, New Mexico. *Geophysics*, 43(7):1441–1448, 1978.
- [42] E Donini, F Bovolo, C Gerekos, L Carrer, and L Bruzzone. An Approach to Lava Tube Detection in Radar Sounder Data of the Moon. In *IGARSS 2018-2018 IEEE International Geoscience and Remote Sensing Symposium*, pages 8424–8427. IEEE, 2018.
- [43] E Donini, S Thakur, F Bovolo, and L Bruzzone. An automatic approach to map refreezing ice in radar sounder data. In *Image and Signal Processing for Remote*

Sensing XXV, volume 11155, page 111551B. International Society for Optics and Photonics, 2019.

- [44] JA Doolittle and LE Asmussen. The years of applications of ground penetrating radar by the United States department of Agriculture. In *Fourth International Conference on Ground Penetrating Radar*, pages cp–303. European Association of Geoscientists & Engineers, 1992.
- [45] MAH El-Said. Geophysical prospection of underground water in the desert by means of electromagnetic interference fringes. *Proceedings of the IRE*, 44(1):24–30, 1956.
- [46] W Fa and Y Jin. Simulation of radar sounder echo from lunar surface and subsurface structure. *Science China Earth Sciences*, 53(7):1043–1055, 2010.
- [47] A Ferro and L Bruzzone. A novel approach to the automatic detection of subsurface features in planetary radar sounder signals. In *Geoscience and Remote Sensing Symposium (IGARSS), 2011 IEEE International*, pages 1071–1074. IEEE, 2011.
- [48] A Ferro and L Bruzzone. Analysis of radar sounder signals for the automatic detection and characterization of subsurface features. *IEEE Transactions on Geoscience and Remote Sensing*, 50(11):4333–4348, 2012.
- [49] A Ferro and L Bruzzone. Automatic extraction and analysis of ice layering in radar sounder data. *IEEE Transactions on Geoscience and Remote Sensing*, 51(3):1622–1634, 2013.
- [50] A Freeman, X Pi, and E Heggy. Radar sounding through the Earth’s ionosphere at 45 MHz. *IEEE Transactions on Geoscience and Remote Sensing*, 55(10):5833–5842, 2017.
- [51] GJ Freeman, AC Bovik, and JW Holt. Automated detection of near surface Martian ice layers in orbital radar data. In *Image Analysis & Interpretation (SSIAI), 2010 IEEE Southwest Symposium on*, pages 117–120. IEEE, 2010.
- [52] L Fu, S Liu, and L Liu. Numerical simulations and analysis for airborne ground penetrating radar. In *Ground Penetrating Radar (GPR), 2012 14th International Conference on*, pages 200–203. IEEE, 2012.
- [53] C Gerekos, L Bruzzone, and M Imai. A Coherent Method for Simulating Active and Passive Radar Sounding of the Jovian Icy Moons. *IEEE Transactions on Geoscience and Remote Sensing*, 2019.

-
- [54] C Gerekos, A Tamponi, L Carrer, D Castelletti, M Santoni, and L Bruzzone. A Coherent Multilayer Simulator of Radargrams Acquired by Radar Sounder Instruments. *IEEE Transactions on Geoscience and Remote Sensing*, pages 1–17, 2018.
- [55] GK Gilbert. *The Moon's face: A study of the origin of its features*. Philosophical Society of Washington, 1893.
- [56] S Gogineni, D Tammana, D Braaten, C Leuschen, T Akins, J Legarsky, P Kanagaratnam, J Stiles, C Allen, and K Jezek. Coherent radar ice thickness measurements over the Greenland ice sheet. *Journal of Geophysical Research: Atmospheres*, 106(D24):33761–33772, 2001.
- [57] O Grasset, MK Dougherty, A Coustenis, EJ Bunce, C Erd, D Titov, M Blanc, A Coates, P Drossart, LN Fletcher, H Hussmann, R Jaumann, N Krupp, J P Lebreton, O Prieto-Ballesteros, P Tortora, F Tosi, and T Van Hoolst. JUperiter ICy moons Explorer (JUICE): An ESA mission to orbit Ganymede and to characterise the Jupiter system. *Planetary and Space Science*, 78:1–21, 2013.
- [58] R Greeley. The role of lava tubes in Hawaiian volcanoes. *US Geol. Surv. Prof. Pap.*, 1350(2):1589–1602, 1987.
- [59] RE Grimm, E Heggy, S Clifford, C Dinwiddie, R McGinnis, and D Farrell. Absorption and scattering in ground-penetrating radar: Analysis of the Bishop Tuff. *Journal of Geophysical Research: Planets*, 111(E6), 2006.
- [60] T Hagfors. Backscattering from an undulating surface with applications to radar returns from the Moon. *Journal of Geophysical Research*, 69(18):3779–3784, 1964.
- [61] JW Head and R Roth. Mars pedestal crater escarpments: Evidence for ejecta-related emplacement. In *Planetary Cratering Mechanics*, volume 259, page 50, 1976.
- [62] E Heggy, SM Clifford, RE Grimm, CL Dinwiddie, JA Stamatakos, and SH Gonzalez. Low-frequency radar sounding investigations of the North Amargosa Desert, Nevada: A potential analog of conductive subsurface environments on Mars. *Journal of Geophysical Research: Planets*, 111(E6), 2006.
- [63] E Heggy, SM Clifford, RE Grimm, CL Dinwiddie, DY Wyrick, and BE Hill. Ground-penetrating radar sounding in mafic lava flows: Assessing attenuation and scattering losses in Mars-analog volcanic terrains. *Journal of Geophysical Research: Planets*, 111(E6), 2006.
- [64] E Heggy, A Fadlelmawla, TG Farr, and M Al-Rashed. Probing Shallow Aquifers in Northern Kuwait Using Airborne Sounding Radars. In *AGU Fall Meeting Abstracts*, 2011.

-
- [65] E Heggy, Ph Paillou, F Costard, N Mangold, G Ruffie, F Demontoux, G Grandjean, and JM Malezieux. Local geoelectrical models of the Martian subsurface for shallow groundwater detection using sounding radars. *Journal of Geophysical Research: Planets*, 108(E4), 2003.
- [66] E Heggy, EM Palmer, W Kofman, SM Clifford, K Richter, and A Hérique. Radar properties of comets: Parametric dielectric modeling of Comet 67P/Churyumov–Gerasimenko. *Icarus*, 221(2):925–939, 2012.
- [67] E Heggy, PA Rosen, R Beatty, T Freeman, and Y Gim. Orbiting Arid Subsurface and Ice Sheet Sounder (OASIS): Exploring desert aquifers and polar ice sheets and their role in current and paleo-climate evolution. In *2013 IEEE International Geoscience and Remote Sensing Symposium-IGARSS*, pages 3483–3486. IEEE, 2013.
- [68] E Heggy, G Scabbia, L Bruzzone, and RT Pappalardo. Radar probing of Jovian Icy Moons: Understanding subsurface water and structure detectability in the JUICE and Europa missions. *Icarus*, 2016.
- [69] VJ Hipkin, MA Voytek, MA Meyer, R Léveillé, and SD Domagal-Goldman. Analogue sites for Mars missions: NASA’s Mars Science Laboratory and beyond: Overview of an international workshop held at The Woodlands, Texas, on March 5-6, 2011, 2013.
- [70] VM Horner and R Greeley. Pedestal craters on Ganymede. *Icarus*, 51(3):549–562, 1982.
- [71] I Howat. MEaSURES Antarctic Boundaries for IPY 2007-2009 from Satellite Radar, Version 2. Boulder, Colorado USA. NASA National Snow and Ice Data Center Distributed Active Archive Center. Accessed:2019-09-12.
- [72] I Howat. MEaSURES Greenland Ice Mapping Project (GIMP) Land Ice and Ocean Classification Mask, Version 1. Boulder, Colorado USA. NASA National Snow and Ice Data Center Distributed Active Archive Center. Accessed:2019-09-12.
- [73] IM Howat, A Negrete, and BE Smith. The Greenland Ice Mapping Project (GIMP) land classification and surface elevation data sets. *The Cryosphere*, 8(4):1509–1518, 2014.
- [74] A-M Ilisei and L Bruzzone. A model-based technique for the automatic detection of earth continental ice subsurface targets in radar sounder data. *IEEE Geoscience and Remote Sensing Letters*, 11(11):1911–1915, 2014.

-
- [75] A-M Ilisei and L Bruzzone. A system for the automatic classification of ice sheet subsurface targets in radar sounder data. *IEEE Transactions on Geoscience and Remote Sensing*, 53(6):3260–3277, 2015.
- [76] A-M Ilisei, M Khodadadzadeh, E Dalsasso, and L Bruzzone. Automatic detection of subglacial lakes in radar sounder data acquired in Antarctica. In *Image and Signal Processing for Remote Sensing XXIII*, volume 10427, page 1042718. International Society for Optics and Photonics, 2017.
- [77] Ya A Ilyushin, R Orosei, O Witasse, and B Sánchez-Cano. CLUSIM: A synthetic aperture radar clutter simulator for planetary exploration. *Radio Science*, 52(9):1200–1213, 2017.
- [78] T Kobayashi, T Ono, and H Oya. Computer simulation on investigation of lunar subsurface structure by radar sounders—Studies related to the SELENE project. *Earth Planets Space*, 2000.
- [79] W Kofman, A Herique, Y Barbin, V Barriot, J-Pand Ciarletti, S Clifford, P Edenhofer, C Elachi, C Eyraud, J-P Goutail, et al. Properties of the 67P/Churyumov-Gerasimenko interior revealed by CONSERT radar. *Science*, 349(6247):aab0639, 2015.
- [80] Anders Kusk and Jørgen Dall. SAR focusing of P-band ice sounding data using back-projection. In *2010 IEEE International Geoscience and Remote Sensing Symposium*, pages 4071–4074. IEEE, 2010.
- [81] D Landmann, D Plettemeier, C Statz, F Hoffeins, U Markwardt, WE Nagel, A Walther, A Herique, and W Kofman. Three-dimensional reconstruction of a comet nucleus by optimal control of Maxwell’s equations: A contribution to the experiment CONSERT onboard space craft Rosetta. In *2010 IEEE Radar Conference*, pages 1392–1396, May 2010.
- [82] FW Leberl, JK Thomas, and KE Maurice. Initial results from the Magellan stereo experiment. *Journal of Geophysical Research: Planets*, 97(E8):13675–13689, 1992.
- [83] JJ Legarsky, SP Gogineni, and TL Akins. Focused synthetic aperture radar processing of ice-sounder data collected over the Greenland ice sheet. *IEEE Transactions on Geoscience and Remote Sensing*, 39(10):2109–2117, 2001.
- [84] C Leuschen, S Clifford, and P Gogineni. Simulation of a surface-penetrating radar for Mars exploration. *Journal of Geophysical Research: Planets*, 108(E4), 2003.

-
- [85] R L evell e. A half-century of terrestrial analog studies: From craters on the Moon to searching for life on Mars. *Planetary and Space Science*, 58(4):631–638, 2010.
- [86] GV Levin and AH Heim. Gulliver and Diogenes-exobiological antitheses. *Life sciences and space research*, 3:105–119, 1965.
- [87] C Lewis, S Gogineni, F Rodriguez-Morales, B Panzer, T Stumpf, J Paden, and C Leuschen. Airborne fine-resolution UHF radar: an approach to the study of englacial reflections, firn compaction and ice attenuation rates. *Journal of Glaciology*, 61(225):89–100, 2015.
- [88] C Liu, H Ye, and Y Jin. Simulation of radar echoes from Mars’ surface/subsurface and inversion of surface media parameters. *Radio Science*, 49(7):473–484, 2014.
- [89] MB Lythe and DG Vaughan. BEDMAP: A new ice thickness and subglacial topographic model of Antarctica. *Journal of Geophysical Research: Solid Earth*, 106(B6):11335–11351, 2001.
- [90] K Matsuoka, A Skoglund, and G Roth. ”Quantarctica”, url=<https://doi.org/10.21334/npolar.2018.8516e961>, 2018.
- [91] DH Menzel and RS Damon. Lunar rays and the dike system of the Spanish Peaks, Colorado. *The Astronomical Journal*, 53:201, 1948.
- [92] SP Mitra, MR Chowdhury, and AB Bhattacharya. Radio emission from Jupiter as recorded by Juno spacecraft and simultaneous earth based observatories. In *2017 International Conference on Computer, Electrical & Communication Engineering (ICCECE)*, pages 1–6. IEEE, 2017.
- [93] Sh Miyamoto. A geological interpretation of the lunar surface. *Planetary and Space Science*, 2(4):256–260, 1960.
- [94] A Moreira, J Mittermayer, and R Scheiber. Extended chirp scaling algorithm for air-and spaceborne SAR data processing in stripmap and ScanSAR imaging modes. *IEEE Transactions on Geoscience and Remote Sensing*, 34(5):1123–1136, 1996.
- [95] J Mouginot, W Kofman, A Sfaeini, and A H erique. Correction of the ionospheric distortion on the MARSIS surface sounding echoes. *Planetary and Space Science*, 56(7):917–926, 2008.
- [96] A Moussessian, DD Blankenship, JJ Plaut, GW Patterson, Y Gim, DM Schroeder, KM Soderlund, C Grima, DA Young, and E Chapin. REASON for Europa. In *AGU Fall Meeting Abstracts*, 2015.

-
- [97] A Moussessian, RL Jordan, E Rodriguez, A Safaeinili, TL Akins, WN Edelstein, Y Kim, and SP Gogineni. A new coherent radar for ice sounding in Greenland. In *IGARSS 2000. IEEE 2000 International Geoscience and Remote Sensing Symposium. Taking the Pulse of the Planet: The Role of Remote Sensing in Managing the Environment. Proceedings (Cat. No. 00CH37120)*, volume 2, pages 484–486. IEEE, 2000.
- [98] Gerhard Neukum and Ralf Jaumann. HRSC: The high resolution stereo camera of Mars Express. In *Mars Express: The Scientific Payload*, volume 1240, pages 17–35, 2004.
- [99] J-F Nouvel, A Herique, W Kofman, and A Safaeinili. Radar signal simulation: Surface modeling with the Facet Method. *Radio Science*, 39(1), 2004.
- [100] DC Nunes and RJ Phillips. Radar subsurface mapping of the polar layered deposits on Mars. *Journal of Geophysical Research: Planets*, 111(E6).
- [101] DC Nunes, SE Smrekar, B Fisher, JJ Plaut, JW Holt, JW Head, SJ Kadish, and RJ Phillips. Shallow Radar (SHARAD), pedestal craters, and the lost Martian layers: Initial assessments. *Journal of Geophysical Research: Planets*, 116(E4), 2011.
- [102] GR Olhoeft. THE ELECTRICAL PROPERTIES OF PERMAFROST. 1977.
- [103] GR Olhoeft. Electrical properties from 10^{-3} to 10^{+9} HZ— Physics and chemistry. In *AIP conference proceedings*, volume 154, pages 281–298. American Institute of Physics, 1987.
- [104] O Olsson, L Falk, E Sandberg, O Forslund, and L Lundmark. Crosshole investigations—Results from borehole radar investigations. Technical report, Swedish Nuclear Fuel and Waste Management Co., 1987.
- [105] T Ono, A Kumamoto, H Nakagawa, Y Yamaguchi, S Oshigami, A Yamaji, T Kobayashi, Y Kasahara, and H Oya. Lunar Radar Sounder observations of subsurface layers under the nearside Maria of the Moon. *Science*, 323(5916):909–912, 2009.
- [106] T Ono, A Kumamoto, Y Yamaguchi, A Yamaji, T Kobayashi, Y Kasahara, and H Oya. Instrumentation and observation target of the Lunar Radar Sounder (LRS) experiment on-board the SELENE spacecraft. *Earth, Planets and Space*, 60(4):321–332, 2008.

-
- [107] SE Orosei, Rand Lauro, E Pettinelli, A Cicchetti, M Coradini, B Cosciotti, F Di Paolo, E Flamini, E Mattei, M Pajola, et al. Radar evidence of subglacial liquid water on Mars. *Science*, 361(6401):490–493, 2018.
- [108] N Otsu. A threshold selection method from gray-level histograms. *IEEE transactions on systems, man, and cybernetics*, 9(1):62–66, 1979.
- [109] TR Owen. Cavity detection using VHF hole-to-hole electromagnetic techniques. In *Proc. 1st Tech. Symp. Tunnel Detection*, pages 126–141, 1981.
- [110] SJ Palmer, JA Dowdeswell, P Christoffersen, DA Young, DD Blankenship, JS Greenbaum, T Benham, J Bamber, and MJ Siegert. Greenland subglacial lakes detected by radar. *Geophysical Research Letters*, 40(23):6154–6159, 2013.
- [111] RT Pappalardo, GC Collins, JW Head, P Helfenstein, TB McCord, JM Moore, LM Prockter, PM Schenk, and JR Spencer. Geology of Ganymede. *Jupiter: The Planet, Satellites and Magnetosphere*, pages 363–396, 2004.
- [112] JG Patel, RT Pappalardo, JW Head, GC Collins, H Hiesinger, and J Sun. Topographic wavelengths of Ganymede groove lanes from Fourier analysis of Galileo images. *Journal of Geophysical Research: Planets*, 104(E10):24057–24074.
- [113] GW Patterson, GC Collins, JW Head, RT Pappalardo, LM Prockter, BK Lucchitta, and JP Kay. "Global geological mapping of Ganymede". *Icarus*, 207(2):845 – 867, 2010.
- [114] WJ Peeples, WR Sill, TW May, SH Ward, RJ Phillips, RL Jordan, EA Abbott, and TJ Killpack. Orbital radar evidence for lunar subsurface layering in Maria Serenitatis and Crisium. *Journal of Geophysical Research: Solid Earth*, 83(B7):3459–3468, 1978.
- [115] S Perna, G Alberti, P Berardino, L Bruzzone, D Califano, I Catapano, L Ciofaniello, E Donini, C Esposito, C Facchinetti, et al. The ASI Integrated Sounder-SAR System Operating in the UHF-VHF Bands: First Results of the 2018 Helicopter-Borne Morocco Desert Campaign. *Remote Sensing*, 11(16):1845, 2019.
- [116] ME Peters, DD Blankenship, and DL Morse. Analysis techniques for coherent airborne radar sounding: Application to West Antarctic ice streams. *Journal of Geophysical Research: Solid Earth*, 110(B6):n/a–n/a, 2005. B06303.
- [117] ME Peters, DD Blankenship, and DL Morse. Analysis techniques for coherent airborne radar sounding: Application to West Antarctic ice streams. *Journal of Geophysical Research: Solid Earth*, 110(B6), 2005.

-
- [118] ME Peters, DD Blankenship, DE Smith, JW Holt, and SD Kempf. The distribution and classification of bottom crevasses from radar sounding of a large tabular iceberg. *IEEE Geoscience and Remote Sensing Letters*, 4(1):142–146, 2007.
- [119] E Pettinelli, F Cosciotti, Band Di Paolo, SE Lauro, E Mattei, R Orosei, and G Vannaroni. Dielectric properties of Jovian satellite ice analogs for subsurface radar exploration: A review. *Reviews of Geophysics*, 53(3):593–641, 2015.
- [120] RJ Phillips, GF Adams, WE Brown Jr, RE Eggleton, P Jackson, R Jordan, WI Linlor, WJ Peeples, LJ Porcello, J Ryu, et al. Apollo lunar sounder experiment. 1973.
- [121] RJ Phillips, MT Zuber, SE Smrekar, MT Mellon, JW Head, KL Tanaka, NE Putzig, SM Milkovich, BA Campbell, JJ Plaut, et al. Mars north polar deposits: Stratigraphy, age, and geodynamical response. *Science*, 320(5880):1182–1185, 2008.
- [122] G Picardi, JJ Plaut, D Biccari, O Bombaci, D Calabrese, M Cartacci, A Cicchetti, SM Clifford, P Edenhofer, WM Farrell, et al. Radar soundings of the subsurface of Mars. *Science*, 310(5756):1925–1928, 2005.
- [123] G Picardi, S Sorge, R Seu, G Fedele, and RL Jordan. Coherent cancellation of surface clutter for radar sounding. In *IEEE 1999 International Geoscience and Remote Sensing Symposium. IGARSS'99 (Cat. No. 99CH36293)*, volume 5, pages 2678–2680. IEEE, 1999.
- [124] JJ Plaut, A Safaeinili, JW Holt, RJ Phillips, JW Head, R Seu, NE Putzig, and A Frigeri. Radar evidence for ice in lobate debris aprons in the mid-northern latitudes of Mars. *Geophysical research letters*, 36(2), 2009.
- [125] LJ Porcello, RL Jordan, JS Zelenka, GF Adams, RJ Phillips, WE Brown, SH Ward, and PL Jackson. The Apollo lunar sounder radar system. *Proceedings of the IEEE*, 62(6), June 1974.
- [126] B Rabus, M Eineder, A Roth, and R Bamler. The shuttle radar topography mission—a new class of digital elevation models acquired by spaceborne radar. *ISPRS journal of photogrammetry and remote sensing*, 57(4):241–262, 2003.
- [127] MC Raguso, M Mastrogiuseppe, R Seu, and L Piazzo. Super Resolution and Interference Suppression Technique applied to SHARAD Radar Data. In *AGU Fall Meeting Abstracts*, 2017.
- [128] RK Raney. Radar sounder: Cross-track polarimetric selectivity. In *7th European Conference on Synthetic Aperture Radar*, pages 1–4. VDE, 2008.

-
- [129] REMCOM. *xFDTD Reference Manual*, 2017.
- [130] E Rignot, S Jacobs, J Mouginot, and B Scheuchl. Ice-Shelf Melting Around Antarctica. *Science*, 341(6143):266–270, 2013.
- [131] C Riley and S Dustin. Radar Scattering in firn and its implications for VHF/UHF orbital ice sounding. In *IGARSS 2019-2019 IEEE International Geoscience and Remote Sensing Symposium*, page in press. IEEE, 2019.
- [132] F Russo, M Cutigni, R Orosei, C Taddei, R Seu, D Biccari, E Giacomoni, O Fuga, and E Flamini. An incoherent simulator for the SHARAD experiment. In *Radar Conference, 2008. RADAR'08. IEEE*, pages 1–4. IEEE, 2008.
- [133] A Safaeinili, W Kofman, JF Nouvel, A Herique, and RL Jordan. Impact of Mars ionosphere on orbital radar sounder operation and data processing. *Planetary and Space Science*, 51(7-8):505–515, 2003.
- [134] RS Saunders, GH Pettengill, RE Arvidson, WL Sjogren, WTK Johnson, and L Pieri. The Magellan Venus radar mapping mission. *Journal of Geophysical Research: Solid Earth*, 95(B6):8339–8355, 1990.
- [135] H Scheffe. *The analysis of variance*, volume 72. John Wiley & Sons, 1999.
- [136] DM Schroeder, DD Blankenship, and DA Young. Evidence for a water system transition beneath Thwaites Glacier, West Antarctica. *Proceedings of the National Academy of Sciences*, 110(30):12225–12228, 2013.
- [137] DH Scott and MH Carr. Geologic map of Mars. Technical report, 1978.
- [138] T Scuccato, L Carrer, F Bovolo, and L Bruzzone. Compensating Earth Ionosphere Phase Distortion in Spaceborne VHF Radar Sounders for Subsurface Investigations. *IEEE Geoscience and Remote Sensing Letters*, 15(11):1672–1676, 2018.
- [139] R Seu, RJ Phillips, D Biccari, R Orosei, A Masdea, G Picardi, A Safaeinili, BA Campbell, JJ Plaut, L Marinangeli, et al. SHARAD sounding radar on the Mars Reconnaissance Orbiter. *Journal of Geophysical Research: Planets*, 112(E5), 2007.
- [140] CE Shannon and W Weaver. The mathematical theory of communication. 1949. *Urbana, IL: University of Illinois Press*, 1963.
- [141] L Shi, CT Allen, JR Ledford, F Rodriguez-Morales, WA Blake, BG Panzer, SC Prokopiack, CJ Leuschen, and S Gogineni. Multichannel coherent radar depth sounder for NASA operation ice bridge. In *2010 IEEE International Geoscience and Remote Sensing Symposium*, pages 1729–1732. IEEE, 2010.

-
- [142] AH Sihvola. *Electromagnetic mixing formulas and applications*. Number 47. Iet, 1999.
- [143] RA Simpson, GL Tyler, B Häusler, R Mattei, and M Pätzold. Venus Express bistatic radar: High-elevation anomalous reflectivity. *Journal of Geophysical Research: Planets*, 114(E9), 2009.
- [144] MI Skolnik. Radar handbook. 1970.
- [145] DE Smith, MT Zuber, HV Frey, JB Garvin, JW Head, DO Muhleman, GH Pettingill, RJ Phillips, SC Solomon, HJ Zwally, et al. Mars Orbiter Laser Altimeter: Experiment summary after the first year of global mapping of Mars. *Journal of Geophysical Research: Planets*, 106(E10):23689–23722, 2001.
- [146] MG Spagnuolo, F Grings, P Perna, M Franco, H Karszenbaum, and VA Ramos. "Multilayer simulations for accurate geological interpretations of SHARAD radargrams". *Planetary and Space Science*, 59(11):1222 – 1230, 2011. Geological Mapping of Mars.
- [147] M Studinger, RE Bell, GD Karner, AA Tikku, JW Holt, DL Morse, TG Richter, SD Kempf, ME Peters, DD Blankenship, et al. Ice cover, landscape setting, and geological framework of Lake Vostok, East Antarctica. *Earth and Planetary Science Letters*, 205(3-4):195–210, 2003.
- [148] FT Ulaby, RK Moore, and AK Fung. Microwave Remote Sensing Active and Passive-Volume II: Radar Remote Sensing and Surface Scattering and Emission Theory. 1982.
- [149] AH Waite and SJ Schmidt. Gross errors in height indication from pulsed radar altimeters operating over thick ice or snow. *Proceedings of the IRE*, 50(6):1515–1520, 1962.
- [150] Z Wang, AC Bovik, HR Sheikh, EP Simoncelli, et al. Image quality assessment: from error visibility to structural similarity. *IEEE transactions on image processing*, 13(4):600–612, 2004.
- [151] TR Watters, B Campbell, L Carter, CJ Leuschen, JJ Plaut, G Picardi, R Orosei, A Safaeinili, SM Clifford, WM Farrell, et al. Radar sounding of the Medusae Fossae Formation Mars: Equatorial ice or dry, low-density deposits? *Science*, 318(5853):1125–1128, 2007.
- [152] TR Watters et al. MARSIS radar sounder evidence of buried basins in the northern lowlands of Mars. *Nature*, 444(7121):905, 2006.

-
- [153] RD Watts and AW England. Radio-echo sounding of temperate glaciers: ice properties and sounder design criteria. *Journal of Glaciology*, 17(75):39–48, 1976.
- [154] CF Wilson, RC Ghail, and T Widemann. EnVision, a Proposed ESA Venus Orbiter Mission. In *Venus Modeling Workshop*, volume 2022, 2017.
- [155] CA Wood. Ice cauldrons and basins in Iceland and on Callisto. In *Multi-ring Basins: Formation and Evolution*, volume 414, page 118, 1980.
- [156] A Wright and M Siegert. A fourth inventory of Antarctic subglacial lakes. *Antarctic Science*, 24(6):659–664, 2012.
- [157] S. Xiong et al. A new method for automatically tracing englacial layers from MCoRDS Data in NW Greenland. *Remote Sensing*, 10(1):43, 2017.
- [158] K Yee. Numerical solution of initial boundary value problems involving Maxwell’s equations in isotropic media. *IEEE Transactions on Antennas and Propagation*, 14(3):302–307, 1966.
- [159] DA Young, DM Schroeder, DD Blankenship, Scott D Kempf, and E Quartini. The distribution of basal water between Antarctic subglacial lakes from radar sounding. *Philosophical Transactions of the Royal Society A: Mathematical, Physical and Engineering Sciences*, 374(2059):20140297, 2016.

**DOCTORAL PROGRAM IN
INFORMATION AND COMMUNICATION TECHNOLOGY**

Doctoral candidate

Sanchari Thakur

Cycle	32
Thesis	Advanced methods for simulation and performance analysis of planetary radar sounder data
Advisor	Lorenzo Bruzzone (University of Trento)
Co-advisor	

1. List of publications

International Journals

1. **S. Thakur** and L. Bruzzone, "An Approach to the Simulation of Radar Sounder Radargrams Based on Geological Analogs," in IEEE Transactions on Geoscience and Remote Sensing, vol. 57, no. 8, pp. 5266-5284, Aug. 2019. doi: 10.1109/TGRS.2019.2898027
2. Perna, S.; Alberti, G.; Berardino, P.; Bruzzone, L.; Califano, D.; Catapano, I.; Ciofaniello, L.; Donini, E.; Esposito, C.; Facchinetti, C.; Formaro, R.; Gennarelli, G.; Gerekos, C.; Lanari, R.; Longo, F.; Ludeno, G.; Mariotti d'Alessandro, M.; Natale, A.; Noviello, C.; Palmese, G.; Papa, C.; Pica, G.; Rocca, F.; Salzillo, G.; Soldovieri, F.; Tebaldini, S.; **Thakur, S.** The ASI Integrated Sounder-SAR System Operating in the UHF-VHF Bands: First Results of the 2018 Helicopter-Borne Morocco Desert Campaign. Remote Sens. 2019, 11, 1845.

International Conferences

3. **Thakur, S.**, Vettor, A., & Bruzzone, L. (2019, July). Analysis of Subsurface Hypotheses through Simulation of Rime Radargrams Based on Available Analogous Data. In IGARSS 2019-2019 IEEE International Geoscience and Remote Sensing Symposium (pp. 3546-3549). IEEE.
4. Donini, E., **Thakur, S.**, Bovolo, F., & Bruzzone, L. (2019, July). Assessing the Detection Performance on Icy Targets Acquired by an Orbiting Radar Sounder. In IGARSS 2019-2019 IEEE International Geoscience and Remote Sensing Symposium (pp. 997-1000). IEEE.
5. Perna, S., Alberti, G., Berardino, P., Bruzzone, L., Califano, D., Catapano, I., Ciofaniello, L., Donini, E., Esposito, C., Facchinetti, C., Formaro, R., Gennarelli, G., Gerekos, C., Lanari, R., Longo, F., Ludeno, G., d'Alessandro, M. M., Natale, A., Noviello, C., Palmese, G., Papa, C., Pica, G., Rocca, F., Salzillo, G., Soldovieri, F., Tebaldini, S., **Thakur, S.**, "The ASI P-Band Helicopter-Borne Integrated Sounder-Sar System: Preliminary Results of The 2018 Morocco Desert Campaign" in IGARSS 2019 - 2019 IEEE International Geoscience and Remote Sensing Symposium, Yokohama, Japan: IEEE, 2019, p. 8550-8553. - ISBN: 978-1-5386-9154-0. Proceedings of: IGARSS 2019, Yokohama, Japan, Jul 28 - Aug 2. - DOI: 10.1109/IGARSS.2019.8898502
6. Sbalchiero, E., **Thakur, S.**, & Bruzzone, L. (2019, October). 3D radar sounder simulations of geological targets on Ganymede Jovian Moon. In Image and Signal Processing for Remote Sensing XXV (Vol. 11155, p. 111551J). International Society for Optics and Photonics.
7. Donini, E., **Thakur, S.**, Bovolo, F., & Bruzzone, L. (2019, October). An automatic approach to map refreezing ice in radar sounder data. In Image and Signal Processing for Remote Sensing XXV (Vol. 11155, p. 111551B). International Society for Optics and Photonics.

2. Publications in review

1. **Thakur, S.**, and L. Bruzzone, "An approach to the generation and analysis of databases of simulated radar sounder data for performance prediction and target interpretation," IEEE Transactions on Geoscience and Remote Sensing, (in review)
2. Gerekos, G., Grima, C., Steinbrügge, G., **Thakur, S.**, Scanlan, K., Young, D., Bruzzone, L., Professor Donald Blankenship, "Martian roughness analogues of European terrains and implications on radar backscatter," Icarus (in review)

8. Research/study activities

Research projects:

Italian Space Agency's RIME phase A/B1 of the JUICE mission

Italian Space Agency's RIME phase C/D of the JUICE mission

Italian Space Agency's STRATUS

Teaching

Master thesis co-supervision = 3 students

Course project co-supervision = 2 students

Bachelor thesis co-supervision = 1 student